The Nature and Characterization of M Dwarf Terrestrial Planetary Atmospheres: A Theoretical Case Study of the TRAPPIST-1 Planetary System

Andrew Peter Lincowski

A dissertation
submitted in partial fulfillment of the
requirements for the degree of

Doctor of Philosophy

University of Washington

2020

Reading Committee:

Victoria Meadows, Chair

David Crisp

Tyler Robinson

Program Authorized to Offer Degree:
Astronomy

©Copyright 2020
Andrew Peter Lincowski

University of Washington

Abstract

The Nature and Characterization of M Dwarf Terrestrial Planetary Atmospheres:
A Theoretical Case Study of the TRAPPIST-1 Planetary System

Andrew Peter Lincowski

Chair of the Supervisory Committee:
Professor Victoria Meadows
Astronomy

In the next few years, the launch of the *James Webb Space Telescope* (*JWST*), along with the construction of new ground-based observatories, will provide the opportunity to attempt atmospheric characterization of terrestrial planets in the habitable zones (Kasting et al., 1993; Seager et al., 2009; Kopparapu et al., 2013) of nearby M dwarf stars. For the first time, the assessment of habitability and the possibility of detecting biosignatures from planets around other stars will be within the capabilities of astronomical observatories. Truly Earth-like planets (i.e. orbiting a Sun-like, G-type star) are not yet accessible, and may not be until the selection, construction, and launch of a next-generation space telescope, such as LUVOIR (Roberge and Moustakas, 2018) or HabEx (Gaudi et al., 2018), which are under consideration for potential prioritization by the 2020 Decadal Survey on Astronomy and Astrophysics. In the immediate future, it will only be possible to characterize the atmospheres of Earth-sized planets that orbit M dwarf hosts, because the methods of observation for imminent observatories favor shorter-period planets and stronger signal can be achieved with smaller star-planet size ratios.

However, planets orbiting M dwarfs face an evolutionary history very different than a planet like Earth, orbiting a Sun-like, G-type star. Additionally, these stars go through a much longer superluminous pre-main-sequence phase than G dwarfs, which can drive ocean loss via the runaway greenhouse effect, subsequent photolysis from stellar UV radiation, and, finally, permanent

loss of hydrogen to space. As a result, M dwarf habitable zone planets can be stripped of their volatiles before life could originate and proliferate (Luger and Barnes, 2015). Even if life did originate, M dwarf stars generally exhibit intense levels of high-energy activity throughout their main-sequence lifetimes, so the planetary surface can experience much more extreme irradiation than the early Earth environment (Segura et al., 2005, 2010; Ranjan et al., 2017; Tilley et al., 2019).

Additionally, because M dwarfs are small and dim, planets must orbit much closer to the star than Earth does to the Sun to allow for the possibility of liquid water on their surfaces. This proximity increases the probability for such planets to be synchronously rotating with their host star (e.g. Kasting et al., 1993; Ribas et al., 2016), which may result in large temperature differences between the permanent day and permanent night sides, raising the possibility of atmospheric collapse on the night side of the planet (Joshi et al., 1997).

Despite these challenges, the observational advantages of M dwarf stars mean that they will be the first place to search for habitability and life outside the Solar System. Several small planets have recently been discovered in the habitable zones around nearby M dwarf stars during ground-based surveys (e.g. TRAPPIST, MEarth, and HARPS). Of these, I focus on the TRAPPIST-1 planetary system, whose seven Earth-sized planets provide an unprecedented opportunity to study planetary evolution and habitability in a single system, which includes three planets in the traditional habitable zone. As TRAPPIST-1 is an ultra-cool dwarf star (spectral type M8V), its planets are more easily amenable to near-term observations compared to other terrestrial-sized planet discoveries around earlier-type stars (e.g. LHS 1140 b and c, Ross 128 b), because of the exceptionally diminutive size of the TRAPPIST-1 star (barely larger than Jupiter), maximizing the planet-to-star signal.

To support upcoming observations of nearby M dwarf planetary systems, I provide foundational modeling efforts to understand the range of likely environmental states of the TRAPPIST-1 planets and how to spectrally discriminate them. I developed a versatile, coupled climate-photochemical model for terrestrial exoplanets. Using this model, I present self-consistent climate-photochemical

model atmospheres of a wide range of potential TRAPPIST-1 planetary states, and generate and analyze synthetic spectra of these planets to identify observational features that can be used to distinguish between these planetary environmental outcomes. The modeled planetary states span evolved, post-runaway, desiccated planets with thick atmospheres, to a variety of water worlds. To assess a variety of environments that could be possible using a robust radiative transfer model, but also consider the day-night differences these planets may experience, I develop a two-column, day-night mode for an advanced 1D radiative-convective climate model, VPL Climate (Robinson and Crisp, 2018).

The diversity of possible environments modeled here supports the habitable zone as probabilistic: encompassing a range of possible states for each planet, which may or may not be habitable. Planets within the habitable zone could be either freezing, temperate, or hot, depending on their atmospheric composition. Planets beyond the outer edge, such as TRAPPIST-1 h, could also have temperate or hot atmospheres, if they have a Venus-like greenhouse effect. Potential observational discriminants for these atmospheres in transmission and emission spectra are influenced by photochemical processes and aerosol formation. The atmospheric states simulated here include collision-induced oxygen absorption (O_2-O_2), and O_3, CO, SO_2, and H_2O absorption features, with transit signals of up to 200 ppm, well above the 20–30 ppm putative noise floor of *JWST* in the NIR (Greene et al., 2016). These simulated transmission spectra are consistent with K2, *Hubble Space Telescope*, and *Spitzer Space Telescope* observations of the TRAPPIST-1 planets.

To help discriminate ambiguous observations, including the detection of water vapor, I assess the possibility of detecting isotopic evidence for ocean loss in transit transmission spectra. In the Solar System, differences in isotopic abundances between the Solar abundance and planetary atmospheres have been used to infer the history of ocean loss and atmospheric escape (e.g. Venus, Mars). I show that H_2O and CO_2 isotopologues could similarly be used as indicators of past ocean loss and atmospheric escape of terrestrial planets around M dwarfs. These measurements may be possible with *JWST* if the escape mechanisms and resulting isotopic fractionation were similar to

Venus, but exist in a more transparent atmosphere, such as N_2-dominated, or an O_2-dominated atmosphere that may result from extreme water loss. In these atmospheres, isotopologue bands are detectable throughout the near-infrared (1–8 μm), especially 3–4 μm. These are not likely detectable in CO_2-dominated atmospheres because the saturated CO_2 bands obscure key HDO features, and at the high temperatures exhibited by a Venus-like atmosphere, the ro-vibrational quantum states of the rare isotopologues are not occupied (see e.g. Mollière and Snellen, 2019). The results of spectral modeling suggest that the detection of O_2-O_2 along with increased fractionation in HDO relative to Earth would be strong evidence that a planet is not habitable, despite detections of atmospheric oxygen and water, which would normally be considered evidence of an inhabited Earth-like world.

In the last investigation of this dissertation, I use the newly-developed two-column model to assess observational implications for planets with large day–night temperature contrasts. I find that transit transmission spectroscopy is not likely sensitive to large surface temperature variations. Together with the importance of photochemistry on atmospheric observables demonstrated in this thesis and previous work, these results imply that 1D coupled climate-photochemical models are ideally suited for predicting and assessing upcoming terrestrial planet observations for *JWST*. With both 1D and two-column models, I present several simple climate validation tests compared with 3D GCM results. To demonstrate the flexibility of this model, I simulate a selection of synchronously-rotating planets with Earth-like, Venus-like, O_2, and H_2-dominated cases. I present two-column model atmospheres with globally-averaged photochemical results, and associated observational discriminants in transit transmission spectra. For hotter atmospheres, I produce day–night phase amplitude variation spectra (Selsis et al., 2011), made possible by the two-column model.

The results of this dissertation have demonstrated a small but diverse selection of plausible planetary conditions given current knowledge of planetary processes that may exist on other worlds, which nonetheless have provided a broad exploration of environmental states for the

TRAPPIST-1 planets. The combined studies point to multiple spectral discriminants to identify past ocean loss and to differentiate between different environmental states. Although spatially-resolved models (from two columns to full 3D GCMs) can assess the climate distribution on a planet, transit transmission spectra are most sensitive to regions of the atmosphere where temperature gradients are usually small, and where the primary processes are radiation and photochemistry, a regime ideally suited to 1D coupled climate-photochemical models. The spectral discriminants presented here and in future work will help guide and interpret upcoming observations of planets in and around the habitable zones of M dwarf stars, particularly the TRAPPIST-1 system, which is already scheduled for observation with *JWST*.

TABLE OF CONTENTS

LIST OF FIGURES

LIST OF TABLES

ACKNOWLEDGMENTS

The work in this dissertation would not have been possible without the sponsorship, support, and guidance of many people, of whom I owe a debt of gratitude. I thank my primary advisor, Victoria Meadows, for the sponsorship, support, and many hours of effort she spent with me in meetings, talking science, and writing papers. I thank my two other advisors, David Crisp and Tyler Robinson, for responsive support in the fine details of model development and atmospheric physics, and in great conversations, which often meandered into many other interesting topics.

No one works for free, and so I also thank the NASA Astrobiology Program for support through the NASA Astrobiology Institute Virtual Planetary Laboratory, and the NASA Planetary Sciences Directorate through the Earth and Space Fellowship (NESSF) program. I also thank the John Mather Nobel Scholar program, which provided early support and funded my first conference trip, as an undergraduate.

At the University of Washington, I would like to thank the students and members of the Astrobiology Program and Virtual Planetary Laboratory, who drew me to attend graduate school at UW, and with whom I shared many great conversations at colloquia, speaker lunches, and field workshops. In particular, I would like to thank my longtime office-mate, Jacob Lustig-Yaeger, for his unwavering positivity and support, and for our many great and fruitful science discussions. I would also like to thank Chris Suberlak, Hayden Smotherman, Sebastian Demasi, and Kim Bott for time away from science when it was needed the most.

I am grateful to several other UW Astronomy faculty, Julianne Dalcanton, Tom Quinn, and Eric Agol, for personal and scientific support over the years. Outside of UW, I owe thanks to Aki Roberge, with whom I interned at NASA Goddard Space Flight Center before coming to UW and whose support and advice over the years have always been helpful and astute. Thanks to Brian

Seastone, whose encouragement and permission for a leave of absence allowed me the opportunity for that internship, and without which I would never have been admitted to graduate school.

I owe a deep debt of gratitude to my family and friends outside of academia, without whose support I would never have survived graduate school.

Chapter 1

INTRODUCTION

Within the next few years, small planets in and around the habitable zones of M dwarf host stars will be observed with extremely large ground- and space-based telescopes to assess their atmospheres for markers of habitability, or even for signs of life (Rodler and López-Morales, 2014; Cowan et al., 2015; Snellen et al., 2015; Quanz et al., 2015; Greene et al., 2016; Lovis et al., 2017). These will likely be the only types of small planets amenable to atmospheric characterization in the next two decades. Because these small, cool, yet UV-active M dwarf stars affect the evolution and bulk and trace gas composition of planetary atmospheres differently than G dwarf stars like our Sun, rigorous atmospheric climate, photochemical, and spectral modeling can improve planning and interpreting these observations.

1.1 Detecting and Characterizing Exoplanets

Astronomers have proven wildly successful at detecting planets outside of our Solar System (i.e. exoplanets), including those in the respective habitable zones of other stars. The *Kepler* space telescope has been used to discover thousands of planets and planet candidates around a variety of stars (Dressing and Charbonneau, 2015; Borucki, 2016; Twicken et al., 2016; Kruse et al., 2019) using the transit method (by measuring the dip in light from a star when a planet passes in front of it, Charbonneau et al. 2007). Ground-based surveys have long been successful at discovering planets using the radial velocity method (by measuring the doppler shift in stellar spectral lines due to an orbiting mass, such as a planet). These radial velocity surveys include HARPS (Mayor et al., 2003), which helped discover the nearest possible (only 1.3 pc away) habitable zone planet candidate Proxima Centauri b (Anglada-Escudé et al., 2016) at visible wavelengths. More recent surveys, such as CARMENES (Quirrenbach et al., 2018), are using IR spectrographs, which are more sensitive to planets orbiting cooler stars. Dedicated M dwarf surveys such as MEarth (Nutzman and Charbonneau, 2008) and TRAPPIST (Gillon et al., 2011, 2013) have been successful using the transit method. The successor to *Kepler*, the *Transiting Exoplanet Survey Satellite* (TESS; Ricker et al., 2015; Barclay et al., 2018), is actively searching for planets around the nearest stars, including M dwarfs, and is covering the entire sky over a two year period. The ability to characterize planets from these discovery observations is limited; alone, the radial velocity method provides the

minimum mass of the planet, and the transit method provides the radius. In a multi-planet system, the transit method can also be used to constrain planetary masses by carefully analyzing the transit timing variations (TTVs), which results from the planet-planet gravitational interactions during the closest approaches in their orbits (Agol et al., 2005). The mass and radius together can be used to constrain the density, and thus a degenerate selection of bulk compositions (Brugger et al., 2016; Barr et al., 2018; Dorn et al., 2018; Unterborn et al., 2018a,b).

Although not yet possible for terrestrial-sized planets, characterization of giant exoplanet atmospheres has been underway for decades. Important features of exoplanetary atmospheres discovered include: detection of gas absorption, providing insight into the atmospheric constituents (e.g. Charbonneau et al., 2002; Vidal-Madjar et al., 2004); evidence of water vapor (e.g. Tinetti et al., 2007); evidence of the atmospheric temperature structure, including an inversion, from measurement of the thermal emission (e.g. Knutson et al., 2008); inference of hazes, an indication of photochemical processes that can demonstrate the interaction between the star and planetary atmosphere (e.g. Sing et al., 2011); and demonstration of the usefulness of high-dispersion spectroscopy from ground-based instruments, which can be used to "see" through the Earth's atmosphere (e.g. Snellen, 2014). However, true spectroscopic characterization of small exoplanets remains outside the capabilities of current flagship observatories, including the *Hubble Space Telescope* (e.g. Kreidberg et al., 2014; de Wit et al., 2016; de Wit et al., 2018). In the future, even when high-precision spectra are obtained from terrestrial exoplanets, the determination of whether a planet is actually habitable and could or does host life will require a sophisticated retrieval analysis of the observed spectra to understand the nature of the planetary environment. Interpretation of these data will require a breadth of knowledge of the processes that impact the observed spectra: stellar and planetary processes, spanning the disciplines of stellar astrophysics, atmospheric physics and chemistry, planetary science, geophysics, geochemistry, and biology.

1.2 Imminent Terrestrial Planet Observations

The construction of extremely large ground-based telescopes and the imminent launch of the NASA flagship *James Webb Space Telescope* (*JWST*) will provide the unprecedented opportunity

to attempt terrestrial exoplanet characterization. In particular, due to the ubiquity and diminutive sizes, M dwarf stars host a rich planetary target sample. M dwarfs are the most common type of star, comprising approximately 75% of stars in our Galaxy (Henry et al., 2006). Despite the observing biases of current detections (Gaidos and Mann, 2012), M dwarfs have no shortage of small planets, exhibiting a high occurrence rate of both multi-planet systems (e.g. Ballard and Johnson, 2016; Gillon et al., 2017), and Earth-sized planets in the habitable zone (Dressing and Charbonneau, 2015). Consequently, M dwarfs host the most potentially habitable planets of any stellar type by a large margin, and are therefore key to understanding the broader evolution of potentially habitable terrestrial planets and the distribution of life beyond the Solar System.

The small size of M dwarf stars produces a more favorable signal for both the transit and radial velocity methods, for the same size planet. M dwarf stars are faint because they are smaller and have cooler effective temperatures than the Sun, so their habitable zones are very close to the star (Kopparapu et al., 2013). For example, the habitable zone for an M8V star is as close as $\sim$0.02 au, with corresponding orbital periods as short as $\sim$4 days. These close, short-period planets allow for rapidly repeated transit observations (because the planet must orbit and pass in front of the star to be observed), and a higher amplitude radial velocity curve, due to the smaller stellar mass and short-period planetary orbits. The transit depth is similarly favorable around a small star because the transit depth is given as $\delta F/F = (R_p/R_s)^2$, where F is flux from the star and R is the planetary (p) or stellar (s) radius. The differences in transit depth as a function of wavelength, due to atmospheric gas absorption and scattering (i.e. "transit transmission spectra"), are also far more favorable for planets around smaller stars. Thus, planets orbiting smaller stars can produce higher signal-to-noise per observation, with the opportunity for a higher frequency of observations. The latter is particularly important for space-based observatories, which have more limited lifetimes.

For the best targets, upcoming facilities may have the precision required to undertake the first spectroscopic search for atmospheric water vapor and biosignature gases, such as O_2 and CH_4 (Des Marais et al., 2002; Rodler and López-Morales, 2014; Meadows, 2017; Meadows and Barnes, 2018; Schwieterman et al., 2018; Catling et al., 2018; Fujii et al., 2018; Walker et al., 2018). Of these facilities, *JWST* is particularly promising in the next few years. *JWST* is a near-to-mid-

infrared, 6.5 m segmented-mirror space telescope scheduled for launch in 2021. Although *JWST* has a coronagraph, an instrument that blocks the light of a stellar target to directly image orbiting material, it does not have the inner working angle to image habitable zone planets. Direct observation of M dwarfs will be challenging with all but the closest targets and largest telescopes (Meadows et al., 2018). However, *JWST* will employ the transit method (which does not use a coronagraph) to spectroscopically probe the atmospheres of a small number of terrestrial planets for signs of an atmosphere, habitability, and potentially for life (Morley et al., 2017; Krissansen-Totton et al., 2018; Lincowski et al., 2018; Lustig-Yaeger et al., 2019a). Because the transit method relies on the host star for signal, the most favorable wavelengths are in the bandwidth of NIR instruments (1–5 μm—near the peak of the M dwarf SED), particularly NIRSpec (Greene et al., 2016; Batalha et al., 2018; Lustig-Yaeger et al., 2019a). This wavelength range is rich in molecular absorption for assessing the atmosphere and habitability, especially absorption by H_2O, CO_2, and CH_4. While CH_4 and CO_2 together may be considered a strong signature of chemical disequilibrium, commonly attributed to life (Krissansen-Totton et al., 2016), this conclusion may not be as robust around M dwarf stars—I will show in Chapter 3 that even geological outgassing can produce Earth-like levels of methane (Lincowski et al., 2018), due to the longer photochemical oxidation timescales for planets orbiting M dwarfs (Segura et al., 2005). Furthermore, stellar flaring activity, specifically particle events that are not currently constrained for stars other than our Sun, can also drastically affect the lifetimes and abundances of key biosignature gases, such as O_3 and CH_4 (Scheucher et al., 2018; Tilley et al., 2019).

Large and extremely large ground-based observatories will also employ the transit method (Pallé et al., 2011; Rodler and López-Morales, 2014; Cowan et al., 2015; López-Morales et al., 2019), along with direct imaging techniques using high-dispersion spectroscopy with template matching (Snellen et al., 2013; Snellen, 2014; Snellen et al., 2015; Mollière and Snellen, 2019). The extremely large telescopes are the Giant Magellan Telescope (GMT, with seven 8 m monolithic mirrors), the Thirty Meter Telescope (TMT, a 30 m segmented mirror telescope), and the European Extremely Large Telescope (E-ELT, a 39.6 m segmented mirror telescope). Medium resolution observations from the ground will be limited, due to telluric absorption lines and thermal

contamination from the telescope and atmosphere. However, high-dispersion spectroscopy with template matching can be used with radial velocity shifts to directly image an atmosphere in reflectance (Snellen et al., 2013; Snellen, 2014; Snellen et al., 2015; Mollière and Snellen, 2019). In this thesis, I focus on medium-resolution transit spectra with *JWST*. All of the atmospheres modeled in this dissertation are equally suited to generating high-dispersion ($R \sim 100,000$) spectra for ground-based telescopes, the consideration of which will be left to future work.

Several planets that are likely to be terrestrial have been found orbiting M dwarfs, which would be excellent targets for observation with these upcoming facilities. These include Proxima Centauri b, a habitable zone planet candidate around the nearest star (Anglada-Escudé et al., 2016); the seven-planet TRAPPIST-1 system (Gillon et al., 2016, 2017; Luger et al., 2017c); LHS 1140 b and c (Dittmann et al., 2017; Ment et al., 2019); Ross 128 b, an Earth-sized planet in a distant 1 au orbit (Shvartzvald et al., 2017); and recently two planet candidates around the nearby Teegarden's Star (Zechmeister et al., 2019). In addition to the potential for discoveries by current dedicated M dwarf planet searches MEarth, CARMENES, TRAPPIST, and SPECULOOS, future observatories and observing programs will certainly find more small planets.

1.3 Factors Affecting Planetary Habitability

Before I introduce studies of the habitability of planets orbiting M dwarfs, here I review factors affecting planetary habitability in general. From the perspective of planetary atmospheres, habitability falls into two broad areas: 1) the creation, maintenance, and loss of the atmosphere, and 2) climate modulation and buffering. These are closely coupled to the presence or loss of surface water.

The understanding of planetary habitability begins with Earth, the single known inhabited planet. Life requires energy (either from the host star, chemical reactions, or planetary internal heat); a solvent in which to conduct reactions / metabolism; and a source of nutrients, the building blocks of molecules. Water is favored as a solvent because of its large range of stable temperatures as a liquid and its large cosmic abundance. Planetary habitability is broadly focused on how well liquid water is maintained, and how well the water interacts with minerals, the source of nutrients.

For Earth, the most abundant source of energy is the Sun. Photosynthetic life takes advantage of this energy source directly.

More fundamentally, the Solar energy absorbed by the atmosphere and surface of Earth maintains a temperate climate. To first order, the climate of the planet is controlled by the total stellar irradiance (instellation) S and the albedo A of the planet. In the absence of significant internal heat flux, this determines the effective (emitting) temperature of the planet, which can be calculated by

$$T_{\rm eq}^4 = \frac{S(1-A)}{4\sigma}, \tag{1.1}$$

where more generally the instellation at a given orbital distance d for a star of luminosity L is

$$S = \frac{L}{4\pi d^2}. \tag{1.2}$$

Apart from the size and mass (i.e. density, if known) of a planet, the first indication that can be used to determine the potential habitability of a planet is to calculate the instellation received by a planet relative to that flux received at the orbit of Earth. The flux at the orbit of Earth is called the "Solar constant," $S_\oplus = 1361$ W m^{-2} (though this value does vary with the solar cycle). The fraction of flux for a given planet compared to Earth is

$$\frac{S}{S_\oplus} = \left(\frac{1\text{au}}{d}\right)^2. \tag{1.3}$$

Many other planetary processes may affect habitability, and there is significant overlap between the categories of creating and maintaining an atmosphere, and buffering of planetary climate. Clouds, water abundance, bulk planetary characteristics, planetary and orbital dynamics, geological processes, and interactions between the star and atmosphere all affect planetary climate. These processes are discussed individually in the following sections.

1.3.1 Planetary Albedo and Clouds

The albedo given in equation (1.1) refers to the Bond albedo, not the surface albedo. The Bond albedo can be significantly affected by clouds. Though not habitable, a good example is Venus: although closer to the Sun than Earth, Venus has a cooler equilibrium temperature because the high-altitude sulfuric acid clouds are extremely reflective. Even though atmospheric cloud treatments have been employed in 1D models for decades (e.g. Manabe and Strickler, 1964; Mischna et al., 2000), typical habitability calculations have not included the radiative effects of clouds other than by an adjustment to surface albedo (Kasting et al., 1993; Kopparapu et al., 2013). The lack of radiatively-active clouds are shortcomings, because planetary climate is extremely sensitive to albedo (Kitzmann et al., 2010), particularly in 1D models (Godolt et al., 2016), though the climate results of 3D models are also sensitive to cloud formation parameterizations (Yang et al., 2013, 2014; Kopparapu et al., 2016; Bin et al., 2018; Yang et al., 2019c), which affect the planetary albedo by changing the abundance, optical depth, and distribution of clouds.

In addition to their reflectivity, which increases planetary albedo, clouds can have a warming or cooling effect depending on their properties such as composition, size, and height distribution (Kitzmann et al., 2010, 2013). Due to these properties and because clouds scatter anisotropically, estimates of the climate effects of CO_2 ice clouds on cold, potentially habitable planets, such as early Mars, have varied widely over time (c.f. Forget and Pierrehumbert, 1997; Pierrehumbert and Erlick, 1998; Mischna et al., 2000; Forget et al., 2013; Kitzmann, 2016, 2017). Clouds are computationally expensive to model and are formed from micro-scale processes (e.g. coagulation), so they remain a burdensome component of climate modelling, subject to significant uncertainty (Yang et al., 2019c).

1.3.2 Climate Buffering by Water Abundance

Planetary climate is directly coupled to surface and atmospheric water abundance. Abundant surface water allows a large reservoir from which water vapor can evaporate, and can be transported either horizontally to dry regions, or vertically. There is a direct feedback between climate and

water abundance, because the atmospheric temperature determines how much water vapor can be contained per unit volume. Because water vapor is a powerful greenhouse gas, extra water vapor causes the temperature of the gas to rise. Water vapor further controls the climate and transport from the surface to the upper atmosphere, due to the condensable nature and large latent heat of water vapor. As a saturated air parcel rises from near the ground, it expands and cools adiabatically. However, as the temperature decreases, the water carrying capacity of the air parcel also decreases, so water vapor condenses and forms a cloud and/or precipitates. Condensation releases heat, decreasing the change in temperature with altitude. This process continues until the air parcel rises to the "cold trap", above which the temperature no longer decreases. In the atmosphere of Earth, the temperature becomes stable and stratified with altitude above this height due in part to stratospheric heating caused by ozone absorption. The boundary between the lower atmosphere (troposphere) and stratosphere is the tropopause, which prevents escape of water vapor due to evaporation and transport from the surface because the cold temperature and condensation inhibits the upward transport of water vapor. Therefore, a strong (i.e. more cold) tropopause would improve habitability, while unfortunately also decreasing water vapor in the region of the atmosphere probed by transit spectroscopy.

1.3.3 Bulk and Orbital Planetary Properties

Bulk characteristics of the planet and its orbital/rotational configuration have been shown to affect habitability, by changing the column depth of the atmosphere, by changing the planetary albedo, or by influencing atmospheric dynamics. Higher planetary mass can extend habitability to higher instellation, due to the thinner atmospheric extent, which lowers the H_2O column depth (Kopparapu et al., 2014).

Planets with short-period orbits are subjected to significant tidal forces, which scale with distance as d^{-3}. These forces can slow the orbit of a planet until it becomes "tidally-locked", either in a synchronous state (1:1 spin:orbit period) or into a resonance state, like Mercury (e.g. 3:2 spin:orbit). Tidal forces can induce extreme internal heating that can also induce extreme outgassing of volatiles from the interior, such as experienced by the Jovian moon Io.

A slow rotation rate can give rise to a thick sub-stellar cloud deck due to strong convection from intense surface heating, which can allow a planet to remain temperate at a higher instellation, due to the high cloud albedo. A faster rotational state reduces this effect (Yang et al., 2014; Kopparapu et al., 2016; Way et al., 2018; Komacek and Abbot, 2019). The evaporation or advection of clouds away from the sub-stellar point may in fact be the deciding factor for the inner limit of habitability for synchronously rotating planets (Yang et al., 2013, 2014; Kopparapu et al., 2016, 2017; Way et al., 2018; Wolf, 2017; Wolf et al., 2019).

Though not likely a factor for planets orbiting M dwarfs because of tidal locking, high planetary obliquity (i.e. the tilt of the planetary rotational axis with respect to the orbital plane) shifts irradiation to polar latitudes, which affects the general circulation of the atmosphere and global climate (e.g. Hunt, 1982; Williams and Pollard, 2003; Wang et al., 2016; Nowajewski et al., 2018). This circulation regime may result in a moist stratosphere (Kang, 2019), which can make H_2O more detectable but also more easily lost by top-of-atmosphere escape processes. For M dwarf planets in particular, the reduction in sub-stellar clouds results in planetary warming, which may move the inner edge of the habitable zone to lower instellation (Wang et al., 2016). Non-zero orbital eccentricity can affect climate by causing extreme seasonal changes; on average, the long-term climate stability depends on the time-average stellar flux (Williams and Pollard, 2002), but obliquity will also affect the climate of high-eccentricity planets, resulting in several different possible climate states (Dressing et al., 2010; Linsenmeier et al., 2015; Kilic et al., 2017). Varying orbital obliquity (i.e. Milankovitch cycles, Milankovitch 1941, and other dynamical regimes) can also cause extreme ice ages, reducing long-term climate stability (Deitrick et al., 2018).

1.3.4 Geological Climate Buffering

Aside from water vapor, CO_2 is perhaps the most important greenhouse gas, and is among the most abundant atmospheric gases, comprising the bulk of the atmospheres of both Venus and Mars, and is a key greenhouse ingredient in the atmosphere of Earth. On a planet with an ocean, atmospheric CO_2 is in equilibrium with dissolved carbonates in the ocean. Long-term planetary CO_2 levels are controlled by the balance of outgassing and carbon burial deep in the ocean. This balance

is thought to be controlled by carbonate-silicate weathering (Walker et al., 1981), where runoff following surface interactions between minerals and water leads to eventual marine burial. This process is a negative feedback for CO_2 because higher temperatures from increased greenhouse forcing encourage faster weathering, and eventually faster removal of CO_2 from the atmosphere.

Carbonate burial is generally thought to require plate tectonics, because crust subduction is the primary mechanism for burial of carbon. If not buried, seafloor minerals can release carbon back into the ocean, as by "reverse weathering" (Isson and Planavsky, 2018). Because the carbonate-silicate cycle (and hence assumptions for planetary habitability) depend on plate tectonics, recent studies have investigated the bulk planetary properties and interior dynamics that give rise to plate tectonics, as opposed to a stagnant lid regime. Earth and Venus may represent evolutionary end-points of the bifurcation between these two tectonic states (Lenardic et al., 2016). Furthermore, the result of a planetary state in one regime or another may be related to evolutionary history (driven by e.g. solar irridiation), and not solely bulk properties—note that Earth and Venus are similar in bulk size and composition (Lenardic et al., 2016).

Interior dynamics can be affected by bulk properties, such as planetary mass. Planets more massive than Earth, if in a stagnant lid regime, may not outgas sufficiently to remain habitable at lower irradiation (Noack et al., 2017). Conversely, Earth-mass planets with similar CO_2 budgets may retain sufficient outgassing, even in a stagnant lid regime (Noack et al., 2017; Foley and Smye, 2018). Unfortunately, the only way to probe an exoplanetary interior remotely is by studying its atmosphere, which can only give evidence for volatiles expelled from the interior that remain in the atmosphere.

1.3.5 Star-Planet Interactions

The interactions between the host star and planet are key to understanding planetary habitability, especially as a function of stellar type and stellar activity. This interaction is not limited to total irradiation; atmospheric gas absorption, the albedo of the surface, atmospheric chemistry initiated by photolysis by UV photons, and atmospheric escape can also affect habitability. The interaction of radiation with specific atmospheric gases means that interactions between the star, atmosphere,

surface, and interior affect planetary habitability in complex ways.

The trapping of stellar energy by greenhouse gases is a well-known example of these interactions. Traditionally (for the Earth), greenhouse gases warm the surface by being transparent to incoming stellar radiation but opaque to outgoing thermal radiation, trapping the heat. For the Earth and Venus, H_2O and CO_2 together are very effective greenhouse gases, due to overlapping IR bands. The effect depends on both the stellar type and on each gas (or combination of gases). In addition to H_2O and CO_2, other greenhouse gases can potentially affect habitability (particularly at lower instellation). Thick ($\gtrsim$ 1 bar) hydrogen-dominated atmospheres can produce strong greenhouse warming due to collision-induced absorption by H_2-H_2, H_2-N_2, H_2-CH_4, H_2-CH_4, or even CH_4-CO_2 (Pierrehumbert and Gaidos, 2011; Wordsworth et al., 2013; Ramirez and Kaltenegger, 2017; Wordsworth et al., 2017), though for M dwarf planets CH_4 itself may actually be an anti-greenhouse gas (Ramirez and Kaltenegger, 2018), due to mid-atmospheric warming by strong NIR absorption.

Planetary albedo, a measure of the net effects of reflection and absorption of stellar radiation, is a function of the stellar spectrum, atmospheric composition, clouds, and the wavelength-dependent surface reflectance, which is dependent on the surface composition. A well-known effect for Earth is the ice-albedo feedback. When a planet is cold enough to form ice, the albedo increases significantly because waterice is highly reflective at visible wavelengths. This can cause runaway glaciation. However, volcanic outgassing then increases atmospheric CO_2 over time due to the reduced weathering and burial rates. Once the CO_2 greenhouse forcing warms the surface enough, the ice would melt and reduce the planetary albedo, allowing the planet to continue to warm. However, this environment would more quickly weather and bury CO_2, reducing the greenhouse forcing and cooling the climate. The balance of weathering, outgassing, and albedo can lead to climate oscillations called limit cycles (Tajika, 2003; Kadoya and Tajika, 2014; Haqq-Misra et al., 2016) that can reduce planetary habitability, due to the long periods of global glaciation. However, this effect is non-existent for planets orbiting M dwarfs. Ice has strong NIR absorption bands, so there is no large albedo difference between ice and water under a star with a NIR energy peak (Shields et al., 2013).

Atmospheric chemistry, in particular photochemistry, can drastically affect planetary climate. The existence of the sharp tropopause of Earth is in part due to ozone absorption, which creates the strong stratospheric temperature inversion. This inversion inhibits mixing between the troposphere and stratosphere (e.g. Fleming et al., 1999). Ozone is generated in a complex cycle but the source is oxygen split by UV radiation in the stratosphere. Because ozone absorbs UV in bands complementary to O_2, it provides important UV protection for surface life; without photochemistry, the surface of Earth would not be as habitable as it is today. Atmospheric chemistry also helps keep the atmosphere "clean": the primary cleaning agent in the troposphere is OH^-, a radical produced by photolysis of water vapor, which is highly reactive and destroys complex molecules.

Stellar irradiation is also the primary driver of atmospheric loss. Water vapor is ionized by FUV radiation in the mesosphere, releasing atomic hydrogen, which can diffuse upward to the exobase, from which it easily escapes. Escape is driven by a variety of stellar processes. XUV radiation ($\lambda < 912$ nm) is absorbed in the ionosphere, causing heating and higher rates of thermal escape. Stellar winds, including ion processes, can drive high escape rates. These processes are more extreme for more active stars and for planets in closer orbits.

1.3.6 Atmosphere Generation and Maintenance

Due to rapid escape timescales and the current states of the inner planets of our Solar System, terrestrial planets do not likely maintain primordial, H/He-dominated atmospheres. Instead, they slowly outgas secondary atmospheres. Due to atmospheric escape processes, lighter gases either escape or are oxidized into heavier, more stable gases, which comprise current terrestrial atmospheres (e.g. N_2, O_2, and CO_2). These gases are comparably heavy, so they do not easily escape via thermal processes and require stronger non-thermal forces to induce their escape. These gases are also more resilient to photochemical destruction, and when split are rapidly recombined in catalytic cycles.

Despite atmospheric escape processes, rocky planets that incorporated volatiles during formation can generate and maintain an atmosphere from outgassing volatiles from the interior. Whether an atmosphere can persist may be a function of atmospheric escape processes, the outgassing rate

of volatiles, and the size of the volatile reservoir. In the case of Mars, the planet was small enough that its volatile reservoir was depleted. In the case of Venus, its remaining volatile content does (at least partially) reside in its thick CO_2 atmosphere. In the case of Titan, which has a surprisingly substantial (1.5 bar) N_2 atmosphere, the CH_4 abundance has been shown to require replenishment due to the destruction timescale (Yung et al., 1984).

1.4 The Habitable Zone

Understanding of stellar and planetary processes can be integrated into the calculation of the "Habitable Zone" (HZ), defined as the region around a star for which an Earth-like planet could maintain liquid water on its surface (Huang, 1959, 1960; Kasting et al., 1993). The HZ allows newly discovered planets to be ranked for follow-up observations based on the potential for habitability. Several important assumptions are invoked within the definition of the HZ: it is assumed that habitable planets are Earth-like, so have N_2-CO_2-H_2O atmospheres with substantial liquid surface water that is in contact with a geologically-active, mineral-based crust.

Failures of these assumptions and the physical processes described earlier help define the boundaries of the habitable zone. Toward the inner edge, H_2O increases with higher temperature (because the water carrying capacity of air increases with temperature, so higher temperatures trigger more evaporation to maintain surface vapor pressure equilibrium) until triggering the runaway greenhouse effect (Ingersoll, 1969; Kasting, 1988; Kasting et al., 1993). The runaway greenhouse can occur because as temperature increases, water opacity in the IR flattens to a continuum, preventing thermal radiation from escaping to space from the warming planet. The planet must then warm until it can radiate from spectrally clear regions in the visible spectrum. The thermal emission threshold is approximately 282 W m^{-2} (Goldblatt et al., 2013). The surface temperature required to radiate in the visible and reach equilibrium is approximately 1600–1800 K (Goldblatt et al., 2013; Kopparapu et al., 2013), far too hot to be habitable. During this process, water is boiled off, can no longer condense, and can be photolyzed and lost via hydrogen escape (Hoyle, 1955; Ingersoll, 1969; Kasting, 1988; Kasting et al., 1993; Kopparapu et al., 2013).

Toward the outer edge, increasing amounts of greenhouse gases (traditionally, CO_2) are re-

quired to maintain a temperate surface until the additional gases can no longer sufficiently warm the surface. Traditional HZ calculations assume that the carbonate-silicate cycle works to maintain the ideal level of CO_2, although it may require unrealistic outgassing and burial rates. The outer limit is more specifically and optimistically defined by the "maximum greenhouse effect"—there is a CO_2 abundance at which the greenhouse warming by additional CO_2 is offset by the additional effectiveness of Rayleigh scattering (Kasting et al., 1993; Kopparapu et al., 2013). Roughly 10 bars of CO_2 are required to maintain a global average surface temperature of 273 K at the outer edge.

1.4.1 Venus and the Inner Edge

As the sister planet to Earth in terms of size and composition, Venus is a useful laboratory for understanding the failure of planetary climate buffering at the inner edge. It is optimistically assumed that Venus may have had surface liquid water approximately 1 billion years ago, before the last global resurfacing event, when the Sun was fainter (Solomon and Head, 1991; Kasting et al., 1993). Decades of theoretical work coupled with observations suggest—probably due to the increasing luminosity of the Sun—that Venus underwent a runaway greenhouse state, during which it lost its surface water. Venus likely outgassed its massive (92 bar) CO_2 atmosphere after surface weathering by water-rock interactions ceased, marking the end state of a runaway greenhouse planet.

The strongest evidence that Venus once had water is the observation of the deuterium to hydrogen (D/H) ratio from mass spectroscopy and spectral observations of water vapor absorption in the atmosphere. Assuming the inner planets of the Solar System all formed from roughly the same set of materials, they should all have formed with similar isotopic abundances. The D/H ratio of Earth, known as Vienna Standard Mean Ocean Water (VSMOW), is enhanced by a factor of about 8 compared to the solar nebula (c.f. Hagemann et al., 1970; Asplund et al., 2009). Compared to VSMOW, Venus is enhanced by another factor of 120–140 (McElroy et al., 1982; Donahue et al., 1982; Hartle and Taylor, 1983; Kumar and Taylor, 1985; De Bergh et al., 1991; Matsui et al., 2012). While the specific escape mechanism(s) remain debated, it is widely accepted that a mass-dependent difference in escape of hydrogen (compared to deuterium) from the atmosphere of Venus during or

following the runaway greenhouse phase was responsible for the enhanced D/H ratio (see reviews by Chassefière et al., 2012; Bullock and Grinspoon, 2013; Lammer et al., 2018).

1.4.2 Mars and the Outer Edge

Mars was likely habitable in the past as well: there is wide-scale evidence of past fluid flows on the surface (see review by Wordsworth, 2016). While the small size of Mars likely contributed to its loss of habitability, Mars still provides evidence for processes that control the outer edge and habitablity in general—atmospheric loss due to escape or to atmospheric collapse. Like Venus, Mars has isotopic evidence of hydrogen escape, with a D/H enhancement of ~ 4 times VSMOW (Owen et al., 1988; Villanueva et al., 2015; Encrenaz et al., 2018). The atmosphere of Mars may also be in vapor equilibrium, as CO_2 condenses to form clouds (Montmessin et al., 2007) and the polar caps of Mars grow and shrink with the seasons, with evidence suggesting the poles include CO_2 ice (Hu et al., 2012).

Originally, the conservative outer edge of the habitable zone was suggested to be the CO_2 condensation limit (Kasting et al., 1993), but this was later ignored in favor of the "maximum greenhouse" limit (Kasting et al., 1993; Kopparapu et al., 2013). Because the levels of CO_2 required to maintain the maximum greenhouse limit are idealized, it could be that atmospheric collapse is actually the limiting factor, which has been the case for system-specific 3D GCM work for planets around M dwarf stars, depending on the methods for CO_2 collision-induced absorption and the abundance of CO_2 assumed (Turbet et al., 2016; Wolf, 2017; Turbet et al., 2018), though these studies did not include dynamic ocean heat transport, which could warm the night side.

1.4.3 A Statistical Approach

With the large number of processes influencing planetary habitability, a more useful way to think about the habitable zone may be in terms of the probability of a planet being habitable given what can be observed from initial astronomical observations, such as its bulk composition and orbital parameters. For spectroscopic characterization, potential target planets could be assigned

a habitability index (Barnes et al., 2015). A true determination of the habitable zone, and its associated probability density function, will require a robust statistical sample (Bean et al., 2017).

Planets in the habitable zone are not guaranteed to be habitable or host life; the HZ helps determine which targets for observation are most likely to host *detectable* life. Because exoplanets are accessible only by remote observation methods (unlike the astrobiological targets in the Solar System), only *global* signs of habitability or life (i.e. a global biosphere) can be detected. After inferring the existence of an atmosphere (Lustig-Yaeger et al., 2019a), the first goal of terrestrial planet observations is to detect signs of habitability, which could include: the detection of surface liquid (Williams and Gaidos, 2008; Robinson et al., 2010; Lustig-Yaeger et al., 2018) and evidence of a surface temperature at which water is likely that liquid; detection of water vapor in the atmosphere; and detection of other atmospheric gases that would suggest a hospitable environment. The temperature of a planet could be measured by thermal direct imaging or secondary eclipse spectroscopy (e.g. Knutson et al., 2008), but for terrestrial planets this low-signal measurement is outside the capabilities of current or planned instruments, including *JWST* (Lustig-Yaeger et al., 2019a). However, at a given instellation, characterization of the abundances of atmospheric greenhouse gases using retrieval methods (e.g. Krissansen-Totton et al., 2018) can be used with forward (i.e. climate) modeling to assess the likely climate of the planet. Bulk non-condensable, non-greenhouse gases can also affect climate and habitability (Wordsworth and Pierrehumbert, 2014), but these are sometimes much more difficult to detect and quantify (e.g. Schwieterman et al., 2015, 2016).

Observations to detect this evidence for habitability in the next two decades will be difficult, and will be largely dictated by the observatories being built (i.e. *JWST* and ELTs). These observatories and the potential methods of characterization available to them will favor planets orbiting the smallest stars, M dwarfs.

1.5 M Dwarf Planetary Habitability and Challenges

Although M dwarfs provide invaluable observational advantages for transit spectroscopy with *JWST*, these stars exhibit very different properties compared to our Sun. Compared to what is

known about what makes Earth habitable, the differences in planetary processes for planets orbiting M dwarfs can drastically affect the observables, the potential for habitability, and the development of life.

Differences between M dwarfs and Sun-like stars begin with the birth of the star. After a star has begun fusion but is still accreting gas from the protosolar nebula, the star exhibits a much higher luminosity (the superluminous pre-main-sequence phase), which is much longer for stars smaller than the Sun and can extend up to a billion years for the smallest M dwarfs (Baraffe et al., 2015). This phase begins approximately 100 times more luminous than the main-sequence luminosity and also exhibits high XUV luminosity. As planets form and accrete volatile materials, the high XUV flux drives the photoevaporation of the volatiles and subsequent planetary atmospheres by heating the upper atmosphere and driving escape through a variety of thermal and nonthermal processes (Khodachenko et al., 2007; Lammer et al., 2007, 2011; Luger et al., 2015; Luger and Barnes, 2015; Tian, 2015; Ribas et al., 2016; Airapetian et al., 2017; Garcia-Sage et al., 2017; Dong et al., 2017, 2018). High XUV flux can also potentially sterilize the surface (Tarter et al., 2007; Shields et al., 2016). In particular, this super-luminous phase could drive an ocean-bearing terrestrial planet into a runaway greenhouse state for up to a billion years until the planet enters the habitable zone, as the star dims and enters the main sequence (Luger and Barnes, 2015; Meadows et al., 2018). This effect is far more extreme for M dwarf planets than for Earth around the Sun and may be a key factor in determining M dwarf planet evolutionary outcomes and prospects for habitability. This may lead to a ubiquity of Venus-like planets, leading to the possibility of a "Venus zone" (Kane et al., 2014). As a result of the intense pre-main-sequence phase and its affect on planets even within the main sequence circumstellar habitable zone, the Venus zone may displace the habitable zone.

As introduced in §1.3.5, planetary climate is strongly influenced by the interplay between the stellar spectral energy distribution, atmospheric gas absorption, and wavelength-dependent surface reflectivity (Figure 1.1). The cooler M dwarf SED is red-shifted into the near-infrared (compared to the visible peak of the Sun), which affects the amount of atmospheric and surface absorption, depending on composition. The atmosphere of Earth is mostly transparent to the incident SED

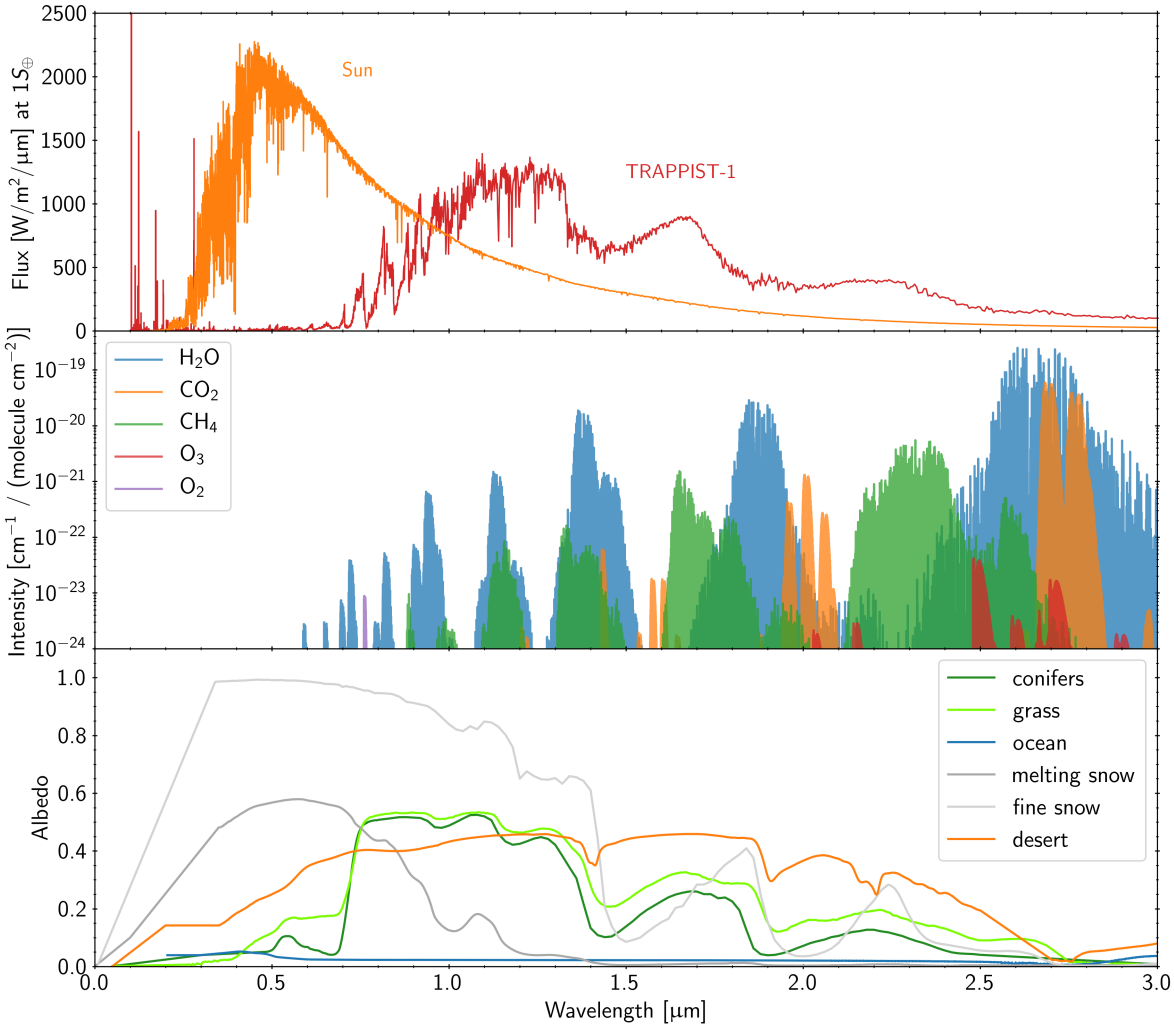

Figure 1.1: *Top:* Spectral energy distributions (SEDs) of the Sun and M8V star TRAPPIST-1 (synthetic spectrum from Peacock et al., 2019) at the equivalent distance for an integrated flux of $1S_\oplus = 1361$ W m^{-2}, which for the Sun is 1 au. The red-shifted SED reduces photosynthetically-active radiation, which could pose barriers to the origin of oxygenic life (e.g. Buccino et al., 2007). The deep absorption bands in the TRAPPIST-1 spectrum are due to water vapor in the stellar atmosphere. Rayleigh scattering is not as effective for cooling a planetary atmosphere because there is little flux at shorter wavelengths where that process is more effective. *Center:* Gas absorption intensity from HITRAN2016 (Gordon et al., 2017) for key gases absorbing in the stellar spectral range (note actual gas absorption is defined by the abundance, temperature, and pressure broadening). There are an abundance of gas absorbers in the peak emission of TRAPPIST-1 at 0.7–3 μm, and line intensities increase with wavelength. *Bottom:* surface reflectance albedos for key planetary surfaces. The albedo of snow is highly variable depending on grain size and state (i.e. snow or slush), and whether there is particulate contamination, which lowers the albedo.

of the Sun, so most of the light can warm the planetary surface and cause strong convection. However, most terrestrial greenhouse gases—including water, carbon dioxide, and methane—have absorption bands in the NIR, so instead of heating the surface by direct absorption of light from the host star, the atmosphere will absorb and re-emit much of the radiation. This atmospheric absorption leads to a warmer cold trap and potentially an anti-greenhouse effect for gases such as methane (Ramirez and Kaltenegger, 2018) that more strongly absorb in the NIR (stellar absorption) than the MIR (planetary thermal emission). For light that does reach the surface, cold M dwarf planets do not experience the same ice-albedo feedback that occurs around Sun-like stars, because ice and snow have significant absorption bands in the NIR, so do not exhibit the high albedo apparent under visible light (Shields et al., 2013). As a result, climate oscillations due to freezing and melting are unlikely (Haqq-Misra et al., 2016).

Notwithstanding global effects caused by the stellar SED, the close proximity of habitable zone planets to an M dwarf host star is expected to result in tidal locking within a short geological time (Dole, 1964; Kasting et al., 1993). The most common state is likely a 1:1 spin:orbit synchronous rotation, though higher order asynchronous states such as 3:2 are possible (Leconte et al., 2015; Ribas et al., 2016). The synchronous rotation state may be problematic for planetary climate, due to the permanent day and night sides that may result in large day–night temperature contrasts and potentially collapse of the atmosphere on the night side (Joshi et al., 1997; Joshi, 2003; Wordsworth, 2015; Turbet et al., 2016, 2018). Many studies have assessed and addressed atmospheric and dynamical conditions that would prevent collapse (e.g. Joshi et al., 1997; Joshi, 2003; Merlis and Schneider, 2010; Leconte et al., 2013; Yang et al., 2013; Yang and Abbot, 2014; Cullum et al., 2014; Hu and Yang, 2014; Kopparapu et al., 2016), and ocean heat transport (Hu and Yang, 2014; Way et al., 2018) or glacier transport (Turbet et al., 2018; Yang et al., 2019b) may also help ameliorate this problem. Due to the large and permanent day–night temperature contrast, the habitability and climate of terrestrial planets around M dwarfs may rest critically on the efficiency of global heat transport. Earlier studies (before discoveries such as the TRAPPIST-1 planets) considered extreme cases, with rotation periods between 60–365 days (Joshi et al., 1997; Joshi, 2003), which produced extreme day-night contrasts, slow circulation, and what has been deemed the “eyeball”

climate state (Pierrehumbert, 2011). Late-type M dwarf planets, however, have much faster orbits, and hence the maximum rotation period for such planets is only several days. Such rotation rates bring these planets into regimes closer to a rapid-rotator (Haqq-Misra et al., 2018), which may mitigate day–night concerns for such planets. This is an advantage that extremely late-type M dwarf planets such as those orbiting TRAPPIST-1 may have over other, earlier-type discoveries.

There are also significant differences between early-type and late-type M dwarf stars that make late-type M dwarfs the most advantageous for observation. Although early-type M dwarfs have shorter pre-main-sequence phases, they are significantly larger, hotter, and more luminous than the later type stars, so many of the discussed observational advantages are not as significant. These earlier-type stars also exhibit strong main-sequence activity when young, though this activity decreases over time (Schneider and Shkolnik, 2018). Because they are much smaller, late-type M dwarf stars have a significant advantage in producing a much larger transit depth for small planets (Figure 1.2), although the signal from the faint star itself can pose challenges (Batalha et al., 2018; Lustig-Yaeger et al., 2019a) and so can variability from the stellar photosphere (Morris et al., 2018; Rackham et al., 2018, 2019). Furthermore, the activity levels of these stars may not significantly decline with age (Schneider and Shkolnik, 2018). Nonetheless, the late-type M dwarfs transit depth advantage is compelling for observations with *JWST* (Morley et al., 2017; Lincowski et al., 2018; Lustig-Yaeger et al., 2019a).

Based on their abundance, detectability, and fundamental differences compared to planets around Solar-type stars, determining whether M dwarf HZ planets are in fact habitable is therefore a key focus in astrobiology and exoplanet science (see e.g. Shields et al., 2016; Meadows and Barnes, 2018, for reviews). Because M dwarf terrestrial planets are likely to experience very different evolutionary paths compared to those in our Solar System, their HZ planets may have atmospheres that have evolved considerably from their primordial composition. Reflecting their extreme evolution, these atmospheres may not be Earth-like or N_2-dominated, and the planets may not be habitable (Meadows et al., 2018).

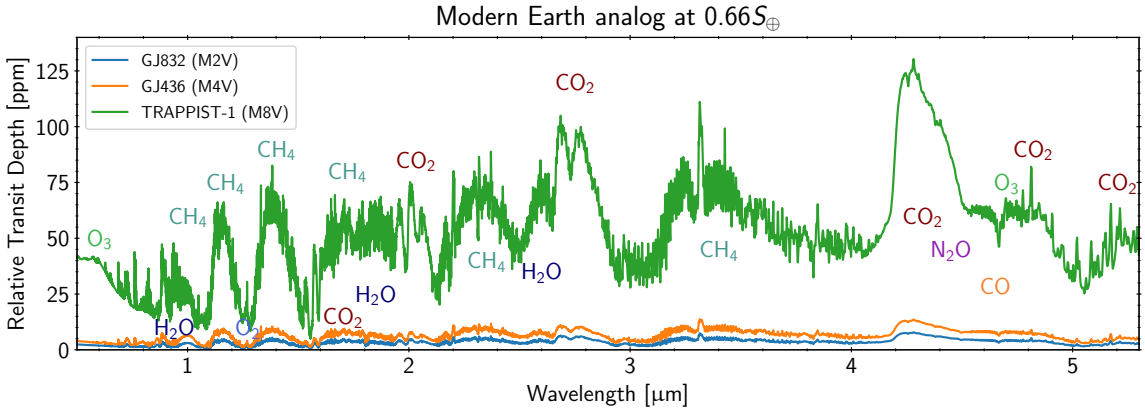

Figure 1.2: Transit transmission spectra for clear-sky, photochemically self-consistent modern Earth analogs at $0.66S_\oplus$ for three stellar types, with radii $0.48R_\oplus$, $0.3761R_\oplus$, and $0.121R_\oplus$ (GJ832, GJ436, and TRAPPIST-1, respectively). Because ultra-cool dwarf stars like TRAPPIST-1 are much smaller stars, an orbiting planet will have much larger transit depths than around earlier types, which makes the later types much more plausible for transit observations.

Parameter	**Modeled**	**Measured**[a]					
Star		TRAPPIST-1—2MASS J23062928-0502285					
Magnitudes[b]		V = 18.80±0.08, R = 16.47±0.07, I= 14.0±0.1, J = 11.35±0.02, K = 10.30±0.02					
Mass ($M_\odot$)[e]		0.089 ± 0.007					
Radius ($R_\odot$)[d]	0.121	0.121 ± 0.0030					
Luminosity ($L_\odot$)	0.000524	0.000524 ± 0.000034					
Effective Temperature (K)[d]	2500	2,511 ± 37					
Metallicity [Fe/H]	0.	+ 0.04 ± 0.08					
Planets[a]	**b**	**c**	**d**	**e**	**f**	**g**	**h**
Period (days)[d]	1.510876	2.42181	4.050	6.0990	9.2056	12.3545	18.768
Semi-major axis (AU)[d]	0.0115	0.016	0.022	0.029	0.038	0.047	0.062
Irradiation ($S_\odot$)[d]	3.88	2.07	1.04	0.60	0.35	0.24	0.13
Radius[d] ($R_\oplus$)	$1.121^{+0.032}_{-0.031}$	$1.095^{+0.031}_{-0.030}$	0.784±0.023	$0.910^{+0.027}_{-0.026}$	$1.046^{+0.030}_{-0.029}$	$1.148^{+0.033}_{-0.032}$	$0.773^{+0.027}_{-0.026}$
Mass[c] ($M_\oplus$)	$1.107^{+0.143}_{-0.154}$	$1.156^{+0.131}_{-0.142}$	$0.297^{+0.035}_{-0.039}$	$0.772^{+0.075}_{-0.079}$	$0.934^{+0.078}_{-0.080}$	$1.148^{+0.095}_{-0.098}$	$0.331^{+0.049}_{-0.056}$
Density[c] ($\rho_\oplus$)	$0.726^{+0.091}_{-0.092}$	$0.883^{+0.078}_{-0.083}$	$0.616^{+0.062}_{-0.067}$	$1.024^{+0.070}_{-0.076}$	$0.816^{+0.036}_{-0.038}$	$0.759^{+0.033}_{-0.034}$	$0.719^{+0.102}_{-0.117}$
Gravity[c] (m/s^2)	$7.96^{+1.02}_{-1.00}$	$9.47^{+0.90}_{-0.85}$	$4.73^{+0.51}_{-0.47}$	$9.11^{+0.67}_{-0.62}$	$8.36^{+0.39}_{-0.38}$	$8.54^{+0.39}_{-0.38}$	$5.44^{+0.86}_{-0.75}$
Impact parameter b (R_*)[d]	0.157±0.075	0.148±0.088	$0.08^{+0.10}_{-0.06}$	$0.240^{+0.056}_{-0.047}$	$0.337^{+0.040}_{-0.029}$	$0.406^{+0.031}_{-0.025}$	$0.392^{+0.039}_{-0.043}$

Note: We use nominal values for our modeling. Error bars (1σ) are shown for reference. Standard errors on the period are smaller than the precision reported here. Errors on semi-major axes are approximately 3% of the quoted values. Irradiation is computed from the reported semi-major axis, assuming the luminosity quoted here.

[a] Data from Gillon et al. (2017) unless otherwise noted.
[b] Data from Gillon et al. (2016).
[c] Data from Grimm et al. (2018).
[d] Data from Delrez et al. (2018).
[e] Data from Van Grootel et al. (2018).

Table 1.1: Current stellar and planetary system parameters for TRAPPIST-1.

1.6 The TRAPPIST-1 Planetary System

Of late-type stars, the recently discovered TRAPPIST-1 planetary system provides an unprecedented opportunity to study terrestrial exoplanet evolution and planetary habitability in the near future. TRAPPIST-1, 12.43 pc away (Gaia Collaboration et al., 2016, 2018), is known as an ultra cool dwarf star, spectral class M8V (Liebert and Gizis, 2006), with an effective temperature of only 2516 K, a radius of only $0.121 R_{\odot}$ (similar to Jupiter), and mass of $0.089 M_{\odot}$ (Van Grootel et al., 2018). TRAPPIST-1 is currently known to host seven transiting terrestrial-sized planets (Gillon et al., 2016, 2017; Luger et al., 2017c), approximately three of which (e, f, and g) lie in the habitable zone. Planet b receives about twice the instellation as Venus, and c receives a similar amount to Venus, while d sits within the uncertainties of the habitable zone inner edge. TRAPPIST-1 h sits firmly outside estimates of the outer edge.

Because the semi-major axes of the orbits of the seven transiting TRAPPIST-1 planets encompass and extend beyond both the inner and outer boundaries of the habitable zone, the TRAPPIST-1 system enables the possibility of testing evolutionary processes as a function of semi-major axis and position relative to the HZ. Modeling studies provide significant uncertainties for where the true inner limit may be and what processes may effect it (Kasting et al., 1993; Kopparapu et al., 2013; Kopparapu et al., 2014; Hu and Yang, 2014; Yang et al., 2014; Kopparapu et al., 2016; Bin et al., 2018; Way et al., 2018; Yang et al., 2016, 2019a,b,c). With several planets in and around the IHZ, this system provides the opportunity to assess the mechanisms of atmospheric escape (Lammer et al., 2007), as these planets will have been subjected to different levels of radiation from the host star. This system is an observational point for assessing possible factors controlling the outer edge, particularly atmospheric collapse due to condensation on the night side of a synchronously rotating planet (e.g. Kasting et al., 1993; Wolf, 2017; Turbet et al., 2018), and on the functioning of the carbonate-silicate cycle to act as a climate buffer and control CO_2 levels on terrestrial worlds (Walker et al., 1981; Kasting et al., 1993).

1.7 A Hierarchy of Models

In advance of imminent observations by upcoming space- and ground-based observatories, a large-scale assessment of atmospheric processes and characteristics applicable to M dwarf planets is needed to effectively plan and interpret these observations. To most effectively sweep the parameter space of known processes, a hierarchy of models can be used.

1.7.1 Global Climate / General Circulation Models

Models are always a simplification of reality. Depending on the complexity (and corresponding computational expense), exoplanet GCMs must inevitably have shortcuts and exclude physics to be able to consider other parameters. Sometimes, known critical physics are ignored. For example, GCMs often employ radiative transfer algorithms that are oversimplified, or even hard-coded for Earth-like optical properties with N_2-O_2 atmospheres with trace abundances of H_2O and CO_2. Others neglect or oversimplify the radiative forcing by clouds and aerosols. Most terrestrial GCMs also oversimplify or completely ignore the role of atmospheric chemistry in the determination of the atmospheric composition or climate (with recent developments by Chen et al. 2018, 2019; Yates et al. 2020, and off-line attempts, e.g. Fauchez et al. 2019; Pidhorodetska et al. 2020). Due to hard-coded Earth parameters and/or inflexible radiative transfer physics, GCMs do not deviate significantly from Earth-like (i.e. N_2-CO_2-H_2O) compositions. Up until recently, GCM studies rarely present observables that could be used by astronomers to plan observations (exceptions include Turbet et al., 2016; Boutle et al., 2017; Wolf et al., 2019; Chen et al., 2019; Fauchez et al., 2019; Pidhorodetska et al., 2020). Other GCMs exclude dynamic ocean heat transport, which can also alter the climate (Hu and Yang, 2014; Yang and Abbot, 2014; Way et al., 2017; Way et al., 2018; Del Genio et al., 2019; Yang et al., 2019a,b), and which is a substantial component of heat transport on Earth (Hastenrath, 1980; Carissimo et al., 1985; Savijärvi, 1988; Trenberth and Caron, 2001; Wunsch, 2005).

The effects considered most by 3D GCM studies, including the details of atmospheric dynamics, cloud coverage, and details of the meridional and zonal temperature distributions, will be

difficult to observe with existing or planned instruments (c.f. Turbet et al., 2016; Meadows et al., 2018; Lustig-Yaeger et al., 2019a). Exoplanet observations will be limited to single-pixel data, so high-fidelity, time-dependent observations will be required to infer spatial phenomena, which will require commensurately better data, due to the reduction in time-averaging permissible. Spatial differences in temperature may be derived from thermal phase curves (Knutson et al., 2009; Demory et al., 2016; Kreidberg et al., 2019), but this is and will remain difficult for temperate planets, even with *JWST* (Morley et al., 2017; Meadows et al., 2018; Lustig-Yaeger et al., 2019a). However, time-dependent information may be retrieved from phase curves in reflected light, which may be possible for next-generation visible-light flagship instruments under consideration, particularly LUVOIR (e.g. Lustig-Yaeger et al., 2018). Unfortunately, the interpretation of any observations may be compromised by inherent biases in model predictions, introduced in shortcomings in the parameterizations for radiative, chemical, or dynamical processes or limited spatial or temporal resolution.

1.7.2 Global Single-Column Models

Globally-averaged, single-column models (1D models) have been in use for decades to study a larger parameter space or investigate individual planetary processes. These models are generally much less computationally complex and can be applied to a wider variety of atmospheric compositions, though some common 1D models are still limited by Earth heritage (c.f. Meadows et al., 2018; Wunderlich et al., 2019). 1D models can be very useful for exoplanet studies because they often employ fewer assumptions about the environmental processes that cannot by easily observed. Phase-dependent assessments (to distinguish spatial properties) will only be feasible with a large next-generation instrument for a very small sample of potential planets (Lustig-Yaeger et al., 2018).

Historically, 1D models have been used to investigate a wide parameter space unavailable to or intractable by 3D models, and to include other processes, such as more detailed treatments of radiative transfer, cloud processes, and photochemistry. More recently, 1D models with accurate radiative transfer have been used to demonstrate important radiative physics that may impact climate (Kitzmann et al., 2013) and have been used to demonstrate the versatility of accurate physics

(Robinson and Crisp, 2018). However, 1D models may not provide an accurate surface climate assessment for planetary environments with large day-night differences arising from slow planetary rotation, due to the lack of spatial resolution or a realistic treatment of horizontal heat transport (c.f. Turbet et al., 2016; Meadows et al., 2018). Lastly, 1D models are most likely to be incorporated into the first retrievals of atmospheric properties from observations due to the large parameter space and noisy data (e.g. Kreidberg et al., 2014). The ease and versatility with which 1D model results can be used to predict and interpret exoplanetary spectral observations makes 1D models critical for exoplanet habitability characterization.

Although they have been used to model exoplanetary atmospheres for more than a decade, exoplanet models for H_2-dominated worlds (e.g. Miller-Ricci et al., 2009; Hu and Seager, 2014) may not be applicable for small M dwarf planets, which may be more terrestrial in composition, and are therefore likely to have solid or liquid surfaces and secondary outgassed (i.e. high molecular weight) atmospheres. Though excluding low molecular weight atmospheres with certainty is not always possible with current instruments (Moran et al., 2018), there is growing evidence that the bulk properties of planets with radii $\lesssim 1.5R_\oplus$ are more similar to our Solar System terrestrials than to sub-Neptune planets with H_2-dominated atmospheres (Weiss and Marcy, 2014; Rogers, 2015; de Wit et al., 2016; Fulton et al., 2017; de Wit et al., 2018). The densities of nearby M dwarf HZ planets (e.g. GJ1132 b, 6.0$\pm$2.5 g cm^{-3}, Berta-Thompson et al., 2015, and LHS1140 b, 12.5$\pm$3.4 g cm^{-3}, Dittmann et al., 2017) are similar to or greater than Earth's (5.5 g cm^{-3}) and Venus' (5.3 g cm^{-3}) densities, consistent with mixtures of silicate rock and iron. The TRAPPIST-1 planets have currently measured densities that span 0.6 to 1.0 times Earth's density (i.e. 3.3–5.5 g cm^{-3}; see Table 3.1). The generally lower nominal densities of the TRAPPIST-1 planets (Gillon et al., 2017; Grimm et al., 2018), along with their resonant orbits, suggest migration (Luger et al., 2017c; Unterborn et al., 2018a). If this is the case, they may have formed at larger distances from the star with a more volatile-rich composition. Single-column models with versatile and accurate atmospheric radiative transfer, chemical and cloud models may play a rciritcal role in assessing the factors that influence the surface climates on these terrestrial bodies with evolved, secondary outgassed atmospheres.

1.7.3 Recent M Dwarf Climate Studies—TRAPPIST-1

To plan and support the interpretation of future observations, particularly with *JWST*, numerical models are being used to study the possible evolutionary pathways and resultant climates of the TRAPPIST-1 planets and to generate simulated thermal emission and transit transmission spectra. These models and simulated observations can be used to predict observable phenomena that may help discriminate between habitable and uninhabitable planetary environmental states, and help identify the evolutionary processes that generated them. These have included the effects of stellar evolution (Bolmont et al., 2017) and planet formation (Quarles et al., 2017). Planetary atmospheric models have been used to assess climate and atmospheric composition. Simple energy balance climate models (EBMs) were used to assess the climate response to globally parameterized variables such as albedo and vegetation coverage (Alberti et al., 2017), and identified TRAPPIST-1 d as the planet most likely to maintain surface water over a large range of albedo/vegetation parameters, with f, g, and h unlikely to host surface liquid water. To explore potential atmospheric states of the TRAPPIST-1 planets as a function of semi-major axis, Morley et al. (2017) distilled the bulk atmospheric compositions of Earth, Venus, and Titan into their lowest Gibbs free energy components using thermochemistry. They used this approximation to explore a broad parameter space of atmospheric pressures spanning 0.0001–100 bars, with prescribed atmospheric thermal profiles and surface temperatures adjusted to be consistent with planetary equilibrium temperatures for different assumed values of planetary Bond albedo. Morley et al. assessed the observational signatures of these atmospheres in transmission and emission, and concluded that planet b would require fewer than 10 eclipse observations with *JWST*/MIRI to detect thermal emission and constrain the planetary emission temperature. They suggested that planets d–f could have surface liquid water and that their environments may be probed using *JWST* photometry.

Wolf (2017) and Turbet et al. (2018) used 3D GCMs to model climates for HZ and outer TRAPPIST-1 planets with N_2 and pure CO_2 atmospheres and surface pressures up to 10 bars. In contrast with the EBM study (Alberti et al., 2017), Wolf (2017) concluded that only planet e resided within the classical habitable zone, and that it would require substantially more CO_2

than Earth to maintain an Earth-like surface temperature. Turbet et al. (2018) assessed the outer planets, and found that atmospheres consisting of N_2, CO, or O_2 are resistant to collapse, even for synchronously rotating planets. They argued that greenhouse gases like CO_2, NH_3, and CH_4 would be difficult to maintain in the atmospheres of the TRAPPIST-1 planets after outgassing, due to easy condensation of CO_2 on the night side and the likely photochemical destruction of NH_3 and CH_4 (they did not actually calculate this). They noted that if the planet started with larger amounts of CO_2 (> 10 bar), then the greenhouse effect and heat redistribution would allow CO_2 to remain stable in the atmosphere. Turbet et al. (2018) agreed with Wolf that TRAPPIST-1 e has the highest potential for habitability, although they concluded that several bars of CO_2 would be sufficient for TRAPPIST-1 f and g to also support liquid surface water. Turbet et al. (2018) may be correct in this assessment, due to a more up-to-date radiative transfer parameterization, particularly for CO_2 CIA.

The above studies do not include photochemistry, and are largely insensitive to the effect of TRAPPIST-1's redder, more variable stellar spectrum on planetary atmospheric composition, which can be significant for terrestrial atmospheres at the range of instellation levels received by the TRAPPIST-1 planets (e.g. Segura et al., 2005; Segura et al., 2007; Grenfell et al., 2014; Meadows et al., 2018). Without coupled climate-photochemistry models forced by the incoming stellar spectrum, it is not possible to obtain self-consistent solutions for planetary atmospheric composition and corresponding temperature structures. This could have large effects on predicted spectra, especially for emission spectra at MIR wavelengths, which are strongly dependent on the vertical temperature structure of the atmosphere (note again that temperate planet emission spectra will be nearly impossible for currently planned instruments, Lustig-Yaeger et al. 2019a).

1.7.4 Two-Column Models: Bridging the Model Gap

Two-column models have been used in Earth studies, and could bridge the gap between the spatial coverage of 3D models with more accurate radiative physics possible in 1D models. Earlier Earth studies have used two-column models to approximate the primary circulation cells of the tropics and associated cloud formation (i.e. Hadley cells with an upwelling column and downwelling

column, Emanuel 1991; Nilsson and Emanuel 1999), or the energy budget between different parts of the atmosphere (Pierrehumbert, 1995). Two column models have been used for a number of other specific studies for Earth climate (Raymond and Zeng, 2000, 2005).

Haberle et al. (1996) developed a low-order, global-average two-column model for Earth, which used a simple two-box (day-night) advection scheme for the atmosphere but did not include surface heat transport. Yang and Abbot (2014) developed a similar two-column model, which included surface heat transport, and compared and validated their model against 3D results. Goldblatt (2016) extended the work of Haberle et al. (1996) and provided the model equations, applying this work to Proxima Centauri b. While the community entrenches in 1D and 3D modeling frameworks, there is precedent for the use of two-column models, which may be used to fuse some of the advantages of both 1D and 3D models.

1.8 Structure of this Thesis

In this dissertation, I simulate possible climates and observables of planets in and around the habitable zone of late-type M dwarf stars that will be observed in the near future. I use a generalized, physically rigorous line-by-line climate model coupled to a terrestrial photochemical model to simulate plausible environmental states and their discriminants from Earth-like environments. I develop a new two-column mode for this model to bridge the flexibility of accurate radiative transfer of our rigours 1D model to the spatial coverage of 3D models.

In Chapter 2, I introduce the VPL Climate model, the photochemical model, the coupling between them, and present details of my implementation of the two-column mode in VPL Climate. Inputs for these models are also discussed, while details specific to individual planet simulations are left to the later chapters. In Chapter 3, I present modeled climates and photochemistry in 1D for evolved climate states and associated spectra. In Chapter 4, I assess how different isotopic fractionation levels for these evolved climates (which would likely have a higher fraction of heavier isotopes) could be observed, and how that enhancement is a signature for ocean loss. In Chapter 5, I present day, night, and globally-averaged climate states of a wide variety of worlds using the two-column climate model, coupled to global photochemistry, and present spectra for detectability. I

summarize the key results of this dissertation and suggest future work in Chapter 6.

Chapter 2

MODEL SUITE

To predict and interpret upcoming observations of tidally-locked M dwarf terrestrial planets, in this dissertation I use the versatile, recently developed 1D VPL Climate model (§2.1), and an updated terrestrial photochemical-kinetics-transport model (§2.4), which I couple together. I develop a new two-column mode for the climate model (§2.6) and introduce a Python framework for interfacing these models (§2.7).

2.1 The Virtual Planetary Laboratory Climate Model

The modeling work in this dissertation relies on a new climate model, the Virtual Planetary Laboratory 1D climate model (VPL Climate), which is capable of simulating a wide variety of planetary atmospheres. VPL Climate was originally developed and presented by Robinson and Crisp (2018). The model incorporates a framework for executing a radiative transfer solver and a set of convection-condensation routines. A number of models support VPL Climate, including the Spectral Mapping Atmospheric Radiative Transfer code (SMART, Meadows and Crisp, 1996; Crisp, 1997) based on the Discrete Ordinates Radiative Transfer (DISORT, Stamnes et al., 1988; Stamnes et al., 2000) and the Line-By-Line Absorption Coefficients code (LBLABC, Meadows and Crisp, 1996).

I have completed a number of tests and improvements to these models, particularly a Python framework to generate standardized input scripts and external coupling of VPL Climate to a photochemical-kinetics code (Kasting et al., 1979; Zahnle et al., 2006; Arney et al., 2016). I have improved and vetted the convection-condensation routines and of the photochemical model. The climate model components and improvements are described in detail below. The photochemical model is described separately in §2.4. A diagram of the coupled model framework is shown in Figure 2.1.

2.1.1 Radiative Heating Rates from SMART Spectrally-Dependent Flux Jacobians

A major advantage of the VPL Climate model is its radiative accuracy and flexibility, due to its core radiative transfer solver, SMART (Spectral Mapping Atmospheric Radiative Transfer, Meadows

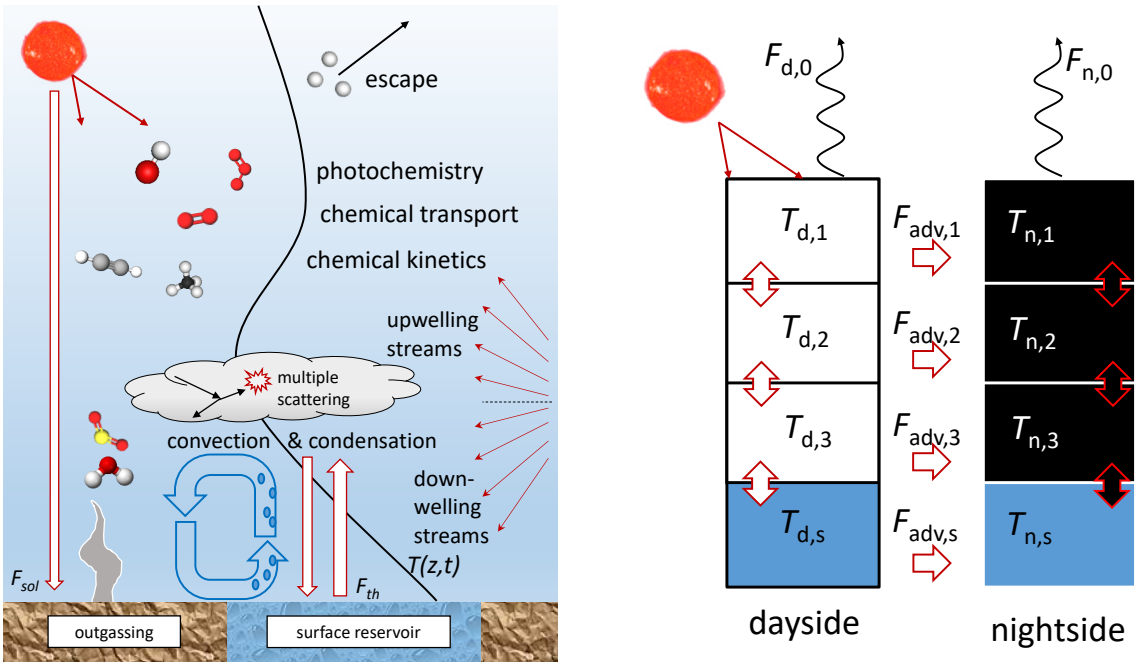

Figure 2.1: Diagram of coupled climate-chemistry physics (left) and day–night transport mode (right). The climate–chemistry diagram illustrates the physical and chemical processes present in their respective models. These models are coupled through iteration of their temperature, gas abundance, and eddy diffusion profiles. Unlike recent simpler models (Haberle et al., 1996; Yang et al., 2014; Goldblatt, 2016; Koll and Abbot, 2016), the day–night mode is a layer-by-layer advection framework, where the advective flux is proportional to the horizontal wind speed and temperature difference. A surface flux can be specified.

and Crisp 1996; Crisp 1997). SMART is a multi-stream, multi-scattering, spectrum-resolving radiative transfer code that incorporates the Discrete Ordinates Radiative Transfer solver, DISORT (Stamnes et al., 1988; Stamnes et al., 2000). SMART has been shown to faithfully reproduce the spectra of Earth (Robinson et al., 2011), has been used to produce disk-averaged spectra for Mars (Tinetti et al., 2005), and has been used to fit spatially-resolved spectra of the night side of Venus in a retrieval of gas mixing ratios and cloud optical depths (Arney et al., 2014).

VPL Climate solves the 1D surface-atmosphere thermodynamic energy equation as an initial value problem using timestepping. To step towards equilibrium in a model atmosphere without incurring the computational penalty of a full radiative transfer calculation at every timestep, VPL Climate uses SMART to generate spectrally-resolved Jacobians describing the response of the radiative fluxes to changes in temperature and, where applicable, gas mixing ratios. Jacobians for other variable components of the atmospheric or surface state can also be used (aerosol optical depth, surface pressure, and surface albedo), but these require further development for the climate model. At each time step, the stellar and thermal fluxes at each wavelength are derived at each level using a layer-adding approach that uses layer-by-layer reflectivity and transmissivity, and stellar and thermal source terms and their derivatives (Jacobians). These quantities are used in a linear flux-adding approach to determine radiative fluxes and heating rates (Robinson and Crisp, 2018). As the temperature structure changes from its initial state, the flux Jacobians are used to estimate new fluxes and heating rates given the perturbed temperatures (or other state quantities). If, at any timestep, the atmospheric properties are outside the specified linear range of the Jacobians, timestepping is suspended, and updated fluxes and layer radiative properties and their Jacobians are re-computed using SMART. High-resolution fluxes from SMART are spectrally binned, typically to 10 cm^{-1} (stellar) or 1 cm^{-1} (thermal) intervals for calculating the stellar heating and thermal cooling in each model layer at each timestep.

Spectrally-dependent molecular absorption cross-sections for rotational-vibrational transitions of gases used by SMART are evaluated using the line-by-line model, LBLABC (Meadows and Crisp, 1996). LBLABC employs nested spectral grids that fully resolve the narrow cores of individual absorption lines for every atmospheric layer and include the line contributions up to 1000

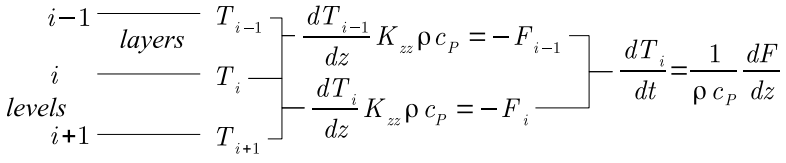

Figure 2.2: Diagram of layers and levels in the VPL Climate model.

cm^{-1} from line center. Cross-sections for CO_2 are computed using sub-Lorentzian wings with experimentally-determined χ correction factors to simulate the effects of quantum-mechanical line mixing (Perrin and Hartmann, 1989). Lines for H_2O are computed using a line shape model with super-Lorentzian wings to parameterize the far-wing quasi-continuum absorption due to the finite duration of molecule collisions (Clough et al., 1989). Opacities for O_2 are computed using super-Lorentzian line wings (Hirono and Nakazawa, 1982), with an exponent of 1.958. Line parameters, collisional-induced absorption, and UV–visible cross sections are obtained from a variety of sources (see §2.2.1).

At each time step, the atmospheric heating rates, q, define the instantaneous rate of change of temperature of each atmospheric level. In general, the heating rate in a given layer of a medium is related to the divergence of energy flux across that layer, which in hydrostatic equilibrium is

$$q = \Gamma \frac{\partial F}{\partial P} = -\frac{1}{\rho c_P} \frac{\partial F}{\partial z}, \tag{2.1}$$

where $\Gamma = c_P/g$ is the dry adiabatic lapse rate, c_P is the specific heat at constant pressure, g is the acceleration due to gravity, F is the energy flux, P is pressure, and z is altitude. These two definitions are related by the assumption of hydrostatic equilibrium:

$$\frac{dP}{dz} = -\rho g. \tag{2.2}$$

SMART calculates outputs for radiative fluxes on the input grid (i.e. at the *levels*, which are the specified *layer* boundaries; see Figure 2.2), but because heating rates are proportional to the divergence of the radiative fluxes, the heating rates are calculated across *layers*. VPL Climate

requires the heating rates at the levels to iterate changes in the temperature state, but the heating rates are defined as averaged values, integrated over layers. To calculate level heating rates, VPL Climate may use either the input atmospheric grid, or a doubly-sampled grid to improve numerical stability. The double grid is effective at preventing numerical artifices, but at the cost of additional computation time. The heating rates for the single grid are taken as the density-weighted average of the layer heating rates. The top-of-atmosphere (TOA) level heating rate is taken as the top layer heating rate and the surface boundary level heating rate is taken as a linear extrapolation from the lowest two layer heating rates. The heating rates for the output grid are calculated using the center difference method from the doubled grid values. With the finer double radiation grid, the output surface boundary level heating rates are taken as the lowest high-resolution layer heating rates.

2.1.2 Convection by Mixing Length Theory

Convective processes transport heat vertically in planetary atmospheres. Convection can result in both sensible heating (related to the energy required to change the temperature of an air parcel due to vertical mixing) and latent heating (related to the energy required to change the phase of a substance, e.g. due to condensation and evaporation). For planets with substantial greenhouse gases but transparent to radiation from the host star, these processes can transport substantial amounts of heat from the surface to the upper troposphere. For example, early 1D modeling results showed that convective processes reduce Earth's surface temperature relative to pure radiative equilibrium conditions by $\sim$50 K (Manabe and Strickler, 1964). Convective processes are also responsible for transport of trace species in the atmosphere, substantially altering atmospheric chemistry (e.g. Fleming et al., 1999; Charnay et al., 2015).

In VPL Climate, mixing length theory is used to calculate convective heat fluxes and heating rates, as this approach is more physically rigorous and versatile than the convective adjustment typically used in 1D exoplanet models. Convective adjustment sets the troposphere temperature profile to a moist or dry adiabat defined by Earth's atmospheric conditions (e.g. Kopparapu et al., 2013; Godolt et al., 2016). In these regimes, convective adjustment does not allow for atmospheric lapse rates that exceed the adiabat, which occurs on planets with more tenuous atmospheres, like

Mars (e.g. Hinson and Wilson, 2004). Convective adjustment also stabilizes atmospheric layers perfectly at every timestep, even if such instantaneous stability is unphysical (e.g. may require convective motions faster than the speed of sound). Furthermore—and especially problematic for coupling to chemistry models—convective adjustment provides no direct insight into the vertical transport of mass in the atmosphere. In contrast, mixing length theory uses fundamental physical properties of the atmosphere and its constituents (e.g. air parcel temperature, density, specific heat capacities, and static stability) to estimate the vertical heat transport rate, expressed as a vertical "eddy diffusivity," K. This quantity is then used to calculate the resulting heat and mass fluxes. Mixing length theory is therefore applicable to a wider variety of atmospheric temperature and composition regimes, and can be used to model convection for a diverse range of exoplanet atmospheres.

The convective heating rate is related to the divergence of the convective energy flux:

$$q_c = -\frac{1}{\rho c_\mathrm{p}} \frac{\partial F_\mathrm{c}}{\partial z}, \tag{2.3}$$

where z is altitude, c_p is the specific atmospheric heat capacity, and ρ is the air density. The convective energy flux F_c is given by:

$$F_\mathrm{c} = -\rho c_\mathrm{p} K_\mathrm{h} \left(\frac{\partial T}{\partial z} + \Gamma_\mathrm{ad} \right), \tag{2.4}$$

where K_h is the eddy diffusion coefficient for heat and the adiabatic lapse rate is $\Gamma_\mathrm{ad} = g/c_\mathrm{p}$, where g is the acceleration due to gravity. The atmosphere is unstable to convection when $\partial T/\partial z < -\Gamma_\mathrm{ad}$. In this case, the eddy diffusion coefficient for heat K_h is given by:

$$K_\mathrm{h} = kl^2 \left[-\frac{g}{T} \left(\frac{\partial T}{\partial z} + \Gamma_\mathrm{ad} \right) \right]^{1/2}, \tag{2.5}$$

where k is a proportionality constant equal to 1.32 (Priestley, 1959) and l is the mixing length. VPL Climate includes several choices for calculating the mixing length: a given constant value, proportional to scale height, or the nominal case for this dissertation, an asymptotic profile given

by Blackadar (1962):

$$l = \frac{k_{\mathrm{vk}} z}{1 + k_{\mathrm{vk}} z / l_0}. \tag{2.6}$$

Here, k_{vk} is von Kármán's constant and l_0 is the mixing length in the free atmosphere, which we express as

$$l_0 = f_{\mathrm{z}} H, \tag{2.7}$$

where H is the pressure scale height, given by:

$$H = \frac{RT}{\mu g}, \tag{2.8}$$

where R is the ideal gas constant, μ is the mean molar mass, and f_{z} is the proportionality constant.

The preceding convection parameterization was used by Robinson and Crisp (2018), with $f_{\mathrm{z}} = 1.0$ and with $K_{\mathrm{h}} = 0$ under stable conditions. However, turbulent eddies still provide some vertical mass transport in stable conditions, due to shear instability and gravity wave breaking (e.g. Hodges, 1969; Kondo et al., 1978; Lindzen and Forbes, 1983; Canuto et al., 2008). Based on measurements of Earth and Venus eddy diffusion rates (see Figure 2.3), I specify the following parameterization for the eddy diffusion coefficient for mass transport:

$$K_{\mathrm{m}} = K_{\mathrm{m},0} \left(\rho / \rho_0\right)^{-1/2} \left(1 - e^{-P/P_0}\right) + K_{\mathrm{m},1} \Lambda + K_{\mathrm{m},2}, \tag{2.9}$$

where Λ is a stability-related parameter (in concept from Ackerman and Marley 2001). To determine Λ, I iterate the following from the surface upward, layer-by-layer:

$$\Lambda_k = \begin{cases} \Gamma / \Gamma_{\mathrm{ad}}, & \text{if } \Gamma / \Gamma_{\mathrm{ad}} > \Lambda_0 \\ \Lambda_{k+1} e^{-z_k / z_{k+1}}, & \text{otherwise} \end{cases} \tag{2.10}$$

where $\Gamma = -\partial T / \partial z$. In the first term of equation (2.9), the density dependence represents the correlation of eddy diffusion with breaking gravity waves in terrestrial atmospheres (Lindzen and Forbes, 1983; Izakov, 2001) and the exponential decay term allows the reduction in eddy diffusion

as the gravity wave amplitude decreases to zero around pressure P_0. Molecular diffusion is not calculated in the climate model, though this is calculated in the photochemical model. The vast majority of 1D and 3D climate models do not reach the molecular diffusion level because this is not relevant to climate. I calculate the temperature structure to low pressures here to provide to the photochemical model and for the strongest bands (e.g. for CO_2) in transit spectroscopy, which can reach 1 Pa (see Lustig-Yaeger et al., 2019b).

The second term in equation (2.9) is stability-dependent and includes additional eddy diffusion in neutral and unstable conditions, such as in Earth's troposphere, which may represent the extra buoyancy experienced by moist air parcels that rise and release latent heat. Equation (2.10) slowly reduces the contribution of stability in the transition between unstable and stable regions. The overall profile is then consistent with Earth measurements presented in Massie and Hunten (1981) and Brasseur and Solomon (2006), and with the eddy diffusion profiles assumed in exoplanet photochemical-kinetics studies by other authors (e.g. Segura et al., 2007; Hu et al., 2012). The dry environments I simulate have thick atmospheres and no oceans, and therefore are more like Mars and Venus, whose eddy diffusivities are well-modeled by breaking gravity waves alone (Izakov, 2001), so in those cases $\Lambda = 0$. See Table 3.2 for nominal values.

Parameter	**Dry**	**Moist**	**Description**
f_z	0.01	0.03	Mixing length fraction
U [m s^{-1}]	0.1–1	7–10	Surface wind speed
z_0 [m]	0.005	0.0002–0.001	Surface roughness length
ρ_0 [kg m^{-3}]	1	1	Baseline density for eddy diffusion
P_0 [Pa]	1	1	Pressure for breaking of gravity waves in eddy diffusion
$K_{m,0}$ [m^2 s^{-1}]	0.5	0.01–0.5	Eddy scaling coefficient for mass, gravity waves
$K_{m,1}$ [m^2 s^{-1}]	–	20–100	Eddy scaling coefficient for mass, stability
$K_{m,2}$ [m^2 s^{-1}]	0.5	0.5	Constant minimal eddy diffusion
Λ_0	–	0.1	Stability threshold
f_{min}	10^{-4}	10^{-4}	Minimum stability scaling factor for heat
f_{max}	0.15	0.15	Maximum stability scaling factor for heat

Table 2.1: Adjustable Convection Model Parameters

In stable conditions, the eddy diffusion coefficient for heat is reduced compared to that for

momentum (e.g. Kondo et al., 1978). This reduction occurs gradually as a function of stability; Kondo et al. (1978) provided a fit based on Richardson number (*Ri*). However, the mixing length code cannot compute *Ri* in the free atmosphere, because it does not include an explicit description of the vertical shear in horizontal wind, so I use $\Gamma/\Gamma_{\rm ad}$ (also as in Λ, similar to Ackerman and Marley 2001) as a representative stability parameter for this purpose and reduce the eddy diffusion coefficient for heat by:

$$K_{\rm h} = f_{\rm h} K_{\rm m} e^{-\alpha\Gamma/\Gamma_{\rm ad}}, \tag{2.11}$$

where I set

$$\alpha \equiv \frac{1}{2} \ln\left(\frac{f_{\rm min}}{f_{\rm max}}\right), \tag{2.12}$$

and

$$f_{\rm h} \equiv f_{\rm max} e^{\alpha}. \tag{2.13}$$

The minimum and maximum scaling from $K_{\rm m}$ to $K_{\rm h}$ are denoted by $f_{\rm min}$ and $f_{\rm max}$, respectively, and given in Table 3.2. The values chosen for $K_{\rm m,X}$ are chosen for best results with the Earth and Venus validations to represent the moist and dry planets, respectively.

For Chapter 5, I add additional logic to improve continuous transition between stable and unstable regions of the eddy diffusivity. The mixing length equation for eddy diffusivity in unstable layers goes to zero as stability goes to zero (i.e. neutral conditions). To smoothly transition from the unstable layers to stable layers, I set a transition stability value of $\pm$0.1 K/km. If the calculated stability falls within this range, the stability is set to 0.1 K/km. Here I change $K_{\rm m,add}$ to a calculated value rather than a parameter, given by the value of K_m calculated at 0.3 bar with a stability term equal to 0.1 K/km.

Equations (2.3)–(2.9) are comprised almost entirely of fundamental physical properties of the local atmospheric conditions: pressure, temperature, density, gravity, and specific heat capacity. Because the vertical transport of heat, mass, and momentum in terrestrial exoplanet atmospheres are generally unknown, I chose to use this physically-motivated approach to convection (with some ad-hoc additions to eddy diffusion), rather than using convective adjustment to a prescribed lapse

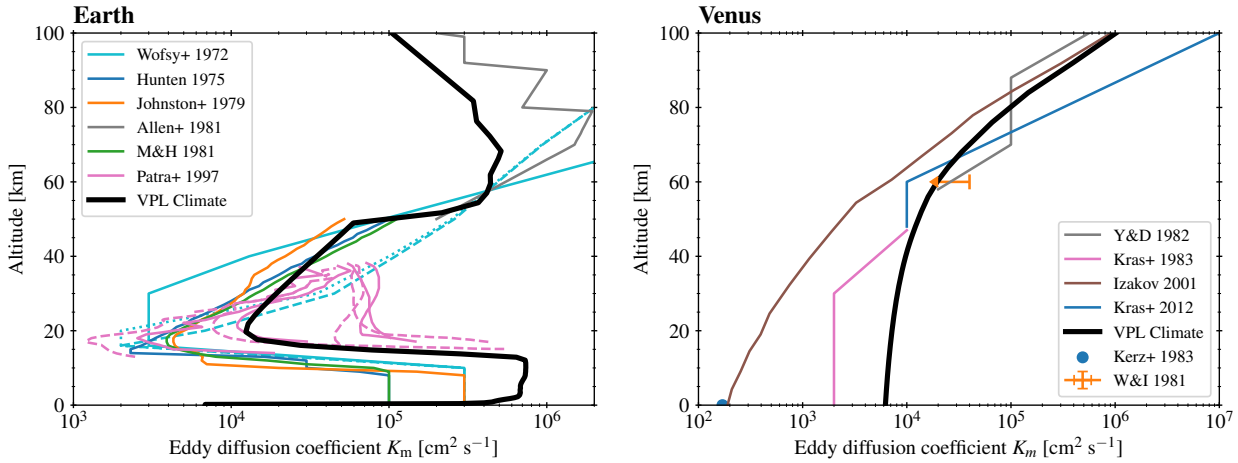

Figure 2.3: Eddy diffusion profiles for Earth (*left panel*) and Venus (*right panel*). For Earth, model fits to observations are shown from Wofsy et al. (1972), Hunten (1975), Johnston et al. (1979), Allen et al. (1981), Massie and Hunten (1981), and Patra and Lal (1997). For Venus, I show two points derived from probes of the atmosphere (Woo and Ishimaru, 1981; Kerzhanovich and Marov, 1983), profiles used with chemical kinetics modeling to fit tracer species (Krasnopolsky and Parshev, 1983; Krasnopolsky, 2012), and theoretical modeling (Izakov, 2001). The VPL Climate Earth eddy profile is calculated using the Intercomparison of Radiation codes in Climate Models (ICRCCM) case 62 mid-latitude summer temperature profile (Programme and Luther, 1984; Luther et al., 1988; Ellingson and Fouquart, 1991). The VPL Climate Venus eddy profile is calculated from the Venus International Reference Atmosphere temperature profile (Seiff et al., 1985). For both planets, a reasonable fit is obtained, considering that observations and studies of eddy diffusion rates vary widely.

rate, which can differ from the adiabatic lapse rate (e.g. Earth is $\sim$ 6.5 K/km, Mars $\sim$ 2.5 K/km, and Venus $\sim$ 8.0 K/km; Catling and Kasting 2017). The parameterizations and parameters I have chosen reproduce eddy diffusion coefficients for mass consistent with measurements and kinetics studies of Earth and Venus (see Figure 2.3).

2.1.3 Condensation and Kinematic Mixing

To simulate moist convection, which would occur on planets with substantial surface condensible (e.g. oceans), an option for latent heat exchange and kinematic mixing of a condensible gas is available. The layer-by-layer vertical mixing of a condensible species is calculated by solving the

continuity-transport equation in 1D:

$$\frac{\partial r}{\partial t} = -\frac{1}{\rho}\frac{\partial F_m}{\partial z}, \tag{2.14}$$

where the kinematic flux is given by:

$$F_{\rm m} = -\rho K_{\rm m}\frac{\partial r}{\partial z}. \tag{2.15}$$

Here, $K_{\rm m}$ is the eddy diffusion coefficient for mass transport and r is the mixing ratio of the condensible species. As a result of either radiative cooling or an upwelling condensible species, a gas may become super-saturated (i.e. when the partial pressure at a level exceeds the saturation vapor pressure). I assume sufficient cloud condensation nuclei such that any condensate above the saturation point condenses immediately (i.e. within a single time-step). The saturated mass mixing ratio (more precisely, the saturated specific humidity, because VPL Climate assumes all mixing ratios are with respect to the full air parcel mass, not the dry component) is determined by:

$$r_{\rm sat} = \frac{\mu}{\mu_{\rm atm}}\frac{P_{\rm sat}}{P}. \tag{2.16}$$

At the globally-averaged temperatures, it is unlikely that the globally-averaged water mixing ratios will approach saturation, though there is nonetheless condensation, evaporation, and latent heat exchange due to saturation of individual air parcels. The simplest solution here is to use a different mixing ratio criterion for saturation. I compute condensation if relative humidity exceeds that maximum humidity using a modified, more generalized form of equation 2 from Manabe and Wetherald (1967) for Earth:

$$rh = rh_{\rm s}\max\left(\frac{p/p_{\rm s} - 0.02}{1-0.02}, 0.2\right), \tag{2.17}$$

where s refers to the surface value. The modification is the specification of a minimum value that depends on the surface humidity (Manabe and Wetherald made a similar adjustment to obtain Earth's stratospheric H_2O abundance). While Manabe and Wetherald (1967) use $rh_{\rm s} = 0.77$, a

thorough climate validation matched fluxes better with $rh_{\rm s} = 0.88$ (§2.3). This profile is also broadly consistent with globally-averaged GCM results for M dwarf planets (e.g. Wolf, 2017).

Under these saturation humidity assumptions, the condensation criterion during a convective timestep is:

$$r + \frac{\partial r}{\partial t}\Delta t > rh \cdot r_{\rm sat}. \tag{2.18}$$

Formulations for the calculation of latent heat fluxes in climate models vary. Here I use a flux formulation as follows to directly tie the latent heat flux to the condensible mixing that causes it. The change in latent heat flux giving rise to the release of latent heat is given by:

$$\delta F_{\rm lh} = -\rho c_{\rm P} K_{\rm m} \frac{\partial F_{\rm m}}{\partial z}, \tag{2.19}$$

where the eddy diffusivity and flux are directly from the kinematic mixing. The heating rates are related to the flux divergence, as with the radiative and convective heating rates:

$$q_{\rm lh} = -\frac{1}{\rho c_{\rm p}} \frac{\partial F_{\rm lh}}{\partial z}. \tag{2.20}$$

Latent heat fluxes (2.19) are added upwards from the surface. That is, evaporation draws a large positive (upward) flux of energy from the surface, and each condensing layer deposits heat into the layer, reducing the upward flux of latent heat.

2.1.4 Surface Fluxes

The surface fluxes of sensible heat, latent heat, and condensible gas are calculated in accordance with similarity theory (e.g. Pierrehumbert, 2011, pp. 395–409):

$$F_{\rm c,sh} = \rho c_{\rm p} C_{\rm D} U (T_{\rm s} - T_{\rm sbl}) \tag{2.21}$$

$$F_{\rm m} = \rho C_{\rm D} U (r_{\rm s} - r) \tag{2.22}$$

$$F_{\rm c,lh} = \frac{H_v}{\mu_c} F_{\rm m} \tag{2.23}$$

where U is the surface wind speed, T_s is the temperature of the surface, T_{sbl} is the temperature of the lowest atmospheric layer, r_s is the surface mixing ratio boundary condition (determined from a humidity assumption or fixed mixing ratio), and C_D is the coefficient of drag at the surface, which we calculate as in Pierrehumbert (2011):

$$C_D = \left(\frac{k_{vk}}{\log z/z_0} \right)^2, \tag{2.24}$$

where z_0 is the surface roughness height. Surface wind speeds and roughness heights are chosen based on the modeled planet surface type and in accordance whenever possible with Earth or other measurements (Davenport et al., 2000; Jarraud, 2008).

2.1.5 Aerosols

I include the radiative effects of aerosols in cloudy cases for both the aqua planet and Venus-like atmospheres. Because this is a 1D climate model, I enter cloud optical depths representative of a global average. For the validation of Earth (§2.3), this is calibrated for the planetary albedo and radiative forcing. For later work with the two-column model, this is from area-weighted, log-based averages. Because I have not implemented a cloud microphysics model in the climate model, I specify altitude-dependent differential optical depths and aerosol optical properties from Earth or Venus, as appropriate. Aerosol parameters are described in §2.2.2.

2.1.6 Convergence

I first approach convergence using 4-stream radiative transfer for a single, global-average approximation solar zenith angle of 60 degrees. The final convergence of VPL Climate is conducted using 8-stream radiative transfer with four-point Gaussian quadrature integration of the stellar radiance over solar zenith angle, which increases the accuracy of the convergence result (Cronin, 2014; Hogan and Hirahara, 2015). Kitzmann (2016) determined that increasing the number of radiative transfer streams from 8 to 16 had no effect on the radiative fluxes.

2.2 Model Inputs

2.2.1 Gas Absorption Data

Gas absorption cross sections are calculated from three sources: vibrational-rotational transitions at visible and infrared wavelengths, continuum absorption from electronic transitions and predissociation bands at UV wavelengths, and dimer- and pressure-induced absorption bands at visible to infrared wavelengths. Absorption lines associated with vibrational-rotational transitions are calculated using the line-by-line model, LBLABC (Meadows and Crisp, 1996) with the HITRAN2012, HITRAN2016, HITEMP2010, or Ames line databases (Rothman et al., 2013; Gordon et al., 2017; Rothman et al., 2010; Huang et al., 2017). These line lists assume Earth-like isotopic abundances. I include foreign broadening by the dominant gases in the atmosphere (CO_2, N_2, O_2, and/or H_2).

Collisional-induced absorption data is used for CO_2-CO_2 (Moore, 1972; Kasting et al., 1984; Gruszka and Borysow, 1997; Baranov et al., 2004; Wordsworth et al., 2010; Lee et al., 2016), for N_2-N_2 (Lafferty et al., 1996; Hartmann et al., 2017), and for H_2-H_2 (Borysow, 2002). Updates were made to O_2-O_2 during this dissertation research. Absorption data for O_2-O_2 was originally from sources used in Schwieterman et al. (2016) (Greenblatt et al., 1990; Hermans et al., 1999; Maté et al., 1999). This was later regenerated from the HITRAN compilation (Maté et al., 1999; Baranov et al., 2004; Tran et al., 2006; Spiering et al., 2011; Spiering and van der Zande, 2012; Thalman and Volkamer, 2013; Karman et al., 2018).

UV–visible cross section data is incorporated from a variety of primary sources available from the MPI-Mainz UV/VIS Spectral Atlas of Gaseous Molecules of Atmospheric Interest[1] (Keller-Rudek et al., 2013). Updated sources are listed in Appendix 2.5.

---

[1] `http://satellite.mpic.de/spectral_atlas`

2.2.2 *Aerosol Optical Properties*

Aerosols are included in some of the atmospheres modeled here. The single-scattering optical properties of clouds and aerosols are defined in pre-computed tables for a range of specific particle types. Each particle type is defined by its composition, associated wavelength-dependent refractive indices, and its particle size and shape distributions. Given these properties, a single scattering model is used to compute the wavelength-dependent extinction and scattering efficiencies (Q_{ext} and Q_{abs}) and the phase function moments (for Mie scattering) or the particle asymmetry parameter (g for some non-spherical particles) used in radiative transfer calculations.

For ocean-bearing planets, I specify Earth-like cirrus (water-ice) and stratocumulus (liquid water) clouds. For cirrus clouds, the optical properties from B. Baum's Cirrus Optical Property Library (Baum et al., 2005)[2] are used. The particles consist of a distribution of 45% solid columns, 35% plates, and 15% 3D bullet rosettes, spanning 2–9500 μm with a cross-section weighted mean diameter of 100 μm. Stratocumulus cloud optical properties are based on refractive indices of water from Hale and Querry (1973) and calculated using Mie scattering, with a two-parameter gamma distribution ($a = 5.3$, $b = 1.1$) and mean particle radius 4.07 μm. The optical depths and cloud altitudes are specified for each planet and are described in their respective sections.

For Venus-like sulfuric acid aerosols, I use refractive indices for a range of specific acid concentrations between 25 and 100% from Palmer and Williams (1975). The sulfuric acid concentration is computed assuming vapor pressure equilibrium of the H_2O and H_2SO_4 gases with the condensed solution. The effective optical properties are then calculated by spline interpolation of the tables. The photochemical model calculates the monodisperse aerosol radii at every atmospheric layer given the coagulation, sedimentation, and diffusion timescales (see e.g. Pavlov et al., 2001), in phase equilibrium. For climate and spectral modeling, I convert the monodisperse distributions into log-normal distributions, with the modal radii equal to the monodisperse particle radii, as in Arney et al. (2016). The geometric standard deviation is set to 0.25, similar to the particle distribution findings for individual Venus aerosol modes as described in Crisp (1986). The differential

[2] `http://www.ssec.wisc.edu/~baum/Cirrus/Solar_Spectral_Models.html`

optical depth profile used in the radiative transfer calculations for each planet is calculated from the log-normal distribution, assuming that the total mass in each layer is the same as in the monodisperse distribution. The optical depth $d\tau$ is calculated by:

$$d\tau = dz \int_{R_{\min}}^{R_{\max}} \pi r^2 Q_{\text{ext}}(\lambda, r) n(r) dr, \tag{2.25}$$

where Q_{ext} is the extinction efficiency at a reference wavelength and n is the number density distribution.

2.2.3 Thermodynamic Data

The thermodynamic data required for condensibles in VPL Climate (e.g. H_2O) consist of saturation vapor temperature, pressure, and enthalpy of formation. For water, above 273 K I use data sourced from NIST[3]. Below 273 K, I use the saturation vapor temperature and pressure from Wagner et al. (1994). The enthalpy of condensation is from a fit to data provided in Rogers and Yau (1989). For sulfuric acid (H_2SO_4), I use a fit calculated by Gao et al. (2015) (see references therein). I also compiled data for CO_2; from the triple point (216 K) to the critical point (303 K), I used data tabulated from NIST; below the triple point, I averaged enthalpy of formation data from several sources (Giauque and Egan, 1937; Stull, 1947; Ambrose, 1956; Bryson III et al., 1974; Stephenson and Malanowski, 1987).

2.2.4 Surface Spectral Albedo

I use different surface compositions based on the type of climate being simulated. Basalt was used for the volcanic, Venus-like planets and a desert surface (primarily kaolinite) was used for the post-ocean-loss O_2-dominated atmospheres. For the ocean-bearing planets, "open ocean" and/or snow was used. Surface reflectance data is from the U.S.G.S. spectral library (Clark et al., 2007)[4], except

[3] `http://webbook.nist.gov/chemistry/fluid/`

[4] `http://speclab.cr.usgs.gov/spectral.lib06`

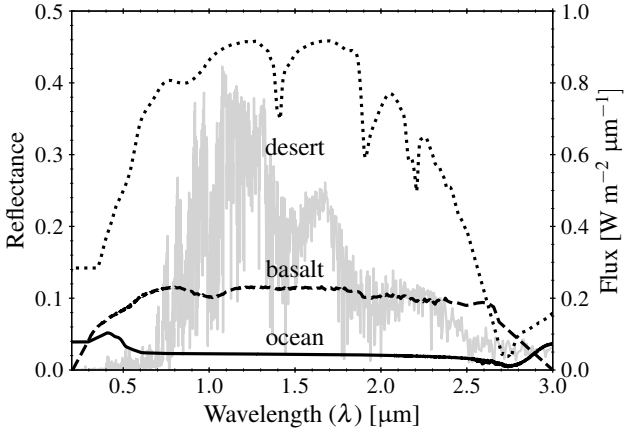

Figure 2.4: Wavelength-dependent surface reflectance for modeled planetary environments with stellar irradiation plotted for comparison. The desert surface is primarily kaolinite and was used for the desiccated O_2-dominated climates. The basaltic surface was used for Venus-analog climates. The ocean surface was used for the habitable aqua planet. These data are from the U.S.G.S. spectral library (Clark et al., 2007)[4], except for the ocean longward of 2 μm, which is from the ASTER spectral library (Baldridge et al., 2009)[5]

for the ocean longward of 2 μm, which is from the ASTER spectral library (Baldridge et al., 2009)[5] (see Figure 2.4). The integrated, energy flux-weighted surface albedos for these surfaces for the TRAPPIST-1 stellar spectrum are: 0.09 (basalt), 0.37 (desert), 0.02 (ocean), and 0.16 (snow).

Some of the planets simulated used multiple surfaces. In the 1D model, this is possible in two different ways: 1) splitting the solar-source surface and thermal-source surface, and 2) splitting the surface based on solar zenith angle. The split for solar and thermal was necessary for some direct comparisons with GCMs, which may specify grey surfaces in this manner. In that case, a grey surface is specified for the solar source, and a blackbody for the thermal source. To better simulate an ocean-bearing world with ice, in some cases I split the surface based on solar zenith angle, where small angles represent regions around the substellar point, and large angles represent the poles and/or terminator region. Emissivity in the thermal source is similar in either case. The degree of splitting depends on the number of solar zenith angles used in the solar calculation and on where the split is made between the surfaces. In this dissertation, I used four solar zenith angles, and split the surfaces at 60 degrees (i.e. 21 and 47 degree angles are ocean, while 71 and 86 degree angles are snow). This better approximates the radiative impact of a planet with some ocean and some ice, even if the global average temperature is below freezing, and particularly for a synchronously rotating planet.

---

[5] https://speclib.jpl.nasa.gov/

2.2.5 Stellar Spectrum

The stellar spectrum of TRAPPIST-1 (2MASS J23062928-0502285) is needed to characterize the climate and generate reflected light spectra of the TRAPPIST-1 planets. The available data on this star in the UV to IR is limited to photometry and to measurements of Lyman-α from the Hubble Space Telescope (Bourrier et al., 2017). TRAPPIST-1 has an effective temperature of 2516 ± 41 K, [Fe/H] = 0.04 ± 0.08, $M_* = 0.089 \pm 0.006\ M_\odot$, and $R_* = 0.121 \pm 0.003\ R_\odot$ (Van Grootel et al., 2018).

To model the panchromatic UV–NIR stellar spectrum necessary for line-by-line climate-photochemical modeling for the evolved climates described in Chapter 3, I constructed a plausible spectrum using the 2500 K, [Fe/H] = 0.0, log g = 5.0 spectral model from the PHOENIX v2.0 spectral database, which spans from 0.25 to 5.5 μm, and has been shown to faithfully reproduce the visible–NIR spectra of M dwarfs (France et al., 2013). I compared this PHOENIX model to the photometric observations (Gillon et al., 2016), and found that the model spectral energy distribution (SED), binned to available photometric bands, is within 3σ of the available measurements.

The intensity and wavelength dependence of the stellar UV spectrum is a critical factor affecting atmospheric chemistry, and subsequent atmospheric composition and climate. For example, Grenfell et al. (2007) noted UV-induced changes in the atmospheres of planets around F-G-K stars as a function of orbital distance, including the impact of outgassed species on climate, and Grenfell et al. (2014) noted that UV changes within 200–350 nm have the largest effect on ozone levels for planets around late-type M dwarfs.

Because a complete UV spectrum of TRAPPIST-1 is not available, initially I fit a UV spectrum compiled for Proxima Centauri (Meadows et al., 2018, and references therein), the latest-type M dwarf star for which a near-complete UV spectrum was available. I scaled the UV spectrum of Proxima Centauri by the ratio of the Lyman-α flux of TRAPPIST-1 to Proxima Centauri, a factor of 1/6 at 1 au (Bourrier et al., 2017). The UV flux was stitched to the PHOENIX SED at 0.3 μm, where photospheric emission began to dominate (i.e. where the flux from the PHOENIX model began to rise above the UV). This method provides only a possible UV flux environment for the

planets of TRAPPIST-1 and does not represent the star's actual activity (except the reconstructed Lyman-α). Given the variable activity of M dwarfs, UV observations of TRAPPIST-1 are needed to properly characterize its planets.

After Lincowski et al. (2018) was published (see also Ch 3), Peacock et al. (2019) published synthetic high-resolution panchromatic spectra for TRAPPIST-1, calibrated to the available UV photometric data. In Ch. 5, I used an average of the three Peacock et al. spectra for all modeling, except in comparison cases with GCMs, where I used the high-resolution version of the quiescent input spectrum used in the GCM.

2.3 Validation for Earth

The VPL Climate model has been validated for Earth for radiation only (Robinson and Crisp, 2018). In this section, I validate this model in radiative-convective mode, with condensation and associated latent heat fluxes that help control the temperature structure and surface climate of Earth. The stability criterion remains the dry adiabatic lapse rate. The parameterized eddy diffusivity for mass drives vertical mixing of water vapor, which can release latent heat in the middle troposphere to decrease the overall lapse rate and increase the tropopause temperature. I present a traditional clear-sky case, with an associated increase in surface albedo to account for the missing clouds (Kasting et al., 1993; Kopparapu et al., 2013), and a full cloudy case, where the optical depths of vertically-distributed cirrus (water-ice) and stratocumulus (water) clouds have been tuned for this validation. In Table 2.2, I compare the radiative, sensible heat, and latent heat fluxes with sophisticated Earth 3D climate models (Trenberth et al., 2009).

2.3.1 Clear-Sky Earth

A classic short-cut to modeling an Earth-like atmosphere is to ignore clouds and instead increase the surface albedo to account for net cloud reflectivity (Kasting et al., 1993; Kopparapu et al., 2013), though other types of studies also set surface albedo values based on e.g. stellar type (Wolf, 2017; Turbet et al., 2018). Here I demonstrate that for Earth, I can obtain a consistent radiative-

	Trenberth et al. (2009)		Earth Clear	Earth Clouds
Surface Temperature [K]	289.1	(288.7–289.25)	286.85	289.06
Direct Solar	341.3	(339.1–341.8)	344.3	344.3
Net Reflected Solar	101.9	(94.6–117.0)	87.5	91.7
Solar reflected by atmosphere and clouds	78.8	(69–82.4)	10.0	69.2
Solar reflected at surface	23.1	(22.8–45.2)	77.5	22.5
Net Solar flux at surface	161.2	(160.4–169.8)	182.9	183.5
Net thermal flux at surface	63	(48.5–72.8)	98.1	96.0
Outgoing thermal flux	238.5	(235.6–253.6)	259.3	255.0
Surface sensible heat flux	17	(15.3–24)	2.4	4.6
Surface latent heat flux	80	(78–85.1)	83.0	83.0

Table 2.2: Comparison of the global energy budget for Earth (Trenberth et al., 2009) with VPL Climate model results. Except surface temperature, all quantities are flux [W m^{-2}]. Values from Trenberth et al. (2009) include the range from several studies compared (in parentheses).

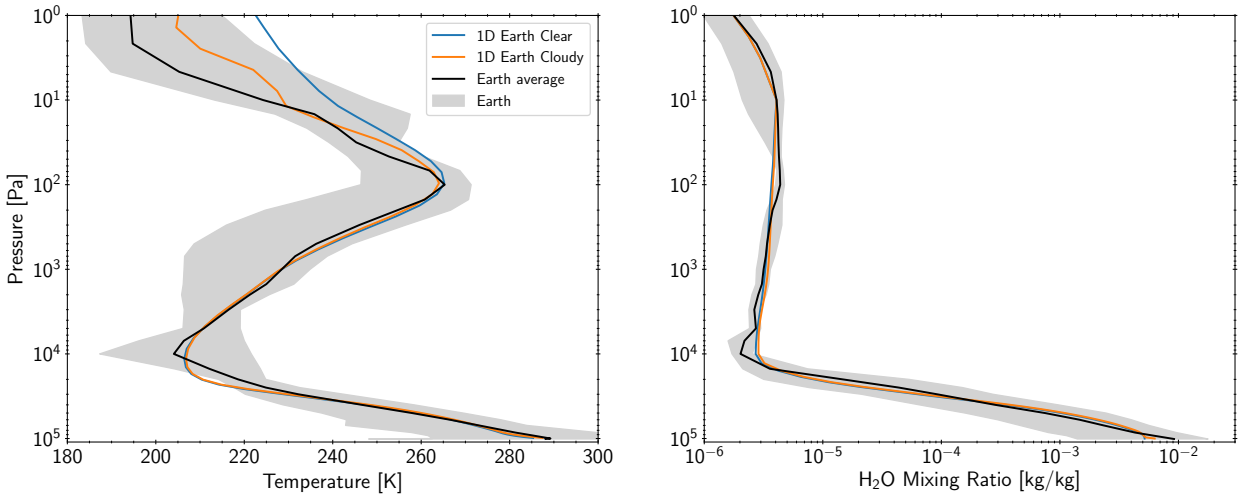

Figure 2.5: Comparison of clear-sky and cloudy versions of the VPL Climate model for modern Earth with the VPL 3D Spectral Earth model, derived from Earth observing data. There is excellent agreement in temperature and water vapor for both cases with the global average of Earth.

convective-equilibrium surface temperature using this method with VPL Climate. However, this method does not result in the correct energy fluxes within the atmosphere. The first obvious difference is that most of the reflected radiation is reflected from the surface, rather than the clouds, which changes the altitudes in which the atmosphere absorbs radiation. Even though this method

uses the same surface albedo (30%) as the net bond albedo of Earth, the net top-of-atmosphere solar (and thermal) fluxes are higher, completely outside the range from a variety of studies compared by Trenberth et al. (2009).

2.3.2 Cloudy Earth

To represent an average state for partially-cloudy Earth, here I weight the cloud coverage fraction with the average optical depths presented in Kitzmann et al. (2010). Compared to Kitzmann et al. (2010), which assessed a range of water cloud types, here the liquid water clouds are simplified to be composed only the most abundant type, stratocumulus. I use slightly lower globally-averaged optical depths to obtain the correct surface temperatures ($\tau_{\rm ice} = 0.05$ and $\tau_{\rm liq} = 1.25$). With properly chosen mixing length parameters, eddy diffusivity for heat, and parameterization for eddy diffusivity for mass mixing, VPL Climate is capable of excellent reproduction of the global temperature and water vapor profile for Earth. The net heat fluxes at the top of the atmosphere and at the surface are balanced, though the surface heat fluxes for solar and thermal are both higher than measured. which may indicate sensitivity in atmospheric components that do not strongly affect the overall temperature profile. The small differences near the surface may play an outsize role in this discrepancy, as the largest differences are in thermal flux balance at the surface and surface sensible heat flux. The surface sensible heat flux is too small, meaning convection is not cooling the surface as much as it should, while both solar and thermal fluxes are too high, with the balance being extra radiative cooling. The radiative balance is due to insufficient downward thermal radiation, which could be caused by lower temperature and lower water vapor content in the lower troposphere.

2.4 1D Photochemical-Kinetics-Transport Model

Here, I describe several updates made to the photochemical model to allow more robust modeling of the alien environments in this dissertation. I modified the wavelength grid to accommodate an input SED with wavelengths shorter than Lyman-α and have increased the resolution to

100 cm^{-1}, which now includes 750 flux bins versus the standard 118. I updated cross-sections for the molecules listed in Table 2.3. Additionally, based on the recommendations in Burkholder et al. (2015), I updated the quantum yields of O_3 with fits by Matsumi et al. (2002) and Nishida et al. (2004). These updates extended the O_3 photochemistry to cooler temperatures necessary for modeling the range of planets simulated here.

I made several other changes to the photochemical model for consistency and flexibility. First, as a result of the cross-sections and grid update, I set the solar zenith angle to the daytime-mean of 60 degrees, to approximate the global diurnal average when using a two-stream radiative transfer model (e.g. Manabe and Strickler, 1964; Li, 2017). For the non-moist templates, I modified treatment of the water vapor profile so that it was no longer specified to a fixed humidity, moist adiabat, or Earth-like profile, but instead was treated like every other long-lived trace species. This was required to model atmospheres with water abundances significantly less than that of Earth, such as the atmosphere of Venus and the evolved post-ocean-loss O_2-dominated atmospheres. Likewise, I also treated CO_2 as a long-lived gas, as in Kopparapu et al. (2011), rather than as a fixed species (c.f. Meadows et al., 2018). Long-lived gases are included in the Jacobian solved at each time step, and transport between layers is calculated. This modification allowed more accurate modeling the photolysis and longer recombination lifetimes of CO_2 in desiccated atmospheres, where CO_2 photolysis can outpace recombination, resulting in a steady-state equilibrium between CO_2, CO, O_2, and O_3 (Gao et al., 2015). Lastly, I adjusted the grid spacing for the atmospheric scale heights necessary to model each planet. Because the climate model and photochemical model have different grids (the photochemical model uses a constant altitude grid, while the climate model has whatever grid the user supplies), I interpolate the atmospheric structure values when passing data from one model to the other. Both model grids extend to 0.01 Pa.

2.5 Photochemical Validation of Earth and Venus

With the updates presented in the preceding sections, I present a new validation for the atmospheres of Earth and Venus.

Species	Wavelengths (nm)	References	Species	Wavelengths (nm)	References
CO_2	121–169	Lewis and Carver (1983)	O_2	120–179	Lu et al. (2010)
	169–200	Shemansky (1972)		179–203	Yoshino et al. (1992)
	200–225	Power law extrapolation		205–240	Yoshino et al. (1988)
H_2O	120–194	Mota et al. (2005)	O_3	120–845	Serdyuchenko et al. (2011)
H_2O_2	125–190	Schürgers and Welge (1968)	OCS	120–210	Limão-Vieira et al. (2015)
	190–350	Sander et al. (2011)		210–300	Molina et al. (1981)
	350–557	Power law extrapolation	SO_2	120–403	Manatt and Lane (1993)
H_2S	120–160	Feng et al. (1999)		403–500	Power law extrapolation
	160–260	Wu and Chen (1998)	SO_3	120–140	Power law extrapolation
	260–313	Power law extrapolation		140–180	Hintze et al. (2003)
H_2SO_4	120–200	Lane and Kjaergaard (2008)		180–330	Sander et al. (2011)
	512–745	Mills et al. (2005)		330–350	Power law extrapolation
H_2CO	120–226	Cooper et al. (1996)	S_3	350–475	Billmers and Smith (1991)
	226–375	Sander et al. (2011)	S_4	425–575	Billmers and Smith (1991)
HNO_2	120–184	Power law extrapolation	CH_4	120–153	Lee et al. (2001)
	184–396	Sander et al. (2011)	CH_3O_2	205–295	Sander et al. (2011)
HNO_3	120–192	Suto and Lee (1984)	CH_3OOH	210–405	Sander et al. (2011)
	192–350	Burkholder et al. (1993)	HCl	120–135	Brion et al. (2005)
NO	120–207	Iida et al. (1986)		135–220	Cheng et al. (2002)
NO_2	120–422	Vandaele et al. (1998)	ClO	236–312	Simon et al. (1990)
		QY: Sander et al. (2011)	OClO	125–183	Hubinger and Nee (1994)
N_2O	120–160	Zelikoff et al. (1953)		290–460	Bogumil et al. (2003)
	160–240	Sander et al. (2011)	$COCl_2$	168–305	Sander et al. (2011)
N_2O_5	152–200	Osborne et al. (2000)	SO_2Cl_2	190–300	Uthman et al. (1978)
	200–420	Sander et al. (2011)			

Note: Most data obtained from the MPI-Mainz UV/VIS Spectral Atlas of Gaseous Molecules of Atmospheric Interest (Keller-Rudek et al., 2013, http://satellite.mpic.de/spectral_atlas).

Table 2.3: Updated UV–Vis. Cross Sections

2.5.1 Earth

In addition to the updates presented in the preceding sections, I validated this model for Earth using the boundary conditions given in Table 2.4. In particular, this includes fluxes (not fixed mixing ratios) from an Earth atmospheres textbook (Seinfeld and Pandis, 2006) or primary sources of the important Earth constituents CO, CH_4, NO, H_2S, H_2SO_4, OCS, N_2O, CS_2, dimethyl sulfide (C_2H_6S), SO_2, and CH_3Cl (see Table 2.4). Oxygen is fixed at the surface at 21% and nitrogen at 78%. Carbon dioxide is fixed at the surface to the recent value of 400 ppm. The flux of NO is calibrated to best reproduce the effects of NO_x chemistry, as this Earth template does not include many pollutants not listed here. The water vapor profile is from a modified form of relative humidity (rh) from Manabe and Wetherald (1967), equation (2):

$$\mathrm{rh} = \mathrm{rh}_0 \left(\frac{P(z)/P(0) - 0.02}{1 - 0.02} \right), \tag{2.26}$$

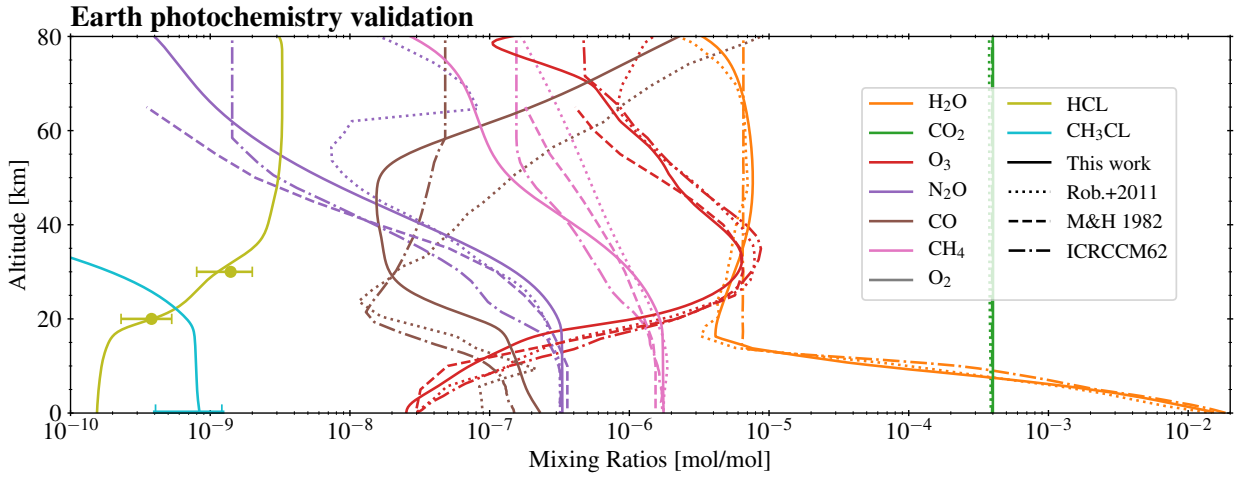

Figure 2.6: Photochemical equilibrium validation for Earth, using the average temperature from the data-derived 3D Spectral Earth model (Robinson et al., 2011). Calculated mixing ratio profiles of key species are shown in solid lines. For comparison, plotted are an average derived from the 3D Spectral Earth model (Robinson et al., 2011, dotted lines), measurements from (Massie and Hunten, 1981, dashed lines), the ICRCCM Earth mid-latitude summer sounding case 62 (dash-dotted lines), and data points for HCl (Ackerman et al., 1976) and for CH_3Cl (Hu et al., 2010).

using a fixed surface humidity (rh_0) of 88%, assuming the tropopause is at 14 km, and that the minimum saturation value in the troposphere is 10% of the surface value. Vertical profiles of important species are shown in Figure 2.6 along with several data sources for comparison.

2.5.2 Venus

This is the first time this photochemical model has been used for a Venus-like planet, which has required careful selection of boundary conditions, reactions, and of the eddy diffusion profile. Few additional changes were required to the model itself to model the Venusian photochemistry. In addition to the model updates discussed in the previous sections, I updated saturation vapor pressure data, added an additional lower boundary condition, compiled a new Venus input template, and conducted a validation against recent Venus literature.

The saturation vapor pressure and temperature data for sulfuric acid solutions were updated using finer intervals of 1% by fitting splines to published refraction and absorption data, which are

Species	Boundary Condition	References
O	$v_{dep} = 1.$	
O_2	$r_0 = 0.21$	
H_2O	$rh_0 = 0.88$	
H	$v_{dep} = 1.$	
OH	$v_{dep} = 1.$	
HO_2	$v_{dep} = 1.$	
H_2O_2	$v_{dep} = 0.2$	
H_2	$v_{dep} = 2.4 \times 10^{-4}$	
CO	$v_{dep} = 0.03$, $F = 3.7 \times 10^{11}$	Hauglustaine et al. (1994), Seinfeld and Pandis (2006)
HCO	$v_{dep} = 1.$	
H_2CO	$v_{dep} = 0.2$	
CH_4	$F = 1.0 \times 10^{11}$	
NO	$v_{dep} = 1.6 \times 10^{-2}$, $F = 1.0 \times 10^{9}$	Hauglustaine et al. (1994), F calibrated
NO_2	$v_{dep} = 3.0 \times 10^{-3}$	
HNO	$v_{dep} = 1.$	
H_2S	$v_{dep} = 0.02$, $F = 2.0 \times 10^{8}$	Seinfeld and Pandis (2006)
SO_2	$v_{dep} = 1.$, $F = 9.0 \times 10^{9}$	Sehmel (1980), Seinfeld and Pandis (2006)
H_2SO_4	$v_{dep} = 1.$, $F = 7.0 \times 10^{8}$	Seinfeld and Pandis (2006)
HSO	$v_{dep} = 1.$	
OCS	$v_{dep} = 0.01$, $F = 1.5 \times 10^{7}$	Hu et al. (2012), F calibrated, fluxes uncertain (Seinfeld and Pandis, 2006)
HNO_3	$v_{dep} = 0.2$	
N_2O	$F = 1.53 \times 10^{9}$	Seinfeld and Pandis (2006), IPCC2013
HO_2NO_2	$v_{dep} = 0.2$	
CO_2	$r_0 = 4.0 \times 10^{-4}$	
CS_2	$F = 2.0 \times 10^{7}$	
C_2H_6S(DMS)	$F = 3.3 \times 10^{9}$	Lana et al. (2011)
CH_3Cl	$F = 3.0 \times 10^{8}$	Hu et al. (2010)
N_2	$r_0 = 0.78$	

Note: All unlisted species have a lower boundary condition $v_{dep} = 0$. Deposition velocities (v_{dep}) are given in cm s^{-1}, fluxes (F) are given in molecules cm^{-2} s^{-1}, r_0 is a fixed surface mixing ratio, and rh_0 is the surface relative humidity.

Table 2.4: Earth Validation Lower Boundary Conditions.

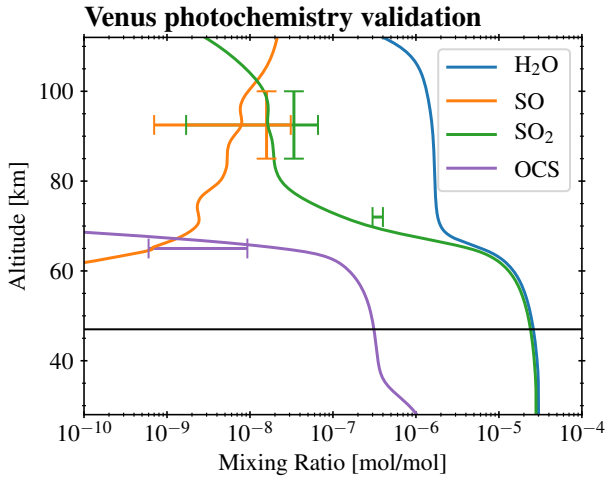

Figure 2.7: Photochemical equilibrium validation for Venus. Mixing ratios from our model for select species are shown, along with a selection of published measurements. Note that there is considerable variation in these abundances as a function of day vs night and latitude (e.g. Ignatiev et al., 1999; Arney et al., 2014).

available at sulfuric acid concentrations of 25, 38, 50, 75, 84.5, and 95.6% (Palmer and Williams, 1975). Addition details on this are discussed in §3.2.

I drew heavily on recent Venus literature (primarily Krasnopolsky 2012 and Zhang et al. 2012) to construct the Venus template, consisting of important species, their boundary conditions, and relevant reactions. The boundary conditions are listed in Table 2.5. As in previous work (e.g. Krasnopolsky, 2012; Zhang et al., 2012), the photochemical template for Venus is not extended to

Species	**Boundary Condition**
O_2	$v_{dep} = 2v$
H_2O	$r_0 = 3.0 \times 10^{-5}$
H_2	$r_0 = 4.5 \times 10^{-9}$
NO	$r_0 = 5.5 \times 10^{-9}$
SO_2	$r_0 = 2.8 \times 10^{-5}$
OCS	$r_0 = 1.0 \times 10^{-6}$
HCl	$r_0 = 4.0 \times 10^{-7}$
CO_2	$r_0 = 0.965$
N_2	$r_0 = 0.035$

Table 2.5: Venus Validation Lower Boundary Conditions. All unlisted species have a lower boundary condition $v_{dep} = v = K_m/2H$. Boundary conditions are either deposition velocities (v_{dep}), given in cm s^{-1}, or a fixed surface mixing ratio r_0. The Venus lower boundary is at 28 km ($\sim$ 11.5 bar).

the surface. Instead, the lower boundary is set at 28 km ($\sim$ 11.5 bar), as thermochemical reactions, which are typically treated as a separate regime from the photochemical region (e.g. Krasnopolsky, 2013), are not included. Because the lower boundary is not the surface, the "deposition velocity" v must be calculated to obtain the correct lower boundary flux. This depends on the scale height and eddy diffusion coefficient (Krasnopolsky, 2012):

$$v = \frac{K_m}{2H}. \tag{2.27}$$

The reactions in the Venus template are primarily reproduced from those given in Krasnopolsky (2012).

The validation for Venus was primarily for major climate and observable species, particularly those involving Venus' sulfuric acid clouds (e.g. H_2O and SO_2). I find good agreement with recent modeling by Krasnopolsky (2012), on which this reaction and boundary condition template is based. However, there are still disagreements between Venus photochemical modeling in the literature among the abundances retrieved from different observations, particularly observed oxygen abundances and in the features of the SO_2 profile. Future improvements to the Venus reactions can be made as those researchers who focus on Venus solve these outstanding issues.

The photochemical model includes simplistic aerosol formation, including sulfuric acid aerosols, based on production/loss lifetimes (Pavlov et al., 2001). This model fails to produce the specific distribution of the multiple aerosol models found in the atmosphere of Venus. This model is also unable to generate aerosols as large as the mode 3 (3.85 μm) particles. Nonetheless, this model and Venus template do self-consistently generate aerosols at altitudes consistent with the Venus cloud deck. I find that the transmission spectrum for the model Venus is roughly consistent with the cloud parameterization from Crisp (1986). Therefore, this template should provide an acceptable starting point for self-consistent climate-chemistry modeling of Venus-like exoplanets with aerosol formation.

2.6 A Two-Column Climate Model for Terrestrial Exoplanets

To model the day–night climate contrast for synchronously rotating planets, I extend the 1D VPL Climate model with a two-column mode that separates the model into two semi-independent radiative-convective-equilibrium columns, linked by horizontal advection of temperature and condensibles between the columns. To develop a global-scale advective transport system, I follow from the basic circulation assumptions outlined for simple two-column models developed by Yang et al. (2014) and Koll and Abbot (2016). Instead of constructing an analytic model, I numerically calculate zonal winds from the primitive meteorological equations, with approximations applied on a global scale. The global zonal winds then directly determine the advection of heat and condensible species (e.g. water).

To distill the 3D primitive equations into a two-column framework, I make several assumptions about the thermal structure and circulation that affect the accuracy and range of validity of this model. I assume that the temperature differences across the day and night sides are sufficiently small such that each hemisphere can be represented by a hemispherical average. For the night side, Yang et al. (2014) and Koll and Abbot (2016) called this the "weak temperature gradient" (WTG) approximation. I demonstrate the validity of this in §5.3.1.2. To calculate the zonal winds using the primitive equations, the mass divergence is required, and therefore also the vertical winds profile. The 1D model does include a diffusive vertical transport scheme, based on mixing length theory, which can yield a dimensional estimate of the vertical winds. Here, I improve the approach by simplifying the thermodynamic energy equation and solving for the vertical winds, similar to earlier Earth and Mars climate studies (e.g. Shine, 1989) and recent two-column work (Yang et al., 2014; Koll and Abbot, 2016). Horizontal distances are featured in the primitive equations, for which I approximate the day–night distance as πR.

Earlier studies made many additional assumptions, particularly for radiative transfer, such as emission height, emissivity, the height of the tropopause (Yang et al., 2014; Koll and Abbot, 2016). Here, I do not make analytic assumptions about the tropopause or which layers of the atmosphere may be in radiative equilibrium vs radiative-convective-advective equilibrium. However, those

studies nonetheless critically showed that two-column models are capable of reproducing the primary day–night contrasts produced by 3D models for exoplanet climate studies. Here, I take a different approach and use the versatile, radiatively-rigorous line-by-line RCE code, VPL Climate, and extend it with a two-column mode.

To distill global-scale transport into a two-column framework, I use simplified forms of the primitive equations:

$$\frac{\partial u}{\partial t} = -u\frac{\partial u}{\partial x} - w\frac{\partial u}{\partial z} - \frac{\partial \Phi}{\partial x} - f_{\text{cor}}v - F_D, \tag{2.28}$$

$$\frac{1}{r\cos\phi}\frac{\partial(\rho u)}{\partial \lambda} + \frac{1}{r\cos\phi}\frac{\partial(\rho v)}{\partial \phi} = -\frac{1}{r^2}\frac{\partial(\rho r^2 w)}{\partial r}, \tag{2.29}$$

$$\frac{dT}{dt} = \frac{u}{R}\frac{\partial T}{\partial \lambda} - w\left(\frac{\partial T}{\partial z} + \Gamma\right) + q_{\text{diab}}. \tag{2.30}$$

The first equation is the horizontal momentum equation in the zonal direction, the second is the continuity equation, and the third is the thermodynamic energy equation.

The two columns are connected by advective heat transport. The advective heating rate is given by the first term on the right-hand side of the thermodynamic energy equation:

$$q_{\text{ad}} = \frac{u}{R}\frac{\partial T}{\partial \lambda}, \tag{2.31}$$

where I assume the day–night hemispherical angular distance for λ is π. To calculate the horizontal wind speed u, I use the horizontal momentum equation, neglecting the Coriolis force:

$$\frac{\partial u}{\partial t} = -u\frac{\partial u}{\partial x} - w\frac{\partial u}{\partial z} - \frac{\partial \Phi}{\partial x} - F_D, \tag{2.32}$$

where ∂x is the horizontal distance scale, w is the wind velocity, Φ is the geopotential, and F_D is the drag force. The geopotential Φ is:

$$\Phi = gz + \frac{(\Omega r\cos\theta)^2}{2}, \tag{2.33}$$

where I have included the centrifugal force (the last term). Simulations of M dwarf planets using 3D models have demonstrated that meridional terms are small compared to the other terms (e.g. Kopparapu et al., 2017).

The vertical wind speed w is required to calculate u. Similar to Santee and Crisp (1993) and Koll and Abbot (2016), I assume that thermodynamic forcing is a primary driver of the general circulation, which has the benefit of being directly related to an atmospheric property that is calculated by a spectrum-resolving radiative transfer model. This approximation has been in use in diagnosing the zonal circulation in earlier Earth studies (see Shine, 1989, for a review). Because this model is iterative (using time-steps), I solve the thermodynamic energy equation for w:

$$w = \frac{q_{\text{diab}} - q_{\text{ad}}}{\frac{\partial T}{\partial z} + \Gamma}, \tag{2.34}$$

where q_{diab} is the net diabatic heating rate (i.e. due to solar, thermal, and latent heating) and the denominator is the static stability, where $\Gamma = g/c_P$ is the dry adiabatic lapse rate. The advective heating rate q_{ad} is zero in the first time step, and each subsequent time step uses the advective heating from the previous step. Though this method is only approximate and there exist a number of potential complications (Shine, 1989), the fact remains that atmospheric studies of Earth require a higher level of precision and accuracy than exoplanet studies, due to the depth and breadth of studies of Earth and corresponding dearth of such data for terrestrial exoplanets. The use of this methodology (though not without error for spatially-resolved studies of the atmosphere of Earth) serves as an adequate basis for constructing physically reasonable circulations for this exoplanetary model, for which the various sources of error outweigh the concerns present in the many Earth studies discussed in Shine (1989). The ability to neglect eddy heating terms in the dynamical equations is a key assumption underlying the calculation of a radiation-driven diabatic circulation (Dunkerton, 1978; Gille et al., 1987).

After calculation of vertical wind speeds, I assume that the zonal flow dominates over the meridional flow, such that the zonal mass divergence can be approximated as equal to the vertical mass divergence. In spherical coordinates, the divergence of the mass flux from the continuity

equation is:

$$\frac{1}{r\cos\phi}\frac{\partial(\rho u)}{\partial\lambda} \approx -\frac{1}{r^2}\frac{\partial(\rho r^2 w)}{\partial r}, \tag{2.35}$$

where r is the radial distance from the center of the planet, λ is latitude, and ϕ is longitude. Equation (2.35) allows linearization of the primitive equation for horizontal transport, assuming steady state:

$$\frac{\partial u}{\partial t} = 0 \approx u\frac{1}{\rho r^2}\frac{\partial(\rho r^2 w)}{\partial r} - w\frac{\partial u}{\partial z} - \frac{1}{r}\frac{\partial\Phi}{\partial\lambda} - F_D, \tag{2.36}$$

and a solution for u using finite differences via tridiagonal methods (Press, 1996). Lastly, I include Rayleigh friction as a dissipation force directly proportional to the zonal wind velocity: $F_D = D(\rho)u(z)$, with the following parameterization for $D(\rho)$:

$$D(\rho) = D_0\frac{\rho^\alpha}{P_{\text{orb}}}, \tag{2.37}$$

where D_0 and α are parameters and P_{orb} is the orbital period in seconds.

The validation of this two-column mode is presented in §5, with the corresponding climate results.

2.7 A Python Framework for VPL Model Coupling

The core model codes are written in Fortran. To aid ease-of-use and to couple these models together, I developed a Python framework, which writes out the run scripts and plots outputs. For coupling, the Python code reads model outputs for one model and writes them to the model inputs for the other model. A schematic is shown in Figure 2.8.

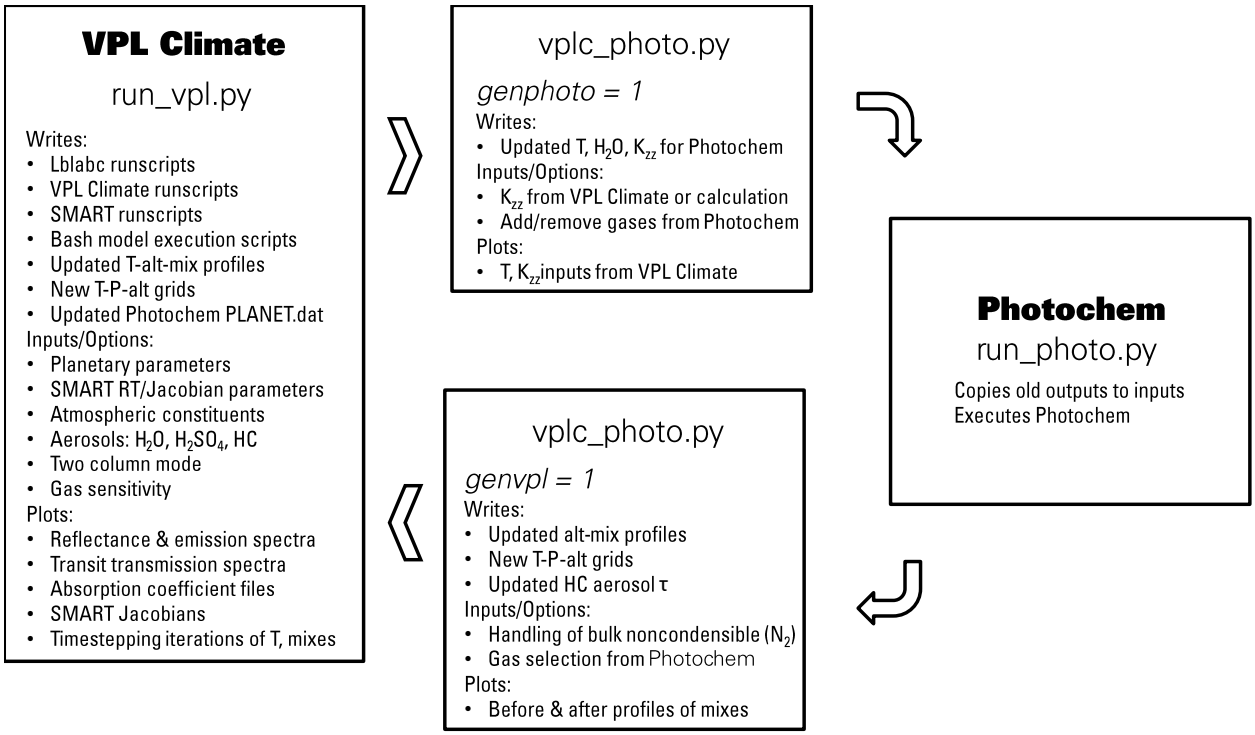

Figure 2.8: Schematic overview of climate-photochemistry model coupling.

Chapter 3

EVOLVED CLIMATES AND OBSERVATIONAL DISCRIMINANTS FOR THE TRAPPIST-1 SYSTEM

Portions of this chapter were originally published in collaboration with V. S. Meadows, D. Crisp, T. D. Robinson, et al. in The Astrophysical Journal (Lincowski et al., 2018, The Astrophysical Journal, ©2018 The American Astronomical Society), and in collaboration with J. Lustig-Yaeger and V. S. Meadows in The Astronomical Journal (Lustig-Yaeger et al., 2019, The Astronomical Journal, ©2019 The American Astronomical Society), and are reproduced below under the Creative Commons Attribution 3.0 license (https://creativecommons.org/licenses/by/3.0/).

This chapter represents the first comprehensive application of the versatile 1D VPL Climate model. This work focuses on plausible evolved, post-ocean-loss atmospheres for all seven planets in the TRAPPIST-1 system, and includes a single water world ("aqua planet") for TRAPPIST-1 e for maximum breadth of comparison with other contemporary work (particularly 3D GCM studies).

3.1 Introduction

As described in detail in the Introduction to this thesis, M dwarf stars are not simply scaled-down versions of our Sun; M dwarfs have a different evolutionary history and different life-long UV activity levels that can adversely affect the evolution of planetary atmospheres and the development of life. Early stellar evolution and planetary disk migration may have caused changes in the planetary bulk and atmospheric compositions, and the subsequent evolutionary paths of M dwarf planets in ways unlike those seen in our Solar System. For example, Ribas et al. (2016), Coleman et al. (2017), and Barnes et al. (2018) assessed evolutionary outcomes for a single planet in the habitable zone of an M5.5 dwarf star, Proxima Centauri b. Their work suggests that these evolutionary paths could produce desiccated planets that rapidly lost their oceans by evaporation, photolysis, and subsequent hydrogen loss to space, leaving massive O_2-dominated atmospheres (Kasting, 1995; Luger and Barnes, 2015; Barnes et al., 2018), or runaway greenhouse conditions with CO_2-dominated atmospheres (i.e. Venus-like; Kasting, 1995; Meadows et al., 2018). The former hypothesized planetary environment assumes O_2 build-up as a result of the super-luminous pre-main-sequence phase and subsequent water loss, with inefficient atmospheric loss or surface

sinks for oxygen. Processes other than XUV-driven hydrodynamic escape may cause O_2 loss, such as surface interactions (Hamano et al., 2013; Schaefer et al., 2016; Wordsworth et al., 2018) and non-thermal processes favoring ion escape (Collinson et al., 2016; Airapetian et al., 2017; Dong et al., 2017; Garcia-Sage et al., 2017; Dong et al., 2018).

The current understanding of the history of Venus suggests that oxygen loss may be efficient. If so, a CO_2-dominated atmosphere is also a likely case that may evolve from the loss processes that the TRAPPIST-1 planets may have experienced, because these planets could continue to outgas volatiles (Donahue and Pollack, 1983), eventually producing Venus-like atmospheric conditions. These planets could also have migrated inwards to their current positions (Luger et al., 2017b; Unterborn et al., 2018a), which would have allowed primordial H_2 envelopes to be stripped by the young star to reveal a terrestrial core (Lammer et al., 2011; Luger et al., 2015) that may be volatile-rich and result in a more Earth-like H_2O- or N_2-rich atmosphere.

Here I model O_2- and CO_2-rich, evolved atmospheres, which may be common on planets orbiting M dwarfs. In §3.3, I present results of coupled climate-chemistry simulations of several different atmospheric compositions, and the associated simulated direct imaging and transmission spectra. In §3.4, I discuss the climate-photochemistry results, identify observational discriminants for the modeled environments, compare these results with other recent work, and assess recent observations.

3.2 Model Inputs

The climate, photochemical, and atmospheric escape models I use here require a number of inputs that tailor the model to the planetary atmosphere studied. Inputs include planetary properties (e.g. orbit, radius, etc.), atmospheric gas mixing ratios for each constituent in each layer, gas absorption properties (i.e. cross section data and line lists), thermodynamic data for condensible gases, particle optical properties for aerosols, wavelength-dependent surface albedo data, and stellar spectral energy distribution (SED). These are discussed in detail in the Model Inputs section in the Models chapter §3.2. Individual deviations are described here.

Parameter	**Modeled**	**Measured**[a]					
Star		TRAPPIST-1—2MASS J23062928-0502285					
Magnitudes[b]		V = 18.80±0.08, R = 16.47±0.07, I= 14.0±0.1, J = 11.35±0.02, K = 10.30±0.02					
Mass ($M_\odot$)		0.0802 ± 0.0073					
Radius ($R_\odot$)	0.117	0.117 ± 0.0036					
Luminosity ($L_\odot$)	0.000524	0.000524 ± 0.000034					
Effective Temperature (K)	2500	2,559 ± 50					
Metallicity [Fe/H]	0.	+ 0.04 ± 0.08					
Log g	5.	4.8					
Planets[a]	**b**	**c**	**d**	**e**	**f**	**g**	**h**[c]
Period (days)	1.510870	2.42182	4.0496	6.0996	9.2067	12.353	18.767
Semi-major axis (AU)	0.01111	0.01521	0.02144	0.02817	0.0371	0.0451	0.0595
Irradiation ($S_\odot$)	4.245	2.265	1.140	0.6603	0.381	0.258	0.148
Radius[d] ($R_\oplus$)	$1.121^{+0.032}_{-0.031}$	$1.095^{+0.031}_{-0.030}$	0.784±0.023	$0.910^{+0.027}_{-0.026}$	$1.046^{+0.030}_{-0.029}$	$1.148^{+0.033}_{-0.032}$	$0.773^{+0.027}_{-0.026}$
Mass[d] ($M_\oplus$)	$1.107^{+0.143}_{-0.154}$	$1.156^{+0.131}_{-0.142}$	$0.297^{+0.035}_{-0.039}$	$0.772^{+0.075}_{-0.079}$	$0.934^{+0.078}_{-0.080}$	$1.148^{+0.095}_{-0.098}$	$0.331^{+0.049}_{-0.056}$
Density[d] ($\rho_\oplus$)	$0.726^{+0.091}_{-0.092}$	$0.883^{+0.078}_{-0.083}$	$0.616^{+0.062}_{-0.067}$	$1.024^{+0.070}_{-0.076}$	$0.816^{+0.036}_{-0.038}$	$0.759^{+0.033}_{-0.034}$	$0.719^{+0.102}_{-0.117}$
Gravity[d] (m/s^2)	7.94	9.46	4.74	9.15	8.37	8.55	5.43
Impact parameter b (R_*)	$0.126^{+0.092}_{-0.078}$	$0.161^{+0.076}_{-0.084}$	0.17±0.11	$0.12^{+0.11}_{-0.09}$	0.382±0.035	0.42±0.031	$0.45^{+0.06}_{-0.08}$

Note: I use nominal values for the modeling. Error bars (1σ) are shown for reference. Standard errors on the period are smaller than the precision reported here. Error on semi-major axis is approximately 3% of the quoted values. Irradiation is computed from the reported semi-major axis, assuming the luminosity quoted here. Gravity is given without error bars, and is for the nominal values of mass and radius.
[a] Data from Gillon et al. (2017) unless otherwise noted.
[b] Data from Gillon et al. (2016).
[c] Data from Luger et al. (2017c).
[d] Data from Grimm et al. (2018).

Table 3.1: Stellar and planetary system parameters used in this chapter as model inputs for the TRAPPIST-1 system.

3.2.0.1 Planetary Properties and Model Atmospheres

Here I adopt the current best-fit orbital periods, radii, and masses of the TRAPPIST-1 planets (see Table 3.1 and Gillon et al., 2016, 2017; Luger et al., 2017c; Grimm et al., 2018). I assume the planets are in fixed, circular orbits. For all seven known planets, I simulate post-runaway-greenhouse, O_2-dominated atmospheres with and without continuous outgassing, and Venus-like CO_2-dominated atmospheres. These atmospheres are modeled with surface pressures of 10 and 100 bars for O_2-dominated cases and 10 and 92.1 bars (Venus' surface pressure) for Venus-like cases. I also model a potentially habitable aqua planet for TRAPPIST-1 e for comparison, both with the uninhabitable cases that I present here and with other studies of TRAPPIST-1 planetary climates (Wolf, 2017; Turbet et al., 2018) and observables (Morley et al., 2017). The particulars of each case are presented in detail in §3.3.

VPL Climate requires a number of convection parameters, which I vary depending on the

planetary environment. These are shown in Table 3.2. The primary differences are between the dry and moist planets, as additional parameters are specified for vertical mixing in the tropospheres of moist planets.

Parameter	**O_2-dominated**	**Venus-like**	**Aqua planet**	**Description**
f_z	0.01	0.01	0.01	Mixing length fraction
U [m s^{-1}]	0.1	0.1	10	Surface wind speed
z_0 [m]	0.005	0.005	0.0002	Surface roughness length
ρ_0 [kg m^{-3}]	1	1	1	Baseline density for eddy diffusion
P_0 [Pa]	1	1	1	Pressure for breaking of gravity waves in eddy diffusion
$K_{m,0}$ [m^2 s^{-1}]	0.5	1.0	0.5	Eddy scaling coefficient for mass, gravity waves
$K_{m,1}$ [m^2 s^{-1}]	–	–	20	Eddy scaling coefficient for mass, stability
$K_{m,1}$ [m^2 s^{-1}]	–	0.5	–	Constant minimal eddy diffusion
Λ_0	–	–	0.1	Minimum stability factor
f_{min}	10^{-4}	10^{-4}	10^{-4}	Minimum stability scaling factor for heat
f_{max}	0.15	0.15	0.15	Maximum stability scaling factor for heat

Table 3.2: Adjustable Convection Model Parameters

3.3 Results

I present calculated climates and compositions for O_2- and CO_2-dominated atmospheres, and their spectra and observational discriminants. To span plausible pressure and compositional ranges for these evolved atmospheres, I model 10 and 100 bar O_2-dominated atmospheres, with and without trace constituents due to surface outgassing or volatile delivery; and 10 and 92.1 bar CO_2-dominated Venus-like atmospheres, with and without Venus-like haze/cloud aerosols. As a potentially habitable comparison case, I also calculate climate and trace composition of a 1 bar atmosphere for an ocean-covered TRAPPIST-1 e "aqua planet". I show simulated pressure-temperature structures and mixing ratio profiles. A summary of these experiments is shown in Table 3.3.

Planetary State	Surface	clouds	gases	**surf. pres.**
Aqua planet, clear sky	ocean	None	80% N_2, 20% O_2, trace H_2O, CO_2, SO_2, H_2S, OCS, NO, CH_4	1 bar
Aqua planet, cloudy	ocean	50% water, 50% ice	80% N_2, 20% O_2, trace H_2O, CO_2, SO_2, H_2S, OCS, NO, CH_4	1 bar
O_2, desiccated	desert	None	95% O_2, 4.5–4.95% N_2, 0.5 bar CO_2	10, 100 bar
O_2, outgassing	desert	None	95% O_2, 4.5–4.95% N_2, 0.5 bar CO_2, trace H_2O, SO_2, OCS, H_2S	10, 100 bar
Venus-like, clear sky	basalt	None	96.5% CO_2, 3.5% N_2, trace H_2O, SO_2, OCS, H_2S, NO, HCl	10, 92 bar
Venus-like, cloudy	basalt	H_2SO_4	96.5% CO_2, 3.5% N_2, trace H_2O, SO_2, OCS, H_2S, NO, HCl	10, 92 bar

Table 3.3: Modeled Planetary States and Their Environmental Parameters

A number of assumptions underlie the modeling in this work. These atmospheres are assumed to be in hydrostatic equilibrium, though hydrodynamic processes could be occurring on planets b, c, and d, inward of the inner edge of the habitable zone. I assume the modeled atmospheres are stable against collapse on the night side, due to sufficiently high atmospheric mass (10–100 bar) to reduce day-night temperature contrasts (Turbet et al., 2018) or ocean circulation for the 1 bar aqua planets (Hu and Yang, 2014). I assume these planets began in a warm state due to the super-luminous pre-main-sequence phase, and that their secondary atmospheres were formed during this time. I ignore ion and particle effects, though these non-thermal processes may be important drivers of atmospheric loss (Airapetian et al., 2017; Garcia-Sage et al., 2017) and atmospheric chemistry (Segura et al., 2010; Airapetian et al., 2017; Tilley et al., 2019). The recent densities inferred from transit timing variation (TTV) measurements by Grimm et al. (2018) currently indicates high volatile content planets, perhaps with the exception of planet e, which suggests that the most desiccated atmospheres are less probable, and supports ocean-bearing surfaces or large outgassing fluxes. However, the error bars on the planet densities remain quite large, and do not rule out more refractory compositions, supporting the possibility of desiccated atmospheres.

3.3.1 Planetary Environmental States

In the following subsections, I describe the input assumptions and resultant environmental states (atmospheric temperature profiles as a function of pressure, and vertical profiles of principal atmospheric constituent abundances) for each atmosphere. Globally-averaged surface temperatures for all modeled climates are given in Figure 3.4, and O_3 column densities are given in Table 3.5.

3.3.1.1 O_2-Dominated Atmospheres—Desiccated

In Figure 3.1, I present environmental states for completely desiccated, oxygen-dominated atmospheres for the seven TRAPPIST-1 planets, assuming 10 or 100 bars surface pressure. These surface pressure values were chosen as representative of possible states, because although TRAPPIST-1's pre-main-sequence evolution may produce up to thousands of bars of O_2 in the most extreme

	b	c	d	e	f	g	h
Aqua planet, clear				279			
Aqua planet, cloudy 1 bar				282			
O_2, desiccated 10 bar	439	346	281	238	202	180	151
O_2, desiccated 100 bar	428	336	275	226	206	184	159
O_2, outgassing 10 bar	560	438	343	271	225	200	166
O_2, outgassing 100 bar	556	476	407	314	261	201	163
Venus, cloudy 10 bar		616	398	304	263	243	200
Venus, clear 10 bar	714	633	593	496	407	336	259
Venus, cloudy 92 bar		779	634	551	527	491	398
Venus, clear 92 bar	927	816	743	689	642	572	465

Table 3.4: Surface temperatures [K] for every modeled planet and environment combination. Colors represent surface climate: blues are significantly below the freezing point of water, reds are above the runaway greenhouse temperature, and greens are within potentially habitable surface temperatures. The aqua planet environment was only modeled for TRAPPIST-1 e. Venus trace gases have boundary values of 30 ppm H_2O, 28 ppm SO_2, and 1 ppm OCS at 10 bar, and photochemical-kinetic equilibrium abundances of CO and H_2S. Temperate surfaces do not imply habitability due to the inhospitable character of the environmental states, including very low water abundance. Planets in the habitable zone may not necessarily have habitable temperatures.

case (Bolmont et al., 2017; Lincowski et al., 2018), much of this O_2 is likely to be re-incorporated into the land surface, ocean, lithosphere, or mantle (e.g. Hamano et al., 2013; Schaefer et al., 2016; Wordsworth et al., 2018), or depending on each planet's magnetic field, lost to non-hydrodynamic, top-of-atmosphere processes over time (e.g. Khodachenko et al., 2007; Lammer et al., 2007, 2011; Ribas et al., 2016), such as the "electric wind" on Venus (Collinson et al., 2016). While an abiotic O_2-dominated planetary atmosphere has yet to be discovered, and Venus does not retain significant quantities of atmospheric oxygen, it may be possible to test the existence of this hypothesized ocean-loss-generated atmosphere with *JWST*.

These atmospheres were initialized with 95% O_2, 0.05 bar CO_2 (consistent with Meadows et al., 2018), and the remainder N_2, each specified as a fixed surface mixing ratio, with no outgassing. Because this case assumes a planet that was severely volatile-depleted in both its at-

Planets	b	c	d	e	f	g	h
Aqua planet, clear, 1 bar				3.1×10^{18}			
Aqua planet, cloudy, 1 bar				2.9×10^{18}			
O_2, desiccated, 10 bar	2.5×10^{18}	6.3×10^{18}	1.1×10^{19}	4.7×10^{19}	2.2×10^{22}	6.0×10^{22}	1.3×10^{23}
O_2, desiccated, 100 bar	7.2×10^{17}	2.4×10^{18}	6.4×10^{18}	8.8×10^{18}	6.1×10^{22}	2.7×10^{23}	1.4×10^{24}
O_2, outgassing, 10 bar	1.6×10^{18}	5.2×10^{18}	9.9×10^{18}	2.7×10^{19}	8.5×10^{20}	2.4×10^{21}	4.0×10^{21}
O_2, outgassing, 100 bar	1.7×10^{19}	2.1×10^{20}	2.7×10^{21}	2.4×10^{22}	7.2×10^{23}	6.6×10^{24}	1.8×10^{25}
Venus-like, clear, 10 bar	2.3×10^{15}	2.1×10^{15}	5.4×10^{15}	1.0×10^{15}	6.9×10^{15}	8.6×10^{15}	1.5×10^{16}
Venus-like, cloudy, 10 bar		1.0×10^{15}	1.1×10^{16}	4.6×10^{15}	7.6×10^{15}	9.1×10^{15}	1.5×10^{16}
Venus-like, clear, 92 bar	1.8×10^{15}	1.9×10^{15}	5.1×10^{15}	1.3×10^{15}	6.7×10^{15}	9.1×10^{15}	1.6×10^{16}
Venus-like, cloudy, 92 bar		1.0×10^{15}	9.5×10^{14}	4.2×10^{15}	7.8×10^{15}	9.8×10^{15}	1.6×10^{16}

Compare to global-average Earth ozone column depth of 8×10^{18} cm^{-2} (`https://ozonewatch.gsfc.nasa.gov/`).

Table 3.5: Ozone Column Densities [cm^{-2}]

mosphere and mantle, these atmospheres are considered completely desiccated (i.e. they contain no water, nor any other hydrogen-bearing species). The remaining composition is dominated by photochemically-produced trace gases.

The composition of photochemically-produced trace gases, principally O_3 and CO, increase monotonically as a function of irradiation from the parent star (i.e. as a function of semi-major axis). The equilibrium concentration of ozone is due to the competing effects of vertical transport and the Chapman cycle, whereby photolysis of O_2 produces atomic oxygen that can combine with O_2 to form O_3, which is directly lost by photolysis if atomic oxygen combines to form O_2. For the hotter planets (b–d), O_3 photolysis is efficient down to the surface from absorption in the broad Chappuis band. However, the colder planets receive less UV flux as a result of distance from the star, so the photolysis rates are slower. In the coldest atmospheres (f, g and h), eddy transport can overwhelm photolysis and reaction rates for O_3, resulting in well-mixed vertical profiles and saturated O_3 absorption bands. Furthermore, photolysis of O_2 drops faster with semi-major axis because its cross-section is limited to the FUV and easily saturates compared to O_3, which is includes a strong NUV band and the weak Chappuis band in visible wavelengths, which are not easily saturated.

After the publication of these results in Lincowski et al. (2018), I further investigated the cause of the ozone accumulation in the atmospheres of the outer planets (an effect previously noticed by Grenfell et al. 2007). While the influence of irradiation on the Chapman cycle is a driving

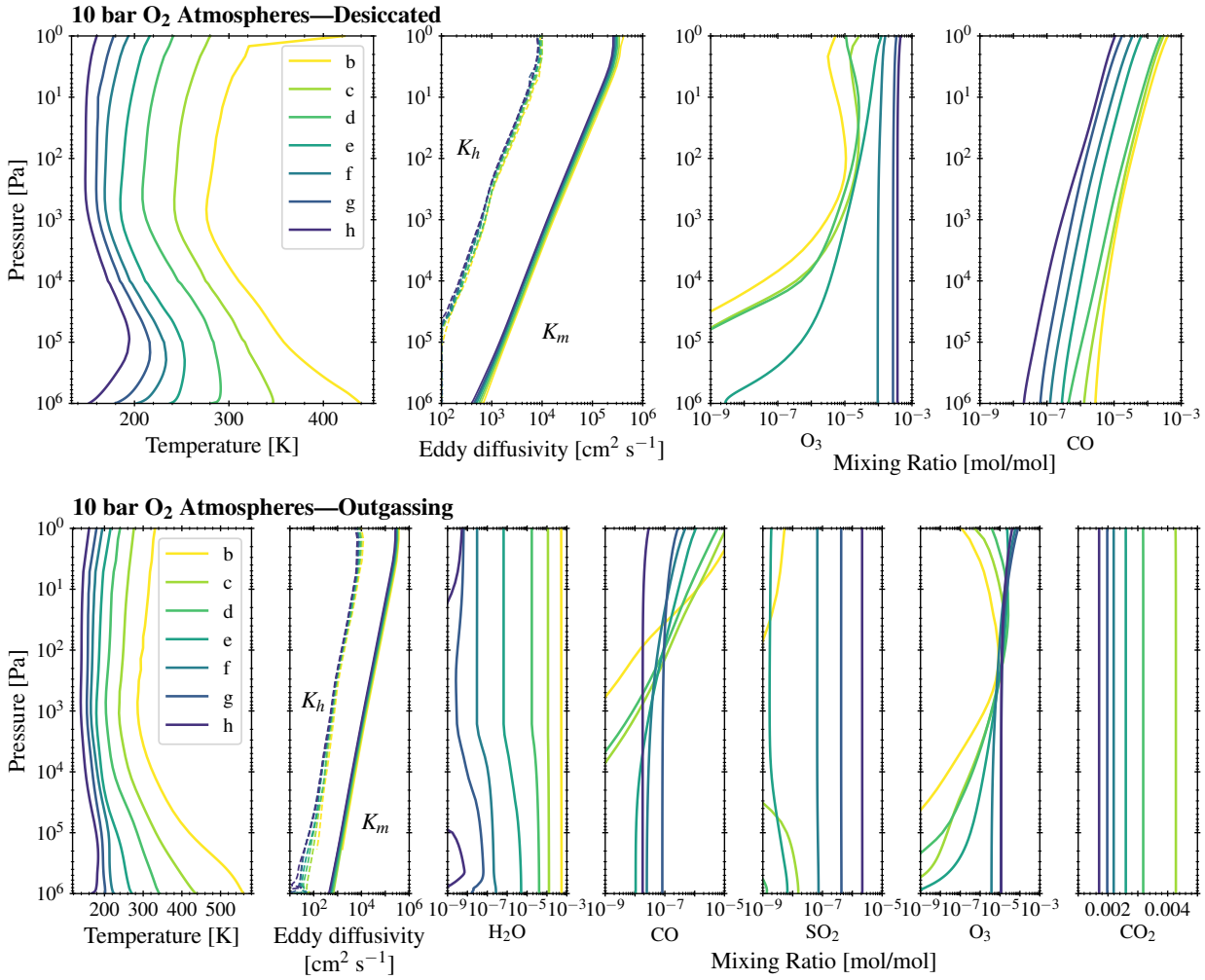

Figure 3.1: Converged structures for the 10-bar desiccated (*upper panel*) and outgassing (*lower panel*) O_2-dominated TRAPPIST-1 atmospheres. The 10 bar atmospheres are generally similar in structure to the 100 bar atmospheres above 10 bars (10^6 Pa), though the 100 bar desiccated atmospheres have even stronger temperature inversions, due to O_2-O_2 CIA. The outgassing atmospheric structures and associated surface temperatures exhibit a continuum from Venus-like hotter atmospheres to colder temperature profiles similar to the desiccated cases.

factor, I noted in Lustig-Yaeger et al. (2019a), §4.2, that the differences among the planets can more specifically be attributed to catalytic cycles of nitrogen oxides (primarily, N_2O, NO, and NO_2), which drive the destruction of O_3, as in the stratosphere of Earth (Seinfeld and Pandis, 2006). Because these atmospheres contain N_2, $O(^1D)$ produced from photolysis of oxygen-bearing

molecules can react with N_2 to generate nitrogen oxides. The availability of O^1D declines with distance from the star due to lower UV fluxes. Beginning with planet e, the production of nitrogen oxides declines substantially, removing them as a mechanism for the destruction of O_3, so that O_3 accumulates and becomes well-mixed, generating a large column density. In the atmosphere dominated by O_2 and without N_2, O_3 levels would likely be higher, due to the lack of NO_x catalysts.

The monotonic increase in CO with semi-major axis in these atmospheres is due to CO_2 photolysis and lack of recombination. In the terrestrial Solar System atmospheres, the recombination to CO_2 is efficient due to photolytic water products (e.g. OH^-). Because this environment is devoid of hydrogen, CO can only recombine with atomic oxygen under a slow, density-dependent three-body reaction (Gao et al., 2015).

These modeled environments exhibit surface temperatures (151–439 K, from h to b) that are similar to their equilibrium values (173–400 K; Gillon et al. 2017; Luger et al. 2017c) largely due to low greenhouse gas abundances. The temperatures shown here differ slightly from those published in Lincowski et al. (2018), because the published work did not include the 6 μm O_2-O_2 collision-induced absorption (CIA) band. This band is mostly irrelevant in moist atmospheres because it coincides with a large H_2O band. In these desiccated atmospheres, however, it has a noticeable impact, particularly on the warmer cases. This occurs because at higher temperatures, a non-negligible portion of thermal flux from the surface blackbody reaches that 6 μm band. This does not occur in the cooler cases, so planets e, f, g, and h are largely unaffected in surface temperature. However, the temperature structures of all desiccated O_2 planets were affected by the additional O_2-O_2 band.

Most of the atmospheric structures for these completely desiccated planets exhibit a stratospheric temperature inversion, like Earth, due to the radiative effects of the photochemically-produced O_3 and O_2-O_2 CIA, which is significant in these dense O_2 atmospheres. For the cooler atmospheres, a sensitivity test removing each constituent to determine the radiative effect suggests that O_3 and O_2-O_2 contribute equally to the heating structure with temperature inversion, but via different mechanisms: O_2-O_2 directly absorbs M dwarf NIR irradiation, while O_3 traps outgoing thermal radiation. The hottest planets did not exhibit a temperature inversion, because they were

hot enough that the 6 μm trapped outgoing thermal radiation, and so functioned like water vapor in the atmosphere of Earth, providing a greenhouse effect near the surface.

The pressure level at which the stratosphere peaks in the cooler atmospheres is different than Earth, again due to the O_2-O_2 CIA. The stratosphere of Earth is caused by O_3 NUV absorption and peaks around ∼0.001 bar, while the pressure level at which the peak in these O_2 atmospheres occurs is much closer to the surface, around 1–10 bar, due to the stronger density dependence of CIA. This stratospheric absorption induces heating in the atmosphere, exceeding heating at the planetary surface, causing a surface temperature inversion similar to Earth and Mars at night (e.g. André and Mahrt, 1982; Hinson and Wilson, 2004), and inhibiting a troposphere from forming. The causes for these conditions on Earth and Mars at night are due instead to rapid cooling of the surface, rather than warming of the atmosphere.

3.3.1.2 O_2-Dominated Atmospheres—Outgassing

Here I consider the case where a planet has lost its oceans, but continues to outgas from a volatile-rich mantle, as is likely the case on Venus (e.g. Bullock and Grinspoon, 2001). For other planetary systems, including TRAPPIST-1, this could also be due to delivery by impactors (Chyba, 1990; Kral et al., 2018). For all seven planets we specify Earth-like outgassing fluxes (F), which are relatively well-known: 1.68×10^{11} cm^2 s^{-1} H_2O ($\sim 10F_{CO_2}$; Burton et al., 2000), 1.0×10^8 cm^2 s^{-1} H_2S, 1.35×10^9 cm^2 s^{-1} SO_2 (Carn et al., 2017), 6.88×10^9 cm^2 s^{-1} CO_2 ($\sim 3.5F_{SO_2}$; Williams et al., 1992), and 3.7×10^5 cm^2 s^{-1} OCS ($\sim 10^{-4}F_{CO_2}$; Belviso et al., 1986). These fluxes represent volcanic outgassing, so are distributed within one scale height of the surface (∼6–20 km). I specify minimal non-zero dry deposition rates of 10^{-8} cm s^{-1} for all outgassed species to prevent a "runaway" state.

As shown in Figure 3.1, identical outgassing fluxes result in different levels of trace gases across the seven planets. Some species vary monotonically with irradiation (H_2O, O_3, CO_2), while others do not (CO, SO_2). These trends are modulated by surface gravity (planets b, d, and h have low surface gravity) and atmospheric temperature. There are several interacting chemical networks: carbon, ozone, and sulfur. First considering the carbon network, the primary carbon species are

CO_2 and its photolytic product, CO. The CO profiles demonstrate the competing effects of photolysis and vertical transport. The hotter planets have a steep CO gradient, driven by strong photolysis, while the colder planets have well-mixed CO profiles, where vertical transport overcomes photolysis rates and the peak abundance drops. The CO_2 levels are not wholly a function of photolysis; for a given surface pressure, they have different atmospheric column masses. Even though the hotter planets have larger *mixing ratios* of CO_2, because of hotter temperatures their atmospheres are less dense, and have smaller *number densities*. Photolysis of CO_2 from identical outgassing fluxes results in lower CO_2 inventories (i.e. number densities) in the more irradiated atmospheres. These CO_2 results differ from the fully desiccated environments due the Earth-like active surface fluxes we assumed here.

The ozone profiles are very similar to the desiccated O_2-dominated planets. The production of O_3 is the same, but the outgassing planets have more sinks, primarily water vapor. As a result, the outgassing cases overall have lower column densities of O_3. Because the outer planets can be very cold, they cannot maintain much water vapor (Figure 3.1), so they too can accumulate substantial quantities of O_3, particularly g and h.

The abundance and vertical distribution of species in the sulfur network (SO_2, SO_3, and H_2SO_4) is a balance between water vapor availability, temperature, and photolysis rates. The colder atmospheres are water-limited due to condensation and lower photolysis rates, so atmospheric SO_2 inventories are highest. The formation of SO_3 is from combination of SO_2 with free oxygen atoms. Sulfuric acid is a primary sink for SO_3 and is formed by (Krasnopolsky, 2012):

$$SO_3 + H_2O + H_2O \longrightarrow H_2SO_4 + H_2O, \tag{3.1}$$

and can either thermally decompose or condense and rain out. The inner planets receive sufficient irradiation to permit efficient conversion of SO_2 to SO_3 and H_2SO_4.

Volatiles in these atmospheres have a large effect on planetary climate and bridge the results of the O_2 desiccated and Venus-like atmospheres. The coldest planets (g and h) maintain temperature profiles similar to the desiccated cases, including near-surface temperature inversions, because

they are too cold to maintain quantities of water vapor sufficient to heat the lower atmospheres. Conversely, the remaining planets generate sufficient water abundances to maintain a positive lapse rate. To prevent a full runaway greenhouse, I limited the stratospheric water relative humidity to 0.1% for b and 1.0% for c, while the remaining planets are limited to 10%. Planets b, c, and d show the tendency to continue into a runaway greenhouse state, which is supported in our results by their abundances of water vapor well-mixed throughout the atmospheric column. Reducing the outgassing of H_2O in our model would more closely approximate Venus-like H_2O abundance. Only TRAPPIST-1 e has a moderate surface temperature (271–314 K) in this outgassing case, which supports the possibility for it to outgas an ocean and recover habitability.

3.3.1.3 Venus-Like Atmospheres

Here I model Venus-like environments, which may be common around M dwarfs (Kane et al., 2014). For this environmental state, I assume that the complete loss of oceans during the super-luminous pre-main-sequence phase removed a potentially strong sink for soluble gases (e.g. CO_2 and SO_2). Subsequent loss or sequestration of oxygen over time (Schaefer et al., 2016; Wordsworth et al., 2018), and initial and subsequent outgassing of volatiles, may have allowed a Venus-like high-CO_2 atmosphere to develop. Even though planet h may not have lost an entire Earth ocean (Lincowski et al., 2018), it could have initially outgassed significant amounts of CO_2. I modeled Venus-like atmospheres for all seven planets (Figure 3.2) using the 10-bar boundary conditions used to validate observations of Venus, following Krasnopolsky (2012) (see my §2.5). Venus atmospheric chemistry is typically modeled in sections: by thermochemistry, which dominates the lower atmosphere below the cloud deck (e.g. Krasnopolsky, 2013), and by photochemistry, which is responsible for the chemistry of gases at directly observable altitudes at and above the cloud deck (e.g. Krasnopolsky, 2012; Zhang et al., 2012). I use photochemistry to model these atmospheres but do not include thermochemical reactions, which could be a useful improvement in future work for the planets with the highest surface temperatures.

The Venus-like atmospheres are initiated as either 10 or 92 bars of total pressure with Venus-like levels of CO_2 (96.5%) and N_2 (3.5%). For the 92 bar cases, I assumed a constant mixing ratio

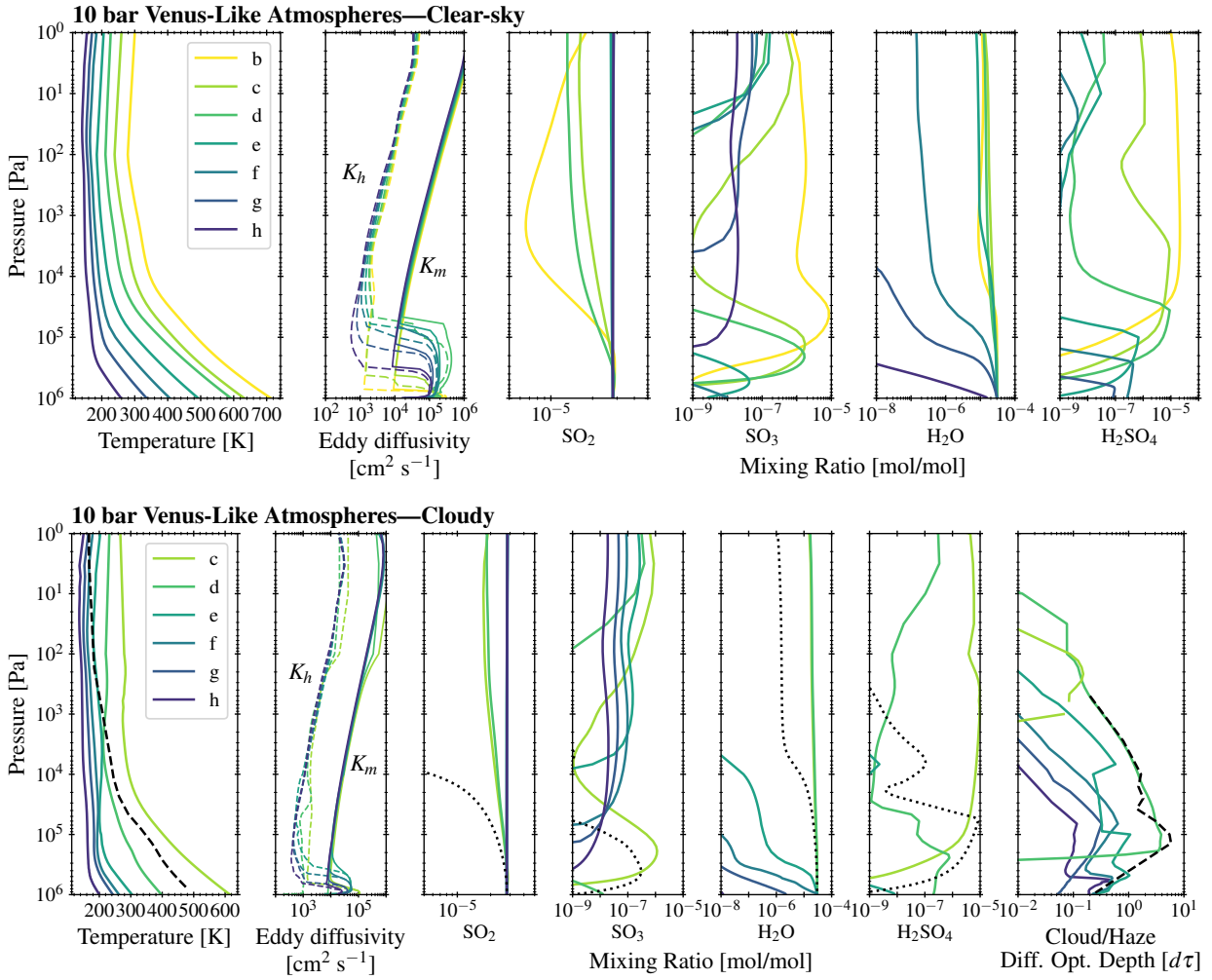

Figure 3.2: Converged structures of the 10-bar clear-sky (*upper panel*) and cloudy (*lower panel*) Venus-like TRAPPIST-1 atmospheres. Note: b is not included in the cloudy case, as aerosols were not formed. The Venus International Reference Atmosphere (VIRA) temperature structure is shown in the cloudy panel (black dashed line). The 92 bar atmospheres are not shown here, but show similar structure to the 10 bar cases. Here we show H_2O, SO_2, SO_3, and H_2SO_4 gases only, as the most relevant to climate and cloud formation. The bulk gases CO_2 and N_2 are 96.5% CO_2 and 3.5% N_2 for the 10 bar and 92 bar atmospheres, respectively. With a (clear-sky) Venus-like atmosphere, TRAPPIST-1 b may exhibit surface temperatures in excess of Venus (due to higher instellation) and is too hot to form sulfuric acid aerosols in our model, even though it was most effective at forming high-altitude H_2SO_4 vapor. Sulfur dioxide survives more readily in these atmospheres due to the lower MUV–NUV flux.

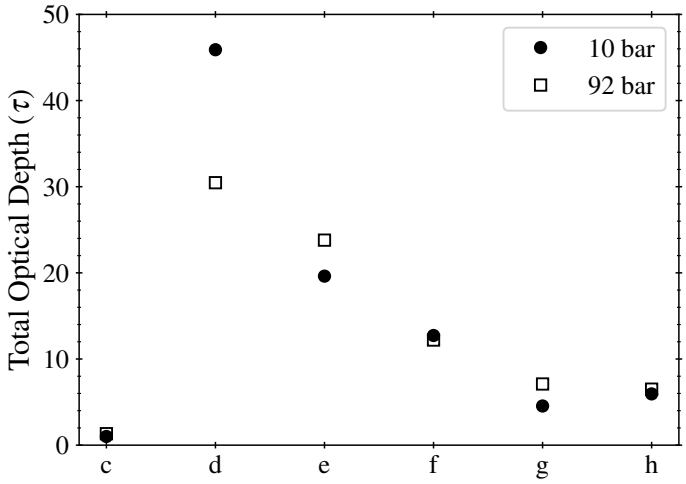

Figure 3.3: Sulfuric acid cloud total optical depths for each cloudy Venus atmosphere. TRAPPIST-1 b did not condense sulfuric acid in the models. TRAPPIST-1 c maintained only thin clouds, because sulfuric acid absorption warms the cloud layer and the local warming can cause the clouds to evaporate. Optical depths peak for planet d, which has vigorous sulfuric acid formation and has lower surface gravity, so can more easily loft aerosols. The planets generally decline in optical depth with distance from the star due to lower photolysis rates and for the 10 bar atmospheres, the lower abundance of water vapor. Note the 92 bar atmosphere photochemistry and cloud formation were truncated at 10 bar. Planets f, g, and h had cloud formation to 10 bar, and so could also form thicker clouds deeper toward the surface.

for every species from 10 bars to the surface. I initiated the photochemical model with trace gas lower boundary conditions required to reproduce observations of Venus following the modeling of Krasnopolsky (2012), consisting of fixed mixing ratios at 10 bar of 30 ppm H_2O, 4.5 ppm H_2, 5.5 ppm NO, 28 ppm SO_2, 1 ppm OCS, and 400 ppm HCl. I calculate the photochemical-kinetic equilibrium profiles of these and other trace gases subject to these boundary conditions. These trace gases absorb at wavelengths that are complementary to CO_2 and can have a substantial effect on climate (Bullock and Grinspoon, 2013; Lee et al., 2016).

For purposes of climate-photochemical modeling for observational discriminants, both clear-sky and cloudy Venus-like atmospheres are separately modeled, except for planet b, which does not condense sulfuric acid aerosols in the photochemistry model. Both clear-sky and cloudy at-

mospheres display a similar, Venus-like profile (dashed black line in Figure 3.2), despite being irradiated by a very different SED than the Sun. The temperature profiles are characterized by long adiabats from the surface each to a $\sim$ 0.05–1.0 bar tropopause. The surface temperatures are the hottest of the environments simulated, ranging from 259–465 K (200–398 K cloudy) for planet h (outside the outer edge of the HZ), to 714–927 K for b, which receives approximately twice Venus' stellar flux.

As in the O_2 outgassing cases, the Venus-like atmospheric photochemistry is dominated by the formation of sulfuric acid from the combination of water with SO_3, a photolytically-derived product of SO_2. This sulfur chemistry is not driven as strongly as Venus' due to lower MUV–NUV flux from TRAPPIST-1, so the rates of both SO_2 and SO_3 photolysis are much lower than for Venus. However, SO_2 is still susceptible to photolytic destruction, which results in the trend seen in Figure 3.2, that SO_2 is more abundant further from the star. The abundance of SO_3 is a balance between its formation rate via SO_2 photolysis and the rate at which it combines with water to form H_2SO_4. In our simulations, water vapor decreases as a function of semi-major axis in both clear-sky and cloudy cases due to this condensation into H_2SO_4 aerosols, as well as into water and water-ice in the cooler planets (e, f, g, and h; although we do not model the water clouds that would form as a result of this process).

The prevalence of H_2SO_4 vapor depends on its chemical formation, where and whether it condenses, and its destruction via thermal decomposition in the lower atmosphere. In these simulations, H_2SO_4 formed in abundances similar to Venus (up to 17 ppm vs 8.5 ppm for Venus, Krasnopolsky 2015) for the hotter TRAPPIST-1 planets and drops in abundance with semi-major axis due to the reduced availability of H_2O at lower temperatures. The highest abundances of H_2SO_4 and SO_3 are seen in the stratospheres of the hotter planets (b and c), with peak vapor concentrations decreasing with semi-major axis and at lower altitudes. Similarly, the peak optical depths of the clouds drop with semi-major axis due to less effective formation processes. Because H_2SO_4 can persist closer to the surface in the colder atmospheres, the semi-major-axis-dependent total optical depth peaks for planet d, due to the competing effects of formation/condensation and thermal decomposition/rainout (see Figure 3.3). Notably, for planet b, the modeled atmosphere

was too hot for condensation. Planet d exhibited the highest aerosol optical depth due to its low surface gravity, which allows aerosols to be more easily lofted in the atmosphere.

Sulfuric acid aerosols in the cloudy Venus atmospheres substantially reduced the surface temperatures. The net top of atmosphere stellar irradiance was reduced by ∼50–60%, resulting in temperature ranges of 200–616 K (10 bar) and 398–779 K (92 bar), h to c. As a caveat, it is possible that sulfuric acid production in Venus' atmosphere may vary by orders of magnitude (Gao et al., 2014), and it is unknown how an alien M dwarf spectrum may affect the more uncertain aspects of Venus-like atmospheric chemistry, particularly of the unknown UV absorber, which I exclude.

3.3.1.4 Aqua Planet

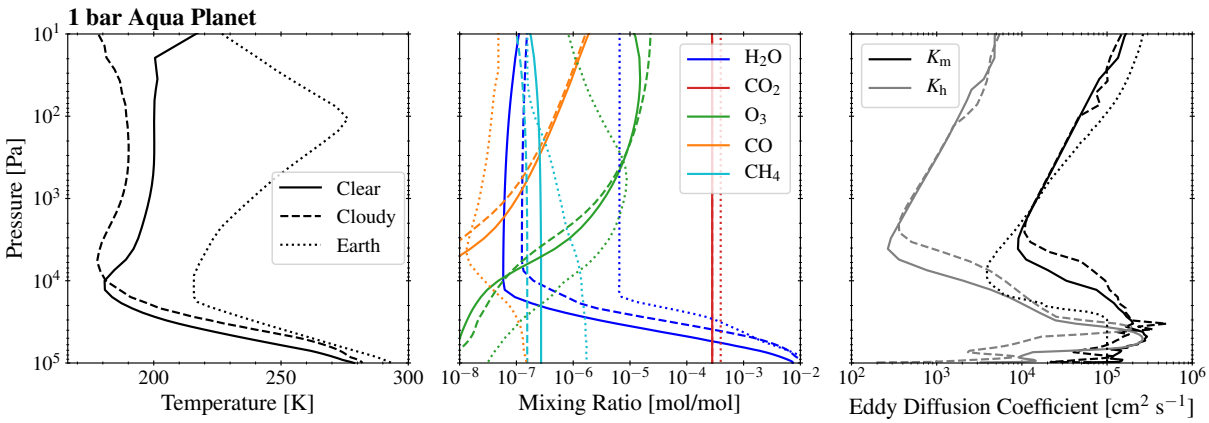

Figure 3.4: Climates, gas mixing ratios, and eddy diffusion profiles for TRAPPIST-1 e, clear-sky and cloudy aqua planets. Included are data from Earth: the temperature and mixing ratio profiles are from case 62 of the Intercomparison of Radiation codes in Climate Models (ICRCCM), and the eddy diffusion rate is that retrieved by Massie and Hunten (1981). The temperatures of our modeled atmospheres are somewhat colder than modern Earth, but still able to maintain surface water. The mixing ratios of trace constituents differ from modern Earth, except CO_2.

For TRAPPIST-1 e only, I modeled a potentially habitable, ocean-covered planet. This initial work and that of contemporary 3D GCM studies (Wolf, 2017, 2018; Turbet et al., 2018) suggest that the other habitable zone planets (f and g) require CO_2-dominated atmospheres for stability,

and cannot be Earth-like. This temperate, Earth-like atmosphere could exist if e had a sufficient volatile inventory to survive the stellar pre-main-sequence, had subsequent outgassing or water delivery, or if these planets migrated after formation (Luger et al., 2015; Meadows et al., 2018). This environment is simulated with an atmosphere of 80% N_2 and 20% O_2, similar to Earth. I assume the O_2 could be either biogenic or have resulted from early ocean loss. In addition to the fluxes assumed for the outgassing O_2 cases, I specify an Earth-like geological source of CH_4 (6.8×10^8 cm^2 s^{-1}; Guzmán-Marmolejo et al., 2013). Water vapor is calculated self-consistently using our mixing-length convection and condensation routine, described in §2.1.3, assuming 100% surface relative humidity.

I model both cloudy and clear-sky atmospheres for the aqua planet. In the cloudy case, cirrus and altostratus clouds are included, each of cumulative optical depth $\tau = 5$. These are based on the VPL 3D Spectral Earth Model, which used Earth observing data with our SMART radiative transfer model to faithfully reproduce Earth's spectrum (Robinson et al., 2011).

I use a wavelength-dependent open ocean surface albedo for this planet. I found that typical snow-covered ice surfaces with albedo up to 0.73 in the visible had little impact on surface temperature, because the SED of TRAPPIST-1 and other late-type M dwarfs emit most of their radiation longward of 1 μm, and both ice and water are efficient absorbers in the NIR (Shields et al., 2013).

These aqua planet cases are able to maintain temperate surfaces (279 K clear, 282 K cloudy). The clouds have a slight greenhouse effect, as the energy lost by scattering incoming stellar light is more than balanced by a colder emission temperature. The cloudy environment exhibits a much cooler tropopause and weak stratosphere, but similar tropospheric profile, since the troposphere is driven by moist convective processes in both cases. The choice of $\tau = 5$ for stratocumulus was reasonable, but the same optical depth for cirrus clouds was unrealistic, and likely caused the warm troposphere, due to ice absorption bands. See 3.4 for further details.

With Earth-like outgassing, the aqua planets exhibit pre-industrial Earth-like abundances of CO_2, but different profiles of other trace gasses. The stratospheric water abundance is reduced by a cold tropopause, more so for the cloudy case. The ozone profile is different than Earth's, with a broader, higher altitude (lower pressure) peak abundance, although the column density is

only slightly lower (Table 3.5). Ozone failed to produce a significant stratosphere, because the stellar spectrum provides very little flux at NUV–visible wavelengths absorbed by O_3. For this modeled environment, we limited CO to photochemical production, so the tropospheric levels are significantly less than Earth's CO, which is primarily from biologically-related sources (Seinfeld and Pandis, 2006). Similarly, the geological fluxes result in a correspondingly lower tropospheric methane abundance but similar abundance in the upper stratosphere.

3.3.2 Spectra and Observational Discriminants

Here I show simulated transit transmission and emission spectra for the modeled evolved worlds to support observation planning with *JWST* for this planetary system or other potential late-type M dwarf terrestrial targets. These are noiseless spectra generated using SMART, sampled at 1 cm^{-1} and convolved with a 1 cm^{-1} half-width at half-max slit function, which can be used as the model input for instrument and observation simulators that calculate noise sources and instrument sensitivity. These spectra can also be compared with known or anticipated instrument noise floors to determine zeroth order signal detectability. Lustig-Yaeger et al. (2019a) used these spectra to quantify the detectability of our simulated atmospheres with *JWST* and assess optimum observing techniques for identifying key planetary characteristics. Lustig-Yaeger et al. (2019b) used the spectra of the Venus-like worlds to study an observational degeneracy between global aerosol deck height and the "cosmic shoreline", stipulating the loss of atmospheres at higher irradiation.

I have also produced direct imaging reflectance spectra. Reflectance spectra of late-type M dwarfs may first be observed by large ground-based instruments, or later by HabEx/LUVOIR. The spectra I simulated, including those not presented here, are available online using the VPL Spectral Explorer[1], or upon request.

[1] `http://depts.washington.edu/naivpl/content/vpl-spectral-explorer`

3.3.2.1 Transit Transmission Spectra

In Figures 3.5 (O_2-dominated), 3.6 (CO_2-dominated), and 3.7 (aqua planet), I show transit transmission spectra of the modeled TRAPPIST-1 planetary environments, covering nearly the entire wavelength range of potential *JWST* exoplanet observations (0.5–20 μm). These spectra are presented as "relative transit depth," i.e. the signal originating from the atmosphere as compared to the solid planetary body. I do not account for stellar limb darkening, so "transit depth" here refers to $(R_p/R_*)^2$, where R_p is the radius of the solid body and R_* the radius of the star. To assess the signal originating from the atmosphere, we can expand the transit depth (c.f. Winn, 2010):

$$\frac{dF}{F} = \left(\frac{R_p + R_a}{R_*}\right)^2 = \left(\frac{R_p}{R_*}\right)^2 + \frac{2R_pR_a}{R_*^2} + \left(\frac{R_a}{R_*}\right)^2, \tag{3.2}$$

and define the relative transit depth of the atmosphere, valid for atmospheres with small scale height:

$$\frac{dF_a}{F} \approx \frac{2R_pR_a}{R_*^2}, \tag{3.3}$$

where R_a is the vertical extent of the atmosphere. Although the radius of the solid body and altitude of the atmosphere for exoplanets cannot be separately measured, this equation relates predicted variations in transit depth of the modeled spectra for different-sized bodies to the physical extent of the modeled atmospheres.

The seven planets exhibit a variety of features in transmission, the strengths of which depend on each planet's characteristics. TRAPPIST-1 b displays the strongest features, owing to its higher temperature and moderately low surface gravity, both of which increase the atmospheric scale height, and therefore its transmission signal. Planet b shows molecular signals exceeding 200 ppm, which is well above the putative 20, 30, and 50 ppm noise floors for *JWST* NIRISS SOSS, NIRCam grism, and MIRI LRS, respectively (Greene et al., 2016). Planet d exhibits molecular signals nearly as strong as b, in large part because d has the lowest surface gravity of these planets. Due to geometry and the effects of refraction (Misra et al., 2014; Meadows et al., 2018), the surface and near-surface atmospheres of the 10–100 bar atmospheres cannot be probed with *JWST* transmission

spectroscopy. All of the modeled atmospheres presented include CO_2, and despite a broad range of abundances, they all exhibit strong CO_2 absorption at 2.0, 2.8, 4.3, and 15 μm, though the hotter and/or higher abundance CO_2 atmospheres have additional CO_2 features, particularly short-ward of 2 μm. In the following subsections, I present the spectra for each environment.

O_2-Dominated Atmospheres, Desiccated Transit transmission spectra for the desiccated, high-O_2 atmospheres are presented in Figure 3.5. As in Schwieterman et al. (2016) and Meadows et al. (2018), the characteristic spectral features of a high-O_2 atmosphere are strong O_3 and O_2-O_2 CIA bands together. The CIA bands are strongest at 1.06, 1.27, and 6 μm. A mixture of O_2, O_3, and O_2-O_2 are present at 0.5–1.3 μm, and a mixture of CO_2, CO, O_3, and O_2-O_2 from 1.5–8 μm. The strongest O_3 bands are the Chappuis band at ∼0.6 μm and the 9.6 μm feature, with weaker bands at 2.5, 3.3, 3.6, 4.75, and 5.6 μm. These weaker bands are generally only available here because of high levels of O_3 combined with relatively low levels of CO_2. Most of this wavelength range could be accessible to *JWST* NIRISS and NIRSpec instruments. Features of CO_2 O_3, and O_2-O_2 are also present from 6–20 μm, which could be probed by the *JWST* MRS instrument. In addition to the complete lack of any water features, the presence of CO features (2.35 μm and 4.6 μm) is characteristic of this severely desiccated atmosphere (e.g. Gao et al., 2015), though these will be very challenging to observe with *JWST* (Lustig-Yaeger et al., 2019a).

O_2-Dominated Atmospheres, Outgassing The transmission spectra of the outgassing atmospheres are shown in Figure 3.5. The detectability of outgassed trace species varies by planet, particularly H_2O and SO_2. Water features at 1.4, 1.9, 2.6, 3.0–3.3, and 6.3 μm rival the strength of CO_2 bands for the hottest planets (b, c, and d), due to stratospheric water vapor in excess of the moist greenhouse limit, indicative of planets experiencing water loss. The colder planets have insufficient H_2O to generate H_2SO_4, so maintain higher levels of SO_2, which shows small features of less than 60 ppm at 4.0, 7.3, 8.7, and 19 μm. Much larger SO_2 fluxes and/or lower water vapor abundances would be required to generate SO_2 features above the putative noise floor of *JWST* (20–50 ppm; Greene et al., 2016).

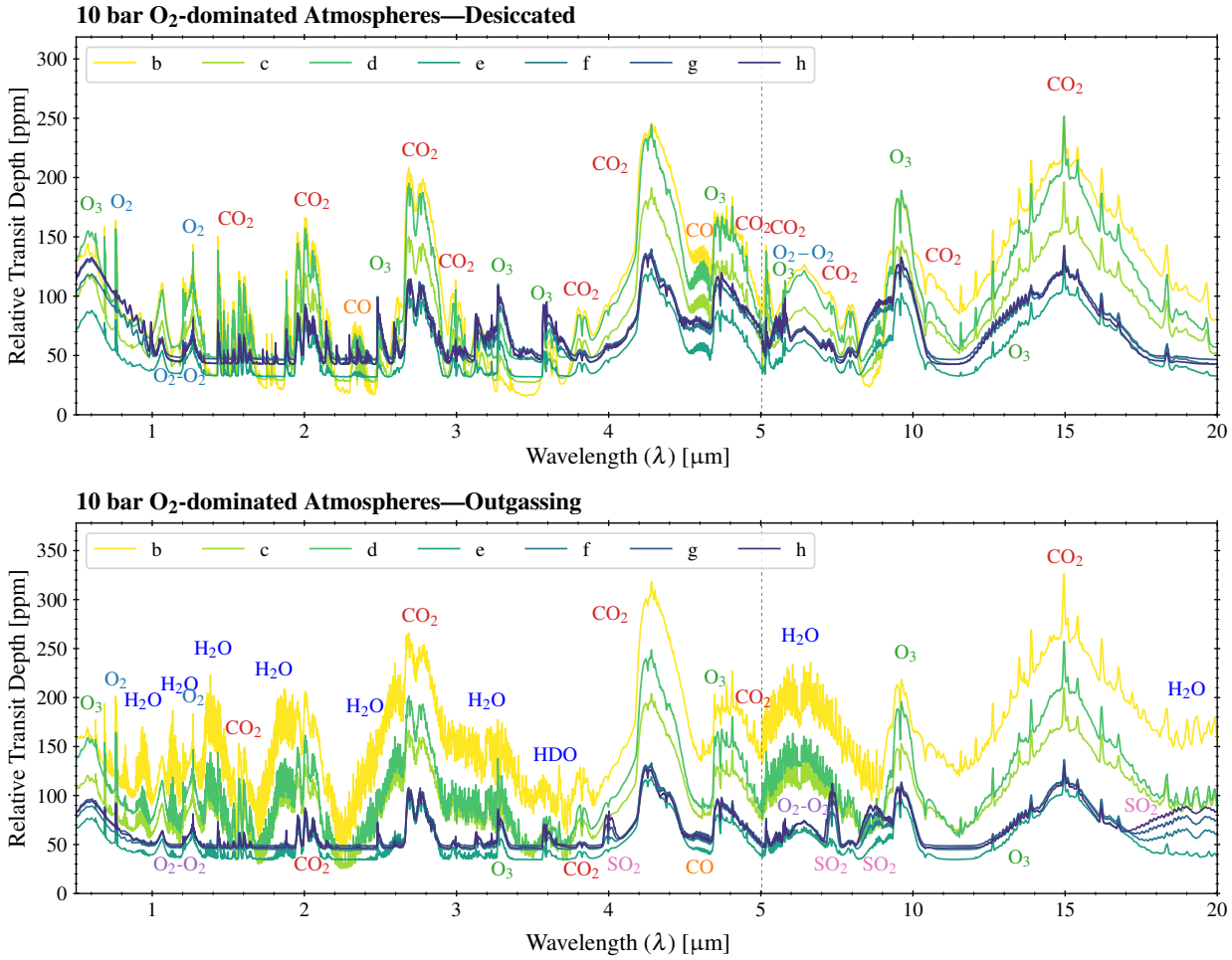

Figure 3.5: Simulated transit transmission spectra for the O_2 desiccated (*upper panel*) and O_2 outgassing (*lower panel*) atmospheres. The y-axes are the relative transit depths, and show the modeled atmospheric signal. I show only the 10 bar atmospheres, as the 100 bar atmospheres are qualitatively similar. The desiccated atmospheres are dominated by CO_2 and O_2-O_2. The presence of weaker O_3 bands and CO are indicative of the desiccated environment. The outgassing atmospheres have additional features from H_2O and SO_2. The hotter atmospheres maintain substantial stratospheric H_2O and the outer planets, too cold for maintaining H_2O, build up SO_2, which would otherwise condense with H_2O to form sulfuric acid. Compared to Lincowski et al. (2018), here I have updated the transmission spectra to include the 6 μm O_2-O_2 CIA band, which affects the desiccated and the colder outgassing atmospheres.

Venus-Like Atmospheres Clear-sky and cloudy Venus-like transmission spectra are shown in Figure 3.6. With a clear sky, Venus-like atmospheres exhibit deep absorption features, primarily

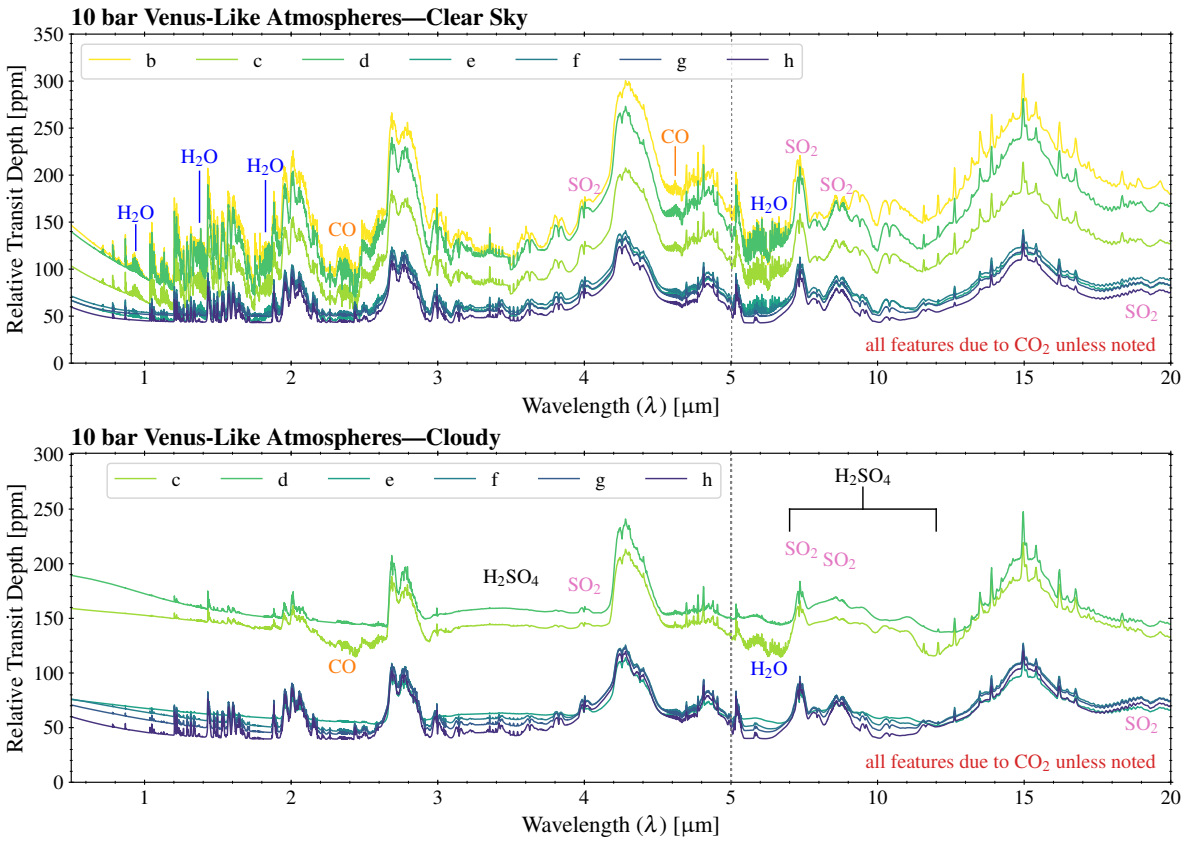

Figure 3.6: Simulated transit transmission spectra for the Venus-like clear-sky (*upper panel*) and cloudy (*lower panel*) atmospheres. The y-axes are the relative transit depths, and show the modeled atmospheric signal. We show only 10 bar atmospheres, as the 92 bar atmospheres are quantitatively similar. All unlabeled features are CO_2, which dominate these spectra. The generally flat, higher transit depths of the cloudy Venus-like spectra are due to the sulfuric acid aerosols. TRAPPIST-1 b is not included, because it did not condense H_2SO_4. The colder cloudy atmospheres have lower cloud decks (see Figure 3.2), revealing deeper relative transit depths.

from CO_2. Water vapor is present in the clear-sky spectra between 0.9–2.0 μm and at 6.3 μm. Sulfuric acid aerosols truncate the minimum altitude probed by the transmission measurement, severely reducing the strength of the absorption features. These Venus-like planets may have absorption features in transmission approaching $\sim$ 90 ppm.

Aqua Planet Clear-sky and cloudy aqua planet transmission spectra for TRAPPIST-1 e are shown in Figure 3.7. Due to the large angular size of TRAPPIST-1 as seen from the planet, the

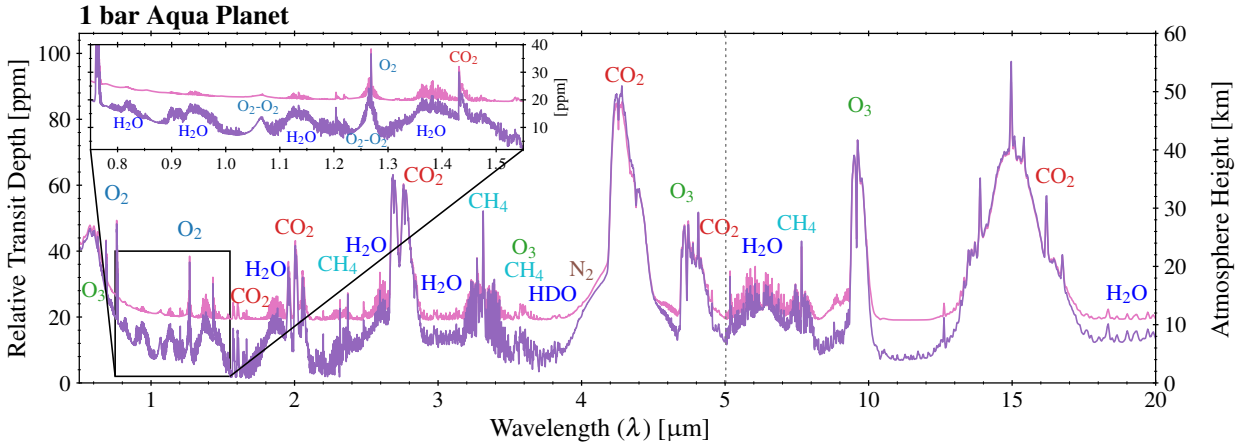

Figure 3.7: Transit transmission spectrum for clear sky and cloudy TRAPPIST-1 e aqua planets. Most of this simulated planet's important and abundant gases, including H_2O, O_2, CH_4, and O_3, have features in this spectral range. These cloudy and clear spectra demonstrate that a potentially habitable planetary atmosphere, some of its trace outgassed constituents, and photochemical byproducts are accessible using transmission spectroscopy, which could be attempted with *JWST* .

clear-sky atmosphere can be probed nearly to the surface, while the cloud deck truncates the spectrum at 11 km. A number of molecular absorption bands are present, including O_3 ($\sim$0.6, 4.7, 9.6 μm), O_2 (0.76, 1.27 μm), CH_4 weakly (3.3 and 7.7 μm), and H_2O (6.3 μm). Even with an abundance of only $\sim$290 ppm, CO_2 is the most observable molecule in these atmospheres (1.6, 2.0, 2.7, 4.3, 15 μm). The bulk atmospheric constituent, nitrogen, exhibits a 4.1 μm CIA band, which could provide a sensitive probe of its partial pressure (Schwieterman et al., 2015), but will not be detectable with *JWST* for realistic (i.e. partly-cloudy) Earth-like atmospheres (Lustig-Yaeger et al., 2019a).

3.3.2.2 Emission Spectra

I present thermal emission spectra as normalized flux (Figures 3.8 and 3.9). Below $\sim$ 5 μm, stellar flux reflected from the surface or scattered in the atmosphere contributes significantly to the spectra.

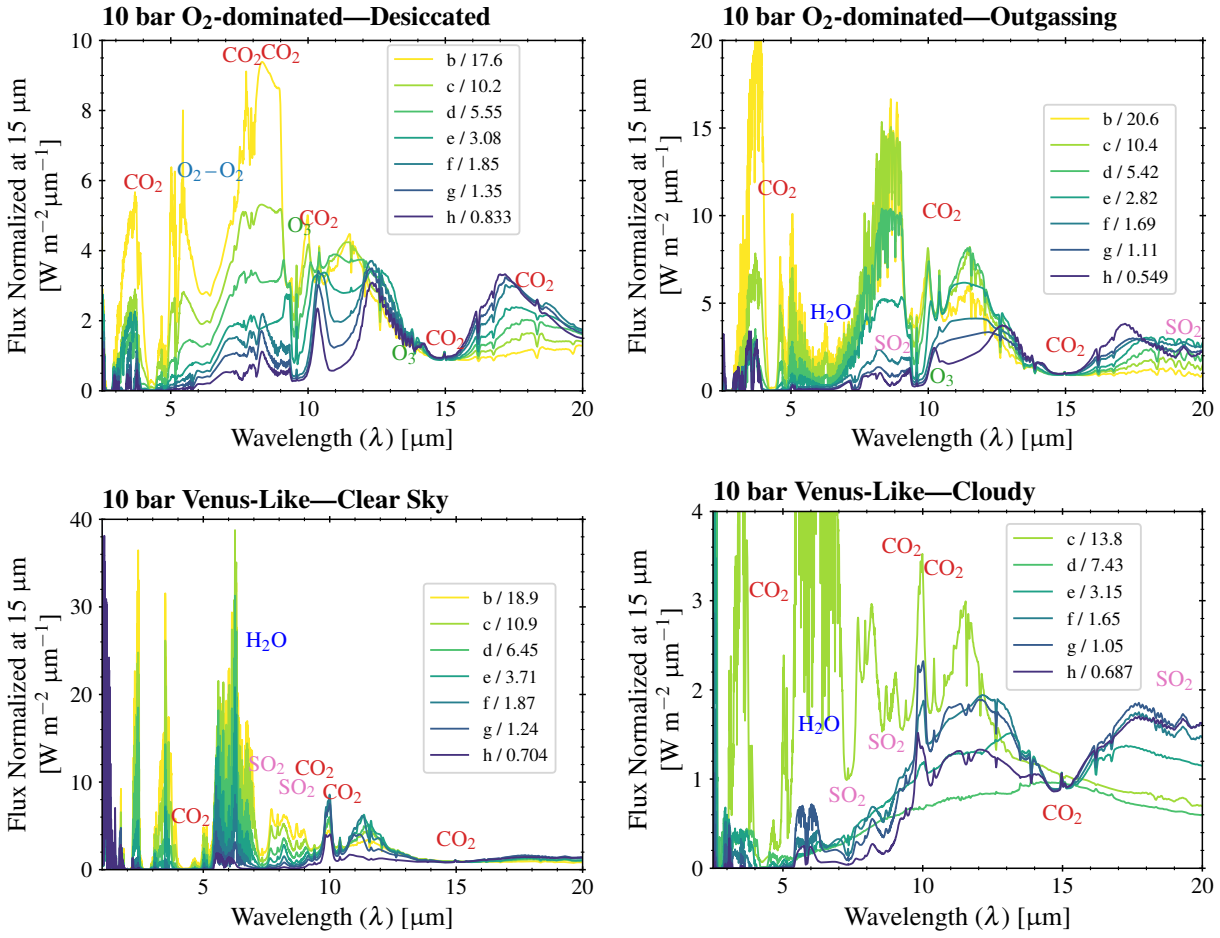

Figure 3.8: Normalized emission (outgoing flux) spectra for the desiccated atmospheres. The legends provide the factors by which the spectra were reduced to normalize the flux to 15 μm for each. The emission spectra are dominated by CO_2 features in both absorption and emission, but also include H_2O, O_3, and SO_2.

O_2-Dominated Atmospheres, Desiccated The desiccated, O_2-dominated atmospheres (Figure 3.8) are distinctive in emission spectra, due to lower temperatures, lack of water bands, and their unusual temperature structures. The stratospheric temperature peak causes some bands to be seen in emission rather than absorption, depending on how cool the particular planet is. In the colder atmospheres, the O_3 band at 9.6 μm exhibits varying hot wing emission at 10.4 μm from the stratospheric temperature peak. In the hotter atmospheres, the other wing of the 9.6 μm O_3 band also emerges in emission at 9.0 μm. CO_2 exhibits varying changes between absorption and emission

between ∼10–18 μm. As a potential insight into isotope fractionation for $^{18}O/^{16}O$, the fundamental asymmetric stretch $\nu_1 = 1 \rightarrow 0$ transition of the $^{16}O^{12}C^{18}O$ isotopologue at 7.9 μm (Rothman et al., 2013) appears in absorption in the hotter atmospheres or emission in the colder atmospheres. The O_2-O_2 band at 6.4 μm exhibits deep absorption in the hotter atmospheres. This band would be partially or completely masked by water vapor (c.f. the O_2 outgassing spectra). Here, CO only exists as a small perturbation at 4.6 μm.

O_2-Dominated Atmospheres, Outgassing The emission spectra of the O_2-dominated, outgassing atmospheres are given in Figure 3.8. The radiative-convective processes and resultant emission spectra are largely dominated by water vapor in the atmosphere. The warmer planets, with larger quantities of water vapor throughout the atmospheric column, exhibit massive H_2O absorption in the 6.3 μm band. Conversely, the colder, drier planets exhibit SO_2 absorption at 7.3, 8.8, and 19 μm. These outgassing atmospheres have much less ozone than the desiccated ones, due to destruction catalyzed by the presence of water vapor, and so their O_3 features are much weaker, particularly for the warmer planets. With updated O_2-O_2 (subsequent to publishing Lincowski et al. 2018), these atmospheres transition from a large H_2O band to O_2-O_2 at 6 μm, as a result of the colder atmospheres maintaining very little atmospheric water vapor.

Venus-like Atmospheres The Venus-like atmospheres (Figure 3.8) emit very little flux, except through narrow windows between strong absorption bands, similar to Venus. This suppression of emitted flux is due to the combined Venus greenhouse of primarily CO_2, H_2O, and SO_2. The emission windows in the hotter atmospheres are at 2.4, 3.5, and 5.5–7.0 μm. The cooler, clear-sky planets emit some flux around 10 μm, between CO_2 hot bands. Water vapor absorbs weakly in the 5.5–7.0 μm window and SO_2 absorbs from 7–9 μm in the clear-sky case, but is obscured in the cloudy case. The remaining emission is reduced by CO_2 absorption. The cloudy spectra exhibit more shallow absorption features and are more similar to blackbody spectra because the thermal emission is primarily from the cloud deck, though the colder planets also emit above the cloud deck from the 15 μm CO_2 band.

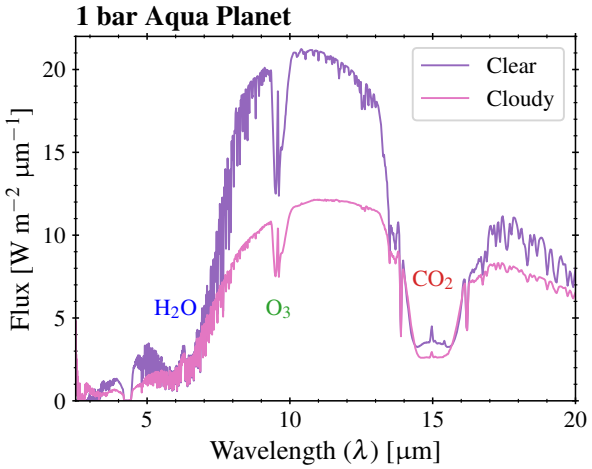

Figure 3.9: Outgoing flux spectra for clear sky and cloudy, 1 bar TRAPPIST-1 e aqua planets. These closely resemble Earth's emission spectrum (c.f. Robinson et al., 2011), characterized by the 6.3 μm water band and weak water features throughout, and the 15 μm CO_2 band. The weak water features mostly disappear in the cloudy case, and the overall emission spectrum is reduced in magnitude by half.

Aqua Planets The potentially habitable aqua planet atmospheres (Figure 3.9) have emission spectra very similar to Earth (c.f. Robinson et al., 2011). The near-surface absorption from the water vapor continuum is apparent in the clear-sky case, particularly between 10–13 μm, and the cloudy case emits from its global cloud deck at a colder temperature. Both cases exhibit absorption from H_2O (6.3 μm), O_3 (9.6 μm), and CO_2 (15 μm).

3.4 Discussion

I have used a new, versatile, coupled climate-photo-chemical model to generate environmental states for the TRAPPIST-1 planets for different assumed evolved atmospheres, including desiccated and water-rich. These atmospheric states are climatically and photochemically self-consistent with the spectral energy distribution from the parent star, and show a diversity of characteristics as a function of bulk composition, orbital distance, and outgassing rates. These characteristics are very different from those expected for H_2-dominated atmospheres. I have shown that the non-Earth-like atmospheric compositions that may result from M dwarf stellar evolution strongly impact planetary climate and surface temperature, potentially reducing habitability within the HZ. Hot temperatures modeled beyond the outer edge require additional study to determine if the habitable zone could be extended with additional trace gases. These different environments produce spectral features that can be observed by upcoming observatories, including *JWST*, to discriminate among the en-

vironments (Lustig-Yaeger et al., 2019a). Here we discuss important implications of this work for M dwarf terrestrial planets in the areas of climate and photochemistry, observational discriminants, and prospects for future observations of these environments.

3.4.1 Climate and Photochemistry in the TRAPPIST-1 Planetary System

These diverse environments produce a wide range of habitable and uninhabitable surface temperatures (Figure 3.4), suggesting that the region around a star where Venus-like planets may be common evolutionary outcomes (Kane et al., 2014) may extend into and beyond the classical habitable zone for late-type M dwarfs. Even though some of these modeled environments do not support surface liquid water, if dense CO_2 atmospheres do form on terrestrial planets after an early runaway greenhouse phase, these results suggest that surface temperatures in the habitable range or hotter may occur beyond the classical maximum greenhouse limit of the HZ outer edge (where warming from additional CO_2 is offset by higher Rayleigh scattering in a temperate H_2O-CO_2 greenhouse; Kasting et al. 1993). Even TRAPPIST-1 h, beyond the HZ outer edge ($S_{\rm h} = 0.148 S_{\oplus}$), could have a surface temperature as hot as 465 K if early atmospheric evolution resulted in a clear-sky Venus-like atmosphere, and 398 K with the expected sulfuric acid clouds. These high temperatures may be stable over long time periods, because known sinks for CO_2—such as deposition to an ocean and carbonate-silicate weathering (Walker et al., 1981)—will not be available, although a surface carbonate buffer may form and keep the atmosphere at an equilibrium CO_2 value that is less than 92 bars (Hashimoto et al., 1997). Table 3.4 also shows that across the diversity of atmospheres considered, the instellation at the modeled distance from the star for TRAPPIST-1 e is most likely to maintain a habitable surface temperature. This suggests that the habitable zone concept is still useful as an initial means of narrowing down the search for habitable conditions on terrestrial planets, even when planetary atmospheres are not truly Earth-like.

For late-type M dwarf stars in particular, this work indicates that the maximum greenhouse limit may not apply, or may apply at a distance much farther from the star than previously calculated (Kopparapu et al., 2013). We have shown that the H_2O-CO_2 greenhouse used in traditional habitability calculations can be enhanced significantly by other greenhouse gases, including SO_2.

While SO_2 is a greenhouse gas in desiccated atmospheres like Venus' (e.g. Lee et al., 2016), it is less likely to be present in the atmosphere of a habitable planet with an ocean because it is highly soluble. If an initially-desiccated planet beyond the HZ were to recover habitability via outgassing, and maintain a warm temperature, other gases such as CH_4 (which may be relatively abundant in planetary atmospheres around M dwarfs; Segura et al. 2005; Rugheimer et al. 2015; Meadows et al. 2018) would be needed to support a strong greenhouse. For a habitable planet, this greenhouse could also be enhanced by collision-induced absorption, such as CO_2-CH_4 CIA, as may have been the case on early Mars (c.f. Batalha et al., 2015; Wordsworth et al., 2017). Greenhouse gas abundances can also be affected by energetic particle events, which can drive chemistry that generates trace amounts of greenhouse gases (Airapetian et al., 2016). These events are likely to remove greenhouse gases, by the destruction of O_3 in Earth-like atmospheres by repeated flaring (Tilley et al., 2019), or by the destruction of CH_4, which may form hydrocarbon hazes if oxygen radicals are not present (Arney et al., 2017). In the absence of sufficient greenhouse gases, the coldest atmospheres (particularly the 10 bar cloudy Venus-like h) may be subject to collapse, but most will be resistant, as the condensation temperature for O_2 is very low and day-night temperature contrasts are lower in thicker atmospheres (Turbet et al., 2018).

The results here indicate that the interplay between stellar irradiation, photochemistry, chemical kinetics, and condensation shaped the simulated planetary atmospheric compositions, with water vapor, ozone, sulfur species, and aerosols displaying the greatest variation. The decreases in H_2O (largely due to temperature) and increases in O_3 abundance (due to an interplay between photolysis rates, water abundance, and vertical transport) as a function of orbital distance are consistent with trends found by previous studies (e.g. Grenfell et al., 2007). The water vapor profiles in the warmer atmospheres are representative of planets in a moist greenhouse state, with substantial water vapor well-mixed throughout the atmospheres, and with no cold traps. Consequently these atmospheres may suffer severe water loss over Gyrs, unless the escape rate is balanced by outgassing. Unless they begin with warm, Venus-like atmospheres, the outer planets are too cold to recover from freezing temperatures without a brightening star or larger inventories of greenhouse gases, which may eventually accumulate from outgassing or impactor delivery.

Ozone and CO both exhibit characteristic patterns across the modeled atmospheres. In all of the simulated atmospheres containing $\gtrsim 0.2$ bar O_2, at $\sim$200 Pa, O_3 is about 10^{-5} mol/mol, despite different levels of irradiation, H_2O, and O_2. Above this layer, the O_3 abundance is controlled by photolysis, while below, mixing and other temperature- and water-dependent loss mechanisms dominate. In desiccated atmospheres, CO abundance is controlled by the slow, three-body CO_2 recombination reaction (Gao et al., 2015), while in atmospheres with water vapor, the abundance of CO is controlled by the availability of H-bearing recombination catalysts, which are more prevalent near the planetary surface, removing the CO at lower altitudes. Large amounts of CO in the presence of O_2/O_3 is a false positive discriminant (Schwieterman et al., 2016), indicating that oxygen is more likely to have been generated by photolysis of CO_2 (Gao et al., 2015) rather than photosynthesis.

Aerosols affect planetary climate by reflecting incoming stellar radiation and either absorbing, emitting, or scattering thermal radiation. Sulfuric acid aerosols can reduce the surface temperatures of hot, partly desiccated planets, which caused the modeled cloudy Venus-like atmospheres to drop by up to nearly 200 K (Figure 3.4) compared to the clear-sky cases. Sulfuric acid production also varied as a function of irradiation. The warmer planets more easily formed H_2SO_4 due to higher water vapor abundances and more rapid SO_2 photolysis. This production was offset at lower altitudes by thermal decomposition. TRAPPIST-1 b did not condense sulfuric acid in our model because atmospheric temperatures were too high. If any of the TRAPPIST-1 planets have Venus-like atmospheres, we expect that b will not form sulfuric acid clouds, but the other planets likely would. Although I did not model the radiative effects of aerosols for the O_2 outgassing environments, sulfuric acid condensation occurred in the photochemical model, so their climates could also be affected by these clouds.

Water and water-ice clouds impacted the temperature structure of the aqua planet, but had little effect on surface temperature (Figure 3.4). This was likely due to an unrealistically high choice for optical depth in the original study (Lincowski et al., 2018). Cirrus clouds are unlikely to support large optical depths (such as $\tau = 5$ chosen here), because the ice absorption bands locally warm the atmosphere and cause self-evaporation (Kitzmann et al., 2010), which is probably enhanced

for an M dwarf host, with the red-shifted SED into the NIR ice bands. This effect is similar to the results from detailed models with CO_2 clouds, where the time-averaged optical depth was unity or less (Forget et al., 2013). This is also consistent with GCM results for TRAPPIST-1 e, for which ice clouds have globally-averaged optical depth much less than unity (Wolf, 2017).

The parameter space for possible planetary characteristics is large, so the assumptions regarding atmospheric surface pressure, surface material, atmospheric bulk composition, geological or biological surface fluxes, and atmospheric transport can have a large impact on the equilibrium atmospheric state. The differences between our O_2 desiccated and outgassing atmospheres demonstrate the effects of surface fluxes on the planetary environment. These factors are important when considering what atmospheres may be possible on a given exoplanet, and for comparing possible planetary states and among different models. Although major TRAPPIST-1 GCM studies by Wolf (2017) and Turbet et al. (2018) agreed that TRAPPIST-1 e requires more CO_2 than Earth to be temperature, they disagreed significantly on surface temperatures and the amount of CO_2 required to maintain temperate conditions in the habitable zone of TRAPPIST-1. This was likely due to two main differences between their studies: 1) Wolf (2017) did not have CO_2 CIA initially, but did update results later (Wolf, 2018) using a method designed for Earth-like abundance of CO_2 that likely underestimates collision-induced absorption (c.f. Clough et al., 2005; Halevy et al., 2009; Wordsworth et al., 2011; Wolf and Toon, 2013; Wolf, 2017; Turbet et al., 2018); and 2) Wolf underestimated the reduction in bolometric albedo due to the late M dwarf SED (Turbet et al., 2018). It is possible that Turbet et al. (2018) also overestimated the surface albedos of ocean-dominated TRAPPIST-1 planets, as they calculated a mean water-ice albedo of 0.21. I used wavelength-dependent surface albedos in climate calculations that depend on the planetary environment (Figure 2.4). I found that both pure ocean and melting ice surfaces had very low stellar flux-weighted average albedos (0.02 and 0.03 respectively), while a typical snow surface averaged only 0.16 around TRAPPIST-1. Wolf (2017) found that 0.1 bar of CO_2 with 1 bar N_2 is required for a surface temperature of $\sim$ 270 K, while modern Earth CO_2 levels of $\sim$ 400 ppm yield 240 K. Turbet et al. (2018) calculated 250 K under similar conditions. It is crucial to note that surface albedo is one of the primary drivers of climate state (Godolt et al., 2016), particularly in an atmo-

sphere transparent to its host star's radiation.

3.4.2 Observational Discriminants of Evolved Terrestrial Atmospheres

Planetary State	**Molecules & Wavelengths [μm]**	**Notes**
Aqua planet, clear-sky	CO_2 (1.6, 2.0, 2.8, 3.6, 3.8, 4.3, 4.8, 9.5, 10.5, 15), H_2O (0.94, 1.4, 1.9, 2.6, 3, 3.3, 6.3), HDO (3.7), O_2 (0.67, 0.76, 1.27), O_2-O_2 (1.06, 1.27), O_3 (0.6, 4.75, 9.6), CH_4 (2.35, 3.3, 7.6), N_2-N_2 (4, 4.6)	Earth-like worlds may be discriminated by CH_4 in conjunction with oxidized species.
Aqua planet, cloudy	CO_2 (1.6, 2.0, 2.8, 3.6, 3.8, 4.3, 4.8, 9.5, 10.5, 15), H_2O (1.4, 1.9, 2.6, 3, 3.3, 6.3), HDO (3.7), O_2 (0.67, 0.76, 1.27), O_2-O_2 (1.06, 1.27), O_3 (0.6, 4.75, 9.6), CH_4 (2.35, 3.3, 7.6), N_2-N_2 (4, 4.6)	Tropospheric water/water-ice clouds are problematic for observing Earth-like planets.
O_2, desiccated	CO_2 (1.6, 2.0, 2.8, 3.0, 3.2, 3.6, 3.8, 4.0, 4.3, 4.8, 7.3, 7.9, 15), O_2 (0.67, 0.76, 1.27, 6.4), O_2-O_2 (1.06, 1.27), CO (2.35, 4.6), O_3 (0.6, 2.5, 3.3, 3.6, 4.75, 9.0, 9.6, 13)	A lower limit of O_2 abundance can be constrained with the O_2-O_2 bands at 1.06 and 1.27 μm. CO and O_3 levels can indicate desiccation. Complete lack of water vapor.
O_2, outgassing	CO_2 (1.6, 2.0, 2.8, 3.0, 3.2, 3.6, 3.8, 4.0, 4.3, 4.8, 15), H_2O (1.4, 1.9, 2.6, 3, 3.3, 6.3), HDO (3.7), O_2 (0.67, 0.76, 1.27, 6.4), O_2-O_2 (1.06, 1.27), O_3 (0.6, 3.3, 3.6, 4.75, 9.6, 13), SO_2 (4.0, 7.3, 8.8, 19)	Water vapor is prominent in the hotter atmospheres.
Venus-like, clear-sky	CO_2 (1.05, 1.3, 1.6, 2.0, 2.8, 3.0, 3.2, 3.6, 3.8, 4.0, 4.3, 4.8, 7.3, 7.9, 9.5, 10.5, 15), H_2O (1.4, 1.8, 2.6, 6.3), CO (2.35, 4.6), SO_2 (4.0, 7.3, 8.8, 19)	High CO_2 abundance may be constrained by the weakest bands (e.g. 1.05 and 1.3 μm).
Venus-like, cloudy	CO_2 (1.5, 2.0, 2.8, 3.0, 3.2, 3.6, 3.8, 4.0, 4.3, 4.8, 7.3, 7.9, 9.5, 10.5, 15), H_2O (6.3), SO_2 (4.0, 7.3, 8.8, 19), H_2SO_4 (3.1–4, 7.5–10)	Sulfuric acid cloud absorption may be the best discriminant for outgassed conditions with no surface water.

Note: Spectral features present in transmission or emission spectra are listed for the modeled environments.

Table 3.6: Observational Discriminants

Here I compare spectra derived from the complete set of simulated atmospheres for TRAPPIST-1 b, c, and d, whose higher temperatures make them more easily observable, and e, which is a potentially habitable candidate, to identify observational characteristics that could be used to discriminate between these environments and their evolutionary histories. Spectral features that can be used to discriminate between the modeled environments are given in Table 3.6. Figure 3.10 shows spectra for the atmospheres modeled for TRAPPIST-1 b, c, and d. The stronger carbon dioxide bands are prominent in all of the planetary spectra, regardless of whether CO_2 is a bulk constituent or a trace gas, and these bands are therefore good indicators of the presence of a terrestrial atmosphere, but are not as useful for discriminating among different environments. However, if the weaker CO_2 bands are also present, this does indicate a higher, more Venus-like abundance. As seen in planet d's transmission spectra in Figure 3.10, cloudy Venus-like atmospheres are well-discriminated by sulfuric acid absorption longward of 3 μm (though these clouds could also form

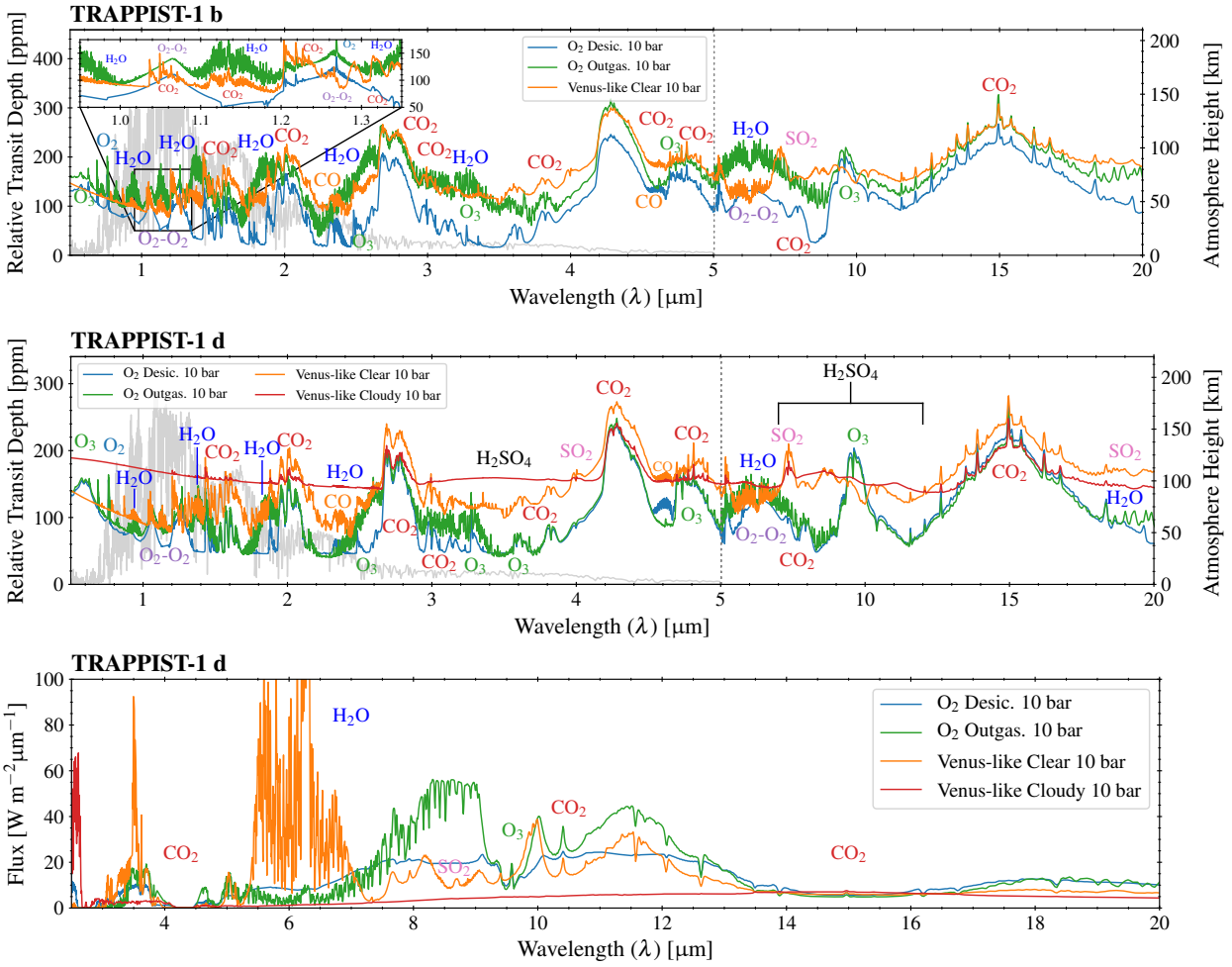

Figure 3.10: TRAPPIST-1 b (*top panel*) and d (*center panel*) transit transmission spectra, and TRAPPIST-1 d thermal emission spectra (*bottom panel*) of the 10 bar atmospheres, for all environments simulated. The higher mass environments exhibit similar spectral features, but different strengths and temperatures. I include the stellar spectrum (grey) in the transmission plots to illustrate the spectral regions with the most available photons for back lighting the atmosphere in transmission. As shown in the previous figures, CO_2 dominates all of these environments. Absorption by O_2-O_2, O_3, SO_2, CO, H_2O, and weaker CO_2 bands can distinguish these environmental states in both transmission and emission. Note the inset for b that shows overlapping CO_2 and O_2-O_2 bands that could be confused at low resolution and/or low signal-to-noise. The H_2O feature of the clear sky Venus-like atmosphere in emission peaks at $\sim$420 W m^2 μm^{-1}. TRAPPIST-1 b is scheduled to be observed by *JWST* and has the strongest features, due to lower gravity and hotter temperatures. Planet d also has strong signal in transmission, even with high-altitude sulfuric acid aerosols. TRAPPIST-1 b, c, and d exhibit strong features in emission due to high temperatures—d is shown here in emission to demonstrate the large difference due to aerosols.

in O_2-dominated atmospheres with outgassing).

The massive O_2 atmospheres may be discovered in transmission via the presence of O_2-O_2 collision-induced absorption at 1.06 and 1.27 μm (Schwieterman et al., 2016), a wavelength region strongly back-lit by the host star, or longward at 6 μm. Note that our photochemical model suggests that cloud formation in the outgassing atmosphere is likely, due to sulfuric acid condensation (at ∼1 ppb concentration). In the absence of a high-altitude sulfuric acid haze, the favorably compact geometry of the TRAPPIST-1 system allows transit transmission to probe relatively deep into the atmosphere, where O_2-O_2 absorption is strongest, producing transit signals as high as 70 ppm (vs ∼3 ppm for an early-type M dwarf; Schwieterman et al., 2016). However, as demonstrated in the inset in Figure 3.10, the broad O_2-O_2 bands at 1.06 and 1.27 μm overlap with CO_2 bands at 1.05, 1.13, 1.24, 1.29, and 1.32 μm in high CO_2 atmospheres. An atmosphere with high levels of both CO_2 and O_2 may be common if a planet that experienced complete ocean loss retained a large fraction of the CO_2 that was dissolved in the oceans or subsequently outgassed from the interior. These weak CO_2 features could confuse retrieval and interpretation of the O_2-O_2 features without sufficient resolution, signal-to-noise, or corroboration from stronger CO_2 features elsewhere in the spectrum. Similarly, the O_2-O_2 band at 6 μm could be easily confused with water vapor, even with relatively good observations, unless NIR observations are taken to independently constrain H_2O and/or O_2.

These O_2-dominated spectra also show strong features from O_3 and SO_2. A strong ozone Chappuis band around ∼0.6 μm may indicate desiccation, as it traces ozone deep in the atmosphere, where water vapor would normally destroy it (Meadows et al., 2018). As clearly shown in Figure 3.10 in all three panels, the 9.6 μm O_3 feature is strong and broad for both O_2-rich atmospheres, but not present in the Venus-like spectra primarily due to the lack of O_2 in the atmosphere. Detection of SO_2 absorption in either transmission or emission would be indicative of an outgassing interior, and possibly an atmosphere and surface with low water abundance, either due to early desiccation, or temperatures below freezing. The O_2 outgassing case is unique among the environments considered for the hotter planets in showing very strong water features, especially near 1.4 and 6.3 μm. This is because these planets have high levels of water vapor (up to

0.1% mol/mol) in their stratospheres, so are in a moist greenhouse state, approaching a runaway greenhouse. These strong H_2O bands are indicative of a planet in the process of losing water vapor, rather than indicating habitable, ocean-bearing conditions. Such a planet could potentially condense water vapor on the night-side, supporting a biosphere there. Or, if in the habitable zone, the condensation of water vapor could eventually form a cold trap and global ocean if water vapor outgassing exceeded hydrogen escape.

The bottom panel of Figure 3.10 demonstrates the differences between the evolved environments in emission using TRAPPIST-1 d as an example of the hotter planets. The water band at 6.3 μm is the primary discriminant. At high temperatures and high abundance (e.g. the O_2 outgassing case), H_2O absorption can dominate over absorption from other interesting molecules between 5–9 μm, such as O_2, SO_2, CO_2, and O_2-O_2. For the Venus-like clear-sky atmosphere, the low abundance of $H_2O \lesssim 1$ ppm fails to suppress the outgoing radiation from the hot lower atmosphere, resulting in an emission peak at these wavelengths. The cloudy Venus case shows that clouds can adversely affect both outgoing flux and the strength of molecular features by truncating the atmosphere at higher, colder altitudes.

Figure 3.11 compares the spectra of the O_2- and CO_2-dominated atmospheres with the clear and cloudy aqua planets for TRAPPIST-1 e. The relative transit depths are naturally offset due to the truncating effects of clouds, which allow transmission to probe only altitudes above the cloud deck, and the obscuring effect of atmospheric opacity for atmospheres of different total atmospheric pressure (i.e. 1 vs 10 bar). In the thermal infrared, clouds reduce the overall outgoing flux by emitting at colder temperatures. The features and their diagnostics are similar for the TRAPPIST-1 e water-poor atmospheres compared to d, with CO_2 features dominating the spectra, prominent (but narrower) O_3 features for the O_2-rich atmospheres, and a more prominent difference in the O_3 Chappuis band strengths between the outgassing and more desiccated case. The O_2 desiccated and Venus-like atmospheres for TRAPPIST-1 e display features and corresponding observational discriminants similar to the hotter planets. However, the O_2 outgassing environment was not hot enough to maintain high levels of stratospheric H_2O, so here the O_2-O_2 absorption dominates over the modestly absorbing 6.3 μm H_2O feature. The overall emission spectrum of that environment is

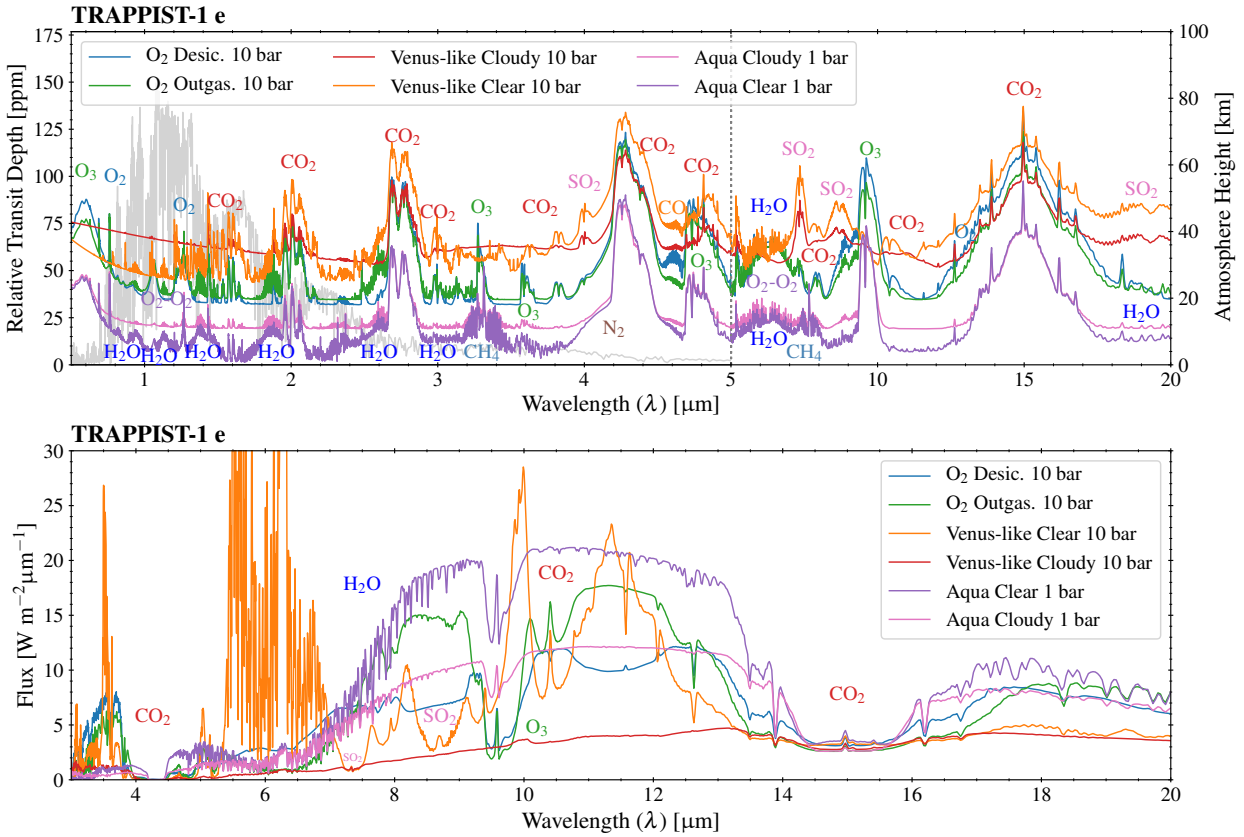

Figure 3.11: TRAPPIST-1 e transit transmission (*top panel*) and thermal emission (*bottom panel*) spectra of the 10 bar atmospheres for the four simulated evolved environments, and a self-consistent pre-industrial Earth. The higher mass environments exhibit similar spectral features, but different strengths and temperatures. I include the stellar spectrum (grey) in the transmission plot to illustrate the spectral regions with the most available photons for back lighting the atmosphere in transmission. As shown in the previous figures, CO_2 dominates all of these environments. Absorption by O_2-O_2, O_3, H_2O, and weaker CO_2 bands can distinguish these environmental states in both transmission and emission. The H_2O feature of the clear sky Venus-like atmosphere in emission peaks at $\sim$60 W m^2 μm^{-1}.

somewhat similar to the aqua planets, with additional CO_2 bands due to the higher levels of CO_2 we assumed and O_2-O_2 in place of H_2O.

Water is not a good discriminant among some of these atmospheres, so discriminating the habitable aqua planet from the uninhabitable environments is not straightforward. The aqua planet has water vapor features in the near-infrared in transmission at 0.94, 1.15, 1.4, 1.9, 2.6, 3.7, and most strongly at 6.3 μm. Unfortunately, these water features have comparable signals among the clear-sky atmospheres (except the completely desiccated case), and among the cloudy cases, despite vastly different levels of tropospheric H_2O, due to the cold trapping of water in the aqua planet atmosphere. Furthermore, the 6.4 μm O_2-O_2 band could be confused with H_2O, with a pathological transition in the habitable zone, as discussed above for the O_2 atmospheres with outgassing.

The bulk composition of these atmospheres can potentially be distinguished by weak spectral effects of their dominant gases O_2, CO_2, and N_2. The Earth-like aqua planet atmosphere exhibits absorption from the collision-induced N_2-N_2 band at 4.1 μm, which is sensitive to the partial pressure, and could be diagnostic of atmospheric pressure if this challenging observation could be made (Schwieterman et al., 2015). At high abundances of CO_2 (at least as as low as 0.5 bar), the wings of the 4.3 μm CO_2 band overpower the N_2-N_2 band. The presence of the weak NIR–MIR CO_2 bands (including the numerous bands shortward of 2 μm, the $^{16}O^{12}C^{18}O$ isotopologue absorption bands at 3.6, 3.8, 4.0, 7.3, and 7.9 μm, and hot bands at 9.5 and 10.5 μm) are indicative of a warm, CO_2-rich atmosphere. As in Earth's atmosphere, O_2-O_2 CIA is weakly present in the aqua planet atmospheres, but the bands are considerably stronger at higher O_2 abundance, which would suggest an abiotic, post-ocean-loss source for the oxygen was more likely.

Potentially habitable environments may be discounted by observing indicators of desiccation, such as O_3, SO_2, and CO, as these gases react with water vapor and its photolytic byproducts. Both the modeled O_2-dominated and aqua planet atmospheres exhibit ozone absorption at 0.6 and 9.6 μm. However, a strong indication of desiccation is high ozone abundance, as constrained by the presence of a long wavelength tail of the Chappuis band (out to 1 μm), the 2.5 and 3.6 μm features, and additional weak bands at 9 and 13 μm, which arise in the O_2 cases, particularly the colder and desiccated environments. Retrievals of ozone abundances in conjunction with climate

and photochemical modeling could help constrain the likely abundances of tropospheric water vapor. The detection of SO_2 would also suggest a desiccated atmosphere, because SO_2 easily combines with H_2O to form sulfuric acid. The presence of CO, if not masked by CO_2 or O_3, would indicate desiccation because H_2O photolytic byproducts such as hydroxyl are efficient catalysts at recombining CO_2 from CO and free oxygen. While the absence of water vapor absorption does not necessarily indicate the lack of tropospheric water vapor or surface water, desiccation indicators from O_3, SO_2, and CO, even with weak water vapor features, would suggest a desiccated and likely uninhabitable environment.

Signs of atmospheric escape and ocean loss may be probed by observing isotopologue bands HDO and $^{18}O^{12}C^{16}O$. Measuring the D/H ratio in H_2O and the $^{18}O/^{16}O$ ratio in CO_2 could be used to probe isotopic fractionation, which occurs during atmospheric escape and ocean loss because lighter elements are preferentially lost over heavy elements (e.g. Hunten, 1982). D/H fractionation from atmospheric loss has been measured for both Venus (D/H$\sim$120 vs Earth; De Bergh et al., 1991) and Mars (D/H$\sim$4 vs Earth; Encrenaz et al., 2018). In particular, such D/H fractionation would indicate an environment that had the majority of its ocean reservoir depleted (Hunten, 1982). I assess the observational implications of this in the next chapter (4), which was published in Lincowski et al. (2019). Future atmospheric escape studies should assess the potential for and degree of oxygen fractionation that may occur from massive ocean loss in an environment with some retained atmospheric oxygen.

3.4.3 Planetary System Effects on Terrestrial Atmospheres and Spectra

The results here and those of others demonstrate that the atmospheres and surfaces of M dwarf terrestrials have likely been strongly shaped by several factors, including stellar evolution, atmosphere and ocean loss, photochemistry, and geological (and biological) surface fluxes (Segura et al., 2005; Grenfell et al., 2014; Rugheimer et al., 2015; Meadows et al., 2018; Meadows and Barnes, 2018). These interconnected processes will impact atmospheric composition, climate, and the resultant spectra of these environments. To best interpret current and upcoming constraints and data on terrestrial exoplanets, the most significant of these processes need to be included in models of

the planetary environments. The stellar spectral energy distribution and activity affect atmospheric loss and photochemistry, and bulk planetary properties (e.g. composition, size) affect outgassing species and rates, which all affect the composition of a terrestrial planet atmosphere, as we have demonstrated here. Atmospheric composition, including greenhouse gases and UV absorbers, in turn affect planetary climate, including the atmospheric temperature profile and surface temperature. This in turn can modify vertical distribution of constituents (e.g. cold trapping water vapor below a stratosphere), which affects features visible in transmission spectra. The thermal temperature structure (e.g. tropospheric lapse rates, thermal inversions and greenhouse warming) also affect the strength and shape of features seen in the thermal infrared. For example, in the desiccated, O_2-dominated atmospheres, the O_3- and O_2-O_2-induced stratospheres caused thermal emission in the stratosphere from CO_2 (Figure 3.8). In particular, interior outgassing and photochemistry are key processes for modeling terrestrial exoplanets, as both drive disequilibria in the atmosphere. The results presented here show a strong effect from outgassing (e.g. from SO_2 and H_2O), which together with their photochemical byproducts and reactions with other species, shape the temperature inversions and lapse rates as well as produce radiative greenhouse (and anti-greenhouse) effects. Although the environments modeled here do not explicitly contain biogenic fluxes, surface fluxes from life processes also drive disequilibria and this is one of the principal means that will be used to search for life on exoplanets (Simoncini et al., 2013; Krissansen-Totton et al., 2016; Meadows, 2017). Photochemistry is critically important in assessing planetary composition and in understanding the formation and destruction of key species, some of which may be outgassed and/or biogenic. As shown here, this is especially for planets at different orbital distances, including those orbiting M dwarfs, where the alien UV spectrum can drive chemistry that the Sun does not induce in the Earth's atmosphere. The species outgassed or generated from photochemistry may be directly observed, and their vertical distribution may affect other gas absorption features due to their effects on climate.

To illustrate the effects of modeling factors—including outgassing and photochemistry—on predicted spectra, I directly compare a sampling of spectra for TRAPPIST-1 d and e with Morley et al. (2017), who used radiative transfer and thermochemical equilibrium models to conduct a

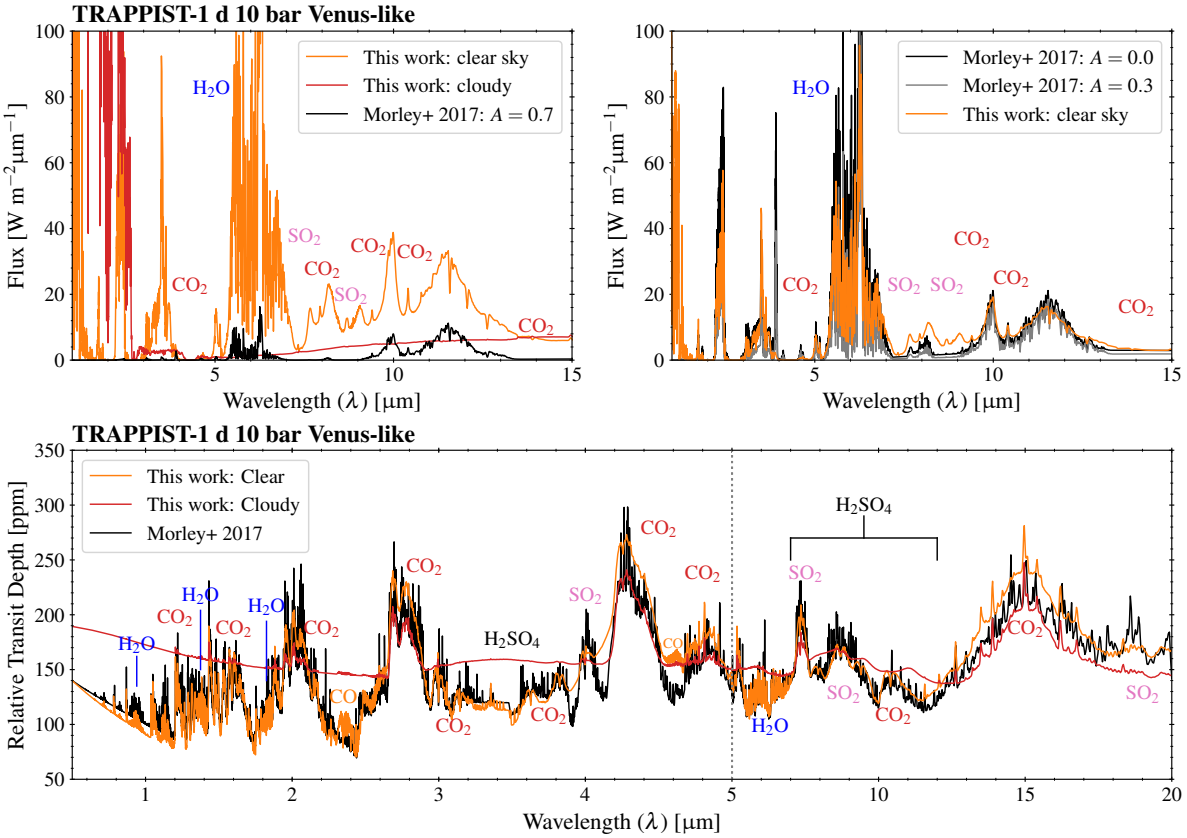

Figure 3.12: Comparison spectra of the 10 bar, TRAPPIST-1 d Venus analogs. To directly compare, Morley et al. (2017) spectra were sampled at 1 cm^{-1} and convolved with a 1 cm^{-1} half-width at half-max slit function. *Upper left panel*: clear-sky and cloudy Venus spectra simulated here compared to the high-albedo ($A = 0.7$) thermochemical equilibrium Venus of Morley et al. (2017). The radiative effects of sulfuric acid aerosols are much more complex than their effect on planetary albedo. The planet effectively emits from the cloud deck, which is not captured in models that assume a higher surface albedo to account for clouds. *Upper right panel*: my clear-sky Venus is qualitatively similar to the lower albedo ($A = 0.0 - 0.3$) of Morley et al. (2017). *Lower panel*: Transmission spectra showing relative transit depth. Clouds substantially impairing the ability to observe gas absorption features. The strong SO_2 features in the Morley et al. spectra are likely due to uniform vertical gas profiles and colder emission temperatures.

broad assessment of spectroscopic observables for the TRAPPIST-1 planets. For planet d, I compare the radiative-convective-photochemical-equilibrium 10 bar clear-sky and cloudy Venus-like atmospheres with the Venus-like atmospheres from Morley et al., identified by their albedos (A = 0.0, 0.3, and 0.7), which correspond to clear-sky to global cloud coverage (Figure 3.12). The

spectra of clear-sky Venus-like atmospheres modeled in both approaches are similar in both transmission and emission, except for stronger SO_2 features from the thermochemical model, which are reduced in my model (and in the true atmosphere of Venus) by H_2SO_4 formation. The SO_2 in the thermochemical model suppresses outgoing flux at wavelengths between 7–10 μm when compared to both my clear and cloudy atmospheres. Although the integrated flux of the $A = 0.0$ atmosphere is very close to the clear-sky Venus, the distribution of flux is different. The photochemically-consistent absorption features are not as deep (e.g. 7–9 μm), which is likely due to our atmospheres having warmer stratospheres. The atmospheres I modeled also show higher emission near 6 microns as weaker water vapor absorption permits escape of radiation from the hot lower atmosphere. This is likely due to different assumptions about the water vapor profile between the two models.

The spectra I simulated differ considerably from Morley et al. (2017) for cloudy Venus-like cases. Photochemical models produce results tailored to the spectrum of the host star, whereas thermochemistry is driven purely by the atmospheric temperature profile at a given orbital position, and so is more generic. The cloudy Venus differs significantly from the clear-sky case in both transmission and emission due to the truncation of the atmospheric column by cloud scattering and absorption at higher, colder altitudes, which reduces the outgoing thermal flux and can raise the tangent height when observed in transmission. Although the effects of clouds on surface temperature can be approximated by changing the Bond albedo in the thermochemical models, this process does not take into account the radiative effect of the clouds on the temperature profile, or on transmission and emission spectra. Sulfuric acid scattering and absorption in the cloudy Venus-like transmission spectrum, and emission from the cloud deck in direct imaging or secondary eclipse, are distinctive features of a Venus-like planet not captured in models without vertical cloud distributions.

As shown in Figure 3.13, the Earth-like atmospheres also show significant differences in composition between the two modeling approaches, primarily because I include the effects of water clouds, photochemically-produced gases such as O_3, and outgassed species such as CH_4. These characteristic features of Earth's spectrum are not seen in the spectra generated by Morley et al. (2017) using a thermochemical equilibrium model. The photochemically-consistent clear-sky aqua

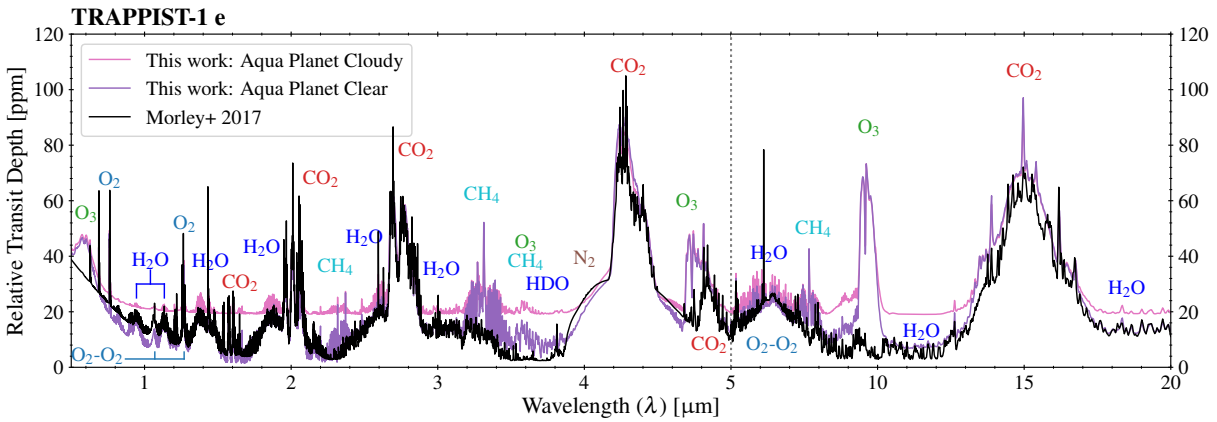

Figure 3.13: Transmission spectra of the 1 bar, TRAPPIST-1 e Earth analogs: the aqua planet modeled here with Earth geological outgassing compared to the thermochemical equilibrium Earth of Morley et al. (2017) (sampled at 1 cm^{-1} and convolved with a 1 cm^{-1} half-width at half-max slit function, scaled to 30%, and offset for this plot). The Morley et al. atmospheres do not have O_3, an abundant stratospheric photochemical by-product of O_2, or CH_4, which together are the most distinctive observational features of Earth (Selsis et al., 2002; Schwieterman et al., 2018).

planet atmosphere also includes isotopologue bands, (e.g. absorption at 3.6μm), which appear to be missing from the models produced by Morley et al..

3.4.4 Assessing Current and Future Observations

Several preliminary observational constraints on atmospheric composition have been obtained of planets in the TRAPPIST-1 system, to which I can compare modeling results. Spectra taken with the *Hubble Space Telescope* (de Wit et al., 2016; de Wit et al., 2018) ruled out low molecular weight atmospheres, although these spectra were also consistent with flat spectra within the error bars of $\sim 200-350$ ppm. For TRAPPIST-1 b, Delrez et al. (2018) observed a signal difference of 208 ± 110 ppm between the 3.6 and 4.5 μm *Spitzer* bands, which they suggest is due to CO_2 absorption. These results, and the K2 photometry from the discovery paper (Gillon et al., 2017) , are shown with error bars in Figure 3.14, along with the band-integrated transit depths for our modeled spectra. I adjusted the assumed solid body radius in these spectra to fit the observations for the solid body and wavelength-dependent atmospheric absorbing radius. The simulated spectra

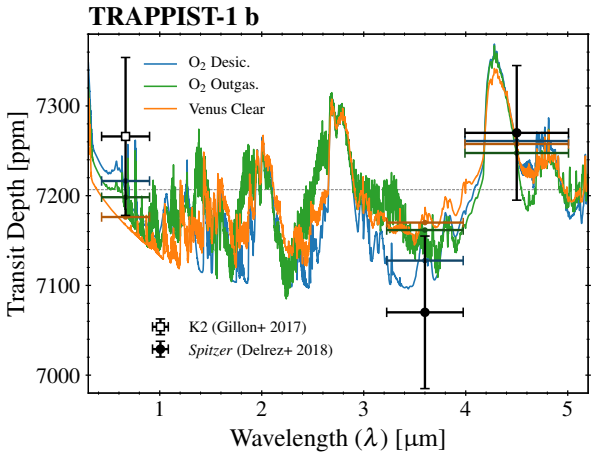

Figure 3.14: Comparison of available photometric transit data from K2 and *Spitzer* (Gillon et al., 2017; Delrez et al., 2018) with 10 bar model spectra for TRAPPIST-1 b. The colored points correspond to the model spectra convolved with the appropriate photometric filters. A vertical offset is applied to each model transmission spectrum so that the models optimally overlap the observations. These offsets correspond to the difference between the assumed radius for TRAPPIST-1 b and the solid body radius assuming a model atmosphere and its associated absorbing radius above the surface. The offsets are -293 km for the desiccated O_2, -308 km for O_2 with outgassing, and -312 km for the clear sky Venus. The desiccated, O_2-dominated atmospheres fits the *Spitzer* data within 1σ, while the other two atmospheres fit within 2σ.

are consistent with this data within 2σ error, and the O_2-dominated atmospheres fit within 1σ. The 3.6 μm filter bandpass contains absorption by the CO_2 isotopologue bands at 3.6, 3.8, and 4.0 μm, plus the wings of the main isotopologue 4.3 μm band, whereas the 4.5 μm band contains the 4.3 and 4.9 μm CO_2, 4.6 μm CO, and 4.75 μm O_3 bands. Rayleigh scattering and ozone absorption may contribute to the larger transit depth measured by K2. A different distribution of UV flux than assumed in this work could enhance ozone levels, further increasing the transit depth in the K2 band and *Spitzer* 4.5 μm band.

The simulated atmospheres are consistent with the observed data, but do not agree with the atmospheric scale height and temperature derived by Delrez et al. (2018) for TRAPPIST-1 b. Delrez et al. assumed the 208 ppm transit signal between the observed *Spitzer* bands was due to two scale heights from the CO_2 signal in an Earth-like atmosphere—with mean molecular mass 28 g mol^{-1}, CO_2 (44 g mol^{-1}) as the only absorbing gas, and excluding CH_4 and H_2O, which have

transitions in the 3.6 μm band. However, their derived temperature of 1400 K and scale height of 52 km (1800 K and 100 km with water vapor included) are not consistent with the assumption of an Earth-like atmosphere. My self-consistent modeled environments, which include a case with a greenhouse comparable to that of Venus, have emission temperatures which vary with wavelength (325–575 K; Figure 3.15), but overall stay close to the equilibrium temperature (∼400 K, Gillon et al. 2017, even though they have surface temperatures spanning 406–714 K.

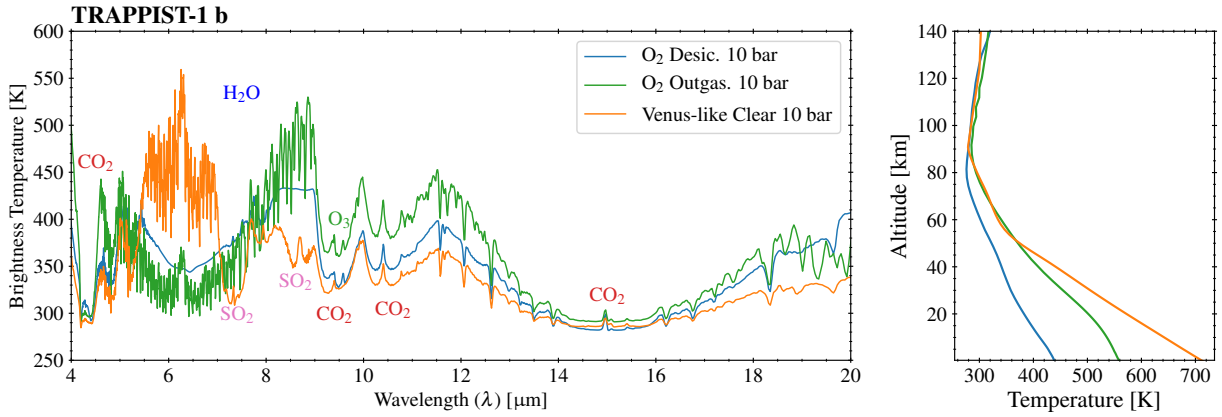

Figure 3.15: Brightness temperature of emergent flux for all three 10 bar environments modeled for TRAPPIST-1 b. The atmospheric structures are plotted on the right for comparison. Brightness temperature represents emergent flux plotted in units of temperature (i.e. the emitting layer temperature as a function of wavelength). As shown by comparing to the temperature profiles, higher brightness temperatures are emitted from lower layers, while lower temperatures represent emission from higher, cooler layers.

In Figure 3.16, I show that the scale heights at the effective transit altitude for the modeled atmospheres vary considerably as a function of wavelength and are within values typical of Solar System terrestrials (i.e. 8–16 km for Venus and Earth; Meadows and Crisp 1996), spanning ∼11–12 scale heights (3–5 scale heights when convolved with the *Spitzer* bands), and are consistent with the *Spitzer* observations. Scale height inferences from the size of potential features are degenerate with temperature, species, abundances, aerosols, and opacities, and so are difficult to accurately assess without properly accounting for a range of atmospheric possibilities within a retrieval framework (e.g. Line et al., 2013).

If the existence of an exoplanetary M dwarf terrestrial atmosphere is confirmed, near-term

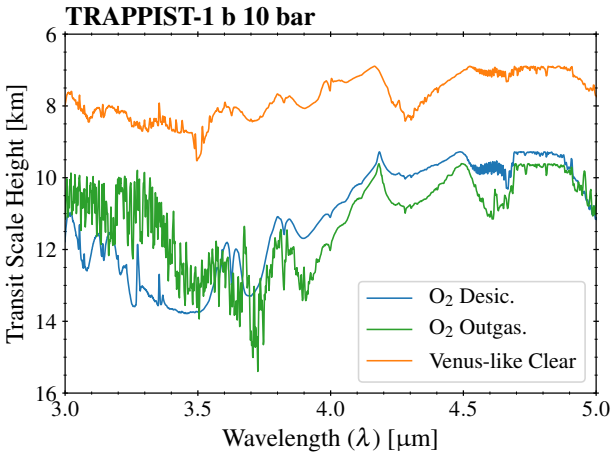

Figure 3.16: Atmospheric scale heights at the effective transit height in the wavelength range relevant for *Spitzer* for modeled TRAPPIST-1 b atmospheres. The calculated scale heights are consistent with Solar System terrestrials (7–16 km). Transmission spectra sample the stratosphere, where the atmospheres are cooler, so the scale heights are smaller. The O_2-dominated atmospheres are more transparent than the Venus-like atmospheres, so their atmosphere are probed deeper into the hotter regions.

observations will provide constraints on the environmental effects of M dwarf stellar evolution on orbiting planets as a function of distance from the star and position in the habitable zone. This modeling work provides hypotheses for planetary states as a result of evolution and composition that could be tested by these upcoming observations, which may constrain atmospheric temperatures and species abundances using the discriminants presented. In a subsequent paper, these modeled planetary states and spectra were used with instrument noise models to predict observational requirements to distinguish the current composition and evolutionary histories of the TRAPPIST-1 planets (Lustig-Yaeger et al., 2019a).

3.5 Conclusions

In this chapter, I have modeled potential O_2/CO_2-dominated and potentially habitable environments, and computed transit transmission and emission spectra for the seven known TRAPPIST-1 planets. These evolved terrestrial exoplanet spectra are consistent with broad constraints from recent HST and *Spitzer* data.

Contemporary work suggests that the current environmental states can include the hypothesized desiccated, post-ocean-runaway O_2-dominated planets (c.f. Luger and Barnes, 2015; Bolmont et al., 2017; Lincowski et al., 2018; Wordsworth et al., 2018), with at least partial ocean loss persisting out to TRAPPIST-1 h. The more temperate O_2-dominated atmospheres have unusual temperature structures, with low-altitude stratospheres and no tropospheres, which result in distinctive features in both transmission and emission, including strong collision-induced absorption from O_2.

Alternatively, if early volatile outgassing (e.g. H_2O, SO_2, CO_2) occurred, as was the case for Earth and Venus, Venus-like atmospheres are possible, and likely stable, throughout and beyond the habitable zone, so the maximum greenhouse limit may not apply for evolved M dwarf planets. If Venus-like, these planets could form sulfuric acid hazes, though we find that TRAPPIST-1 b would be too hot to condense H_2SO_4 aerosols.

From analyzing the simulated spectra, I find that there are observational discriminants for the environments we modeled in both transit and emission, with transit signals up to 200 ppm for TRAPPIST-1 b. Detection of CO_2 in all considered compositions may be used to probe for the presence of a terrestrial atmosphere. The detection of water is not a good indicator of a habitable environment, as Venus-like atmospheres exhibit similar spectral features for water, so the detection of low stratospheric water abundance may be a necessary but not sufficient condition for a habitable environment. The discriminants between these environments involve several trace gases. Careful atmospheric modeling that includes photochemistry and realistic interior outgassing is required to predict the diversity of potentially observable spectral features, to interpret future data, and to infer the underlying physical processes producing the observed features.

Nevertheless, these discriminants may be used to assess the viability of detecting evolutionary outcomes for the TRAPPIST-1 planets with upcoming observatories, particularly *JWST*, which was assessed in subsequent work (Lustig-Yaeger et al., 2019a). While specifically applied here to the TRAPPIST-1 system, these results may be broadly relevant for other late-type multi-planet M dwarf systems.

Chapter 4

OBSERVING ISOTOPOLOGUE BANDS IN TERRESTRIAL EXOPLANET ATMOSPHERES WITH THE *JAMES WEBB SPACE TELESCOPE*—IMPLICATIONS FOR IDENTIFYING PAST ATMOSPHERIC AND OCEAN LOSS

Portions of this chapter were originally published in collaboration with J. Lustig-Yaeger and V. S. Meadows in The Astronomical Journal (Lincowski et al., 2019, The Astronomical Journal, ©2019 The American Astronomical Society), and are reproduced below under the Creative Commons Attribution 3.0 license (https://creativecommons.org/licenses/by/3.0/). J. Lustig-Yaeger conducted the JWST detectability calculations.

This chapter dives deeper into how a post-ocean-loss planet could be identified, particularly by considering the isotopic evidence for atmospheric escape and total ocean loss found in Solar System planetary atmospheres, which could be considered in future observations.

4.1 Introduction

Evidence of past atmospheric escape and ocean loss may help test the inner limits of the habitable zone. The inner edge of the habitable zone (IHZ) is conservatively defined by the moist greenhouse greenhouse limit (where stratospheric H_2O exceeds 1000 ppm and so water vapor is easily lost to space), which lies close to Earth (0.99 au around a Sun-like star). However, an optimistic "recent Venus" limit can be defined under the assumption that Venus may have had surface water prior to approximately one billion years ago, before the last global resurfacing event, when the Sun was fainter (Solomon and Head, 1991; Kasting et al., 1993). Additionally, there have been a number of modeling studies positing revised limits for the IHZ that depend on perturbations to some of the parameter assumptions, including planetary mass (Kopparapu et al., 2014) and rotation rates (e.g. Kopparapu et al., 2016). Because TRAPPIST-1 d is between the recent Venus limit and the conservative inner edge as defined by Kopparapu et al. (2013), it is a valuable target for probing the position of the inner edge of the habitable zone around M dwarf stars.

In a multi-planet system like TRAPPIST-1, evidence of past atmospheric escape from the inner planet(s) could inform the suitability for more difficult follow-up observations of a habitable zone target (e.g. TRAPPIST-1 e). It is much easier to characterize the inner planets, due to the possibility of obtaining more transit observations and the larger scale heights afforded by the hotter atmospheres (Morley et al., 2017; Lincowski et al., 2018). The survival of an atmosphere inward

of the IHZ could be an indicator for the atmospheric survival of the other planets. For example, if TRAPPIST-1 b still has an atmosphere, then planets farther away—including those in the habitable zone—have a higher likelihood of also hosting an atmosphere. However, the presence of an atmosphere on a habitable zone planet does not guarantee the planet is habitable, as even habitable zone planets may have undergone complete ocean loss (§3; Lincowski et al., 2018).

Another piece of evidence that can indicate a planetary environment lost its surface water, so is not likely to be habitable, is severe isotopic fractionation. Both Venus and Mars once likely had surface oceans (e.g. De Bergh et al., 1991; Wordsworth, 2016), evidence for which includes isotopic fractionation in the observed atmospheric deuterium to hydrogen ratios (D/H) compared to the Vienna Standard Mean Ocean Water (VSMOW) for Earth. Compared to VSMOW, the atmosphere of Venus is enhanced by a factor of 120–140 (De Bergh et al., 1991; Matsui et al., 2012) and the atmosphere of Mars is enhanced by a factor of $\sim$4 (Owen et al., 1988; Villanueva et al., 2015; Encrenaz et al., 2018). These enhancements likely occurred from near-complete loss of their available water reservoirs (Hunten, 1982; Owen et al., 1988), because any primordial reservoir would dilute fractionated gas and reduce the total observed fractionation. Note that Earth has the lowest D/H ratio among the solar system terrestrials—VSMOW has D/H $\sim$8 times the solar abundance (c.f. Hagemann et al., 1970; Asplund et al., 2009). Measurements of large isotopic fractionations in the atmospheres of nearby exoplanets relative to their host stars would also likely represent departures from primordial compositions (Mollière and Snellen, 2019).

Atmospheric water vapor observed in transmission is suggestive but not definitive proof of the presence of an ocean (c.f. Earth, Venus; Meadows et al. 2018; Lincowski et al. 2018). Unlike reflectance spectroscopy, transmission spectroscopy cannot detect surface absorption or reflectance features—additional observations would be needed to determine the likelihood of surface liquid water.

Atmospheric escape is the only known mechanism capable of the extreme mass-dependent fractionation observed in the D/H in our solar system (see the summary in Mollière and Snellen, 2019, and references therein). Similarly, the fractionation of oxygen (^{18}O/^{16}O) during hydrodynamic or non-thermal escape of oxygen generated from photolysis of vaporized ocean water is

another potential signature of past ocean loss. If the abiotic oxygen generated via ocean loss is not lost to space, but instead is dissolved into a magma ocean (Schaefer et al., 2016; Wordsworth et al., 2018) or oxidizes the surface, then only a comparably small level of fractionation would occur. Unlike atmospheric loss, adsorption by the surface sequesters heavier isotopes slightly more than lighter isotopes (e.g. Sharp, 2017), and so it would impart a small fractionation signature opposing that of escape. Measuring the hydrogen and/or oxygen isotope fractionation for planets orbiting M dwarfs could provide additional evidence of past extreme ocean loss and atmospheric escape in systems very different from our own.

Because O_2 and its isotopologues are likely to be difficult to observe with *JWST*, isotopologues of CO_2 can be used as a more easily observed proxy for oxygen fractionation. Laboratory experiments (e.g. Shaheen et al., 2007) and numerical modeling (Liang et al., 2007) of CO_2 in the stratosphere of Earth have demonstrated rapid isotopic equilibrium (on the order of days) between CO_2 and O_2, indicating that fractionation in CO_2 can be efficiently induced if it coexists with heavily fractionated O_2. Because this process is UV-driven, it is likely to also occur efficiently in the atmospheres of planets orbiting M dwarfs.

Isotopic fractionation may therefore be a useful indicator for past ocean loss on terrestrial exoplanets and may help to observationally test the inner edge of the habitable zone. Here I assess how large isotopic fractionation could be observed spectroscopically in terrestrial exoplanet atmospheres with *JWST*. I focus primarily on the two TRAPPIST-1 planets most likely to produce the strongest transit signals, due to their large atmospheric scale heights and small semi-major axes: TRAPPIST-1 b, which receives approximately twice the irradiation of Venus, and d, which lies between the conservative and optimistic IHZ limits. I also assess the more observationally challenging TRAPPIST-1 e, a habitable zone candidate. The TRAPPIST-1 system is scheduled to be observed with *JWST* and is likely to produce a favorable signal that could be used to characterize evolved atmospheres (Morley et al., 2017; Lincowski et al., 2018; Lustig-Yaeger et al., 2019a). In §4.2, I methods specific to this chapter; in §4.3 I show the results; in §4.4 I discuss the implications of the results for observations with *JWST*; and in §4.5 I summarize the findings.

4.2 Methods

I adopt the following isotope geochemistry convention (e.g. Sharp, 2017) to describe the isotopic fractionation of hydrogen (note this does not include the multiplier of 1000 typically used in isotope geochemistry, due to the extreme values adopted here):

$$\delta \mathrm{D} = \frac{(\mathrm{D/H})_{\mathrm{model}}}{(\mathrm{D/H})_{\mathrm{VSMOW}}} - 1, \tag{4.1}$$

and similarly, δ^{18}O is the notation for changes in ^{18}O/^{16}O. "VSMOW" refers to the Vienna Standard Mean Ocean Water isotopic standard (Coplen, 1995).

4.2.1 Calculating Isotopologue Abundances

I determine the modified abundances for all isotopologues available for the molecules H_2O, CO_2, O_3, CO, and O_2 in the HITRAN2016 line lists by calculating the abundances for each isotopologue given the specified isotopic fractionation. For oxygen, I assume standard terrestrial linear mass fractionation, such that $\delta^{17}\mathrm{O} = 0.5\delta^{18}\mathrm{O}$ (Sharp, 2017), although around M dwarfs this may depend on the details of atmospheric escape for a given planet. I assume that enhancement of doubly fractionated molecules (e.g. D_2O) is stochastic, and therefore proportional to the production of the isotopic fractionation for each affected atom, which is generally a good assumption, especially at higher temperatures (Eiler, 2007).

To compute isotopologue abundances for each molecule, I numerically solve for the multipliers (X) for the isotopologues of a given molecule to adjust its VSMOW abundances given in HITRAN. These multipliers are not wholly independent, because I assume each substitution is proportional to the abundance. For example, substitution of hydrogen for deuterium in H_2O, $H_2^{17}O$, or $H_2^{18}O$ is equally likely per molecule, in proportion to the abundance of hydrogen in each molecule. The multiplier is squared for doubly substituted isotopes, because it requires the probability that one

atom is substituted *and* the other is also substituted. A generic notation may be written as:

$$X_{\mathrm{A}_m\mathrm{B}_n} = \frac{(x_{\mathrm{A}}[\mathrm{A}])^m \cdot (x_{\mathrm{B}}[\mathrm{B}])^n}{[\mathrm{A}]^m \cdot [\mathrm{B}]^n}, \tag{4.2}$$

where the square brackets (e.g. [A]) are the notation for abundance and the individual multipliers are (x_{A}) for a particular isotope A. This equation reduces to:

$$X_{\mathrm{A}_m\mathrm{B}_n} = x_{\mathrm{A}}^m x_{\mathrm{B}}^n. \tag{4.3}$$

For the example of D_2O (also the example in box 1 of Eiler 2007), if x_{D} is the multiplier for the enhancement in deuterium, the abundance multiplier of D_2O is:

$$X_{\mathrm{D_2O}} = \frac{(x_{\mathrm{D}}[\mathrm{D}])^2 \cdot [^{16}\mathrm{O}]}{[\mathrm{D}]^2 \cdot [^{16}\mathrm{O}]} = x_{\mathrm{D}}^2. \tag{4.4}$$

For a molecule with different isotopic substitutions, such as $HD^{17}O$, the abundance adjustment would be:

$$X_{\mathrm{HD}^{17}\mathrm{O}} = x_{\mathrm{H}} x_{\mathrm{D}} (0.5 x_{^{18}\mathrm{O}}), \tag{4.5}$$

where here I have set $x_{^{17}\mathrm{O}} = 0.5 x_{^{18}\mathrm{O}}$. The multipliers x are solved for simultaneously using a standard minimization code under the constraint that the total number of atoms of each isotope for a given family of molecules (e.g. H_2O and its isotopologues) satisfy the desired fractionation criterion (i.e. for δD=100, that the ratio of abundances for deuterium across all isotopologues for a given molecule is 100 times greater than compared to VSMOW).

I assume that the line intensities (and absorption coefficients) of the adjusted isotopologues scale directly with their abundances, in accordance with the Boltzmann equation:

$$\frac{n_{\mathrm{iso}}}{n_0} = \frac{g_{\mathrm{iso}}}{g_0} e^{-(E_{\mathrm{iso}} - E_0)/kT}, \tag{4.6}$$

where n is the number of molecules in a given energy state (directly proportional to the absorption

coefficient), g represents the multiplicity of states (here, the abundance of molecules of a given isotopologue), E is the energy of each state, k is the Boltzmann constant, and T is the temperature.

4.2.2 Model Planetary Atmospheres and Stellar Inputs

To model post-ocean-loss atmospheres that have undergone isotopic fractionation, I use nominal 10 bar atmospheres for TRAPPIST-1 b, d, and e from §3 (Lincowski et al., 2018). The choice of 10 bars is consistent with the findings of O_2 sequestration by Wordsworth et al. (2018), though other stable climate states with different compositions and higher or lower surface pressures and temperatures are also possible (c.f. Wolf, 2017; Turbet et al., 2018; Wunderlich et al., 2019). TRAPPIST-1 b and d are the planets that require the fewest transits to observe molecular absorption features, due to larger expected scale heights resulting from higher atmospheric temperatures, and a low surface gravity for d (Lincowski et al., 2018; Lustig-Yaeger et al., 2019a). Planet d also sits between the current conservative and recent Venus estimates for the inner edge of the habitable zone, and so could help constrain the actual inner limit of the HZ for the TRAPPIST-1 system. TRAPPIST-1 e is firmly in the conservative HZ, and is perhaps most likely to be temperate (Wolf, 2017; Turbet et al., 2018; Lincowski et al., 2018). Though some or all of the TRAPPIST-1 planets could have much larger water abundances because their densities are generally lower than the density of Earth, here I assume initially terrestrial bulk compositions, as their 3σ error bars also encompass the density of Earth (Grimm et al., 2018). For this isotopic fractionation detection study, I have assumed that all three of these planets, including TRAPPIST-1 e, have lost their surface water, due to an early runaway greenhouse phase and atmospheric escape during the superluminous pre-main sequence of the host star, and so are not habitable (Lincowski et al., 2018).

For all three planets, I modeled O_2-dominated atmospheres, both desiccated and outgassing, and clear-sky Venus atmospheres. A cloudy/hazy Venus case is not included for the detectability studies considered here, as haze opacity (due to Mie scattering at $< 2.5\mu$m and absorption by H_2SO_4 at $> 2.5\mu$m, Palmer and Williams 1975; Pollack et al. 1993; Ehrenreich et al. 2012; Lincowski et al. 2018) likely precludes detection of the isotopologue bands. Furthermore, due to high temperatures, H_2SO_4 will not likely condense in the atmosphere of a Venus-like TRAPPIST-1 b

Planetary State	Key Gases	D/H	$^{18}O/^{16}O$
O_2 outgassing	95% O_2, trace H_2O, CO_2, CO, O_3	10, 100	1, 10
O_2 outgassing, reduced H_2O	95% O_2, trace H_2O, CO_2, CO, O_3	10, 100	1, 10
O_2 desiccated	95% O_2, 4.5% N_2, 0.5% CO_2, trace CO, O_3	-	10, 100
Venus-like clear-sky	96.5% CO_2, 3.5% N_2, trace H_2O, CO	10, 100	1, 10

Table 4.1: Climatically and photochemically self-consistent environments from §3 simulated for spectral analysis, dominated either by O_2 or CO_2, assuming a range of trace species outgassing. TRAPPIST-1 b, d, and e were simulated for all environments with the listed fractionation levels. We model a reduced H_2O case for the O_2 outgassing environments, where the water vapor is scaled down by a factor of 100 (TRAPPIST-1 b) or 10 (TRAPPIST-1 d), which reduces the water vapor to the level observed in the stratospheres of Venus and Earth ($\sim 1-3$ ppm). As a result, the reduced H_2O atmospheres do not have self-consistent climates/photochemistry. There was no reduced H_2O case for TRAPPIST-1 e because the water vapor was already $\sim$1–5 ppm.

(§3; Lincowski et al., 2018). I model a second set of spectra for the O_2-dominated atmospheres that reduce the water abundances for b and d by a factor of 100 and 10, respectively, to simulate lower outgassing rates (and a drier stratospheric water abundance of $\sim$1 ppm) than those assumed in Lincowski et al. (2018).

The model atmospheres are detailed in §3 and listed in Table 4.1. Briefly, they contain 58–66 levels from the surface to 0.01 Pa. The O_2 desiccated atmosphere is 95% O_2, 0.5% CO_2, and 4.5% N_2 in photochemical–kinetic equilibrium with the primary photolytic products CO and O_3 (Figure 3.1). The O_2 outgassing atmosphere is 95% O_2 and 4.5–5% N_2, with Earth-like volcanic outgassing fluxes at the surface for H_2O, CO_2, SO_2, and other molecules not detectable in these spectra (Figures 3.1, 3.5). Note that the O_2 atmospheres with reduced water abundance are not climatically or photochemically self-consistent. However, neither adjustment to water vapor would likely drastically impact the atmospheric chemistry or climate. The Venus-like atmosphere is 96.5% CO_2, 3.5% N_2, with trace amounts of H_2O, SO_2, and others fixed to values at the surface consistent with Venusian abundances at 10 bar (Figure 3.2).

4.2.3 Isotopic Fractionation

Because isotopologues have not been considered in M dwarf terrestrial planetary atmospheric escape modeling (Lammer et al., 2007; Luger et al., 2015; Luger and Barnes, 2015; Schaefer et al., 2016; Ribas et al., 2016; Airapetian et al., 2017; Bolmont et al., 2017; Dong et al., 2017, 2018; Wordsworth et al., 2018; Lincowski et al., 2018; Egan et al., 2019), I use Venus observations to constrain plausible fractionation values for spectral modeling. While the Venus literature is mostly in agreement that hydrodynamic loss was responsible for the primordial loss of water (Hunten, 1982; Kasting and Pollack, 1983; Kasting, 1988; Chassefière, 1996; Gillmann et al., 2009; Chassefière et al., 2012; Bullock and Grinspoon, 2013; Lichtenegger et al., 2016; Lammer et al., 2018) and may have been responsible for the fractionation of D/H (see equation (17), Hunten et al., 1987), the specific mechanism(s) that caused the current D/H fractionation is (are) uncertain (e.g. Kasting and Pollack 1983; Kasting 1988; Grinspoon 1993; Gillmann et al. 2009; Collinson et al. 2016; Lichtenegger et al. 2016 and reviews by Chassefière et al. 2012; Bullock and Grinspoon 2013; Lammer et al. 2018). These processes generally cause some degree of fractionation and favor escape of the lighter elements, either due to the larger escape energy required by heavier species or due to the diffusive stratification of the homosphere and resultant higher abundances of lighter elements near the exobase (i.e. Rayleigh fractionation, Rayleigh, 1896; Hunten, 1982; Sharp, 2017).

Higher fractionation values compared to Venus may be possible, due to the more extreme stellar radiation environment experienced by M dwarf planets. M dwarfs have a much longer superluminous pre-main sequence phase (Baraffe et al., 2015), and they emit comparatively more XUV and FUV flux than our Sun (e.g. Ribas et al., 2016), which enhances atmospheric escape over time through stronger ionospheric heating from XUV absorption and stronger photolysis of water vapor by FUV absorption, a key limiting factor defining the diffusion-limited escape flux (e.g. Luger and Barnes, 2015). Terrestrial planets in and around the habitable zones of M dwarf stars could lose hundreds of bars of oxygen to non-thermal escape processes, such as coronal-mass-ejection- or solar-wind-driven ion pick-up (c.f. Kulikov et al., 2006; Lammer et al., 2007; Gillmann

et al., 2009) and polar winds (c.f. Collinson et al., 2016; Airapetian et al., 2017), both of which may be aggravated for planets without strong (i.e. Earth-like) magnetic fields. Although these studies have not considered isotopes or isotopic fractionation, the large loss potential for oxygen and other heavier species may plausibly result in severe isotopic fractionation.

Without detailed calculations of the possible isotopic fractionation in the atmospheres of planets around M dwarf stars, I assume a range of values for δD and δ^{18}O, both similar to and more severe than Venus. For the environments with water vapor, I conservatively simulate δD up to 100 times VSMOW, consistent with Venus (∼120–140). For cases where δD=100, I also simulate δ^{18}O up to 10 times VSMOW (note Venus exhibits no oxygen fractionation). In the most severe case for atmosphere and ocean loss, I simulate δ^{18}O up to 100 for the desiccated, O_2-dominated environment. For this extreme case, I assume that early complete ocean and hydrogen loss was followed by the continuous escape of oxygen. This severe value may not be possible, but it is useful to calculate a range of values in these spectral experiments to demonstrate the thresholds for detection. Lower fractionation values are included as appropriate for each case.

4.3 Results

I present noiseless simulated transit transmission spectra at 1 cm^{-1} resolution demonstrating the signal present due to different levels of extreme isotopic fractionation for δD up to 100 VSMOW (similar to Venus) and δ^{18}O up to 100 VSMOW. As in §3, these spectra are presented as "relative transit depth":

$$\frac{dF_a}{F} = \frac{2R_pR_a}{R_*^2} + \left(\frac{R_a}{R_*}\right)^2, \tag{4.7}$$

where F is the stellar flux, dF_a is the difference in stellar flux due to occultation by the atmosphere of the transiting planet, R_p is the planet solid-body radius, R_a is the atmospheric height from the surface of the planet, and R_* is the radius of the star. In this work, the relative transit signals discussed are generally relative to the transit signal calculated with the nominal VSMOW abundances. The spectra and data are available online using the VPL Spectral Explorer[1], or upon

[1] http://depts.washington.edu/naivpl/content/vpl-spectral-explorer

δD, δ^{18}O	VSMOW	1, 2	1, 10	1, 100	10, 1	10, 2	100, 1	100, 2	100, 10
CO_2	0.984	0.979	0.938	0.577	0.984	0.979	0.984	0.979	0.938
$^{13}CO_2$	0.011	0.011	0.011	6.48×10^{-3}	0.011	0.011	0.011	0.011	0.011
$^{16}O^{12}C^{18}O$	3.95×10^{-3}	7.87×10^{-3}	0.039	0.313	3.95×10^{-3}	7.87×10^{-3}	3.95×10^{-3}	7.87×10^{-3}	0.039
$^{16}O^{12}C^{17}O$	7.34×10^{-4}	2.49×10^{-3}	0.012	0.099	7.34×10^{-4}	2.49×10^{-3}	7.34×10^{-4}	2.49×10^{-3}	0.012
$^{16}O^{13}C^{18}O$	4.43×10^{-5}	8.84×10^{-5}	4.33×10^{-4}	3.51×10^{-3}	4.43×10^{-5}	8.84×10^{-5}	4.43×10^{-5}	8.84×10^{-5}	4.33×10^{-4}
$^{16}O^{13}C^{17}O$	8.25×10^{-6}	2.79×10^{-5}	1.37×10^{-4}	1.11×10^{-3}	8.25×10^{-6}	2.79×10^{-5}	8.25×10^{-6}	2.79×10^{-5}	1.37×10^{-4}
$C^{18}O_2$	3.96×10^{-6}	9.23×10^{-6}	5.07×10^{-5}	4.19×10^{-4}	3.96×10^{-6}	9.23×10^{-6}	3.96×10^{-6}	9.23×10^{-6}	5.07×10^{-5}
$^{17}O^{12}C^{18}O$	1.47×10^{-6}	5.83×10^{-6}	3.20×10^{-5}	2.65×10^{-4}	1.47×10^{-6}	5.83×10^{-6}	1.47×10^{-6}	5.83×10^{-6}	3.20×10^{-5}
$C^{17}O_2$	1.37×10^{-7}	9.22×10^{-7}	5.06×10^{-6}	4.19×10^{-5}	1.37×10^{-7}	9.22×10^{-7}	1.37×10^{-7}	9.22×10^{-7}	5.06×10^{-6}
$^{13}C^{18}O_2$	4.45×10^{-8}	1.04×10^{-7}	5.69×10^{-7}	4.71×10^{-6}	4.45×10^{-8}	1.04×10^{-7}	4.45×10^{-8}	1.04×10^{-7}	5.69×10^{-7}
$^{18}O^{13}C^{17}O$	1.65×10^{-8}	6.55×10^{-8}	3.60×10^{-7}	2.98×10^{-6}	1.65×10^{-8}	6.55×10^{-8}	1.65×10^{-8}	6.55×10^{-8}	3.60×10^{-7}
$^{13}C^{17}O_2$	1.54×10^{-9}	1.04×10^{-8}	5.69×10^{-8}	4.70×10^{-7}	1.54×10^{-9}	1.04×10^{-8}	1.54×10^{-9}	1.04×10^{-8}	5.69×10^{-8}
H_2O	0.997				0.995	0.992	0.967	0.964	0.944
$H_2{}^{18}O$	2.00×10^{-3}				1.99×10^{-3}	3.98×10^{-3}	1.94×10^{-3}	3.87×10^{-3}	0.019
$H_2{}^{17}O$	3.72×10^{-4}				3.71×10^{-4}	1.26×10^{-3}	3.61×10^{-4}	1.22×10^{-3}	5.99×10^{-3}
HDO	3.11×10^{-4}				3.10×10^{-3}	3.09×10^{-3}	0.031	0.031	0.030
$HD^{18}O$	6.23×10^{-7}				6.22×10^{-6}	1.24×10^{-5}	6.14×10^{-5}	1.22×10^{-4}	5.99×10^{-4}
$HD^{17}O$	1.16×10^{-7}				1.16×10^{-6}	3.92×10^{-6}	1.14×10^{-5}	3.87×10^{-5}	1.89×10^{-4}
D_2O	2.42×10^{-8}				3.45×10^{-7}	3.44×10^{-7}	3.53×10^{-6}	3.52×10^{-6}	3.45×10^{-6}

Table 4.2: **CALCULATED ISOTOPOLOGUE ABUNDANCES.** The column headers list each pair of hydrogen and oxygen isotope fractionation values compared to Vienna Standard Mean Ocean Water (VSMOW, from HITRAN2016; Gordon et al., 2017). Note VSMOW D/H=1.5574×10^{-4} (Meija et al., 2016). Not listed here are adjusted abundances for CO, O_2, and O_3, which we include in our models. The primary potentially observable species are HDO and $^{18}O^{12}C^{16}O$.

request. The detectability of the isotopically-enhanced features of these spectra are assessed by propagation through the PandExo *JWST* instrument noise simulator (Batalha et al., 2017).

4.3.1 Isotopologue Abundances

I solve for the isotopologue abundances of the model atmospheres adopted from §3 numerically as described in §4.2.1. The calculated abundances for all fractionation values for the primary detectable species, H_2O and CO_2, are listed in Table 4.2, which are listed in columns for each iteration of δD and δ^{18}O.

4.3.2 Simulated Spectra

I assessed isotopic fractions of δD up to 100 times VSMOW for two outgassing, O_2-dominated atmospheres, and a (clear-sky) Venus-like, CO_2-dominated atmosphere, for TRAPPIST-1 b, d, and e. I assessed δ^{18}O up to 10 for these atmospheres, and up to 100 VSMOW for a completely

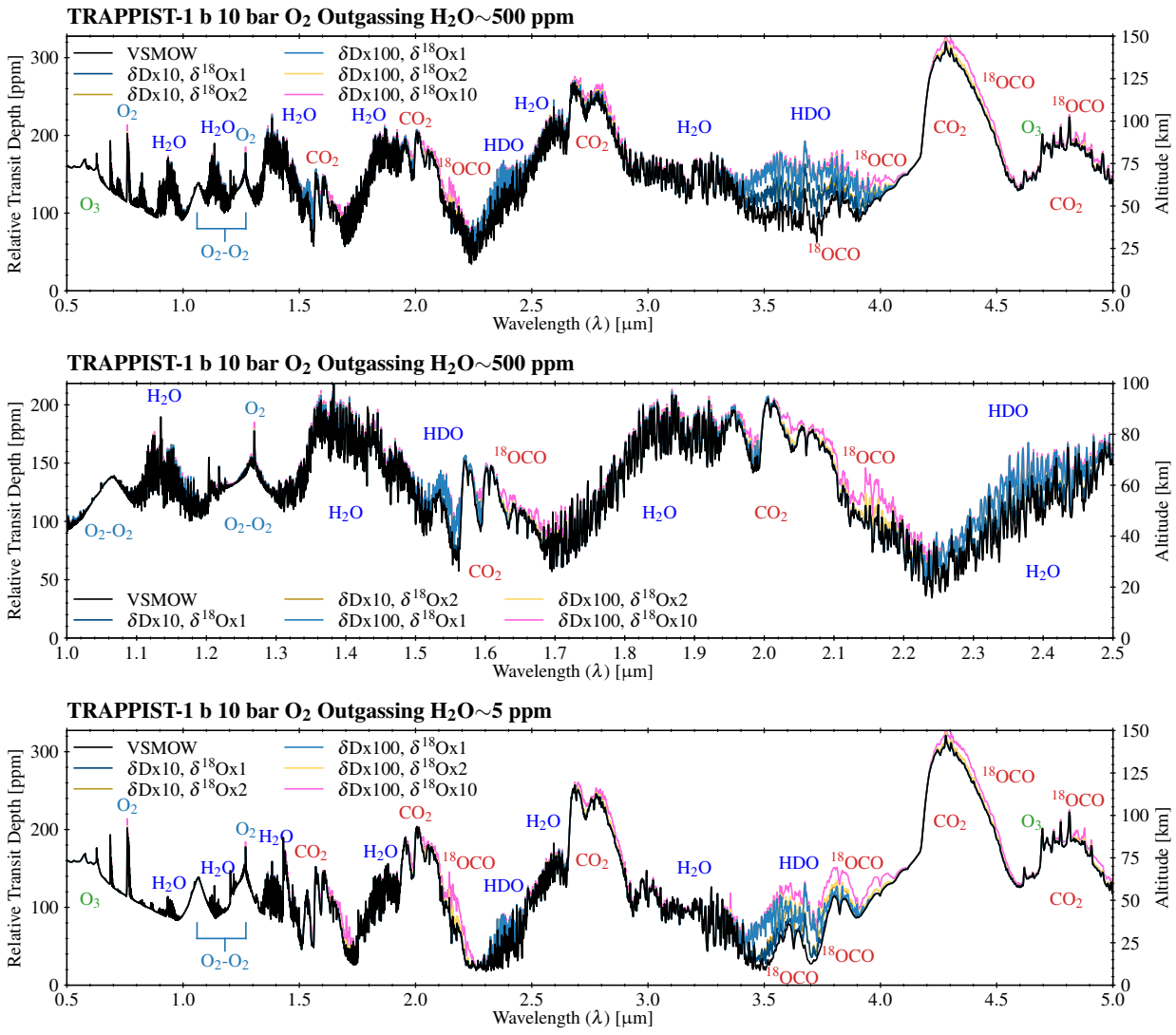

Figure 4.1: **SIMULATED TRAPPIST-1 B ATMOSPHERES EXHIBIT ISOTOPOLOGUE FEATURES THAT MAY BE DETECTABLE WITH *JWST*.** Simulated transmission spectra for the O_2 outgassing environments for TRAPPIST-1 b, which contain ∼500 ppm or ∼5 ppm stratospheric H_2O, comparing up to $\delta D = 100$ and $\delta^{18}O = 10$. These atmospheres exhibit transmission signals at multiple wavelengths up to 79 ppm, primarily from HDO. High HDO abundances partially obscure signals from $^{18}O^{12}C^{16}O$ (notated as ^{18}OCO in the plots). The center panel shows the range of the highest signal from the star, 1.0–2.5 μm, which contains weak isotopologue bands that may contribute significantly to the detection of these species.

desiccated O_2-dominated atmosphere. The justification for these values was discussed in §4.2.3, and these environments are listed in Table 4.1.

Noiseless simulated spectra are shown in Figures 4.1–4.2 for TRAPPIST-1 b. The spectral region around 3–4 μm is rich for observing δD enhancements in HDO and δ^{18}O enhancements in $^{18}O^{12}C^{16}O$. TRAPPIST-1 b exhibits transit transmission signal strengths up to 79 ppm for δD in the reduced H_2O, O_2-dominated atmosphere with outgassing and 94 ppm for δ^{18}O in the desiccated O_2-dominated atmosphere, compared to nominal spectra with VSMOW abundances. For comparison with b, in Figure 4.3 I show simulated spectra for TRAPPIST-1 d and e for the O_2-dominated atmospheres with outgassing. The atmospheres of both planets have smaller absorption features, due to lower water vapor abundances and temperatures, and due to the refraction of stellar photons. TRAPPIST-1 e has very small isotopologue features here compared to VSMOW abundances, but this simulated, uninhabitable environment has a temperate climate and stratospheric water abundance similar to a potentially habitable planet, which makes it an important comparison case.

The transit signals of isotopic fractionation in the individual atmospheres vary considerably and depend on the abundances of water vapor and CO_2 (Figure 4.1). In an O_2-dominated atmosphere with some water vapor still present due to outgassing, Venus-like fractionation of δD could be observable. With ∼500 ppm stratospheric H_2O (Figure 4.1, upper panel), the modeled TRAPPIST-1 b atmosphere may exhibit a transit signal up to 74 ppm in the broad 3.7 μm HDO band. There are also weaker features due to HDO at 1.5 and 2.4 μm if HDO is sufficiently abundant. If fractionation in oxygen was also present, the $^{18}O^{12}C^{16}O$ features between 3.0 and 4.1 μm would overlap with the 3.7 μm HDO band, though the band widths and shapes are different. The climate-photochemistry models in §3 produced lower water abundances in the stratosphere of this environment for TRAPPIST-1 d (10–50 ppm) and e (∼1 ppm), and the transit signal for enhanced HDO is similarly smaller (55 and 11 ppm, respectively). These transit signals are also reduced, due to refraction for both planets and a much smaller scale height for e. With reduced stratospheric water vapor (to ∼1–5 ppm each for b and d), compared to VSMOW the spectra exhibited isotopologue transit signals of 79 and 29 ppm for b and d, respectively.

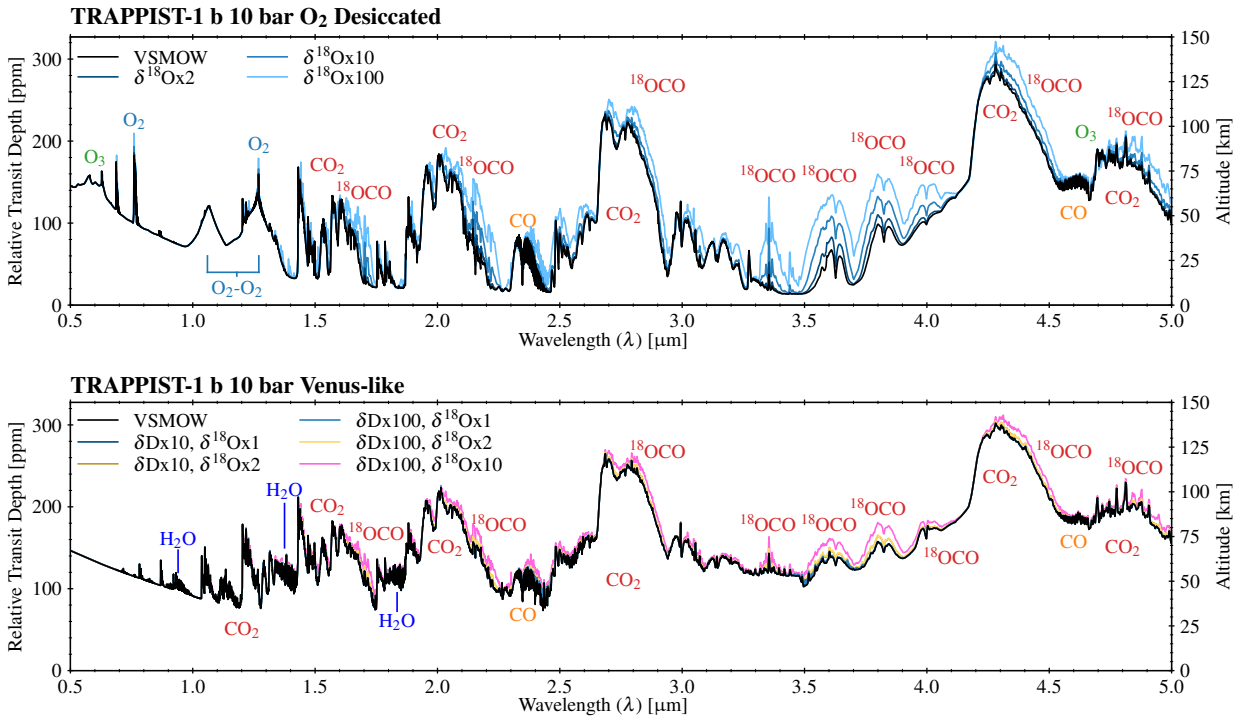

Figure 4.2: **SIMULATED TRAPPIST-1 B ATMOSPHERES EXHIBIT ISOTOPOLOGUE FEATURES THAT MAY BE DETECTABLE WITH *JWST*.** *Upper panel:* simulated transmission spectra for a 10 bar desiccated O_2-dominated atmosphere, demonstrating $\delta^{18}O$ in CO_2 up to 100. *Lower panel*: simulated transmission spectra for a 10 bar Venus-like (CO_2-dominated) atmosphere comparing up to δD=100 and $\delta^{18}O$=10. This case does not have clouds. The desiccated O_2-dominated atmospheres exhibit up to 94 ppm transit signals at multiple wavelengths, primarily from $^{18}O^{12}C^{16}O$ (notated as ^{18}OCO). The Venus-like atmosphere exhibits weak isotopologue fractionation signals because the spectrum is dominated by strong CO_2 absorption.

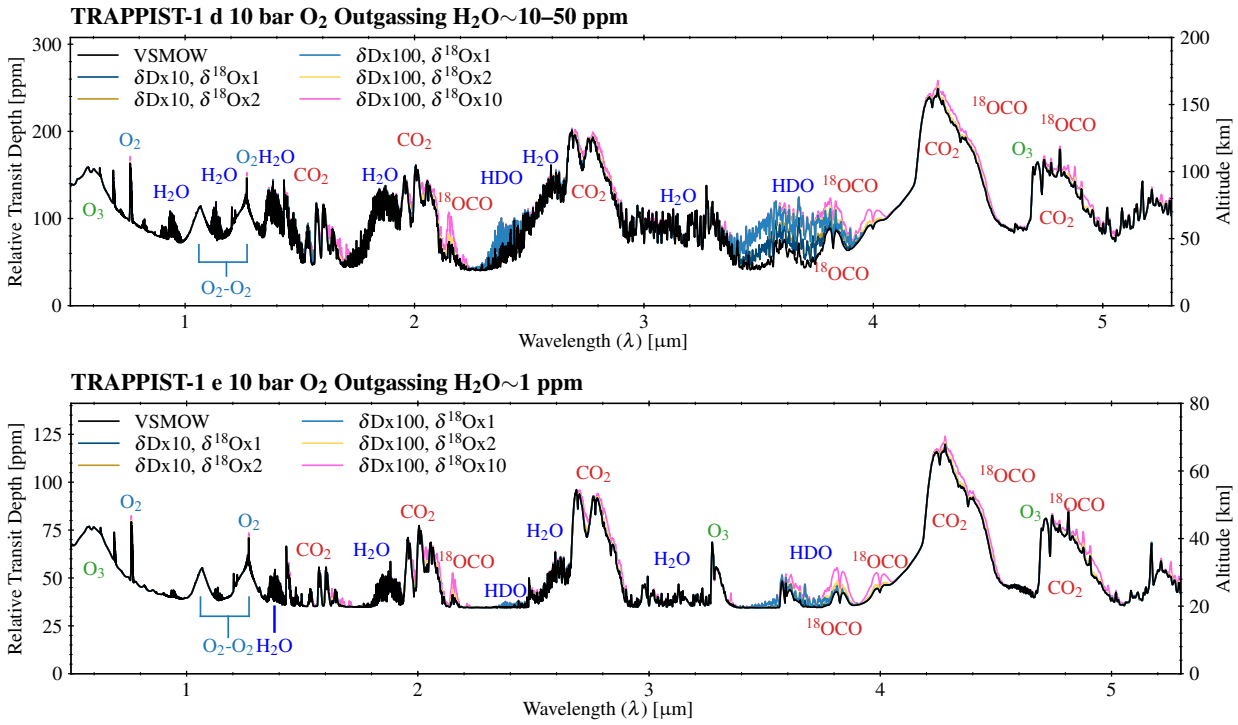

Figure 4.3: **TRAPPIST-1 D AND E O_2-DOMINATED ATMOSPHERES WITH GEOLOGICAL OUTGASSING MAY EXHIBIT DETECTABLE ISOTOPOLOGUE FEATURES IN TRANSIT TRANSMISSION SPECTRA.** Simulated transmission spectra for TRAPPIST-1 d (upper panel) and e (lower panel) compare up to δD = 100 and δ^{18}O = 10. These spectra are similar to the TRAPPIST-1 b case. Planets d and e are farther away from the star and exhibit more refraction of stellar photons in transit, which reduces the sizes of the absorption features. For d, transit transmission signals peak at 55 ppm for δD = 100 and 36 ppm for δ^{18}O = 10, with combined features peaking at 57 ppm. For e, transit transmission signals peak at 11 ppm for δD = 100 and 12 ppm for δ^{18}O = 10.

For a more severe case in a desiccated (water-free) O_2-dominated environment (Figure 4.2, upper panel), enhancements to $\delta^{18}O$ in $^{18}O^{12}C^{16}O$ are evident throughout the NIR (strongest at 1.7, 2.2, and 3–4 μm; labeled as ^{18}OCO), exhibiting transit signals compared to VSMOW of up to 94 ppm for b and 72 ppm for d. With a signal of 29 ppm, this was the only TRAPPIST-1 e atmosphere to exhibit a transit signal near 30 ppm compared to VSMOW (i.e. the putative noise floor for *JWST* NIRSpec, Greene et al., 2016). There are also strong $^{18}O^{12}C^{16}O$ isotopologue bands in these atmospheres at 6.0, 7.3, and 7.9 μm (not shown), though this spectral region is less favorable for *JWST* observations (Morley et al., 2017; Lustig-Yaeger et al., 2019a), and would be partially obscured by O_2-O_2 at 6.4 μm.

For all three modeled planets (b, d, and e), Venus-like atmospheres are thoroughly dominated by CO_2, with minimal differences in spectral features, due primarily to $^{18}O^{12}C^{16}O$ (less than 30 ppm) in the transit signal compared to VSMOW (see e.g. Figure 4.2, lower panel). These differences were at the same wavelengths exhibited by the O_2 atmospheres. With CO_2 absorption saturating the NIR spectrum, HDO was not detectable in the Venus-like cases.

While HDO and $^{18}O^{12}C^{16}O$ were the primary detectable isotopologues, many other bands were included in our spectral models, but were generally not present in the simulated transit transmission spectra, including the O_2 *A* band. No isotopologues containing ^{17}O were distinctly present, due to its lower abundance compared to ^{18}O. Isotopologue absorption by $^{12}C^{18}O$ at 2.4 μm is distinguishable in the completely desiccated atmosphere (see Figure 4.1), but not likely individually discernible with *JWST*.

4.3.3 Detectability Assessment

Lustig-Yaeger et al. (2019a) conducted a comprehensive detectability study for *JWST* instruments using the suite of model spectra from Lincowski et al. (2018) and identified several useful instrument modes for these atmospheres. These optimal instrument modes were used here and are listed along the bottom of Figure 4.4, which provides a summary of the number of transits required to attain an expected signal-to-noise ratio ($\langle S/N \rangle$) of five compared to the transit spectra with nominal VSMOW abundances for each model atmosphere. The number of transits required for a different

	NIRCam F322W2	NIRSpec G235H	NIRSpec G395H	NIRISS SOSS SUBSTRIP256	NIRISS SOSS SUBSTRIP96	NIRSpec Prism SUB512	NIRSpec Prism SUB512s	NIRSpec Prism SUB512 n=6
TRAPPIST-1 b O_2 Desiccated $\delta^{18}O\times10$	37	44	31	72	70	50	32	18
$\delta^{18}O\times100$	9	8	7	12	12	10	7	4
O_2 Outgassing 5 ppm H_2O $\delta D\times10$, $\delta^{18}O\times1$	>100	>100	>100	>100	>100	>100	>100	>100
$\delta D\times100$, $\delta^{18}O\times1$	32	>100	23	>100	>100	83	51	26
$\delta D\times100$, $\delta^{18}O\times10$	17	35	13	60	58	30	19	10
O_2 Outgassing 500 ppm H_2O $\delta D\times10$, $\delta^{18}O\times1$	67	>100	57	>100	>100	>100	>100	58
$\delta D\times100$, $\delta^{18}O\times1$	15	56	13	>100	>100	34	21	11
$\delta D\times100$, $\delta^{18}O\times10$	12	30	10	51	50	24	15	8
Venus-like $\delta D\times10$, $\delta^{18}O\times1$	>100	>100	>100	>100	>100	>100	>100	>100
$\delta D\times100$, $\delta^{18}O\times1$	>100	>100	>100	>100	>100	>100	>100	>100
$\delta D\times100$, $\delta^{18}O\times10$	>100	62	91	88	85	89	56	32
TRAPPIST-1 d O_2 Desiccated $\delta^{18}O\times10$	63	53	57	93	87	73	46	26
$\delta^{18}O\times100$	14	10	11	15	14	14	9	5
O_2 Outgassing 1–5 ppm H_2O $\delta D\times10$, $\delta^{18}O\times1$	>100	>100	>100	>100	>100	>100	>100	>100
$\delta D\times100$, $\delta^{18}O\times1$	>100	>100	>100	>100	>100	>100	>100	>100
$\delta D\times100$, $\delta^{18}O\times10$	63	63	56	>100	>100	81	50	28
O_2 Outgassing 10–50 ppm H_2O $\delta D\times10$, $\delta^{18}O\times1$	>100	>100	>100	>100	>100	>100	>100	>100
$\delta D\times100$, $\delta^{18}O\times1$	27	>100	22	>100	>100	66	40	21
$\delta D\times100$, $\delta^{18}O\times10$	20	41	17	80	75	38	24	13
Venus-like $\delta D\times10$, $\delta^{18}O\times1$	>100	>100	>100	>100	>100	>100	>100	>100
$\delta D\times100$, $\delta^{18}O\times1$	>100	>100	>100	>100	>100	>100	>100	>100
$\delta D\times100$, $\delta^{18}O\times10$	>100	84	50	68	64	76	48	28
TRAPPIST-1 e O_2 Desiccated $\delta^{18}O\times100$	80	54	63	95	89	81	51	28

Figure 4.4: **TRANSITS TO DISTINGUISH ISOTOPOLOGUE FEATURES COMPARED TO VSMOW ABUNDANCES AT $\langle$S/N$\rangle$ = 5 WITH A SELECTION OF *JWST* INSTRUMENTS AND FOR THE MODELED ATMOSPHERES.** NIRSpec Prism and G395H Grism, along with NIRCam with F322W2 filter, are best suited to detect HDO and $^{18}O^{12}C^{16}O$. All modeled TRAPPIST-1 e spectra, except for the case shown, required greater than 100 transits to distinguish isotopologue features compared to VSMOW abundances at $\langle$S/N$\rangle$=5. The cells are colored darker for fewer transits and lighter for more transits required.

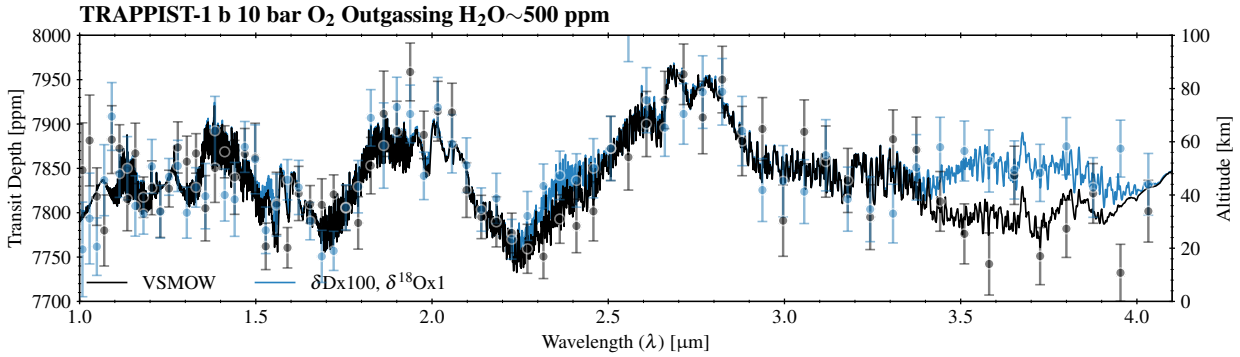

Figure 4.5: **ISOTOPOLOGUE BANDS MAY BE DETECTED IN A TRAPPIST-1 B CLEAR-SKY POST-OCEAN-LOSS O_2-DOMINATED ATMOSPHERE WITH *JWST*.** Simulated transmission spectra for the O_2 outgassing environment for TRAPPIST-1 b with ∼500 ppm stratospheric H_2O, comparing δD = 100 (blue) vs. VSMOW (black). These spectra were processed through the PandExo *JWST* instrument simulator (Batalha et al., 2017) and are presented with error bars at the native resolution for NIRSpec Prism (nominal resolving power $R \sim 100$), using $n_{\text{groups}} = 6$ (Batalha et al., 2018), with 11 transits co-added. The difference between these spectra is detectable at $\langle S/N \rangle$=5. The broad HDO band at 3.7 μm provides a significant contribution to the overall detection. The O_2-O_2 bands at 1.06 and 1.27 μm can also be seen here.

$\langle S/N \rangle$ can be calculated as

$$N' = N \left(\frac{\langle S/N \rangle'}{\langle S/N \rangle} \right)^2, \tag{4.8}$$

where N is the number of transits (here at $\langle S/N \rangle$=5) and N' is the number of transits to attain $\langle S/N \rangle'$.

Except for the CO_2-dominated, Venus-like environments, Venus-like levels of fractionation of D/H consistent with past ocean loss for each TRAPPIST-1 b and d atmosphere may be detectable with *JWST* (see e.g. Figure 4.5). The completely desiccated, O_2-dominated atmospheres modeled for TRAPPIST-1 b and d have $^{18}O^{12}C^{16}O$ bands that are also accessible to *JWST*. Assuming volcanically-outgassed species in the O_2-dominated atmospheres allows detection of HDO bands. Fractionation in oxygen, in addition to hydrogen, increases the detectability of isotopologue bands, due to complementary signal increases in both HDO and $^{18}O^{12}C^{16}O$ bands. As in Lustig-Yaeger et al. (2019a), we find that NIRSpec Prism SUB512 (512x512 sub-array) with a partial saturation strategy (allowing partial saturation at the SED peak to provide higher signal at other wavelengths),

with six groups per integration (Batalha et al., 2018), is generally the ideal instrument/mode for these detections. The NIRSpec G395H grism is nearly as good, or in some cases better, due to coverage of the 3–4 μm region containing broad HDO and $^{18}O^{12}C^{16}O$ bands. Similarly, due to its wavelength coverage, NIRCam F322W2 is also an acceptable instrument for these detections.

With lower levels of stratospheric water vapor similar to Venus and Earth in an O_2-dominated atmosphere (here, 1–5 ppm H_2O), a similar number of transits are required for TRAPPIST-1 b compared to the nominal outgassing atmospheres of Lincowski et al. (2018). This is significantly worse for TRAPPIST-1 d, which may be in part due to its higher refraction altitude.

The Venus-like atmosphere with Venus-like isotopic fractionation is likely very difficult to detect with *JWST*, even without aerosols. This is due to the small scale height and high opacity of a CO_2-dominated atmosphere, which confines the transmission to the upper stratosphere and drastically reduces the signal from H_2O and HDO. To detect a fractionation signal, such a Venus-like planet would also have to exhibit substantial fractionation in oxygen (unlike Venus itself), which could enhance the transit depths of the $^{18}O^{12}C^{16}O$ bands. In a cooler atmosphere such as that of TRAPPIST-1 d, the CO_2 bands are not as broadened, and the occupancy of the lower energy states of isotopologue bands is higher (Mollière and Snellen, 2019), so detecting $^{18}O^{12}C^{16}O$ in a Venus-like (albeit clear-sky) atmosphere of d would require fewer transits than b. Unfortunately, d was also the Venus-like planet that exhibited the most vigorous production of sulfuric acid haze (Figure 3.3).

For TRAPPIST-1 e, detecting isotopic fractionation in H_2O would be difficult, requiring more than 100 transits for all fractionation values, atmospheric environments, and instrument modes considered here. Fractionation in CO_2 oxygen isotopes in the desiccated O_2-dominated atmosphere may be possible, if such extreme fractionation is possible. The HDO and $^{18}O^{12}C^{16}O$ features in the model atmospheres for TRAPPIST-1 e are substantially masked by atmospheric refraction. The cooler temperatures and higher surface gravity compared to TRAPPIST-1 b and d result in small scale heights, which conspire to produce shallow transmission depths.

4.4 Discussion

I have shown that an enhancement of 100 in either δD (via water vapor) or δ^{18}O (via CO_2), which would likely be due to extreme ocean or atmospheric loss, may be detectable with *JWST* for the inner planets of the TRAPPIST-1 system. Simulated spectra for the O_2-dominated atmospheres exhibit transit signals up to 79 ppm and 94 ppm for δD and δ^{18}O, respectively, for TRAPPIST-1 b (55 and 72 ppm, respectively, for d; 11 and 29 ppm, respectively, for e). With optimal use of NIRSpec Prism (Batalha et al., 2018), these signals could be detected at $\langle$S/N$\rangle$=5 in eleven and four transits respectively for b (25 and five for d). In the desiccated, O_2-dominated case with δD = 100 and δ^{18}O = 10, the isotopic enhancement can be distinguished from the nominal Earth VSMOW abundances in as few as eight transits for b (13 for d). This is only a few more transits than the two transits required with NIRSpec Prism SUB512 $n = 6$ to detect an atmosphere by ruling out a featureless spectrum at $\langle$S/N$\rangle$ = 5 for b or d (Lustig-Yaeger et al., 2019a). It is more difficult to observe a fractionation signature in the atmosphere of a habitable zone planet like TRAPPIST-1 e; only extreme fractionation of oxygen is possibly detectable (in 28 transits), due to a smaller atmospheric scale height, lower levels of stratospheric water vapor, and the refraction of stellar rays through the atmosphere during transit (Bétrémieux and Kaltenegger, 2013, 2014; Misra et al., 2014; Robinson, 2017).

The strongest transit signal is due to rotational-vibrational bands in the NIR, 1–5 μm, consistent with *JWST* NIRSpec. Transit observations are dependent on the stellar photons for signal, and this is the spectral region with the most stellar photons from M dwarf stars. These rotational-vibrational transitions are subject to mass-dependent spectral shifts for the bands between 1–3 μm, because such transitions are inversely proportional to the reduced mass of the molecule. Asymmetric molecules such as HDO and $^{18}O^{12}C^{16}O$ provide new degrees of freedom, by breaking molecule symmetries compared to H_2O and CO_2, which produce new absorption bands between 3 and 8 μm.

The severe fractionation considered in this work would not likely be caused by any other known fractionation mechanism, including the composition of the host star (e.g. Mollière and Snellen, 2019, and references therein). Interpreting observed isotopic abundances in the atmospheres of an

exoplanet must be considered in relation to the host star. However, nearby stars differ in D/H by less than a factor of ~ 2 compared to the Sun (c.f. Linsky et al., 2006; Asplund et al., 2009). The fractionation of isotopic abundances compared to the host star value would indicate that a planet evolved from the primordial conditions, which could include a small effect due to formation. However, a large fractionation compared to the host star would likely indicate an evolved atmosphere, though at this time we cannot say which mechanism may be responsible.

The ability to observe isotopic fractionation in H_2O or CO_2 may help to more robustly identify worlds without surface oceans. Transmission spectroscopy cannot directly probe the surface composition of a planet, and water vapor observed in transmission is suggestive, but is not conclusive, proof that an ocean is present. Current planetary hydrogen loss (though also not conclusive evidence of a surface ocean) could be identified via UV measurements of Lyman-α (e.g. Jura, 2004). The detection of O_2-O_2 collision-induced absorption is indicative of a large inventory of oxygen that is most likely produced during the loss of oceans of water (Luger and Barnes, 2015; Schwieterman et al., 2016). A large O_2 inventory does not preclude the possibility that a significant amount of surface water remains, especially for more volatile rich worlds, which may include the TRAPPIST-1 planets. However, the identification of isotopic fractionation in H_2O and/or CO_2 in conjunction with the detection of O_2-O_2 would be strong evidence that the planet lost the bulk of its available water inventory, and that it is unlikely that surface water remains. This is because an extant inventory of surface water would dilute the isotopic fractionation signal.

Isotopic fractionation signals could therefore complement observations of O_2-O_2 for ocean-loss planets, and these two sets of observations may be attainable with *JWST*, at least for the inner planets of TRAPPIST-1. Lustig-Yaeger et al. (2019a) found that O_2-O_2 features in O_2-dominated atmospheres may be detected in as few as ten transits (for TRAPPIST-1 b) in the outgassing case with the NIRSpec Prism SUB512 ($n_{\rm groups} = 6$), equal to the ten transits required to distinguish HDO bands compared to VSMOW. The NIRSpec Prism is particularly useful because the extra wavelength coverage (0.6–5.3 μm) can provide simultaneous evidence of the O_2 abundance (via O_2-O_2 at 1.06 and 1.27 μm) and of isotopic fractionation of hydrogen in H_2O or oxygen in CO_2. Here we have shown that for a planet like TRAPPIST-1 b, the number of transits required to identify

these individual O_2-O_2 bands is sufficient to begin distinguishing isotopologues as well, without the additional observing time necessary to identify a large (abiotic) inventory of O_2.

Although the motivation for assessing atmospheric and ocean loss through measuring the D/H ratio was inspired by remote-sensing measurements of D/H in the atmosphere of Venus, it will not likely be possible to conduct these measurements in the atmospheres of Venus-like exoplanets using transit observations. Sulfuric acid aerosol formation truncates the atmospheric levels that can be probed in transmission, and the saturated CO_2 bands largely blanket the NIR–MIR spectra of CO_2-dominated atmospheres. The effective greenhouses cause high temperatures, which disfavor the occupation of isotopologue ro-vibrational energy states (Mollière and Snellen, 2019).

Isotopologue observations may help constrain the location of the inner edge of the habitable zone by providing evidence for whether water vapor detected in the atmosphere of a planet is consistent with ocean loss or with a primordial reservoir (i.e. surface water or outgassing). Because TRAPPIST-1 d sits between the recent Venus and moist greenhouse limits, it is a valuable target for this observation. The observation of water vapor with no evidence of fractionation in the atmosphere of an IHZ planet like TRAPPIST-1 d would support the optimistic recent Venus limit, though the lack of fractionation could also be due to outgassing fluxes or a high volatile inventory—i.e. it could be a water world in a permanent runaway greenhouse state, which would be indicated by a large abundance of stratospheric water vapor. Conversely, isotopic evidence of ocean loss would strongly support the moist greenhouse limit as the true inner edge. Robust observational evidence for the location of the IHZ would require a survey of multiple planets and multiple systems with high-fidelity observations to constrain both the H_2O abundances and D/H ratios.

It may be difficult to observe isotopologues in the atmospheres of planets within the habitable zone. I found that TRAPPIST-1 e exhibited only small signals, and even in the optimistic assessment conducted, which ignored any systematic noise floor, it would generally require greater than 100 transits to identify isotopologues at $\langle S/N \rangle$=5. This is likely to apply to HZ planets in general, due to the lower atmospheric temperatures (and resultant lower atmospheric scale height), additional refraction due to distance from the star, and lower stratospheric water vapor.

The fractionation I modeled may not be attainable for all small planets that may have undergone ocean and atmospheric loss in and around the habitable zones of M dwarf stars. If a planet targeted for observation is more volatile-rich than Earth, the volatile inventory available to the atmosphere may never be lost, and as discussed above, would not impart a significant fractionation signature to the atmosphere. This may be the case for one or more of the TRAPPIST-1 planets, which may be more volatile-rich than Earth due to slightly lower nominal densities (Grimm et al., 2018) and dynamical evidence of possible migration (Luger et al., 2017c). However, within the calculated error, these densities are still within the range of terrestrial values in a mass-radius relationship (Grimm et al., 2018).

An observation of oxygen fractionation in CO_2 could indicate extreme atmospheric loss but may be difficult to achieve. The fractional mass difference between ^{18}O and ^{16}O is small, and Venus does not exhibit any measured fractionation in oxygen (Hoffman et al., 1980; Bezard et al., 1987; Iwagami et al., 2015). So, significant fractionation in oxygen may require atmospheric escape mechanisms unknown in our solar system, or operating over longer time periods or at higher fluxes than for the solar system planets. However, if it occurred, oxygen fractionation could be retained within CO_2 if oxygen loss occurred in the presence of CO_2. Without surface liquid water, surface weathering processes (i.e. carbonate-silicate weathering, Walker et al., 1981) would no longer draw outgassed CO_2 from the atmosphere. Because the oxygen in CO_2 would dilute the isotopic signal from oxygen loss, the remaining CO_2 inventory must be small compared to the remaining oxygen to prevent significant dilution of the oxygen isotope abundances.

In addition to the potential dilution of oxygen isotopic fractionation, atmospheres with large inventories of CO_2 would make it more difficult to observe any isotopic fractionation signal considered here. Unlike the other typical terrestrial bulk atmospheric gases O_2 and N_2, CO_2 exhibits significant absorption throughout the NIR–MIR, which masks weaker absorption lines, including isotopologues. Large quantities of water vapor can similarly interfere with observing other trace gases. While Earth-like abundances of CO_2 and H_2O may be the most favorable for distinguishing and characterizing important isotopologue bands, low CO_2 abundance may not be likely for a planet that experienced total ocean loss because the lack of liquid surface water would reduce

surface weathering that draws outgassed CO_2 from the atmosphere.

Other factors not considered in this work can affect the possibility of detecting isotopic fractionation, such as surface pressure and clouds. Morley et al. (2017) showed that for atmospheres with a surface pressure of 1 bar and lower, the number of transits required to detect features increased with decreasing pressure. In the spectra §3, the amplitudes of transit transmission features did not change significantly as a result of higher surface pressure at pressures higher than 10 bars, as transmission spectra do not probe deeper than 10 bars in these cases (Lustig-Yaeger et al., 2019b). Clouds and hazes, which may form at high altitude, can significantly truncate transit transmission spectra, particularly hazes such as those in the atmosphere of Venus, which form at much higher altitude than water clouds (§3). For Venus-like clouds in particular, H_2SO_4 has many absorption bands longward of 2.5 μm. These absorption bands are not the same as CO_2 or H_2O, but together with these gases and due to the high altitude of haze aerosols, the presence of H_2SO_4 aerosols can effectively eliminate primary detectable isotopologue features in the 2.8–4.3 μm range, between CO_2 bands. While TRAPPIST-1 d and e may form aerosols, in Ch. 3 I showed that, due to high atmospheric temperatures, the most likely condensates in these oxidized atmospheres, H_2O and H_2SO_4, would not condense in the atmosphere of a Venus-like TRAPPIST-1 b. While other metal aerosols have been suggested for hotter exoplanets (such as sodium- and potassium-based condensates), these are not plausible for the temperature regimes considered here, as it would not be possible to evaporate them from the planetary surface (c.f. Schaefer and Fegley, 2009). Hydrogen-dominated atmospheres could support other types of aerosols, particularly if these planets reached higher temperatures (e.g. He et al., 2018), but the TRAPPIST-1 planets are not likely to have H-dominated atmospheres (de Wit et al., 2016; de Wit et al., 2018; Moran et al., 2018), with the possible exception of TRAPPIST-1 g (Moran et al., 2018), which I do not consider here. Consequently, TRAPPIST-1 b is not likely to support the majority of hypothesized aerosols, and so is more likely to be clear sky than the other planets in the system.

Here TRAPPIST-1 b, d, and e were used as sample planets to assess the possibility of detecting isotopologue bands in exo-terrestrial atmospheres. The results could be extended to other planets in the system, in light of the results of Morley et al. (2017), Lincowski et al. (2018), and Lustig-Yaeger

et al. (2019a), or to other systems. While TRAPPIST-1 c is one of the inner planets with parameters similar to Venus, it is more difficult to observe features in the atmosphere of TRAPPIST-1 c than b or d, due to the higher density of c and the resulting small scale height. Given the results for TRAPPIST-1 e, it is unlikely that isotopologue bands could be observed in the atmospheres of the outer planets, TRAPPIST-1 f, g and h, due to the increase in refraction altitude with distance from the star. The results of this work could be used to assess the detectability of isotopologue bands in the atmospheres of other M dwarf targets of interest, both those currently known and those yet to be discovered by SPECULOOS (Delrez et al., 2018), TESS (Barclay et al., 2018), CHEOPS (Broeg et al., 2013; Benz et al., 2018), and PLATO (Rauer et al., 2014).

I have shown that isotopic fractionation signals inferred from HDO or $^{18}O^{12}C^{16}O$ may be feasible to observe with *JWST* and may provide important clues to the evolutionary history of planets around M dwarfs. Measurements with ground-based high-resolution instruments may also be able to search for isotopic signatures for the very nearest M dwarf planets (Mollière and Snellen, 2019). The values considered here can guide observers considering different levels of fractionation. These levels could also be used to assess the possibility of detecting isotopic fractionation if future comprehensive modeling of atmospheric escape demonstrates at what level hydrogen or oxygen fractionation is possible, and serve as a testable hypothesis for fractionation due to ocean loss. After first determining that a planet has an atmosphere (Lincowski et al., 2018; Lustig-Yaeger et al., 2019a), the next important assessment of the planetary environment may be to search for signs of severe ocean loss. Isotopic measurements can contribute evidence for assessing the atmosphere and ocean loss of M dwarf planets, which will soon be observed with *JWST*. Although severe atmospheric escape is likely to afflict all small planets in or near M dwarf habitable zones, caveats against such fractionation occurring also exist. Observations of one or more inner planets in a multiple-planet system could be used to inform the suitability of more time-consuming follow-up observations of a habitable zone sibling.

4.5 Conclusions

This work has demonstrated that for a Venus-like isotopic fractionation of D/H, or a similar fractionation in $^{18}O/^{16}O$, isotopologue bands may be observable and distinguished from Earth-like isotopic abundances with *JWST* in as few as ten transits ($\delta D=100$) or four transits ($\delta^{18}O=100$) for a clear-sky atmosphere not dominated by CO_2. The large fractionation values considered here are meant to demonstrate the potential for detecting these bands and discriminating them from Earth-like abundances. These fractionation values would require an ocean-free surface and ocean loss at least as severe as that experienced by Venus. A detection of these bands in transit transmission spectra would be evidence of a lack of a surface ocean, and the extreme atmospheric loss and oxygen build-up that has been proposed by a number of authors. This would provide valuable constraints for atmospheric escape models, the location of the inner edge of the habitable zone (whether recent Venus or moist greenhouse), and on the habitability of M dwarf planets. Researchers currently preparing *JWST* observing proposals, and those who will be conducting retrievals on future *JWST* observations, may want to consider different isotopic abundances in line lists used as inputs to retrieval pipelines. Further work modeling atmospheric escape that includes elemental isotopes is also warranted, to understand to what degree isotopic fractionation is theoretically possible in the atmospheres of planets orbiting M dwarfs. A thorough analysis of atmospheric escape should consider thermal and non-thermal escape, including photochemistry and vertical transport, life-long outgassing, and the possibility of deep surface reservoirs (i.e. water worlds).

Chapter 5

BEYOND GLOBAL CLIMATE MODELS: INTRODUCTION OF A NEW TWO-COLUMN MODEL AND APPLICATION TO THE TRAPPIST-1 SYSTEM

This chapter is based on in-progress work in collaboration with V. S. Meadows, D. Crisp, E. Wolf, and T. D. Robinson, to be submitted to The Astrophysical Journal.

This chapter is the first demonstration of the two-column mode for VPL Climate, for studying synchronously rotating planets. Here I primarily focus on validation of this model and include additional applications that are beyond classic Earth-like / habitable-zone planets.

5.1 Introduction

M dwarf stars offer challenges to planetary habitability that are quite different than Earth-like planets around Solar-type stars. Their close-in habitable zones are likely to result in tidal-locking of the planets into synchronously-rotating or asynchronously-rotating resonance states (Kasting et al., 1993; Ribas et al., 2016). A synchronous rotation state may produce a large temperature contrast between the day and night side, mediated by atmospheric heat transport (Joshi et al., 1997; Joshi, 2003; Selsis et al., 2011; Wordsworth et al., 2011; Wordsworth, 2015; Leconte et al., 2013; Yang et al., 2013, 2014; Turbet et al., 2016, 2018; Kopparapu et al., 2016, 2017; Wolf, 2017; Wolf et al., 2019; Haqq-Misra et al., 2018; Komacek and Abbot, 2019), and this may be further ameliorated by planetary-scale ocean heat transport, which has been demonstrated in 3D global climate models utilizing dynamic ocean heat transport physics (Yang et al., 2013; Cullum et al., 2014; Yang et al., 2014, 2019c; Hu and Yang, 2014; Way et al., 2017; Way et al., 2018; Del Genio et al., 2019).

Separately, photochemical processes and their impacts on habitability and observable signatures have been studied extensively with 1D models, which was discussed earlier in §3. The critical point made by studies using photochemical models is that photochemistry and biological/geological surfaces fluxes shape atmospheric composition, with impacts on planetary climate and remote observables. These results are quite different for planets around M dwarf stars vs Solar-type stars, due to the different UV and peak flux distribution.

Globally-averaged planetary climate for rapidly-rotating planets may be well-represented by 1D models, which depends on how well the planetary dynamics transport heat around the planet. Planets like Earth or Jupiter and planets with thermally-massive, rapidly-rotating atmospheres,

like Venus, are efficient at heat redistribution and have been studied accurately with 1D models (Earth: Manabe and Strickler, 1964; Manabe and Wetherald, 1967; Ramanathan and Coakley, 1978; Segura et al., 2003; Robinson and Crisp, 2018; §2.3; Venus: Pollack et al., 1980; Seiff et al., 1985; Crisp and Titov, 1997; Robinson and Crisp, 2018; Jovians: Appleby and Hogan, 1984; Marley and McKay, 1999). Single-column models have been shown to provide globally-averaged surface climate results similar to 3D models, even for synchronously-rotating planets (Godolt et al., 2016; Meadows et al., 2018). Climate dynamics studies have produced various types of dynamical regimes, circulation cells, cloud formation patterns, and other spatially-resolved effects, depending on rotation rate (e.g. Joshi et al., 1997; Merlis and Schneider, 2010; Yang et al., 2013; Kaspi and Showman, 2015; Haqq-Misra et al., 2018; Komacek and Abbot, 2019).

Global climate models have been used to demonstrated that 3D treatment may be required for slow/synchronously-rotating planets with thin atmospheres or with pathological continental configurations that prevent efficient day-night ocean heat transport. In these cases, 1D models no longer obtain results consistent with 3D models, due to the lack of global heat circulation required for 1D models to remain valid (c.f. Joshi, 2003; Leconte et al., 2013; Cullum et al., 2014; Meadows et al., 2018; Del Genio et al., 2019). However, 3D models generally employ grey, coarsely-resolved, simplified, and/or inflexible radiative transfer parameterizations, whereas robust 1D models can employ physically-rigorous, flexible, spectrum-resolving radiative transfer methods, which can allow 1D models to simulate a broader variety of planets with greater accuracy (Robinson and Crisp, 2018; Meadows et al., 2018; Lincowski et al., 2018). The shortcomings of radiative transfer in 3D models has been recognized, and studies are underway to employ line-by-line radiative transfer in GCMs, though this remains at the early stages (Ding and Wordsworth, 2019).

Photochemically-mediated gases can drastically affect climate by altering the abundances of trace greenhouse gases like O_3, CH_4 and even H_2O (Meadows et al., 2018; Lincowski et al., 2018), but most 3D models are not coupled to photochemistry. Some recent studies have passed averaged climate data from 3D models to 1D photochemistry models to produce global atmospheric states with photochemically-mediated trace species for spectral simulations (Fauchez et al., 2019; Pidhorodetska et al., 2020), though these fail to account for the affect that photochemistry has

on increasing stratospheric water vapor under high methane conditions and the associated climate feedbacks from strong NIR absorption by both species (Meadows et al., 2018; Meadows et al., 2020). Only recently have some studies began to use integrated 3D climate-chemistry models, but so far only for Earth-like worlds, due to the Earth heritage of these models (Chen et al., 2018, 2019).

To obtain the coarsest spatial resolution on a tidally-locked planet, globally-averaged models can be extended to include model columns specified separately to represent the hemispherical averages for the day side and night sides of a planet. Earth studies pioneered two-column models to represent the upwelling and downwelling components of atmospheric circulation (Pierrehumbert, 1995; Nilsson and Emanuel, 1999; Raymond and Zeng, 2000). There have also been previous efforts to develop two-column models for exoplanets. Haberle et al. (1996) developed a low-order, global-average two-column model for Mars, which used a simple two-box (day-night) advection scheme for the atmosphere but did not include surface heat transport. Yang and Abbot (2014) developed a similar two-column model, which included surface heat transport, and compared and validated their model against 3D results. Goldblatt (2016) extended the work of Haberle et al. (1996) and provided the model equations, applying this work to Proxima Centauri b. Koll and Abbot (2016) advanced the work of Yang and Abbot (2014) and studied the key atmospheric parameters responsible for the day–night circulation. In all of these cases, the models were developed as simpler, low-order models, in most cases with only a few boxes representing the atmosphere, and using analytic parameterizations for radiative transfer or temperature. Nonetheless, these studies have demonstrated the capability for two-column models to approximate the day–night climates of synchronously rotating planets (Yang and Abbot, 2014; Koll and Abbot, 2016). However, these two-column studies are largely confined to Earth-like compositions and the associated GCMs for calibration.

For exoplanetary studies, particularly for the prediction of atmospheres other than Earth, there is a need for a flexible model capable of simulating synchronously rotating planets around M dwarf stars. This chapter seeks to address that need with a two-column, line-by-line, radiative-convective-advective-equilibrium model, coupled to a photochemical model. I present validations for com-

ponents of the two-column climate model formulation, compare results with GCM studies, and expand the results to include a few cases coupled to the photochemistry model. I present day, night, and globally-averaged climate states and present transit transmission, thermal emission, and day–night phase amplitude variation spectra (Selsis et al., 2011) for detectability.

5.2 Methods

Methods are described extensively in §2. Here, I discuss parameters specific to the models used in this chapter, particularly the eddy diffusivity parameterization.

5.2.1 Vertical Mixing

The tunable parameters are given in Table 3.2. For this chapter, I add a minimum eddy diffusivity for mass of 0.5 m^2 s^{-1} to smoothly and continuously prevent this quantity from dropping below this value. This minimum value is broadly consistent with studies of the diffusivity through the tropopause and into the stratosphere of Earth (Figure 2.3). The minimum value in §3 was 0.01 m^2 s^{-1}, consistent with some inferences of the minimum eddy diffusivity through the tropopause (e.g. Fleming et al., 1999). However, the minimum value at a particular point in space is not a good representative for global vertical transport, and validation for Earth is improved by using a higher minimum eddy diffusivity.

I have simplified the eddy diffusivity for heat in stable conditions to improve model stability and the validation for Earth. As also described in §2.3, here I set a fixed value for K_h in stable layers to 0.5 m^2 s^{-1}.

5.3 Results

To compare the 1D and two-column results with 3D models, I present simplified planetary environments for the TRAPPIST-1 Habitable Atmospheres Intercomparison (THAI, Fauchez et al., 2020), which excludes photochemistry. I then use the two-column model to simulate environments with different degrees of day–night ocean heat transport for two different aqua planet cases. These

results, consisting of temperature and gas profiles, day–night surface temperature differences, and spectra, demonstrate a range of states between GCM-type cases without ocean heat transport and 1D cases that assume effective heat transport. I then apply this two-column model framework to atmospheres that are very different from classical Earth-like habitable zone simulations, consisting of Venus-like atmospheres (c.f. Lincowski et al., 2018), O_2-dominated environments, and a hydrogen-dominated environment for TRAPPIST-1 g, representing a type of state that has not been precluded yet by observations (Moran et al., 2018). The modeled planetary environments are listed in Table 5.1. The aqua planets, moist O_2 environments, and H_2-dominated atmosphere have Earth geological fluxes of CH_4, H_2S, SO_2, and OCS, except the H_2-dominated atmosphere has a higher CH_4 flux, set equal to Earth (10^{11} molecule cm^2 s^{-1}), to simulate the higher rates that may be possible from a more volatile-rich icy planet.

The surface temperature results with corresponding advective fluxes are given in Table 5.3. In §5.3.4, I present transit transmission and day–night phase amplitude variation spectra as appropriate. I identify potentially detectable spectral discriminants that can be used in upcoming observations of the TRAPPIST-1 and similar planets with *JWST*.

5.3.1 Validation and Comparison of Methods

I first conduct a series of validation/comparison experiments against selected 3D GCM temperatures from E. Wolf (private communication) generated for THAI. These are used to calibrate the two-column model and assess differences between the 1D, two-column, and 3D models. These comparisons are instructive to demonstrate how well a two-column needs to replicate the winds to reproduce the hemispherical day–night climate behavior of GCMs.

5.3.1.1 GCM Data and Assumptions

The THAI cases consist of four standard, heavily simplified environments along two axes: two N_2-dominated cases with 400 ppm CO_2 (cases 1) and two 1 bar CO_2 cases (cases 2); each pair of cases has one dry, benchmark (ben) environment and one moist, habitable (hab) environment. I

Planetary state	Surface	Surf. Pres.	Clouds	Gases
THAI ben1, e[a]	grey 30%	1 bar	None	N_2, 400 ppm CO_2
THAI ben2, e[a]	grey 30%	1 bar	None	CO_2
THAI hab1, e[a]	ocean/snow	1 bar	water/ice	N_2, 400 ppm CO_2, trace H_2O
THAI hab1, 10W, e[a]	ocean/snow	1 bar	water/ice	N_2, 400 ppm CO_2, trace H_2O
THAI hab1, 50W, e[a]	ocean/snow	1 bar	water/ice	N_2, 400 ppm CO_2, trace H_2O
Aqua planet, e	ocean/snow	1 bar	water/ice	70% N_2, 20% O_2, 10% CO_2, trace H_2O, CH_4, CO, O_3, SO_2
Aqua planet, 10W, e	ocean/snow	1 bar	water/ice	70% N_2, 20% O_2, 10% CO_2, trace H_2O, CH_4, CO, O_3, SO_2
Aqua planet, 50W, e	ocean/snow	1 bar	water/ice	70% N_2, 20% O_2, 10% CO_2, trace H_2O, CH_4, CO, O_3, SO_2
Modern Earth-like, e	Earth average	1 bar	water/ice	68% N_2, 21% O_2, 10% CO_2, trace H_2O, CH_4, CO, O_3, SO_2, CH_3Cl
Abiotic O_2, b	desert	10 bar	None	95% O_2, 4.5% N_2, 0.5% CO_2, trace CO, O_3
Abiotic O_2, d	ocean	10 bar	water/ice	95% O_2, 5% N_2, 28 ppm CO_2, trace H_2O, CH_4, CO, O_3, SO_2
Abiotic O_2, e	ocean/snow	10 bar	water/ice	95% O_2, 4.5% N_2, 0.5% CO_2, trace H_2O, CH_4, CO, O_3, SO_2
H_2-rich, e	ocean	1 bar	water/ice	95% H_2, 5% N_2, 400 ppm CO_2, trace H_2O, CH_4, CO, O_2
H_2-rich, g	ocean	1 bar	water/ice, hc haze	85% H_2, 5% N_2, 10% CO_2, trace H_2O, CH_4, CO, O_2
Venus-like, b	basalt	10 bar	None	96.5% CO_2, 3.5% N_2, trace H_2O, SO_2, OCS, H_2S, NO, HCl

[a] Irradiation level of 900 W m^{-1} from Gillon et al. (2017) per THAI (Fauchez et al., 2020) for direct comparison with 3D GCM climate results.

Table 5.1: **MODELED PLANETARY STATES AND THEIR ENVIRONMENTAL PARAMETERS**.

generated 1D and two-column atmospheres for comparison with the ben1, ben2, and hab1 cases. To match the standardization as closely as possible, these cases use a quiescent 2600 K, $\log(g) = 4.5$ BT-Settl NextGen spectrum (Rajpurohit et al., 2013) to represent TRAPPIST-1, normalized to 900 W m^{-2}, the irradiation measured for TRAPPIST-1 e from earlier transit timing variation (TTV) results (Gillon et al., 2017). These atmospheres consist only of N_2, CO_2, and/or H_2O, as specified. For the dry cases, the surface is split into a grey 30% albedo surface for the Solar calculation and blackbody (0% albedo) surface for the thermal calculation. In the moist case, the surface in the Solar calculation is split between ocean and ice/snow by solar zenith angle to approximate a hemisphere with a substellar (or "eyeball") ocean.

The GCM cloud data are used to calibrate the two-column model optical depths for the hab1 case. I used the globally-averaged GCM effective particle radii data to produce optical depth profiles in the geometric limit, where the extinction cross-section is equation to twice the geometric cross section. This is suitable for use in VPL Climate by using the equation relating effective particle radius and optical depth from Ackerman and Marley (2001), equation (16). The wavelength-dependent optical properties for cirrus (water-ice) and stratocumulus (liquid water) clouds described in §2.2.2 were used with these optical depth profiles, which may differ slightly from the radii-dependent profiles used in the GCM. The globally-averaged cloud optical depths calculated from the GCM data were $\tau = 1.75$ for water clouds and $\tau = 0.06$ for ice clouds. Although the hemispherical averages differed from the global averages, the best agreement was attained in comparison to the GCM by using the globally-averaged cloud optical depths, rather than specifying different values for the day and night sides.

5.3.1.2 WTG Approximation

To accommodate parametric methods for two-column models, previous studies (Yang et al., 2014; Koll and Abbot, 2016) make the weak temperature gradient (WTG) approximation, requiring that the stratospheric temperatures between the day and night sides are equal. This constraint is not required in the VPL Climate two-column mode, though the model results produce near-equal stratospheric temperatures in all cases. However, a similar assumption, that the dynamical timescale is short compared to the radiative timescale such that the temperature gradient across the planet is small, is implicit in 1D models in general, and for the day and night sides of this two-column model. The WTG approximation is important for thermal emission from each hemispherical surface to predict day–night temperature differences and help with phase curve predictions. This is because flux is proportional to T^4, so large temperature differences across a single hemisphere may result in an average temperature that is smaller than the average effective temperature (i.e. the temperature based on the emitted flux). The deviations in day- and night-side hemispherically-averaged temperatures are discussed in §5.3.2.

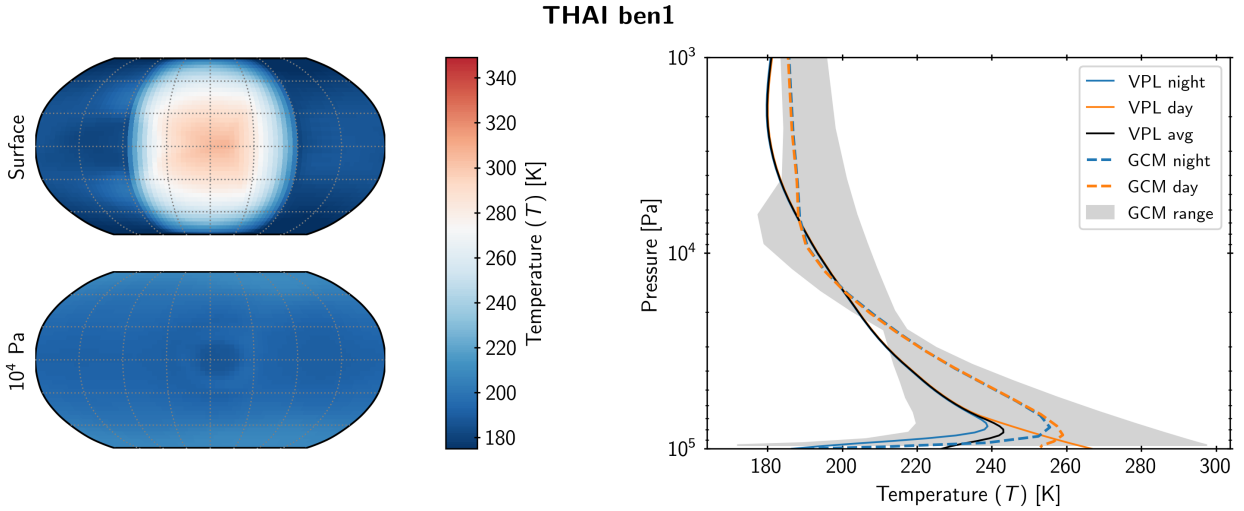

Figure 5.1: **COMPARISON OF THAI CASE BEN 1 ATMOSPHERIC AND SURFACE TEMPERATURES.** Surface (*top left*) and 0.1 bar (*bottom left*) temperature maps of GCM results used for comparison; atmospheric temperature structures for VPL Climate and GCM (*right*). Although the day side from the GCM exhibits a significant surface temperature gradient, the night side surface and planet-wide free atmosphere exhibit only weak surface temperature gradients. The coldest surface areas are the polar areas, primarily on the night side, and on the night side of the eastern terminator (i.e. just before dawn). In the free atmosphere (i.e. above the planetary boundary layer, where vertical transport dominates) the day–night gradients are ameliorated and show mostly uniform zonal temperatures, with only a slight gradient toward the poles, similar to rapidly-rotating planets like Earth, for which 1D models work well. Data for these maps were provided by E. Wolf (private communication).

5.3.1.3 Vertical and Zonal Winds Validation

I validate the zonal winds algorithm in an off-line calculation using hemispherically-averaged GCM data. To do this, I calculate area-weighted averages of the GCM temperature and diabatic heating rate profiles for day or night longitudes, which produces day and night hemispherical profiles. I used these averaged GCM profiles to first calculate the day- and night-side average vertical winds using equation (2.34), the mass divergences using equation (2.35), then conducted a matrix inversion on equation (2.36) to calculate the globally-representative zonal winds. The winds calculated by the two-column algorithm from the GCM data are roughly consistent with the GCM profiles, and are within the range of all of the GCM profiles. In Figure 5.2, I show these key profiles

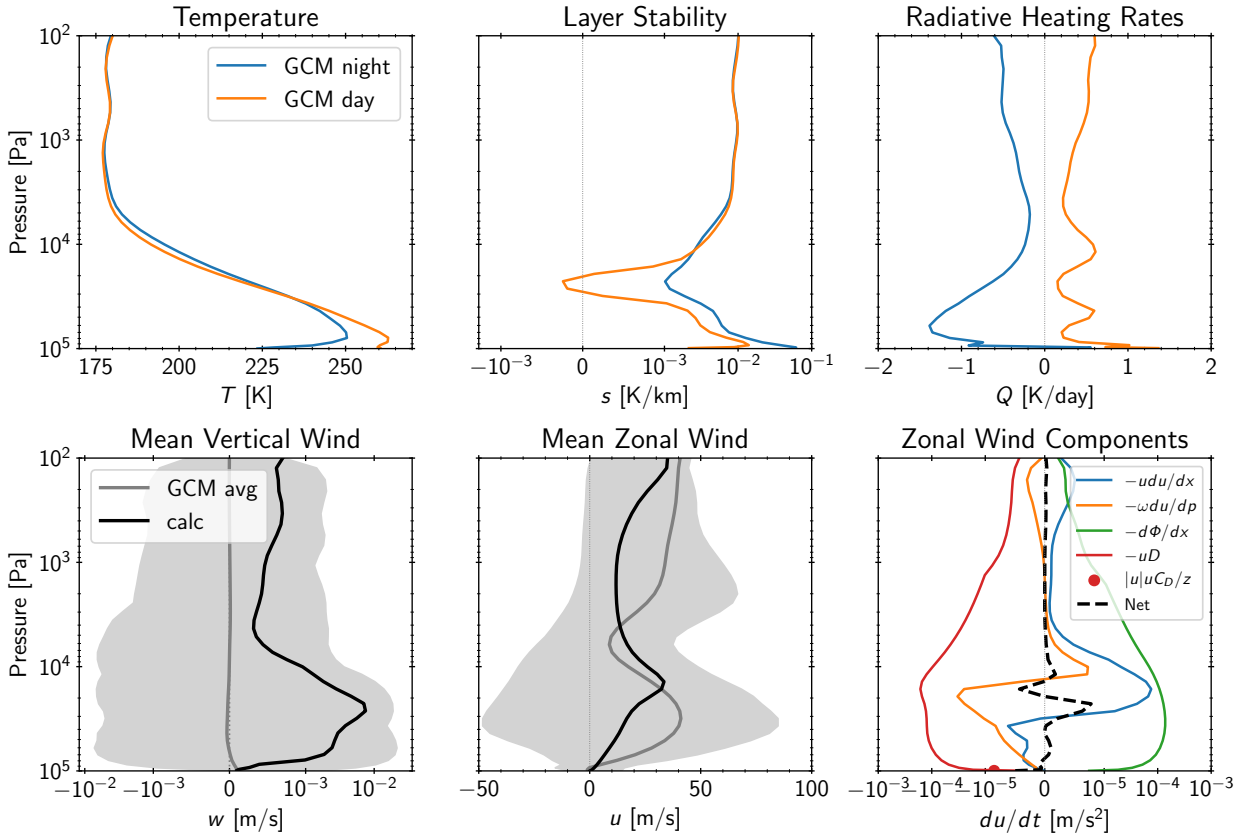

Figure 5.2: **ZONAL WINDS CALCULATION VALIDATION USING GCM HEMISPHERICALLY- OR GLOBALLY-AVERAGED DATA FOR THAI CASE HAB1.** Using the GCM temperature and heating rate profiles (upper left and upper right plots), here I demonstrate the calculation for horizontal (zonal) wind speeds used in VPL Climate. The layer stability (upper center) is derived from the temperatures (upper right) by $s = dT/dz + \Gamma$. The vertical winds are plotted in the lower left and the horizontal winds in the lower center plot, with the range of GCM winds given by the shaded regions. Although the vertical wind calculation differs considerably, this method results in coarsely similar horizontal winds. However, the calculated winds above the middle troposphere (0.5 bar) do not have to be large to produce small day–night temperature differences, which is shown in VPL Climate examples in later figures.

for the THAI hab1 case, along with the contributing components to the zonal wind net acceleration. The lack of meridional transport terms prevents a better calculation here. Nonetheless, this method produces zonal winds of appropriate order of magnitude, and in the following sections it will be shown that this is sufficiently close to simulate GCM day–night behavior.

5.3.2 Model Atmospheres Comparison with 3D GCM

In this section, I present climate results from VPL Climate in 1D and two-column modes and compare them with ExoCAM GCM results as part of the TRAPPIST-1 Habitable Atmosphere Intercomparison (THAI, Fauchez et al., 2020). Table 5.2 lists the 1D, day, night, two-column averages, GCM maximum, minimum, day, night and global average temperatures. The linear average is the most basic, where the day and night temperatures are arithmetically averaged. Because temperature is inferred from observations of flux ($F \propto T^4$), a more appropriate average temperature for comparison in this two-column climate model is to compute the surface emission flux, average the day- and night-side fluxes, then invert the flux equation to obtain the effective surface temperature.

	THAI ben1	THAI ben2	THAI hab1
VPL 1D	239	265	243
VPL two-col global average	227	256	242
VPL two-col flux average	238	263	247
3D GCM global average	221	245	245
VPL Day-side	267	291	272
VPL Night-side	185	220	211
3D GCM Day-side	257	274	267
3D GCM Night-side	184	216	222
3D GCM Maximum	306	329	294
3D GCM Minimum	167	186	206
VPL Day–Night Contrast	83	71	61
GCM Day–Night Hemisphere Contrast	73	58	45
GCM maximum–minimum	139	143	88

Table 5.2: THAI Temperature Comparison [K]

The differences between VPL model and GCM varies across the three THAI cases. For the ben1 case, both the 1D and two-column models produce higher surface temperatures than the GCM (239 and 238 vs 221 K). The 1D and flux-averaged two-column temperature are in good agreement, while the linear average of the two-column model (227 K) is cooler and closer to the GCM result. The ben2 case is more discrepant, with the GCM producing significantly cooler results than the linear average of the two-column model, due in part to the GCM missing key CO_2 absorption

bands, resulting in a weaker greenhouse (see §5.3.2.1). The cooler GCM average temperature may also be in part due to the large temperature contrast (particularly maximum to minimum), as coarser temperature averages appear to bias to higher values. In the hab1 case, where clouds and water vapor increase the potential for increased differences between the VPL model and GCM, the results are in the best agreement of the cases, with the GCM global temperature between the linear and flux averages (by 2–4 K), and 2 K warmer than the 1D model. It is worth noting the cloud optical depths were matched closely to the GCM. These comparisons make it difficult to draw broad conclusions about 1D and 3D model comparisons when under identical model conditions, which are difficult to replicate. However, the largest differences here (in the ben2 case) are explainable (see §5.3.2.1), and so the differences in 1D, two-column average, and 3D GCM average are relatively close, as demonstrated in previous work (Godolt et al., 2016; Meadows et al., 2018).

The VPL Climate model in two-column mode produces day–night contrasts that are slightly more severe than the GCM hemispherical averages, but well within the maximum–minimum contrast. The ben1 case indicates that, if everything else is as equal as possible, the night side thermal emission and hence total day–night advective flux, is in agreement (the night side is 1 K different). However, the day side average temperature is warmer (267 vs 257 K), which is likely due to the larger temperature gradient on the day side. As discussed for the 1D model, a larger gradient within a single column causes a bias toward higher temperature due to the T^4 dependence of flux. The ben2 and hab1 cases have a larger disagreement, however as discussed the ben2 case suffers from issues in radiative transfer in the GCM. It is more difficult to isolate differences in the hab1 case, which has a variable surface, clouds, and water vapor. Nonetheless, the fact that the two-column model produces a slightly larger temperature contrast than the hemispherical averages of the GCM is a more conservative scenario, because the two-column model can provide a conservatively large day–night temperature contrast to compare with the globally-averaged results of the 1D model.

For all three THAI cases, VPL Climate and GCM profiles of temperature, winds, and H_2O (for hab1) are presented in Figure 5.3. The two-column model qualitatively reproduces the day–night temperature behavior of the GCM, including divergence of the temperatures from the mid-troposphere to the surface and globally-averaged temperature inversion at the surface. Quantita-

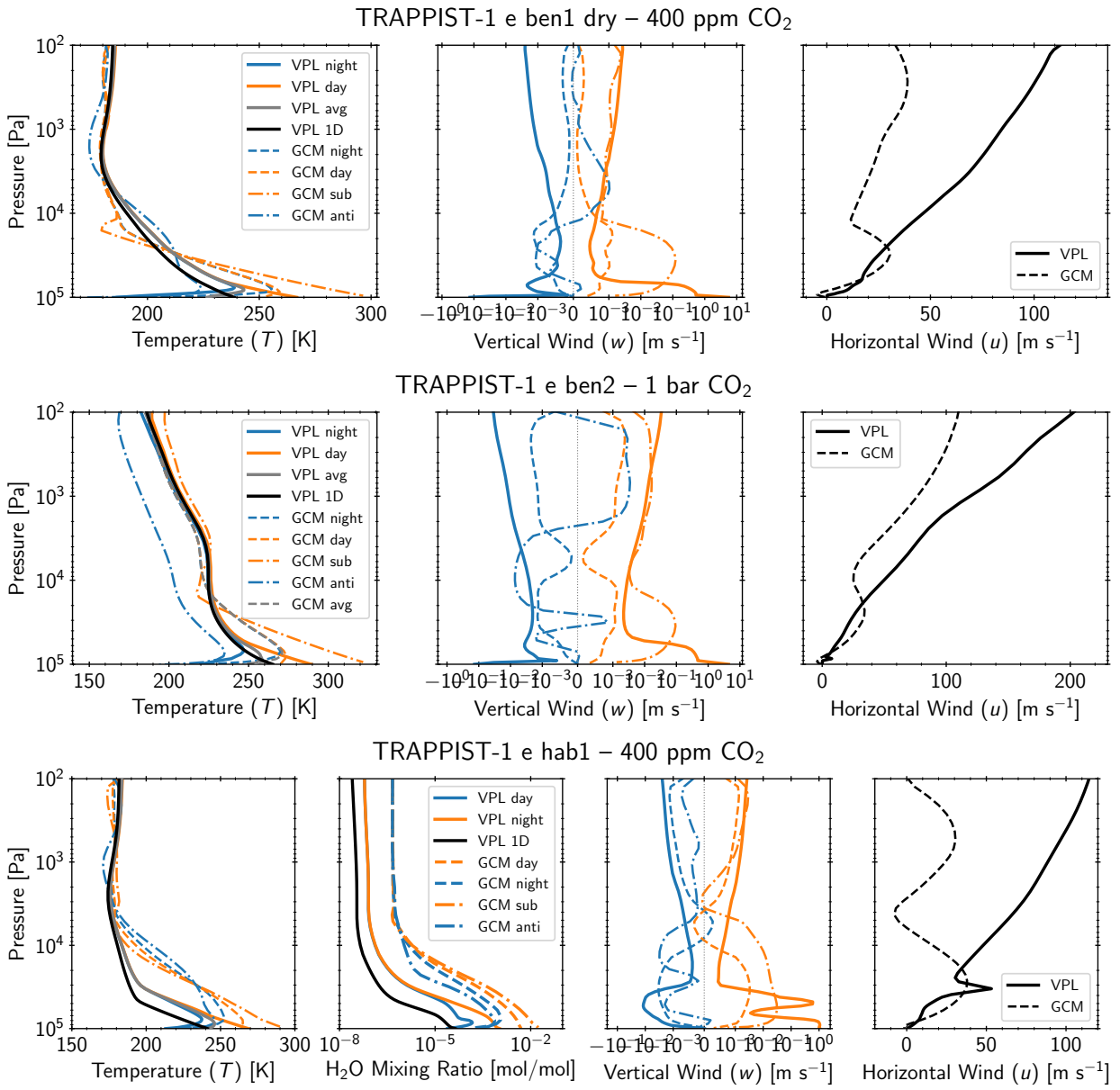

Figure 5.3: Comparison of key atmospheric variables for the three THAI cases, showing VPL Climate and GCM profiles. Temperatures between the day and night sides diverge in the troposphere, primarily due to different vertical transport parameterizations between the models. Even though there is some deviation in horizontal wind speeds between VPL Climate and ExoCAM, above the lower troposphere the temperature profiles are very similar, implying that there may be some critical wind speed that maintains very small day–night temperature differences, which are met by both models. This is consistent with the Weak Temperature Gradient approximation. Solar heating rates, assumed here to drive horizontal transport, differ between the GCM and SMART as a result of RT physics rather than the temperature profile, except for the hab1 aqua planet, where very different water profiles result in different heating rates.

tively, there are temperature differences between the VPL model and GCM. In all three comparison cases, the VPL Climate model produces much colder temperatures in the troposphere, which is likely due to different convective parameterizations. In the hab1 case, the lower tropospheric temperature results in a much lower water vapor abundance throughout the atmosphere, which could impact simulated spectra and inferences from retrievals on observations.

Even with different temperature profiles, there is coarse agreement between VPL Climate and ExoCAM in horizontal winds. Although I have attempted to reproduce GCM global horizontal winds, without a full 3D framework, this calculation is imprecise, because it is missing meridional wind components. Nonetheless, the day–night behavior of the two-column model is qualitatively similar to the GCM in terms of deviation from the global average as a function of altitude. Although in all layers at equilibrium, radiative, convective, and advective heating rates much balance, it is useful to consider the dominant mechanism. At low altitudes, where temperatures diverge, the dominant heating mechanism is convection, which permits a large day–night temperature contrast to be sustained. Above the middle troposphere, the dominant mechanism is radiation, which balances against advection to form a small day–night temperature gradient. Even moderate winds produce large heating rates, which scale scale linearly with the temperature difference. Wind speeds above the lower troposphere do not need to be large to maintain thermal equilibrium between the hemispheres, and the precise calculation of horizontal wind speeds is not important in that region. Solar heating rates, assumed here to drive horizontal transport, differ between the GCM and SMART as a result of RT physics rather than the temperature profile, except for the hab1 aqua planet, where very different water profiles result in different heating rates.

5.3.2.1 Radiative Transfer

GCMs are heavily parameterized to process thousands of latitude-longitude points and dozens of levels. To minimize the computational cost of these calculations, these models often use simplified radiative transfer models, which sometimes produce large errors in the radiative fluxes and heating rates. GCMs typically use correlated-*k* coefficient or other radiative transfer approximation methods to minimize computation time and expense speed computation time and may employ

few spectral intervals (bins) over which these calculations are conducted. The spectral binning and gas absorption choices in these methods were historically made for Solar-type stars, with a relatively smooth spectral energy distribution (SED) that peaks in the visible. Late-type stars, like TRAPPIST-1, have peak emission that is shifted into the infrared and have significantly more variability across the spectrum than earlier-type stars, due to broad molecular absorption bands, which can make coarse bin choices optimized for the Earth orbiting the Sun less optimal. For example, Yang et al. (2016) used an early type M dwarf for a model intercomparison, and stated that coarse binning may have resulted in inaccurate fluxes as a function of altitude and spectral interval in the models compared. In this work, the comparison cases (as simpler atmospheres) are from a GCM template with particularly coarse spectral bins, containing 28 bins across the entire spectrum (Wolf and Toon, 2013; Wolf, 2017). These bins were based on the Earth-Sun regime, and pathologically contain a wide, 1 μm bin between narrow bands for O_2, which results in approximately 50% of the TRAPPIST-1 irradiation contained in this single spectral bin, which may result in large flux and heating rate errors as a function of altitude.

In this section, to demonstrate areas of agreement and disagreement, I compare heating rates and wavelength-dependent thermal fluxes calculated by the GCM for the THAI hab1 and ben2 cases with those generated with SMART, which is used as a radiative transfer standard for exoplanet spectral studies (Kopparapu et al., 2013; Yang et al., 2016). I compare a single column of the GCM for both cases, the sub-stellar point, to make a direct comparison and obtain an accurate 1D calculation using SMART. Figures 5.4 and 5.5 show the temperature profiles for the sub-stellar and anti-stellar points used for comparison and the resultant net radiative heating rates, along with the dynamical core heating rates from the GCM, for the THAI hab1 and ben2 cases, respectively. The lower panels show the emergent flux spectra in the thermal, including the SMART fluxes binned to the GCM grid.

THAI hab1 In the basic habitable aqua planet case (Figure 5.4), the models have variation primarily in the Solar. In the thermal (lower panel), SMART and ExoCAM are generally in good agreement. In particular, there is good agreement in the gas absorption bands for H_2O at 6.1 μm

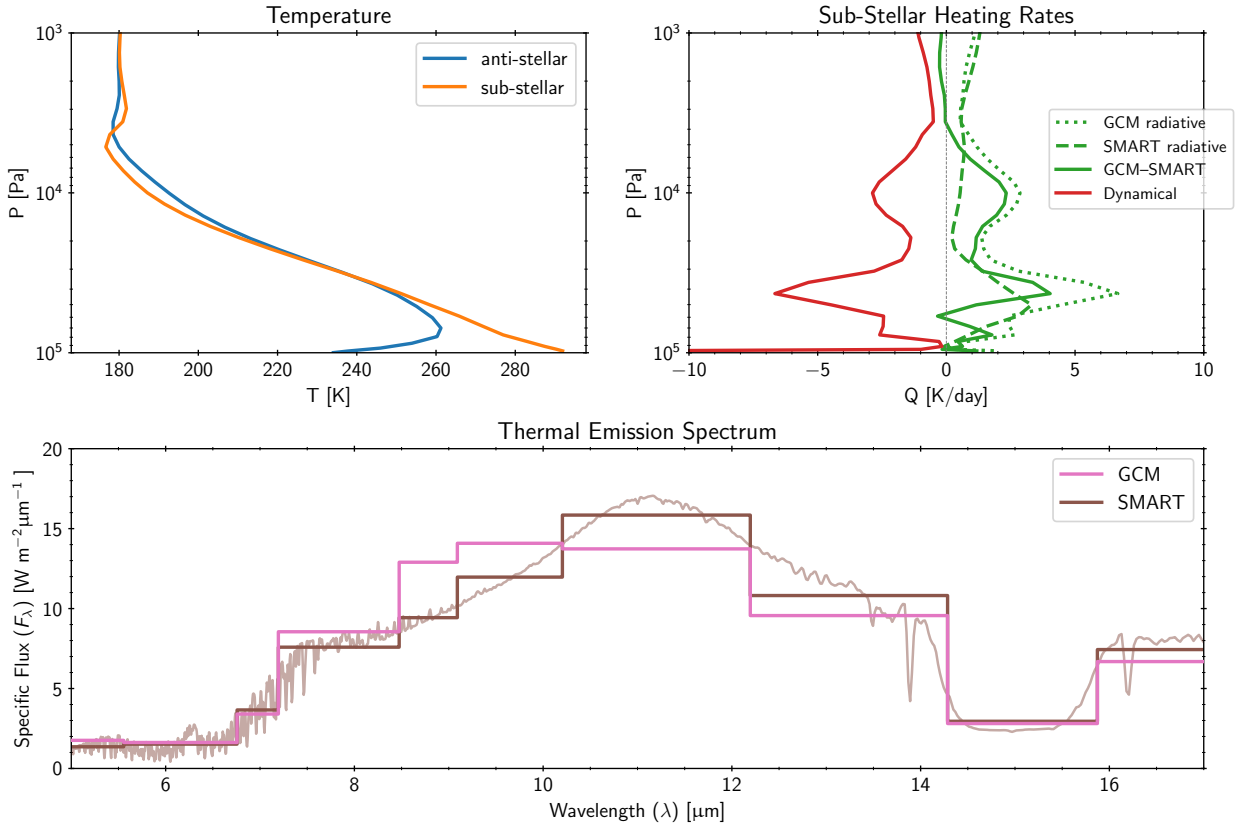

Figure 5.4: **THAI HAB1 GCM HEATING RATES AND EMITTED FLUX FOR THE SUB-STELLAR POINT COMPARED WITH SMART.** *Upper left panel*: the GCM temperate profiles for the sub-stellar and anti-stellar points used as inputs to SMART. *Upper right panel:* compares the heating rates between the GCM and SMART for the sub-stellar profile. The GCM is different from SMART by a factor of 2–5. *Lower panel*: Thermal emission spectra, with SMART spectra presented in both 1 cm^1 resolution (light brown) and binned to the GCM bins (dark brown). The gas absorption bands match well, but the spectral windows (8–14 μm) vary considerably, likely due to different optical properties used between these models.

and CO_2 at 15 μm, with some variation in the window region between 8–14 μm, and at solar wavelengths, which is likely due differences in the cloud parameterization. SMART uses high-fidelity multi-stream, multi-scattering radiative transfer, which is important for accurately modeling the heating rates and fluxes within scattering aerosols (e.g. Kitzmann et al., 2013), but because SMART and VPL Climate do not have explicit aerosol formation subroutines, these models use fixed input data for aerosol properties (i.e. size distribution and intrinsic optical properties). The optical

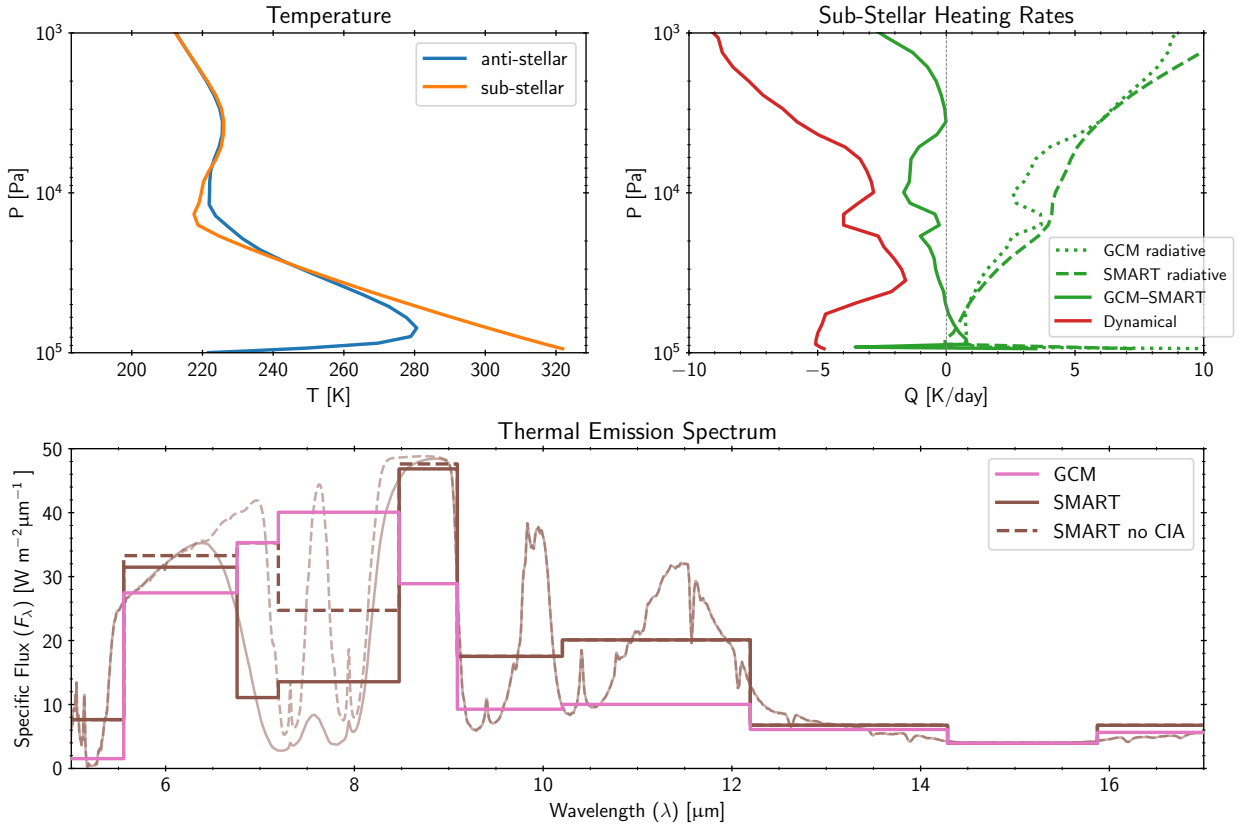

Figure 5.5: **THAI BEN2 HEATING RATES AND EMITTED THERMAL FLUX FOR THE SUB-STELLAR POINT FOR THE GCM COMPARED WITH SMART.** The panels in this figure are the same Figure 5.4, except this case is testing the radiative transfer for CO_2. Here, the error in radiative heating rates by the GCM reaches 38% at 0.1 bar and is approximately 64% of the dynamical heating rate at that layer. This difference could affect the structure of the atmosphere or the dynamical forcing. *Lower panel*: Emitted flux spectra. The GCM *k* coefficients do not include CO_2 between 1100–1800 cm^{-1} (5.5–9.1 μm). The lack of these isotopologue absorption bands and associated CIA continuum reduces the greenhouse forcing and increases the radiative cooling in the GCM. These bands are not material in atmospheres with low CO_2 abundance, such as Earth, but here are demonstrated to be very important at higher CO_2 abundance.

inputs consist of a fixed optical depth input distribution derived from the average from the GCM, which does self-consistently calculate aerosol distributions. The GCM data is scaled such that the total optical depth matches the GCM for each type of aerosol (liquid water and water-ice) for the aerosol properties associated to each cloud type available for SMART (see §2.2.2). Although the GCM self-consistently determines the particle distribution and optical depths, these results can

vary considerably among different models (Yang et al., 2019c). The GCM also uses a more basic multi-scattering, two-stream radiative transfer solver (Toon et al., 1989), which may over-estimate peak heating rates compared to a multi-stream, multi-scattering treatment (Kitzmann et al., 2013).

THAI ben2 In the 1 bar CO_2 case (Figure 5.5), the higher CO_2 abundance illustrates stark differences between SMART and the GCM. The error in radiative heating rates by the GCM reaches 38% at 0.1 bar and is approximately 64% of the dynamical heating rate at that layer. This difference could affect the thermal structure of the atmosphere. Finding differences in radiative CO_2 treatment is the purpose of this THAI case (Fauchez et al., 2020). Here, the differences in GCM and SMART outcomes is due to both a different CO_2 CIA parameterization and the method employed in producing the k coefficients. The GCM is missing CO_2 absorption bands in the 1100–1800 cm^{-1} range, which become important at higher abundances but were excluded from the k coefficients (Wolf and Toon, 2013). The weaker MT_CKD CO_2-CO_2 CIA parameterization (Halevy et al., 2009) may play a role as well (see also §5.4.2). Differences in radiative transfer are not limited to CO_2: another key gas, water vapor, has been evaluated in previous intercomparison tests, where it was found that the differences in radiative forcing due to different H_2O absorption affected the atmospheres by altering the height of the convective column, the stratospheric humidity, and the altitudes of cloud formation (Yang et al., 2016, 2019c).

5.3.2.2 Ocean Heat Transport

The THAI comparison did not include ocean heat transport, which is frequently excluded from GCM studies. However, the ocean and the atmosphere of Earth transport roughly equal amounts of energy away from tropical latitudes (Hastenrath, 1980; Carissimo et al., 1985; Savijärvi, 1988; Trenberth and Caron, 2001; Wunsch, 2005). Several 3D modeling studies have explicitly considered this physics and note significant changes in global temperature distribution and a reduction in day–night temperature contrast (Yang et al., 2013; Cullum et al., 2014; Hu and Yang, 2014; Yang et al., 2014, 2019c; Way et al., 2017; Del Genio et al., 2019).

Here I briefly probe the effect of day–night ocean heat transport in the two-column model,

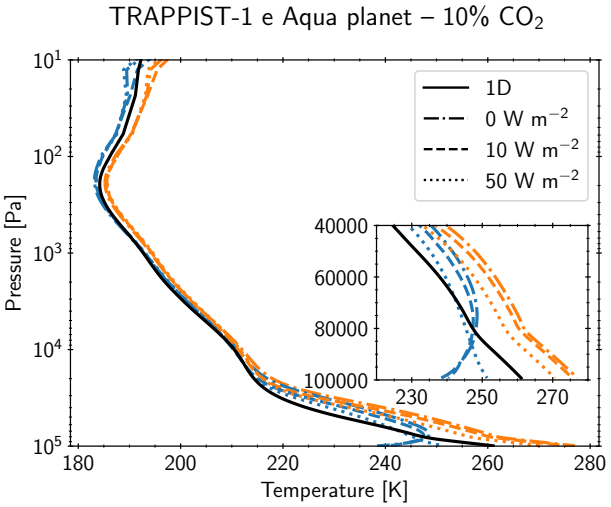

Figure 5.6: **TEMPERATURE PROFILES FOR TRAPPIST-1 E AQUA PLANET WITH A RANGE OF SURFACE HEAT TRANSPORT FLUXES.** The black solid line is the 1D model result, the orange lines represent the day side results, and the blue lines represent the night side results. Day–night surface (ocean) heat transport is represented by different line styles: dash-dotted lines are for none (i.e. only atmospheric heat transport), the dashed lines represent 10 W m^{-2} ocean heat transport, and the dotted lines represent 50 W m^{-2} ocean heat transport. As expected, increasing amounts of surface heat flux reduce the day–night temperature difference. The 1D model is generally consistent with the two-column temperature profiles, though a little cooler in the troposphere.

which causes the average of the day and night profiles to converge on the 1D results as transport increases. This effect is included as a single parameter, the day–night heat transport in terms of energy delivered per unit surface area (W m^{-2}). This parameter is agnostic as to what specific mechanism is carrying heat between the day and night sides. Although "ocean heat transport" is typically assumed to be a dynamic liquid water ocean, where ocean currents advect and carry heat, this parameter can also represent glacier transport from the night side to day side, which carries increased latent heat (c.f. Turbet et al., 2018; Yang et al., 2019b). Using the THAI hab1 case and the photochemically-consistent aqua planet, I ran the two-column climate model with two different specifications for ocean heat fluxes, 10 W m^{-2} and 50 W m^{-2}, which correspond to the extent of ocean heat transport studied by Yang and Abbot (2014). In both cases, the lower flux (10 W m^{-2}) only mildly affected the day–night contrast (reducing the day–night temperature by $\sim$5 K), while 50 W m^{-2} significantly affected day and night-side temperatures (reducing the day–night temperature by $\sim$25 K; see Figure 5.6 and Table 5.3).

Planetary state	Surface Temperatures [K]						Adv Flux [W m^{-2}]
	1D	Day	Night	Day–Night	Average	Flux Avg	
THAI ben1, e	239	269	185	83	227	238	70
THAI ben2, e	265	292	220	71	256	263	138
THAI hab1, e	243	272	211	61	242	247	104
THAI hab1, e, $F_{\rm ocn} = 10$	243	269	212	57	241	246	102
THAI hab1, e, $F_{\rm ocn} = 50$	243	262	225	38	243	246	113
Aqua planet, e	262	278	236	42	257	260	145
Aqua planet, e, $F_{\rm ocn} = 10$	262	277	239	38	258	260	146
Aqua planet, e, $F_{\rm ocn} = 50$	262	271	252	20	262	262	150
Modern Earth-like, e	262	276	244	33	260	262	169
Abiotic O_2 (dry), b	445	490	358	131	424	438	871
Abiotic O_2 (moist), d	302	308	299	9	304	304	264
Abiotic O_2 (moist), e	283	293	282	11	288	288	201
H_2-rich, e			— runaway —				
H_2-rich, g	204	205	200	5	203	203	75
Venus-like, b	704	714	633	81	673	677	1195

Table 5.3: Summary of Climate Results

5.3.3 Atmospheric Models Beyond Earth-like

Here I compare the results obtained for the 1D and two-column coupled climate-photochemical models. Temperatures, day–night contrasts, and advective fluxes are listed in Table 5.3. Generally, the 1D model produces higher temperatures than the average of the two-column model. The moist 10 bar O_2 atmospheres are a counterexample, with 1D temperatures lower than the two-column averages, though the 1D model atmospheres are within the range of the day and night columns. In general, the average top-of-atmosphere thermal flux from the average of the day and night columns in the two-column model are within 2% (0–4 W m^{-2}) of those from the 1D model, because the flux from both models must balance the same global average stellar input.

Advective fluxes are much higher for highly irradiated planets, despite large day–night surface temperature contrasts. The 10 bar O_2 aqua planets demonstrate that water vapor is a strong equalizer in day–night advection, due to the latent heat that can be carried from the day side to the night side. The day–night contrasts from these planets were less than 10 K. This may also be due to atmospheric opacity, as only 11–12% of the incident solar radiation (which is predominantly in the NIR) reaches the surface, therefore the bulk of solar radiation is absorbed by the atmosphere and

can be advected to the night side.

Figure 5.7 shows the 1D, day, and night temperature profiles for all stable modeled environments (including the THAI cases). As described for the THAI cases in the previous subsection, all atmospheres have similar day, night, and 1D temperature profiles above the mid-troposphere (roughly 0.5 bar). In the lower troposphere, the day and night temperatures diverge toward the surface because convective heating via vertical transport dominates over advective heating via horizontal winds, whose speeds are limited by turbulent friction with the surface. As might be expected, the 1D results generally lie between the day and night profiles, although in the THAI cases (but not the photochemically-consistent cases) there is a slight difference in the upper troposphere as well.

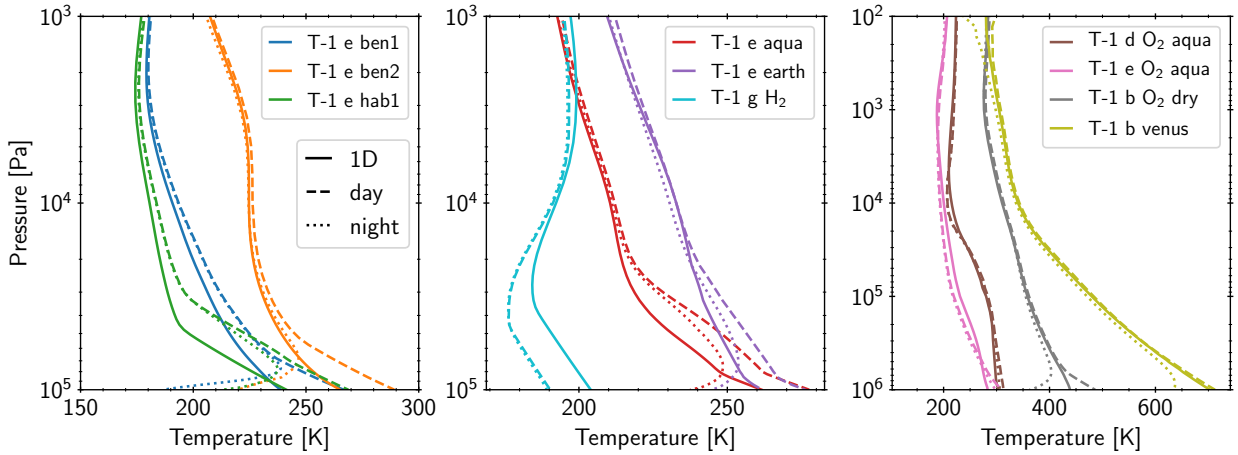

Figure 5.7: 1D (solid lines), day (dashed lines), and night (dotted lines) temperature structures for all nominal modeled atmospheres. The globally-averaged 1D models are generally cooler in the troposphere. The two-column models exhibit temperature profiles that are nearly the same on the day and night sides until the lower troposphere, where vertical transport dominates over radiative-advective processes.

The following paragraphs detail climate-photochemical results for atmospheres beyond the simple THAI test cases. Model atmospheres with previously published 1D results that are not discussed here, but that I modeled and tabulated with two-column results, include the dry, evolved O_2- and CO_2-dominated atmospheres adopted from Ch. 3 (Lincowski et al., 2018) for TRAPPIST-

1 b.

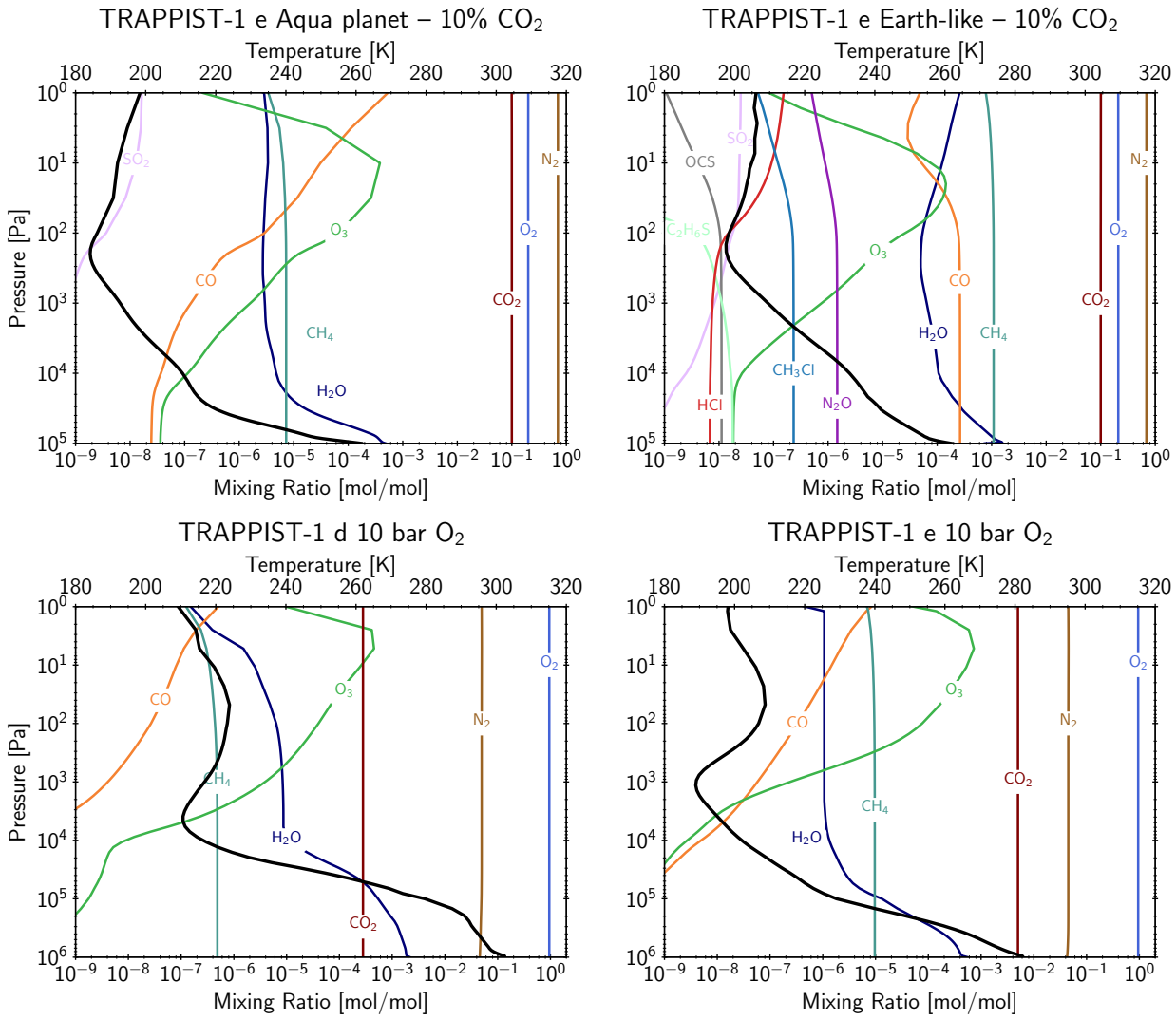

Figure 5.8: **PROFILES OF TEMPERATURES AND KEY GASES FOR POTENTIALLY HABITABLE, PHOTOCHEMICALLY-CONSISTENT SIMULATED ENVIRONMENTS.** The temperature profile for each case is a thick black line. The TRAPPIST-1 e aqua planet and Earth-like planet both have 10% CO_2. The 10 bar O_2 TRAPPIST-1 e planet has 0.5%, while TRAPPIST-1 d here is modeled with 280 ppm. The three completely ocean-covered planets have only geological outgassing fluxes, while the Earth-like case additionally has biogenic fluxes. This strongly influences the CH_4 abundance. The 10 bar O_2 atmospheres generate sufficiently high ozone to form mild stratospheres.

Ocean-Dominated Planets Figure 5.8 shows temperatures and photochemically-consistent gas mixing ratio profiles for a variety of potentially habitable environments. The modern Earth-like planet is based on Meadows et al. (2020), and has a higher CH_4 abundance because it includes both biological and geological fluxes of CH_4. The photochemically-consistent aqua planet included only geological fluxes, which the THAI planets did not include CH_4.

The photochemical results presented here are largely consistent with previous studies. Methane accumulates more readily under these stellar irradiation conditions, due to a much slower destruction timescale. Methane also increases the upper troposphere and stratosphere temperatures, due to strong NIR absorption under the very red TRAPPIST-1 star. This allows a much higher stratospheric water abundance in the Earth-like planet compared to the Aqua and O_2-dominated planets, which have only geological methane fluxes.

TRAPPIST-1 d and the IHZ Included in the aqua planets is a stable, potentially-habitable environment for TRAPPIST-1 d, which at 1.05 $S_\oplus$ lies about 15% inward of the conservative inner edge of the habitable zone (Kopparapu et al., 2013). In modeling attempts with Earth-like 1 bar atmospheres, I found that TRAPPIST-1 d was generally just over the runaway greenhouse threshold, because the stellar irradiation was just slightly too high. It is possible that thicker cloud cover could maintain a habitable environment, but I did not model this. However, the 10 bar O_2 atmosphere modeled here could result from significant water loss early during the pre-main-sequence phase, but if the water fraction of the planet is high, as is suggested by the results of Grimm et al. (2018), a deep water reservoir could persist. In this case, TRAPPIST-1 d could maintain a stable warm surface ocean temperature of 307 K with Earth-like cloud cover. The deeper adiabat in this atmosphere results from latent heat release (i.e. moist convection) and spans two decades in pressure from the surface to the cold trap, which may be critical to its stability.

Evolved Environments The more evolved (post ocean/atmosphere loss), desiccated atmospheres for TRAPPIST-1 b, dominated by CO_2 or O_2 (see Figure 5.7), exhibit some different characteristics compared to ocean-bearing environments. They do exhibit qualitatively similar differences

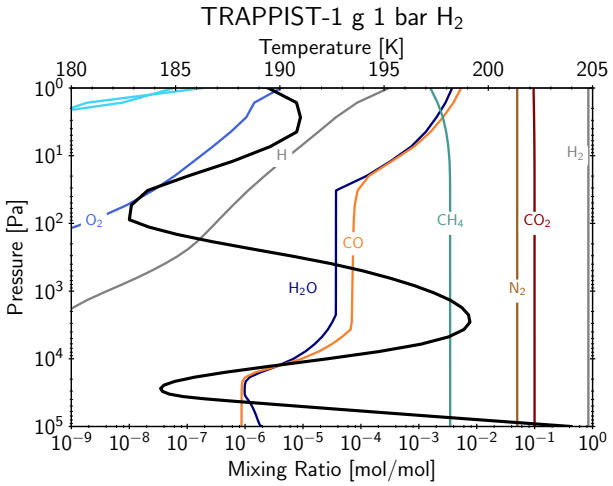

Figure 5.9: **PROFILES OF TEMPERATURE AND KEY GASES FOR THE TRAPPIST-1 G SUPER-EARTH PLANET WITH HYDROGEN-DOMINATED ATMOSPHERE.** The temperature profile is the thick black line. This planetary state assumes the planet was able to accrete some H_2 during formation (e.g. Luger et al., 2015). This planet has Earth-like geological outgassing but with higher levels of CH_4 outgassing, which is assumed to originate from a more reduced interior. CO_2 is specified as 10%. Water vapor increases with altitude likely due to photochemical/catalytic production from CO_2 and CH_4 or H_2.

in the day–night temperature contrasts, which diverge in the lower troposphere toward the surface. However, the differences between hot and temperate environments are significant. Both TRAPPIST-1 b environments transport large amounts of energy from the day to night sides, 5–12 times more energy than the temperate planets, and both still exhibit large (81–131 K) day-night surface temperature contrasts.

5.3.3.1 H_2-dominated Atmospheres

Here I modeled a hydrogen-dominated atmosphere for TRAPPIST-1 g, because a thin hydrogen envelope has not been excluded yet by the available data for this planet (Moran et al., 2018). The temperature profile and gas mixing ratios for this atmosphere are shown in Figure 5.9. Due to its distance from the star and the atmospheric composition assumed here, this planet is much colder and not habitable, in the traditional sense (i.e. it is too cold for liquid surface water). NIR absorption from the large methane abundance produces the most extreme stratosphere of the planets modeled here, with a 35 K increase from tropopause to stratopause. Water vapor increases with altitude due to destruction of H_2, CH_4, and CO_2, followed by generation of H_2O by short-lived intermediate products, just as in the stratosphere of Earth. Condensation limits the stratospheric and mesospheric abundance of H_2O, which here is restricted to 100% humidity. However, it is

possible for water vapor to exist in a super-saturated state without condensing.

Because NH_3 has a warmer condensation temperature than CH_4, this type of planet may have formed with abundant NH_3. While this means this planet could potentially outgas NH_3, the photochemical model used here does not have a functioning, validated NH_x chemical network. Ammonia (NH_3) is expected to be rapidly oxidized to N_2 via photochemistry, shock chemistry from impactors, or in hydrothermal systems, as in the atmosphere of Titan (Atreya et al., 1978; Jones and Lewis, 1987; McKay et al., 1988; Glein et al., 2009; Mandt et al., 2014). Therefore, unless there was or is currently a large source, neglecting NH_3 and its associated chemistry in this work is by not including N_2 as the primary constituent, and the result on the atmospheric structure is primarily to decrease the scale height of the atmosphere, due to the molecular weight of N_2 compared to H_2.

5.3.4 Planetary Spectra and Detectability

To predict spectral discriminants for planning and interpreting upcoming observations of the TRAPPIST-1 system and potentially others with *JWST*, I present a selection of transit transmission and phase amplitude variation spectra for the modeled environments. Transit spectra have been shown to be useful for observing a wide range of terrestrial environments for TRAPPIST-1 with *JWST* (Lustig-Yaeger et al., 2019a). Phase amplitude variation spectra, which characterize the wavelength-dependent difference in emergent flux from the fully-illuminated day side vs thermal emission from the night side (Selsis et al., 2011), may be useful for hotter planets, such as TRAPPIST-1 b.

5.3.4.1 Transit Transmission Spectra

Here I present a selection of transit spectra for the newly modeled environments, primarily using the 1D results, because the day–night contrast has little effect on this type of spectra. The Earth-like atmospheres are discussed in detail in Meadows et al. (2020), and the dry, evolved environments for TRAPPIST-1 b are presented in §3 (Lincowski et al., 2018).

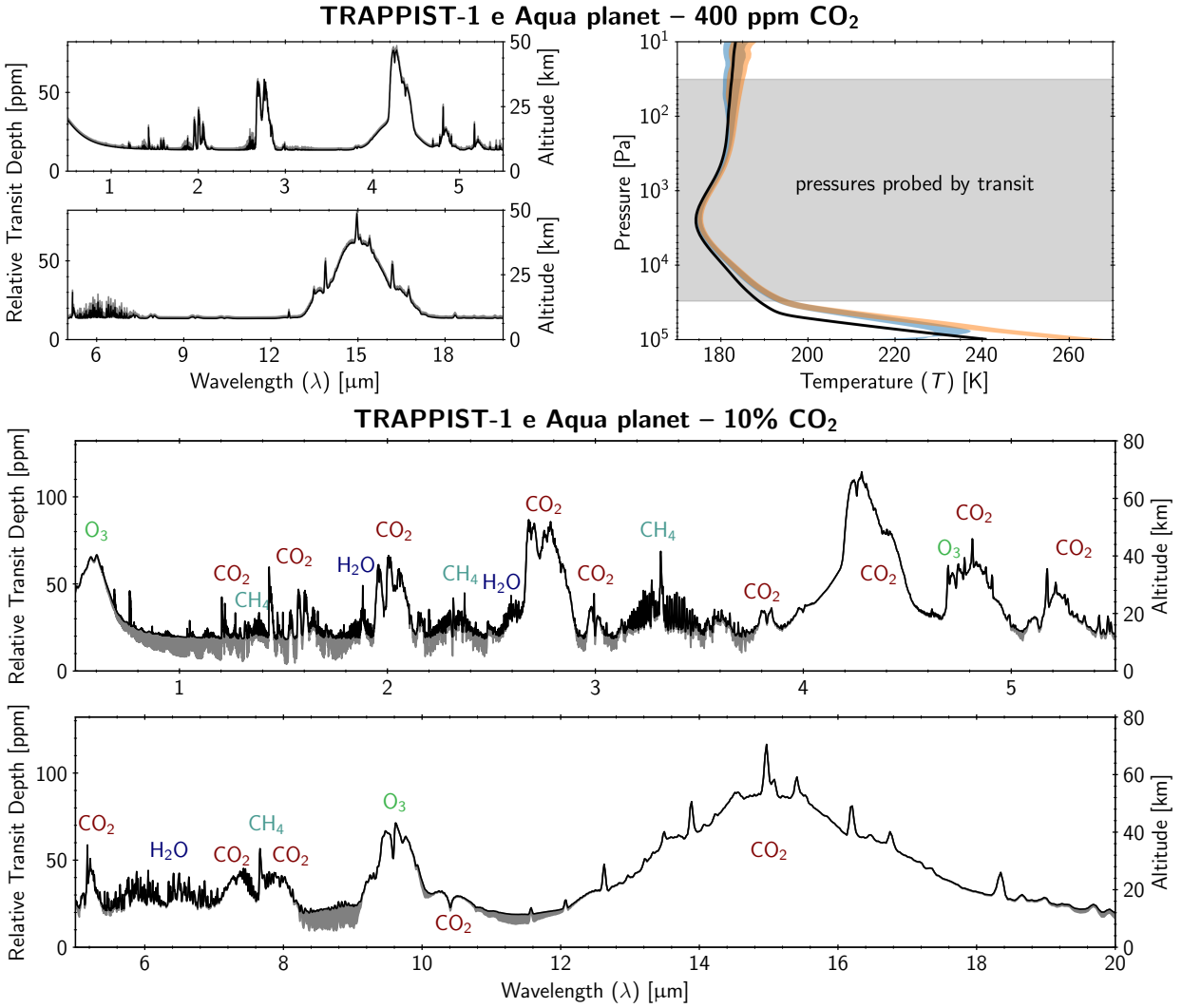

Figure 5.10: Transit transmission spectra (*top left*) and pressure-temperature profiles (*top right*) for the THAI hab1 case, and transit transmission spectra for a photochemically-consistent aqua planet (*bottom*). For THAI hab1, the differences between spectra for the day and night sides and for cases with ocean heat transport between 0–50 W m^{-2} are so small, that they are plotted as a range in grey, with the 1D profile plotted in black. The pressures probed by gas absorption from continuum to peak in transit are shown as a grey shaded band on the temperature-pressure plot, with the ranges for day- and night-side temperatures in orange and blue, respectively, and with the 1D profile plotted as the black line. In the bottom plot, the photochemically-consistent aqua planet shows the cloudy spectrum with the black line, and the difference between the cloudy and clear-sky spectrum filled in with grey. Clouds are uncertain, but their effects on transit are likely to act as a surface in retrievals of future observations.

The Role of Photochemistry, Clouds, and Day–Night Temperatures on Planetary Spectra While large day–night surface temperature contrasts have been demonstrated by decades of climate studies utilizing GCMs, it has yet to be demonstrated that temperature contrasts of the surface and lower troposphere materially affect transit transmission spectra, which will be the most effective spectral observation method for temperate planets with *JWST* (Lustig-Yaeger et al., 2019a). To assess the effects on transit spectra by day–night temperature and water vapor differences, I simulated transit spectra for the THAI hab1 and photochemically-consistent aqua planet, for the 1D atmosphere and for the day and night profiles for the nominal, 10 W, and 50 W atmospheres, which are shown in Figure 5.10.

Photochemical and bio/geological species are a critical component of transmission spectra (§3, Lincowski et al. 2018), particularly because transit transmission observations probe regions of the atmosphere in which outgassed species and their photochemical and catalytic byproducts may be abundant. Chemical kinetics and photochemistry are somewhat influenced by temperature, but the effect of temperature on the gross detectability of these gases is less important. In temperate atmospheres, potentially detectable gases include CH_4 and O_3, which are photochemically-mediated biomarker gases (Krissansen-Totton et al., 2016; Meadows et al., 2018; Schwieterman et al., 2018). Without these gases, key

Besides the inclusion of photochemically-consistent and/or outgassed species, the largest differences in transmission spectra result from the differences in altitude where clouds form, which are affected by vertical transport and the temperature structure. Although typical water clouds on Earth form in the lower troposphere, where temperatures diverge between the day and night sides, higher altitude water-ice clouds form in the upper troposphere, where the day- and night-side temperatures are similar. Although these clouds tend to have low optical depths (modeled here as $\tau \sim 0.05$), due to the tangent path of transmission spectra, even optically thin clouds or hazes can make the atmosphere opaque in transmission. The baseline or continuum of a transit spectrum is critically related to the highest altitude at which clouds form (§3, Lincowski et al. 2018).

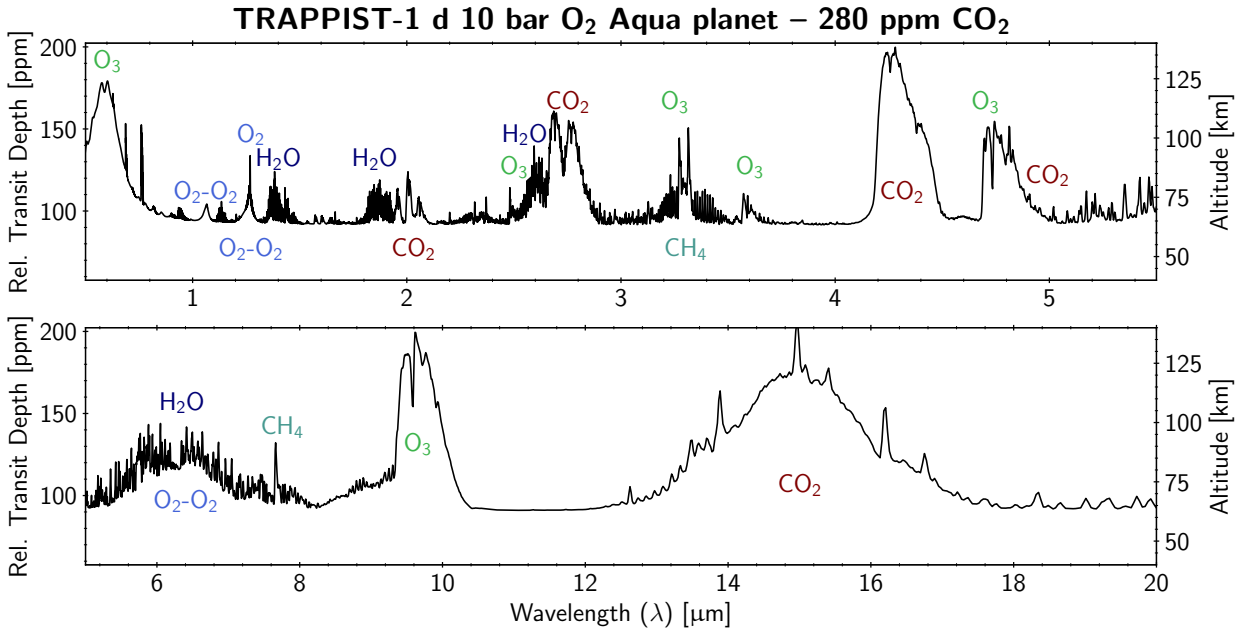

Figure 5.11: Transit transmission spectra for TRAPPIST-1 d O_2-dominated aqua planet. This spectrum displays the classic CO_2 bands at 4.3 and 15 μm. The other strong bands are due to ozone at 0.6, 4.7, and 9.6 μm. Ozone is strong enough here to produce weak bands as well. The 3.3 μm O_3 band overlaps with CH_4. Other methane bands could identify its presence with higher abundances. O_2-O_2 bands indicate a high O_2 atmosphere.

O_2-dominated Atmospheres Transit spectra for the ocean-bearing, O_2-dominated atmosphere for TRAPPIST-1 d are shown in Figure 5.11. This environment has 10 bar of O_2, 280 ppm CO_2 and geological outgassing of CH_4, H_2S, SO_2, and OCS. TRAPPIST-1 e (with 10% CO_2) displays similar features but with amplitudes smaller in general due to the larger gravity and lower temperatures, with some variation due to trace gas abundance differences between the two cases. Both cases include liquid water (stratocumulus) and water-ice (cirrus) clouds, placed at the altitude of 281 K and 227 K, respectively, which are the average temperatures for the cloud tops on Earth (Kitzmann et al., 2010). Despite the cloud decks, O_2-O_2 collision-induced absorption is present at 1.06, 1.27, and 6.4 μm. The NIR bands are small, but at a strength of 10–20 ppm, may collectively be within reach of detection because they are in the highest-signal region of the TRAPPIST-1 SED, which peaks around 1 μm. The CIA band at 6.4 μm overlaps with the 6.3 μm water band, and both

are present in roughly equal strength.

Although the CO_2 abundances for the modeled atmospheres for TRAPPIST-1 d and e O_2-dominated planets vary considerably (only 280 ppm vs 10%), in both atmospheres CO_2 exhibits two of the four strongest features (the other two bands are ozone). Both atmospheres exhibit the classic strong bands at 4.3 and 15 μm, at 100 ppm for TRAPPIST-1 d and 50 ppm for e—but this difference is due to atmospheric scale height, not abundance. TRAPPIST-1 e indicates its higher CO_2 abundance with stronger relative CO_2 absorption features at shorter NIR wavelengths. Whether the weak CO_2 bands are detectable, and how strong they are in relation to the 4.3 μm band, can be used to constrain the CO_2 abundance (see e.g. §3; Lincowski et al. 2018).

The other strong bands in this atmosphere are due to ozone at 0.6, 4.7, and 9.6 μm. Due to its high abundance, O_3 also exhibits absorption at 2.5, 3.3, and 3.6 μm. In particular, the 3.3 μm band may confuse retrieval of the 3.3 μm CH_4 band for observations at low signal-to-noise and/or low resolution. At higher abundance, weaker bands of CH_4 become more prominent at 2.35 and 7.8 μm, as well as several bands in the NIR (see Meadows et al., 2020).

H_2-dominated Atmosphere Due to the high abundance of methane that may exist in the atmosphere of an Earth-like planet around an M dwarf star, an Earth-like planet may resemble a small hydrogen-dominated planet, which due to its more reducing nature, may have a high abundance of CH_4, and may contain some CO_2 as well, with the balance of these gases depending on the redox state of the planetary interior. Both oxygen and ozone may be difficult to detect in transit spectra of an Earth-like atmosphere (Lustig-Yaeger et al., 2019a; Meadows et al., 2020), so in fact the strong features of CH_4 present in the H_2-dominated atmosphere modeled here resemble the composition of an Earth-like atmosphere around an M dwarf star, and depending on the atmospheric scale height, it may be difficult to distinguish between these cases bases on detectable species.

The primary difference between this H_2-dominated atmosphere and other terrestrial atmospheres is the much larger scale height and depth of absorption features exhibited by this atmosphere, due to its low H_2-dominated molecular weight. The amplitudes of features in this atmosphere approach 500 ppm for CO_2, though the abundance chosen here (10% mol/mol) is very high

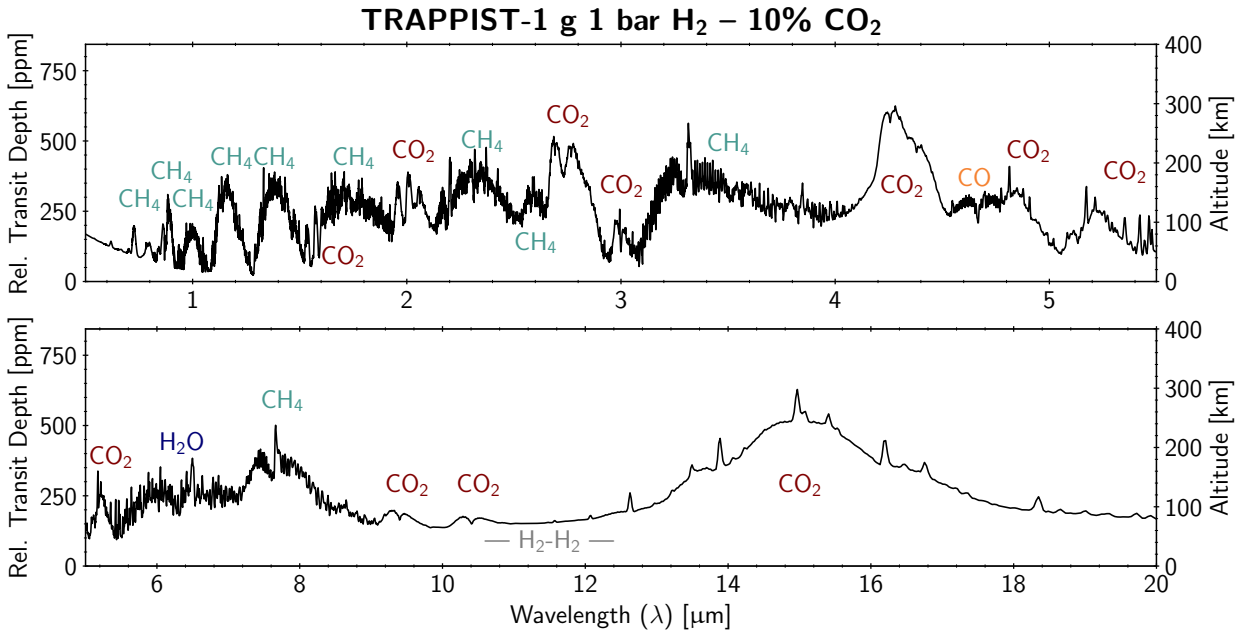

Figure 5.12: Transit transmission spectrum for a putative H_2-dominated TRAPPIST-1 g atmosphere. The strong bands for CO_2 and CH_4 are among the most prominent features. Water vapor is largely masked by CH_4, except at 6.3 μm. Collision-induced absorption due to H_2-H_2 is present but not likely detectable, due to its broad continuum (8–12 μm).

compared to what may be expected for a hydrogen-dominated atmosphere. Regardless of the CO_2 abundance, this reducing atmosphere would be expected to support a large abundance of CH_4, which has absorption bands throughout the NIR, from 0.7–4 μm. Hydrogen CIA is included here and raises the continuum in the 8–12 μm range, though is not likely retrievable in MIR transit observations in this atmosphere because the continuum in an observed atmosphere could also be due to clouds, refraction, or the surface. Aerosols, including those found in hydrogen-dominated but not terrestrial atmospheres, could further reduce the amplitudes of the transit features.

5.3.4.2 Day–Night Phase Variation Spectra

Here I present a selection of phase amplitude variation spectra (Selsis et al., 2011), which can be produced directly from the VPL Climate two-column outputs of flux from the day and night sides of the modeled planets. These spectra are the difference in the day and night side fractions of flux emitted or reflected compared to the host star as observed from the telescope:

$$\frac{\Delta F_p}{F_s} = \frac{F_{\text{day}} - F_{\text{night}}}{F_s} \left(\frac{r_p}{a}\right)^2, \tag{5.1}$$

where ΔF_p is $F_{\text{day}} - F_{\text{night}}$, F is the day or night flux, or the stellar irradiation at the top of the planetary atmosphere (F_s), r_p is the planetary radius, and a is the semi-major axis.

Aqua Planet with Ocean Heat Transport Here I use the photochemically-consistent temperate TRAPPIST-1 e aqua planet to demonstrate the differences that arise in phase amplitude variation spectra due to a reduction in day–night contrast by ocean heat transport, from 0–50 W m^{-2}. Figure 5.13 shows these variation spectra, along with points convolved with the *Spitzer* IRAC and *JWST* MIRI filters. Because ocean heat transport reduces the day–night contrast, the variation spectrum is reduced in amplitude. The greatest reduction is in the bands that probe deepest in the atmosphere, which for the aqua planet occurs at 11.3 μm, with a 50% reduction, from 18 to 9 ppm. Bands that probe higher in the atmosphere due to strong gas absorption (e.g. CO_2 at 4.2 and 15 μm) are unaffected, due to the weak day–night temperature gradient in the free atmosphere. Note that

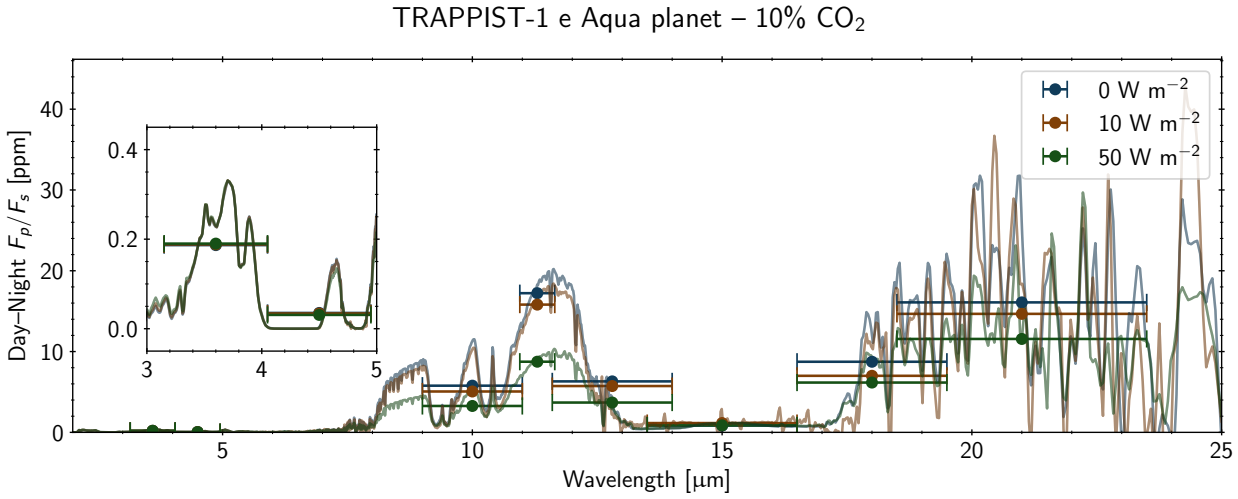

Figure 5.13: **DAY–NIGHT FLUX AMPLITUDE VARIATION SPECTRA FOR TRAPPIST-1 E AQUA PLANETS WITH 0–50 W M^{-2} OCEAN HEAT TRANSPORT.** Full-resolution spectra are plotted with convolved points convolved with the *Spitzer* IRAC and *JWST* MIRI filters. Ocean heat transport of 50 W m^{-2} reduces the day–night contrast by up to 50%, most strongly in the 11.3 μm *JWST* band that probes closest to surface emission. Whether with or without ocean heat transport, temperate planets are likely to be too cool on both sides of the planet to yield useful day–night variation spectra.

phase amplitude variations are small for temperate planets in general, due to cool temperatures that produce insufficient flux for sensitivity with *JWST*. The maximum phase amplitude variation is between the 11.3 μm and 15 μm bands, probing the near-surface environment and stratosphere.

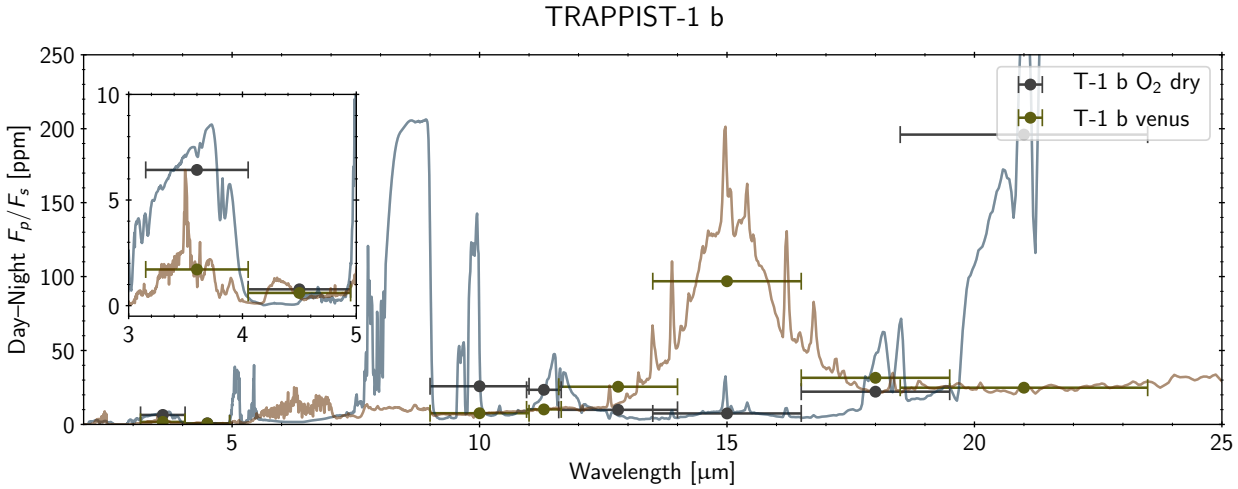

Figure 5.14: Venus-like and desiccated O_2-dominated TRAPPIST-1 b phase amplitude variation spectra convolved with *Spitzer* IRAC and *JWST* MIRI filters. Although these hot atmospheres produce significant flux in the 3.6 μm *Spitzer* IRAC band and almost no flux in the 4.5 μm band (due to CO_2 absorption), neither band provides significant differences in phase curve amplitude, making these bands poor choices to detect atmospheric features. The 15 μm is a good choice for the clear-sky Venus-like atmosphere due to its 100 ppm (convolved) day–night contrast, but a poor choice for the O_2-dominated atmosphere. Due to the complete lack of water vapor and extreme day–night surface temperature contrast, the O_2 atmosphere produces the largest amplitude signal here at 21 μm (over 200 ppm). Unlike the temperate aqua planets, the 11.3 μm filter is not a high-amplitude spectral band. Note that thermal noise in the *JWST* hardware increases with increasing wavelength.

Hot Atmospheres The two post-ocean-loss, TRAPPIST-1 b atmospheres dominated by CO_2 or O_2 presented here from §3 (Lincowski et al., 2018) may represent plausible atmospheres and this planet may be the best hope for *JWST* observations in the MIR in the TRAPPIST-1 system. Both environments have uninhabitable surface temperatures (445–704 K), much higher than any allowed for type of known habitable conditions. They produce very different phase amplitude variation spectra (Figure 5.14). The Venus-like atmosphere produces a significant day–night contrast in

the mesosphere, likely due to rapid cooling by CO_2 on the night side, allowing the strong 15 μm CO_2 absorption band to exhibit large contrast. The completely desiccated O_2-dominated planet permits a large phase amplitude in the 21 μm *JWST* MIRI band, because without water vapor, the atmosphere is transparent nearly to the surface, where the temperature contrast is largest.

5.4 Discussion

I have developed a two-column mode for a versatile climate model, coupled to a photochemical model, which has been used to generate environmental states for a selection of the TRAPPIST-1 planets (b, d, e, and g), which take into account the pre-main-sequence stellar evolution and observational constraints (or lack thereof) for bulk atmospheric composition. These states span hot (445–704 K), heavily-evolved states for TRAPPIST-1 b, to potentially habitable environments for TRAPPIST-1 d and e, to a cold (204 K), hydrogen-dominated atmosphere for TRAPPIST-1 g. With the exception of intercomparison cases, these atmospheres are climatically and photochemically consistent with the redder TRAPPIST-1 spectrum, including UV constraints. I have shown that a two-column model can qualitatively produce climate results consistent with GCM day–night behavior. While 1D models may slightly overestimate surface temperatures for planets with extreme day–night temperature contrasts, I find that day-night temperature contrasts do not strongly influence transit spectra, and transmission spectroscopy is likely the optimal method for observing temperate planets with *JWST* (Lustig-Yaeger et al., 2019a). However, photochemical processes and surface outgassing fluxes strongly influence transmission spectra, so the common coupling of photochemistry in 1D models is a crucial advantage for predicting observational discriminants in transmission spectra. Although 3D climate models currently have self-consistent cloud formation routines, clouds are highly variable and uncertain, and their impact to transmission spectra is to essentially create a pseudo-surface, below which the atmosphere cannot be probed.

Here, I discuss the modeling hierarchy and associated modeling caveats for producing accurate planetary environmental states, the potential for probing the inner edge of the habitable zone within TRAPPIST-1, and discuss how phase amplitude variation spectra can be considered for plausible TRAPPIST-1 b and other hot terrestrial environments.

5.4.1 A Hierarchy of Models

A variety of models are useful in predicting and interpreting exoplanetary climate and spectral observables. These models can include those used here, such as rigorous line-by-line 1D and two-column models, but can also include simpler 1D, two-column, and 2D models, including energy-balance models (EBMs). 3D GCMs are useful to demonstrate the myriad of interesting impacts of rotation rate, topography, land-sea temperature, and albedo contrasts, along with other small-scale processes that affect atmospheric circulation and to demonstrate the degree to which spatial inhomogeneities may impact global planetary climate and telescopic observables, such as phase curve amplitudes. However, 3D GCMs are not without their limitations, particularly in their simplified treatments of radiative transfer and chemistry, which could affect the dynamical responses. Intercomparisons of radiative transfer codes in 1D, two-column, and 3D models that have been conducted (e.g. Yang et al., 2016, 2019b) and that are currently in progress (Fauchez et al., 2020) are a step in the right direction to determine GCM radiative transfer limitations and find ways for improvement.

The limitations of 1D models are due primarily to the difficulty in accurately consolidating spatially-dependent processes into a single column. The use of a versatile, spectrum-resolving two-column model, as I have presented here, significantly ameliorates the lack of spatial coverage exhibited by 1D models, particularly for predicting day, night, and globally-averaged climate. Most of the differences in the THAI cases between the two-column model and the GCM appear to be a result of substantial differences in radiative transfer. Therefore, the results of the two-column model for THAI cases represent an intermodel comparison more than a validation. Nonetheless, the qualitative features of the hemispherically-averaged GCM data demonstrate the utility of this two-column model in simulated GCM day–night behavior.

Critically, this two-column model is coupled to a 1D photochemical model to provide the global chemical state, which can impact climate and spectral observables. While 3D GCMs already employ parameterized cloud formation models and can provide invaluable information about the spatial coverage of clouds, two-column and 1D models could be further improved by robust cloud

and aerosol formation methods, such as by incorporating the Community Aerosol and Radiation Model for Atmospheres (CARMA, Turco et al., 1979; Toon et al., 1988; Jacobson et al., 1994; Ackerman et al., 1995; Bardeen et al., 2008) or other simpler microphysical cloud models (Ackerman and Marley, 2001; Pavlov et al., 2001). Due to the difficulty in parameterizing cloud microphysics, cloud parameterizations remain a source of dispute and error among 3D models (Yang et al., 2019b).

5.4.2 The Importance of Updated and Complete Absorption Data

Two cases encountered while conducting the VPL-GCM comparison raised serious differences as a result of the source of absorption data, rather than the radiative transfer algorithms employed in the models. These differences were largely due to 1) the use of outdated or incomplete line lists, and 2) the use of a parameterized CIA opacity calibrated for Earth, rather than laboratory measurements for CO_2 CIA.

These differences in band and collision-induced absorption across the near to mid infrared yielded significant heating rate differences between SMART and ExoCAM. While the net flux was very similar (outgoing thermal flux must balance incoming solar flux), the distribution of emitted flux was vastly different. Due to its Earth heritage, ExoCAM was missing CO_2 line absorption between 1100–1800 cm^{-1}, which includes the 7–8 μm isotopologue bands. These weak bands produce negligible absorption in the atmosphere of Earth, but can be significant sources of opacity in the high CO_2 atmospheres considered here.

The collision-induced absorption methods for CO_2 differ considerably between SMART and ExoCAM. In SMART (and VPL Climate), I use both empirical and *ab initio* sources as described by Robinson and Crisp (2018) and in section 5.3.2.1, including temperature dependence when available. Continuum absorption is explicitly separated from line absorption (as typically reported). Line absorption calculations include self and foreign broadening, with experimentally-determined sub-lorentzian χ-correction factors (Perrin and Hartmann, 1989; Meadows and Crisp, 1996). I include line absorption for CO_2 to 1000 cm^{-1} from line centers. ExoCAM uses the MTCKD method for computing CO_2 CIA, which is a method designed for Earth-like CO_2 abundances and contains

all absorption beyond 25 cm^{-1} as part of the continuum, including extra absorption from 500–900 cm^{-1} (see Clough et al., 2005, for further information). This source of continuum absorption has not been included in the most recent HITRAN CIA release (Karman et al., 2019).

An intercomparison of CIA for CO_2 was conducted by Halevy et al. (2009). In that intercomparison, the so-called "CBKM" method (using earlier sources but using a similar method to what I have used here, and described in Segura et al. 2007) exhibited the strongest CIA in the Fermi isotopologue bands at 7–8 μm. Compared to "CBKM", I use updated absorption in these bands with measurements from Baranov et al. (2004), which extend to lower temperatures, consistent with temperate terrestrial atmospheres. Baranov et al. (2004) found that at lower temperatures, the CO_2–CO_2 CIA was several times stronger than at higher temperatures. In Halevy et al. (2009), these differences in absorption caused a difference of 20 W m^{-2} (13.5%) emitted flux in a pure, 1 bar CO_2 atmosphere, though that difference narrowed considerably when significant atmospheric water vapor was included. In this regard, the CO_2-CO_2 CIA treatment could be updated in band models without requiring a line-by-line treatment. The latest HITRAN CIA compilation includes these key Fermi bands, with temperature dependence (Karman et al., 2019). In the sensitivity tests with SMART, CIA reduced emitted flux by 17 W m^{-2} (5%). Although weak in atmospheres with only trace (Earth-like) abundances of CO_2, these bands may be critical in accurately simulating the radiative heating rates, influence on dynamical heating rates, and subsequent spectra for dense CO_2 atmospheres.

Differences in radiative heating rates calculated with the latest line lists and laboratory absorption data by accurate, spectrum-resolving models like SMART/VPL Climate compared to GCMs using older inputs could result in significant differences in atmospheric structure. These changes complicated efforts to determine whether this two-column model can capture the bulk day–night characteristics of 3D models. The discrepancy in radiative heating rates in the GCM would require a change in the temperature profiles or circulation (i.e. wind speeds) and associated dynamical heating rates, until the radiative and dynamical heating rates are in equilibrium. More detailed intercomparisons of current 3D models with 1D models like SMART (e.g. Yang et al., 2016) and with 3D spectrum-resolving models under development (e.g. Ding and Wordsworth, 2019) could

prove fruitful in quantifying the effects of such errors in radiative transfer parameterization. These issues demonstrate the need to maintain up-to-date absorption data in climate models and to assess whether parameterizations are being used outside the intended parameter space.

5.4.3 Detecting Hot Terrestrial Atmospheres

The existence of Venus in our Solar System suggests that hot, CO_2-dominated, post-runaway atmospheres are possible. In §3, I presented a variety of Venus-like and O_2-dominated, post-runaway environments. TRAPPIST-1 b was the only planet for which MIR photometry could detect gases for all modeled atmospheres, though NIR transit spectroscopy may be universally superior (Lustig-Yaeger et al., 2019a).

However, phase curves can provide additional information that might be useful, such as to map planetary temperature across the day to night sides. Pioneering observations of nearby hot, small exoplanets have been conducted in the last few years with the *Spitzer Space Telescope* 4.5 μm IRAC band. Demory et al. (2016) observed 55 Cancri e, a 1.9 $R_\oplus$, 8 $M_\oplus$ planet of rocky density receiving 19 $S_\oplus$ orbiting a K-M binary. The day–night temperature contrast was large (2700±270 vs. 1380±400 K) and included a substellar offset. It was proposed that this was due to an atmosphere of unknown composition, but CO_2 was excluded, because the large emergent flux occurred where CO_2 has strong absorption, precluding any significant CO_2 abundance. Similarly, Kreidberg et al. (2019) observed LHS 3844 b, a 1.3 $R_\oplus$ planet orbiting a late-type M dwarf. They found a large temperature difference for that planet as well, 1400 K vs 0–700 K. Along with a suite of GCM simulations to assess this, Kreidberg et al. (2019) argued that the planet may not have an atmosphere, especially one with CO_2.

Further evidence that the atmospheres of 55 Cancri e and LHS 3844 b do not have CO_2 is due to the high fluxes detected on the day-sides of these planets. The modeled flux and day–night contrast is nearly zero in the 4.5 μm *Spitzer* IRAC band (Figure 5.14), due to the very strong absorption by CO_2 at 4.2 μm. With any Earth-like or larger column depth of CO_2, any atmosphere is will be opaque and have very little flux in that band. Therefore, the detection of a large emission flux in the 4.5 μm band on the day side by Kreidberg et al. (2019) suggests that CO_2 is not present.

Furthermore, the 4.5 μm band may generally contain absorption from many other interesting atmospheric molecules, including CO, O_3, and N_2O. In any terrestrial atmosphere, this band is likely to be saturated, and thus low in flux. Therefore, the large fluxes observed by both Demory et al. (2016) and Kreidberg et al. (2019) suggest that neither 55 Cnc e nor LHS 3844 b have terrestrial or Venus-like atmospheres.

Observations of planets that may be terrestrial should not be made solely in bands with CO_2 or other significant absorber. Ideally, several spectral ranges should be observed, where based on possible atmospheric compositions at least one band would differ between the day and night sides. For the two hot atmospheres modeled here for TRAPPIST-1 b, combining observations in the 11.3, 15.0, and 21.0 μm bands with *JWST* or subsequent MIR observatory could discriminate between oxygen-dominated and Venus-like atmospheres.

5.4.4 The Inner Edge of the Habitable Zone

There are simplifications in the various studies used to model the inner edge of the habitable zone, so it is still an open question as to whether TRAPPIST-1 d could be habitable. Furthermore, the habitability of planets in general is not a binary function, it is better characterized as a probability distribution, based on the factors affecting habitability discussed in §1.3 (Barnes et al., 2015; Meadows and Barnes, 2018). For TRAPPIST-1 d in particular, because it lies inward of most generic inner edge calculations, it may be less likely, but not impossible, for it to host a habitable environment. Of the factors affecting habitability introduced in §1.3, the two that may be most relevant for TRAPPIST-1 d are volatile retention and cloud formation.

The impact of clouds on the surface climate has been particularly problematic in assessing the habitable zone. Most early habitable zone studies neglected clouds entirely and assumed a completely saturated troposphere (Kasting et al., 1993; Kopparapu et al., 2013), which is likely unrealistic (e.g. Kasting et al., 1993; Kopparapu et al., 2013; Leconte et al., 2013; Godolt et al., 2016), and may significantly over-estimate tropospheric and surface temperatures compared to an atmosphere that is not completely saturated (Kasting et al., 1984; Leconte et al., 2013; Godolt et al., 2016). GCMs have been used to assess the inner edge as well, but differences in planetary

rotation assumptions and cloud formation have caused discrepant results (Yang et al., 2013; Yang and Abbot, 2014; Kopparapu et al., 2016; Yang et al., 2019c). For tidally-locked planets, thicker sub-stellar clouds and the advection of heat from the sub-stellar point to the night side would increase the likelihood for planet-wide habitability. The globally-averaged optical depth of the cloud I used in this work represents a plausible partly-cloudy state, but no exoplanet climate model is likely to correctly predict the exact cloud fractions, distributions, or optical depths.

Here, TRAPPIST-1 d is assumed to be an O_2-dominated aqua planet, with Earth-like cloud optical depths and altitudes consistent with the formation of clouds on Earth, though clouds may form very differently. The lower gravity for TRAPPIST-1 d could support the formation of larger, heavier droplets, which can produce larger optical depths, especially at thermal wavelengths. Ocean heat transport, which is most effective on Earth at tropical latitudes (Hastenrath, 1980; Carissimo et al., 1985; Savijärvi, 1988; Trenberth and Caron, 2001; Wunsch, 2005), may reduce sub-stellar temperatures and help maintain sub-stellar clouds.

The potentially habitable aqua planet I have modeled for TRAPPIST-1 d, while hosting a high-oxygen atmosphere that is not conducive to complex surface life (Davies, 1995), may still be habitable for marine life. This may not be an Earth-like planet, but it represents a state that could be common around M dwarf stars. For planets that formed large, exchangeable inventories of volatiles, the millions of years of water vapor photolysis and hydrogen loss could allow accumulation of atmospheric oxygen over an oxygen-saturated ocean, the same way Earth biology supports sufficient O_2 production to maintain an oxygen inventory in the atmosphere of Earth. While ocean chemistry may stifle biogenic outgassing fluxes if such gases break down easily in water, there is evidence that biogenic gases such as methyl chloride (CH_3Cl) have sources in the ocean biosphere, so could be an important biosignature for a water world (see also Meadows et al., 2020).

5.4.5 Hydrogen-dominated Atmospheres

Although hydrogen-dominated atmospheres are unlikely for the TRAPPIST-1 planets, due to the extended superluminous pre-main-sequence phase of the TRAPPIST-1 primary (Luger and Barnes, 2015; Bolmont et al., 2017; Lincowski et al., 2018; Wordsworth et al., 2018), a hydrogen-dominated

atmosphere has not been ruled out for all of the TRAPPIST-1 planets, particularly g (Moran et al., 2018), which has also been singled out as a good target to characterize stellar variability, due to its larger size (Wakeford et al., 2019). Therefore, for comparison I modeled an environment for TRAPPIST-1 g with a 1 bar H_2-dominated atmosphere. Although climatically and photochemically self-consistent, the bulk gases and outgassing fluxes are not necessarily consistent with the volatile-rich, icy-terrestrial composition that this planet may have, because I specified a CO_2 abundance and CH_4 flux. This planet is also being modeled with a fixed N_2 abundance of 5% and without NH_3. Nitrogen chemistry could be a key factor in the evolution of this type of planetary atmosphere, but is excluded here because the photochemical model does not have an appropriate, validated chemical network for this, and an update for this network is beyond the scope of this work. Thus I assume that whatever NH_3 was or is present in this type of atmosphere is quickly converted to N_2 (Atreya et al., 1978; Jones and Lewis, 1987; McKay et al., 1988; Glein et al., 2009; Mandt et al., 2014). Additional N_2 would serve to reduce the scale height of this predominantly H_2 atmosphere, while less CO_2 would increase the scale height. It would be useful to have constraints on outgassing fluxes of these gases for this type of planet from geochemical modeling.

Although I include H_2-H_2 collision-induced absorption (CIA), these climate calculations exclude theoretical CIA due to CO_2-CH_4 and CO_2-H_2, both of which have been proposed as mechanisms to enhance the greenhouse effect (Wordsworth et al., 2017). However, laboratory studies have not confirmed the presence or magnitude of these collision pairs, and the line-by-line absorption coefficients model already includes foreign broadening of H_2 by these gases.

5.4.6 Spectral Observation of Terrestrial Planets Using Transit and Phase Amplitude Variation Spectra

In the next few years, the launch of *JWST* will permit observations of planets of the TRAPPIST-1 system, which hosts several potentially habitable planets. This telescope has a finite life and its time is valuable for a large domain of astronomy, from exoplanets to galaxies. It will not be possible to observe all transits of these planets with all instruments and modes. Therefore, atmospheric characterization of these planets requires careful selection of instrument modes and methods to

obtain the most useful data. It has been demonstrated that transit transmission spectra will be ideal in most cases for these planets, though the hotter inner planets may benefit from secondary eclipse (phase-dependent) photometric observations (Lustig-Yaeger et al., 2019a).

Versatile 1D models coupled to photochemistry are ideal for simulating atmospheric states to produce transit transmission spectra. Here, I have shown that large day–night temperature contrasts that can be simulated with 3D GCMs or two-column models do not materially affect transmission spectra. To affect transit spectra, differences between a terminator-averaged (or even day–night averaged) profile of temperature, gas mixing ratios, and aerosols, must induce a difference in spectral features that would affect a retrieval, at roughly the $\sim$10 ppm level or larger. The day–night atmospheres presented here, albeit with globally-averaged chemistry, reach at best a few ppm in the water absorption features. Studies using 3D GCMs have not shown that the planetary terminator differs enough from the global planetary state to affect to simulate or interpret transmission data upcoming with *JWST* (Fauchez et al., 2019). In fact, I have shown here the opposite: that even differences between the day and night sides are much smaller than the likely sensitivity of *JWST*. Therefore, with greater flexibility, versatile 1D coupled climate-photochemical models are ideal for predicting and interpreting upcoming transit transmission observations of terrestrial planets with *JWST*.

Furthermore, the day–night temperature contrasts produced in many 3D GCM studies are unlikely, because many of those studies neglected ocean heat transport, which can serve to reduce the temperature gradient between the hemispheres. At its most efficient, ocean heat transport can yield globally-averaged surface temperatures consistent with 1D model results. Conversely, 1D models overestimate surface temperatures for planets without ocean heat transport, which could include dry planets or some with pathological continental distributions. However, differences in stratospheric temperatures between 1D and 3D models are likely due to gas abundances and radiative transfer, rather than atmospheric dynamics, because very small wind speeds are required above the lower troposphere to reduce temperature gradients across the planet. These differences can be greater when including photochemistry, which can heavily modify the thermal profile of the stratosphere. Coincidentally, these are the altitudes to which transmission spectra are most

sensitive.

JWST can observe the day–night variations in thermal phase curves of hotter planets (Lustig-Yaeger et al., 2019a). This approach favors observations of planets with a large day–night contrast, which I have shown can be successfully simulated using a two-column model. Studies using GCMs would suggest that 3D models are required for interpreting phase curves. This is true to the extent that well-resolved (high signal-to-noise) phase curves can be used to retrieve constraints on the atmospheric circulation (e.g. Knutson et al., 2009), such as by the degree of shift of the substellar point due to advection. However, phase amplitude variation spectra can be used to identify atmospheric gas absorption and infer day- and night-side temperatures. The two-column model presented here is ideally suited to such assessments, given its flexibility in atmospheric composition and inclusion of global photochemistry.

5.5 Conclusions

In this chapter, I have integrated a versatile, 1D spectrum-resolving climate model, coupled with a 1D photochemical model, into a two-column model to study equilibrium climates on tidally-locked planets around M dwarfs. These methods were first validated against an existing 3D GCM to assess model performance. I then used these models to assess the impact of day–night temperature contrasts on transit and day–night phase-dependent spectra that could be observed with *JWST*. I have demonstrated that this two-column model qualitatively emulates GCM day–night behavior. Though the two-column model produces a slightly larger magnitude of hemispherically-averaged day–night contrast, this helps provide a point of comparison against 1D model results in cases where GCM results are not available. This two-column model was then used to study a wide range of cases for which 3D GCM results were not yet available. I found that as ocean heat transport is increased, the two-column model averages closer to the 1D model result. Therefore, in terms of climate, the 1D model is valid in cases where day–night heat transport is efficient, such as habitable cases with an ocean, as assumed previously (e.g. Meadows et al., 2018; Lincowski et al., 2018).

Using the 1D and two-column models, this work has reproduced the weak day–night temperature gradient that exists in GCM results above the middle troposphere. Because there is a lack of

temperature or condensible vapor contrast at altitudes probed by transit transmission spectra, even extreme day–night surface temperature contrasts do not likely materially affect transmission spectra. It has been repeatedly demonstrated that outgassing fluxes and photochemistry are critical to accurately simulating a planetary climate and its remote observables. Because 1D climate models are easily coupled with 1D photochemistry models, they are ideally suited to predict and interpret spectra for upcoming *JWST* observations of the TRAPPIST-1 and potentially other M dwarf terrestrial planets. Two-column modes can augment the habitability calculation, to determine whether trace gases will condense on the night side, and to produce day–night variation spectra, which may be useful for hot terrestrial planets.

Chapter 6

DISCUSSION

In the next decade, the launch of *JWST* and the completion of extremely large ground-based telescopes will provide the unprecedented opportunity to attempt characterization of terrestrial planets orbiting in the habitable zones of their host stars. The best targets are planets transiting small, late-type ultra-cool M dwarf stars, due to their large planet-to-star size ratio. However, these planets face significant challenges to habitability and an evolutionary history unlike Earth. These challenges include high life-long UV irradiation and extreme, rapid tidal-locking, which make modeling and characterizing these planets challenging for models designed for Earth-like planets around Sun-like stars.

Before the first discoveries of habitable zone terrestrial planets around M dwarf stars (Anglada-Escudé et al., 2016; Gillon et al., 2016), studies had already been underway focusing on possible Earth-like climate and photochemical processes for these planets, using models derived for Earth studies. Kasting et al. (1993) published habitable zone distances for a range of stars and suggested that M dwarf planets would be within the tidal-locking distance, so would have permanent day and night sides. Joshi et al. (1997) demonstrated that collapse of the atmosphere on the night side of a synchronously rotating planet would be inhibited by atmospheric heat transport from the day to the night side. Segura et al. (2005) used a photochemical model to demonstrate that biogenic gases would accumulate to several orders of magnitude higher abundances than Earth for a planet in an M dwarf habitable zone with Earth-like biological and geological fluxes, due to slower destruction rates for these gases. Shields et al. (2013) noted that the ice-albedo climate feedback would be diminished under an M dwarf star because the reflectivity of ice drops into the NIR, where ice has strong absorption and where M dwarf irradiation peaks.

Although studies using both 1D and 3D models have continued to incrementally advance understanding of key processes related to planetary habitability and detectability for M dwarf planets, they have focused almost exclusively on Earth-like atmospheres (i.e. those dominated by N_2, CO_2, and H_2O). Until now, studies using 1D models were unable to fully address the potential for extreme day–night temperature contrasts and night-side atmospheric collapse. Hu and Yang (2014) demonstrated that ocean heat transport can further reduce the day–night temperature gradient of a synchronously-rotating planet. Though studies employing 3D models have largely ignored the

climate effects that arise from the different atmospheric chemical processes experienced by planets irradiated by an M dwarf host, and even frequently ignore processes for which 3D models are ideal, such as day–night heat advection due to ocean and glacier transport.

Beyond traditional climate and photochemical models, studies from other disciplines in recent years have assessed other processes related to planetary habitability for M dwarf planets. Luger and Barnes (2015) demonstrated that the evolution of a primordial planetary atmosphere under the long, superluminous pre-main-sequence phase of M dwarf stars could result in up to thousands of bars of oxygen liberated from water vapor, followed by escape of hydrogen, which could result in a secondary atmosphere dominated by oxygen that is abiotic in origin, complicating the detection of oxygen as a biosignature (Meadows, 2017). The consideration of surface interactions by Schaefer et al. (2016) and Wordsworth et al. (2018) demonstrated that oxygen accumulation would be limited, but not completely prevented. Joint laboratory and modeling studies have used constraints by currently-available data to attempt to assess bulk atmospheric properties of the TRAPPIST-1 planets (Moran et al., 2018). Studies also find that the TRAPPIST-1 planets in particular may be more volatile-rich than Earth (Grimm et al., 2018; Unterborn et al., 2018a,b), suggesting an increased possibility that the TRAPPIST-1 system could host one or more water worlds, which may be high in other volatiles as well. Therefore, despite the superluminous pre-main-sequence phase and subsequent stellar activity that may continue to strip volatiles (Airapetian et al., 2017; Garcia-Sage et al., 2017; Dong et al., 2017, 2018), continued outgassing from deep volatile reservoirs could balance the high loss fluxes, maintaining a secondary atmosphere over geological time.

To begin to more completely address the factors affecting M dwarf planetary habitability and ameliorate the biases in previous modeling studies, I have developed a two-column mode for a versatile spectrum-resolving radiative-convective-equilibrium model, and coupled it into a framework including an updated terrestrial photochemical model. This model suite takes into account the synchronously-rotating nature and very different stellar environment experienced by M dwarf planets. I used this framework to explore planetary environments that are Earth-like, and to expand beyond current studies by simulating a wide range of plausible terrestrial planetary environments, including extreme Venus-like planets (both hot and cold) and more hypothetical cases with very

high or low oxidation states. These environments have included water/ice clouds, sulfuric acid aerosols (as seen in the atmosphere of Venus), and hydrocarbon hazes derived from Titan. Building on the use of surface fluxes by Segura et al. (2005) and later studies, I have used different biological and/or geological surface fluxes based on the type of environment simulated. While different "templates" have been created for the photochemical model, separate versions of the codes are not required to simulate this variety of atmospheres, which was first demonstrated for the climate model by Robinson and Crisp (2018). Producing a large variety of environments and assessing their differences, both in terms of planetary climate and what may be inferred in observations, allows me to consider here some broad points concerning planetary habitability and detectability for M dwarf planets in the era of *JWST*.

6.1 Planetary Evolution and Comparative Planetology

Planetary habitability has historically been focused on the development of and support for life on Earth, as the one data point for a habitable planet. However, M dwarfs comprise approximately 75% of all stars (Henry et al., 2006), so the frequency of habitable planets in the galaxy is more likely dominated by whether planets orbiting M dwarf stars can possibly host and develop life. This depends greatly on key factors that affect planetary habitability, including stellar evolution, planetary migration, tidal evolution, delivery of volatiles, geological processes including weathering and outgassing, clouds and overall planetary albedo, and atmospheric photochemistry and escape processes. For planets around M dwarfs, many of these processes differ considerably from Earth, and are currently being explored in theoretical studies. The uncertainties in these processes in general, and for specific planetary targets in particular, leads to an unknown number of planetary environments that could exist. Future observations of these planets are likely to be surprising, as were the discoveries of hot Jupiters (Guillot et al., 1996). Nonetheless, it is useful to make predictions for future observations that are based on what is known about planetary processes. To assess common attributes and discriminants among different types of atmospheres, I have modeled a sampling of different environments that reflect different evolutionary pathways. In future observations, the prevalence or lack of many of these features may provide insights into the processes that shape

their environments.

Of the processes discussed that shape planetary environments, it has been shown (Luger et al., 2015; Luger and Barnes, 2015; Schaefer et al., 2016; Wordsworth et al., 2018) that stellar evolution, and the impact it has on planetary evolution, drives the resultant bulk planetary atmosphere, primarily through the availability of remaining volatiles. Whether a planet retains any volatiles depends on its original bulk composition. Gases that can be emitted from the planetary interior determine the resultant secondary atmosphere. The state of the interior, and hence of the atmosphere, may result from a wide variety of factors, including original formation composition, stellar evolution, orbital state and evolution, internal properties such as radiogenic heating and mantle dynamics, tidal evolution, and the efficiency of outgassing from the interior versus the rate of escape, among others (§1.3; Meadows and Barnes 2018). Despite even the most extreme stellar pre-main-sequence evolution, the interior inventory of volatiles (if sufficiently large) may be outgassed over time to produce and sustain a secondary atmosphere. The atmosphere that is maintained over geological time then depends on the balance of outgassing and escape fluxes. Even for planets outside the habitable zone, an assessment of their bulk atmospheric inventory and associated constraints on likely evolutionary history can inform whether M dwarf planets can sustain atmospheres via outgassing.

As a result of original bulk inventory, escape, and outgassing (among other factors), multiple climate states are possible, even within the classical habitable zone. In traditional climate modeling, planets in the habitable zone are assumed to be Earth-like in composition (N_2, CO_2, and H_2O), with water or ice-covered surfaces, but where the abundance of non-condensible gases is taken to be independent parameters (Kasting et al., 1993; Kopparapu et al., 2013), and even contemporary studies continue to make these same assumptions (Turbet et al., 2018; Wunderlich et al., 2019; Wolf et al., 2019). In this work, I have demonstrated that a wider variety of planetary states is possible, spanning Venus-like to oxygen-rich, ocean-covered worlds. Which environment forms depends on the initial bulk state and evolution of the star, planetary interior, and atmosphere. In the Solar System, evolution of our Sun leads researchers to study planetary climate in a "cold-start" regime, but M dwarf planets inevitably begin life in a "hot-start" environment, because planetary migration

likely occurs well before the star settles to its main sequence luminosity (Unterborn et al., 2018a). Therefore, the assumption that these planets begin cold (e.g. Turbet et al., 2018) may be unlikely.

Conversely, my work shows that Venus-like planets could exist throughout the habitable zone and even beyond the outer edge, if a Venus-like atmosphere was able to form before the star dimmed to its main sequence luminosity. I have also found that if a planet becomes Venus-like, such an atmosphere is radiatively stable even at cold temperatures. Therefore, the region of the star inward of the habitable zone where Venus-like planets are likely common (Kane et al., 2014) could span a much larger range of irradiation and potentially displace the habitable zone. Thus if the "Venus zone" is robust and common, then there may be no habitable zone for M dwarf planets, or for planetary systems with low volatile abundance.

A volatile-rich system like TRAPPIST-1 may be an ideal candidate to assess the edges of the habitable zone. Even though multiple studies suggest TRAPPIST-1 d is not likely in the HZ, my attempts at modeling a habitable atmosphere suggest d lies right on the inner edge, as the net incident stellar flux under reasonable assumptions is very near the runaway greenhouse limit. This low-density, likely volatile-rich world (Grimm et al., 2018) sits within conservative (climate modeling) and optimistic (early Venus) estimates of the IHZ, and so can help distinguish theories of which processes control the true inner edge. TRAPPIST-1 d could demonstrate evidence of these processes, through observation of an active runaway greenhouse (by large H_2O abundance) or of a post-ocean-loss atmosphere (if a dry O_2 or Venus-like atmosphere is detected). The habitability of TRAPPIST-1 d critically rests on its actual volatile abundance and its overall planetary albedo, likely affected by the altitude and types of aerosols that may form. GCMs indicate substellar clouds are eliminated when the planet gets too hot (Wolf, 2017; Kopparapu et al., 2017), but GCM cloud parameterizations differ, with results that are potentially very sensitive to both cloud formation and to the accuracy of radiative transfer (Yang et al., 2016; Bin et al., 2018; Yang et al., 2019c). Unfortunately, clouds may remain a difficult problem for the foreseeable future, due to their microphysical and chaotic nature and their large radiative effect. This uncertainty is compounded because proper radiative transfer may require sophisticated physics implementations (Kitzmann et al., 2013), which are used in this dissertation, but which are lacking in the heavily

parameterized, band model radiative transfer methods implemented in most exoplanet GCMs.

Whether habitable or not, inner planets of a multi-planet system can provide crucial information about the state of a planetary system and inform whether to embark on an expensive observational program to characterize a habitable zone planet. In just a few transits, inner planets may indicate the presence of a high molecular weight atmosphere (Lustig-Yaeger et al., 2019a). Evidence of an atmosphere on a planet inward of the inner edge, even if not habitable, is a good indicator that any habitable zone planets in the system would have been able to maintain atmospheres, and hence raise the probability that they could be habitable, and increase their viability as targets for long-duration observing campaigns. Conversely, the lack of any atmosphere on inner planets, while it would not preclude atmospheres for outer planets, would be evidence of an intense evolutionary history. In a multi-planet system like TRAPPIST-1, this means that early and rapid observation and analysis of the inner planets (b, c, and d) can provide useful evidence to proceed with a campaign to characterize the HZ planets e, f, and g.

6.2 Identifying Habitable and Uninhabitable Atmospheres

A system like TRAPPIST-1 provides the unprecedented opportunity, besides our own Solar System, to study planetary properties and comparative planetology. As planets within a single system, they most likely experienced similar evolutionary histories. Their similarities and differences will provide insightful comparisons for decades to come. No other discovered system has the observational merits across a variety of planets spanning the habitable zone that TRAPPIST-1 has. The TRAPPIST-1 planets have such short period orbits that their transits occur frequently, and likely overlap frequently. Although transit overlaps could interfere with spectral characterization, occultation of one planet by another (on or off the stellar disk) can occur and provide dynamical information that would otherwise be impossible to obtain (Luger et al., 2017a). While in architecture, TRAPPIST-1 may not be unique, and may even be quite common (Ballard and Johnson, 2016), the TRAPPIST-1 system is uniquely characterizable by near-future instruments, especially *JWST*.

M dwarf planets exhibit different atmospheric chemical processes, so correct interpretation

of spectral observations requires consideration of the stellar environment. Inferring whether a detected gas is photochemical, geological, or biogenic requires an assessment of photochemical processes and inferring associated surface fluxes, if any. Methane, an important greenhouse gas, is the center of the most critical differences between M dwarf and G dwarf planetary atmospheres. Due to photochemical and catalytic processes, methane and other key biogenic gases (e.g. N_2O, CH_3Cl) have a much longer lifetime in an M dwarf planetary atmosphere and so can accumulate to higher abundances (Segura et al., 2005; Meadows et al., 2018). Generally, M dwarf stars exhibit higher high-energy UV activity than Solar-type stars, and in conjunction with lower effective photospheric temperatures, this drastically shifts the balance of UV distribution that controls various catalytic cycles, which include atmospheric detergents ozone and HO_x (Segura et al., 2005; Meadows et al., 2020). The interpretation of fluxes and the calculation of photochemistry and catalytic cycles is compounded by uncertainty and variation in UV fluxes across different M dwarf stars (Schneider and Shkolnik, 2018). Determination of whether these key gases are biogenic or geological in origin depends greatly on stellar and planetary environmental context, requiring good characterization of the host star.

Planetary climate is critically affected by chemistry in M dwarf atmospheres differently than for Earth. The cooler M dwarf SED shifts the peak stellar energy received at a planet into NIR absorption bands of strong atmospheric greenhouse gases, including H_2O, CO_2, and CH_4. This affects atmospheric climate structure and radiative forcing, particularly the temperature of the cold trap, depending on greenhouse gas content, which alters the chemistry of the stratosphere and the retention of water vapor. Methane, which accumulates to higher abundances, contains many NIR bands that fill in spectral windows between water bands, significantly warming the stratosphere from direct absorption of stellar NIR photons. Mischaracterizing the methane abundance, regardless of its source, changes stratospheric water abundance by several orders of magnitude and affects a variety of atmospheric chemical cycles.

For the imminent launch of *JWST*, I have focused primarily on transit transmission spectra, and have demonstrated common atmospheric features indicative of the presence of an atmosphere—primarily, CO_2. Carbon dioxide is likely common among terrestrial atmospheres, as carbon and

oxygen are both among the most abundant elements in the galaxy and CO_2 itself is relatively high molecular weight and very stable. In transmission spectra, this gas is generally insensitive to abundance, though the small and weak bands in the high-sensitivity region for *JWST* (i.e. short NIR bands) may be used to characterize abundance. Other important bands can indicate broad atmospheric type, such as the observation of O_2-O_2 bands, which indicate an atmosphere with a large abundance of O_2. Large CH_4 bands likely indicate significant outgassing (Segura et al., 2005; Meadows et al., 2020). Although many fascinating effects may be teased out in climate and photochemical studies with high-precision spectra, the linking of large spectral effects (the observable) with planetary state is a critical component in characterizing an exoplanet. Small time-scale or small amplitude effects will not be discernible in the noise, even under the most optimistic predictions for *JWST* performance for the best targets like the TRAPPIST-1 planets (Lustig-Yaeger et al., 2019a). However, some constraints may be possible on terrestrial exoplanets with *JWST* (Morley et al., 2017; Krissansen-Totton et al., 2018; Lustig-Yaeger et al., 2019a; Fauchez et al., 2019).

Ostensibly, surface water is the primary discriminant between habitable and inhabitable worlds, but in transit spectroscopy, the detection of water vapor is not a conclusive indicator of surface water. The presence or absence of a large surface water reservoir can be inferred or constrained by other gases present in the atmosphere that are accessible by observational methods available with *JWST*. Some gases, like SO_2, react quickly with water, and so the detection of such a gas would suggest the lack of an ocean. Because transit observations primarily probe the stratosphere, the detection of significant atmospheric water in transit transmission observations is more likely evidence of no cold trap and potentially a planet experiencing a runaway greenhouse, and is not conclusive evidence of surface water. A positive aspect of detection of any water vapor is that it indicates the presence of volatiles. Conversely, the lack of detection of water vapor does not mean a planet does not have an ocean; both Earth and Venus have similarly dry stratospheres ($\sim$ 1 ppm).

It may be easier to determine that a planet is not likely to be habitable than to confirm that a planet is habitable. In addition to large amounts of stratospheric water vapor or anti-water indicators like SO_2, enhanced isotopic fractionation in favor of heavier isotopes could be observed,

which would indicate the loss of a reservoir containing that element. In particular, a large D/H ratio in H_2O would indicate a loss of H_2O, while a large $^{18}O/^{16}O$ ratio would indicate a loss of oxygen, which is proposed to occur under extreme conditions (Lammer et al., 2007; Airapetian et al., 2017; Garcia-Sage et al., 2017; Dong et al., 2017, 2018). These bands could be detected most easily at 1–4 μm in atmospheres with lower CO_2 abundance (i.e., not in Venus-like atmospheres). In cases of extreme loss and fractionation, it would be quicker to detect these bands than spectral evidence of a habitable environment (c.f. Morley et al., 2017; Krissansen-Totton et al., 2018; Lustig-Yaeger et al., 2019a; Lincowski et al., 2019; Meadows et al., 2020).

6.3 The Modeling Hierarchy and the Utility of 1D Models in the Exoplanet Era

A variety of models are in use to understand exoplanet climate, chemistry, and predict or characterize spectra for current and next generation telescope observations. The maximum utility will be achieved if research groups work together to incorporate the results of complementary models. One single model cannot incorporate all possible effects because models are fundamentally simplifications of reality and are inherently limited in their complexity, as a trade-off between computation time and accuracy of simulation. Limitations in 1D models most obviously include spatial treatment of clouds, although incorporation of sophisticated aerosol models used in solar system studies (e.g. CARMA) could be greatly beneficial. More spatially complicated models must make greater sacrifices across their range of physics. A modeling hierarchy including 1D and 3D models is important, and results from one should inform the other, either through new experiments, intercomparisons, or to indicate critical needs for improvement. A two-column model, as I developed, synthesizes advantages of both model types.

Because observations of temperate, terrestrial exoplanets in the next decade are will have low signal-to-noise and be largely global in scope, only minimal spatial resolution (if any) is required to predict and interpret observations. Spatially-resolved models can indicate how dynamics affects the distribution of habitability on a planet. This is particularly important for M dwarf planets due to tidal locking and synchronous rotation. The highest utility for 3D models to inform 1D models is through the climate effects of rotation rates, calibration of global cloud cover, and for a two-

column framework, to provide an anchor for advection parameterization. Single column models, along with 2D energy balance models, enable a wider parameter space, such as expanding climate-photochemistry studies to a wider regime of atmospheres, as I have done here. In particular, more accurate physics models like SMART/VPL Climate can indicate where GCMs and other simple models stray from their validity. As with any models, it is important to understand the range of validity for key parameters such as temperature, pressure, and abundance. Many discrepancies between models is due to inputs and assumptions. It has been repeatedly demonstrated that complete lab data for important gases, such as H_2O, CO_2, and CH_4 is required for accurate climate calculations (Halevy et al., 2009; Yang et al., 2016, 2019b; Ch. 5). Line lists, such as HITRAN and ExoMol, continue to be updated, and modeling studies should note when critical improvements have been made, and modelers need to routinely update this data in models. Even band models benefit from updated data for underlying absorptivity and k coefficient calculations.

Photochemistry and ocean heat transport are critical to correctly model an atmospheric state, assess planetary climate, and infer or predict spectral observables. Due to complexity and computation time, even many recent comprehensive climate studies using 3D GCMs include neither of these processes (e.g. Turbet et al., 2016; Boutle et al., 2017; Wolf, 2017; Wolf et al., 2019; Komacek et al., 2020), or use coupling methods for "Earth-like" atmospheres that are not consistent with Earth surface fluxes (Fauchez et al., 2019; Pidhorodetska et al., 2020). It has been demonstrated here and elsewhere that photochemistry critically affects atmospheric climate and observables (Segura et al., 2005; Grenfell et al., 2014; Rugheimer et al., 2015; Arney et al., 2017; Meadows et al., 2018; Wunderlich et al., 2019). Studies have shown that real, dynamic ocean heat transport plays a critical role in transporting heat from the permanent day to permanent night side atmosphere on a synchronously-rotating planet (Cullum et al., 2014; Hu and Yang, 2014; Yang et al., 2013, 2014, 2019c; Way et al., 2017; Way et al., 2018; Del Genio et al., 2019), though some continental configurations may pathologically interfere, such as that of modern Earth (Del Genio et al., 2019) or a sub-stellar continent (Lewis et al., 2018). The lack of dynamic ocean (or glacier) heat transport may have lead to overly pessimistic conclusions about the habitability of M dwarf planets, especially when assessing whether the atmosphere may collapse on the night

side. Day–night surface advective flux is a parameter that is easily included in energy-balance and two-column models (Yang and Abbot, 2014; Koll and Abbot, 2016), including the one I developed, which can help determine the range of plausible day–night temperature differences.

In this dissertation, I have shown that a modern 1D model is capable of simulating a wide variety of planets, including those that are synchronously rotating, beyond the capabilities of other models, particularly GCMs, whose complexity in other ways prohibits the flexibility possible here. Particularly, the routine coupling with photochemistry of 1D models and the properties of transit spectroscopy make 1D models ideally suited for predicting and interpreting *JWST* observations. Furthermore, a two-column approach with a versatile 1D model allows matching major climate features of 3D models for synchronously rotating planets, in terms of hemispherical (day–night) averages, where considerations such as observing day–night temperature differences via phase curves or secondary eclipse spectra are promising for hotter planets. This approach allows a column model to assess atmospheric collapse on the night side. My results and those of GCMs indicate that, once into the radiative-photochemical region of the atmosphere, planetary atmospheres are relatively spatially homogeneous, which is the region of the atmosphere probed by transit observations, which is the optimal method considered for upcoming *JWST* observations of temperate planets (Lustig-Yaeger et al., 2019a).

The two-column model I have developed demonstrates that global-average temperatures by good 1D models are likely rather accurate across a range of atmospheric types. GCMs are not required to predict or interpret transmission spectra, which probe the more globally-homogeneous regions of the atmosphere. GCMs in use for terrestrial exoplanet studies usually neglect key processes—ocean heat transport and photochemistry—that are vital for M dwarf planet climate and detectability studies. For temperate terrestrial exoplanets, GCMs may be more relevant in a few decades when the ability to discern spatial phenomenon in such planetary observations may be possible (i.e. to LUVOIR or beyond, Lustig-Yaeger et al. 2018).

6.4 Future Work

Observations with *JWST* may raise more questions than provide answers. Some questions have the potential to be addressed in the near future with *JWST*. Can a high-mass O_2 atmosphere exist? More so, can such an atmosphere remain stable over a volatile-rich, ocean-bearing world? At high irradiation, can a volatile-rich planet sustain a moist or runaway greenhouse indefinitely? If cooler than the runaway greenhouse threshold, could such a planet look more like Titan, with a hydrocarbon haze? If a planet was unable to retain its water, would it more likely accumulate O_2, or would it resemble Venus?

The versatile modeling framework developed in this dissertation can be used for a broad variety of theoretical investigations of terrestrial exoplanets to predict and interpret upcoming observations to answer current questions and those that arise with new data. The versatility here includes different stellar types (including with some updates, binary stars), a wide range of atmospheric redox states and outgassing rates, and the possibility of assessing eddy diffusion assumptions, photochemistry networks, convection parameters, and advection parameters.

Of particular interest is probing atmospheric compositions unlike those found in our Solar System. Because planets in multi-planet systems like TRAPPIST-1 have likely migrated, they could be more volatile-rich, having formed further away in the protoplanetary disk. That is, planets in the habitable zones of other stars could have formed more similar to icy bodies like Titan, and so their outgassing in the habitable zone when temperate could be more sustained and reducing. Improved interior modeling that provides outgassing fluxes for a variety of gas species can provide critical inputs to atmosphere models. These models need to include both traditional thermodynamic and bulk structure modeling, but also include key chemical networks, such as H, C, O, N, and S, which are needed for atmospheric studies.

Time-dependent phenomena could be important for some types of planets, especially those around flaring M dwarfs. Day-night differences in photochemistry even in synchronously-rotating planets are relatively small (Chen et al., 2018), allowing external coupling of climate and photochemistry for most applications. Internally coupling of photochemistry to VPL Climate would be

a substantial project. However, photochemistry of flaring stars is likely a major problem (Segura et al., 2010; Tilley et al., 2019) that requires time-dependent treatment.

In addition to time-dependent spectra, terrestrial exoplanet climate-photochemical modeling could benefit greatly from the inclusion of ion chemistry. Although the generation of protons by stellar flares is relatively unconstrained, such events affect planetary atmospheres much more than the electromagnetic energy flux received from massive flares (Segura et al., 2010; Tilley et al., 2019). Proton chemistry could be added to the photochemistry capabilities of this model, but would require a substantial upgrade to do so. The chemical reactions could then be used from other established ion chemistry codes, such as those used in atmospheric escape studies (e.g. Airapetian et al., 2016, 2017). Alternatively, because the coupling of chemistry to climate is externally implemented, VPL Climate could be easily coupled in a similar way to any other photochemical model.

Although the photochemical model I used includes basic aerosol formation for H_2SO_4 and hydrocarbon hazes, the climate model would benefit greatly from self-consistent microphysical aerosol treatment. This could include a similar crude treatment as in the photochemical model (Pavlov et al., 2001), or something a bit more complex and generalized (Ackerman and Marley, 2001), or even a full microphysical model such as the Community Aerosol Model (CARMA, Turco et al., 1979; Toon et al., 1988; Jacobson et al., 1994; Ackerman et al., 1995; Bardeen et al., 2008). However, implementation of accurate, time-dependent radiative transfer for such aerosols could be challenging. A two-column convective cell could improve calculation of aerosols and provide explicit partially-cloudy conditions.

While the vertical transport treatment is superior to convective adjustment, there are more advanced schemes available and are currently under development in VPL Climate. Particularly, a higher order closure scheme could improve the boundary layer physics (Mellor and Yamada, 1974; Mellor and Yamada, 1982; Savijarvi, 1999). Moist convection could be improved by implementation of approaches used in 3D GCMs, such as using non-local criteria, including the countergradient flux (Deardorff, 1967; Holtslag and Moeng, 1991; Zhou et al., 2018) and the plume ensemble approach for deep convection (Zhang and McFarlane, 1995).

In the near future, the results of this dissertation can be used to inform *JWST* observing proposals. High-resolution spectra, and other direct-imaging spectra relevant to ground-based observatories, will also be important in the next few years as the extremely large ground-based telescopes begin operation. The atmospheric states produced in this dissertation can be used to produce a variety of spectra, as the radiative transfer code SMART is in principle capable of producing accurate spectra at arbitrary spectra resolution.

Chapter 7

CONCLUSIONS

Within this decade, *JWST* will observe small planets in and around the habitable zone of TRAPPIST-1, and possibly other nearby M dwarf stars. These planets are likely very different from Earth, due to the extreme stellar environment and the impact it can have on planetary atmospheres. In this dissertation, I have updated and coupled climate and photochemical models designed to improve the modeling and understanding of plausible atmospheres for these planets. These models have been applied to a wide range of atmospheres, spanning from Venus-like, to Earth-like, to hypothetical alien atmospheres, which were self-consistently modeled with the likely stellar environment that influences the regions of the atmospheres potentially observable with *JWST*. In this upcoming era of terrestrial planet characterization, where we will likely be surprised, this dissertation has provided some foundational science to help predict and interpret these upcoming observations.

BIBLIOGRAPHY

Ackerman, A. S. and Marley, M. S. (2001). Precipitating Condensation Clouds in Substellar Atmospheres. *The Astrophysical Journal*, 556(2):872–884.

Ackerman, A. S., Toon, O. B., and Hobbs, P. V. (1995). Numerical modeling of ship tracks produced by injections of cloud condensation nuclei into marine stratiform clouds. J. Geophys. Res., 100(D4):7121–7133.

Ackerman, M., Frimout, D., Girard, A., Gottignies, M., and Muller, C. (1976). Stratospheric HCl from infrared spectra. Geophys. Res. Lett., 3(2):81–83.

Agol, E., Steffen, J., Sari, R., and Clarkson, W. (2005). On detecting terrestrial planets with timing of giant planet transits. MNRAS, 359(2):567–579.

Airapetian, V. S., Glocer, A., Gronoff, G., Hébrard, E., and Danchi, W. (2016). Prebiotic chemistry and atmospheric warming of early Earth by an active young Sun. *Nature Geoscience*, 9:452–455.

Airapetian, V. S., Glocer, A., Khazanov, G. V., Loyd, R. O. P., France, K., Sojka, J., Danchi, W. C., and Liemohn, M. W. (2017). How Hospitable Are Space Weather Affected Habitable Zones? The Role of Ion Escape. ApJ, 836:L3.

Alberti, T., Carbone, V., Lepreti, F., and Vecchio, A. (2017). Comparative climates of the trappist-1 planetary system: Results from a simple climate-vegetation model. *The Astrophysical Journal*, 844(1):19.

Allen, M., Yung, Y. L., and Waters, J. W. (1981). Vertical Transport and Photochemistry in the Terrestrial Mesosphere and Lower Thermosphere (50-120 km). *J. Geophys. Res.*, 86(A5):3617–3627.

Ambrose, D. (1956). The vapour pressures and critical temperatures of acetylene and carbon dioxide. *Transactions of the Faraday Society*, 52:772–781.

André, J. and Mahrt, L. (1982). The nocturnal surface inversion and influence of clear-air radiative cooling. *Journal of the Atmospheric Sciences*, 39(4):864–878.

Anglada-Escudé, G., Amado, P. J., Barnes, J., Berdiñas, Z. M., Butler, R. P., Coleman, G. A. L., de la Cueva, I., Dreizler, S., Endl, M., Giesers, B., Jeffers, S. V., Jenkins, J. S., Jones, H. R. A., Kiraga, M., Kürster, M., López-González, M. J., Marvin, C. J., Morales, N., Morin, J., Nelson, R. P., Ortiz, J. L., Ofir, A., Paardekooper, S.-J., Reiners, A., Rodríguez, E., Rodrguez-López, C., Sarmiento, L. F., Strachan, J. P., Tsapras, Y., Tuomi, M., and Zechmeister, M. (2016). A terrestrial planet candidate in a temperate orbit around Proxima Centauri. *Nature*, 536(7617):437–440.

Appleby, J. F. and Hogan, J. S. (1984). Radiative-convective equilibrium models of Jupiter and Saturn. Icarus, 59(3):336–366.

Arney, G., Domagal-Goldman, S. D., Meadows, V. S., Wolf, E. T., Schwieterman, E., Charnay, B., Claire, M., Hébrard, E., and Trainer, M. G. (2016). The Pale Orange Dot: The Spectrum and Habitability of Hazy Archean Earth. *Astrobiology*, 16(11):873–899.

Arney, G., Meadows, V., Crisp, D., Schmidt, S. J., Bailey, J., and Robinson, T. (2014). Spatially-resolved measurements of H_2O, HCl, CO, OCS, SO_2 , cloud opacity, and acid concentration in the Venus near-infrared spectral windows. *Journal of Geophysical Research: Planets*, 119(8):1860–1891.

Arney, G. N., Meadows, V. S., Domagal-Goldman, S. D., Deming, D., Robinson, T. D., Tovar, G., Wolf, E. T., and Schwieterman, E. (2017). Pale Orange Dots: The Impact of Organic Haze on the Habitability and Detectability of Earthlike Exoplanets. ApJ, 836(1):49.

Asplund, M., Grevesse, N., Sauval, A. J., and Scott, P. (2009). The Chemical Composition of the Sun. *Annual Review of Astronomy and Astrophysics*, 47:481–522.

Atreya, S. K., Donahue, T. M., and Kuhn, W. R. (1978). Evolution of a Nitrogen Atmosphere on Titan. *Science*, 201(4356):611–613.

Baldridge, A. M., Hook, S. J., Grove, C. I., and Rivera, G. (2009). The ASTER spectral library version 2.0. *Remote Sensing of Environment*, 113:711–715.

Ballard, S. and Johnson, J. A. (2016). The Kepler Dichotomy among the M Dwarfs: Half of Systems Contain Five or More Coplanar Planets. ApJ, 816:66.

Baraffe, I., Homeier, D., Allard, F., and Chabrier, G. (2015). New evolutionary models for pre-main sequence and main sequence low-mass stars down to the hydrogen-burning limit. A&A, 577:A42.

Baranov, Y. I., Lafferty, W. J., and Fraser, G. T. (2004). Infrared spectrum of the continuum and dimer absorption in the vicinity of the O_2 vibrational fundamental in O_2/CO_2 mixtures. *Journal of Molecular Spectroscopy*, 228:432–440.

Barclay, T., Pepper, J., and Quintana, E. V. (2018). A Revised Exoplanet Yield from the Transiting Exoplanet Survey Satellite (TESS). *The Astrophysical Journal Supplement Series*, 239:2.

Bardeen, C. G., Toon, O. B., Jensen, E. J., Marsh, D. R., and Harvey, V. L. (2008). Numerical simulations of the three-dimensional distribution of meteoric dust in the mesosphere and upper stratosphere. *Journal of Geophysical Research (Atmospheres)*, 113(D17):D17202.

Barnes, R., Deitrick, R., Luger, R., Driscoll, P. E., Quinn, T. R., Fleming, D. P., Guyer, B., McDonald, D. V., Meadows, V. S., Arney, G., Crisp, D., Domagal-Goldman, S. D., Lincowski, A., Lustig-Yaeger, J., and Schwieterman, E. (2018). The Habitability of Proxima Centauri b I: Evolutionary Scenarios. arXiv preprint arXiv: 1608.06919v2.

Barnes, R., Meadows, V. S., and Evans, N. (2015). Comparative Habitability of Transiting Exoplanets. ApJ, 814(2):91.

Barr, A. C., Dobos, V., and Kiss, L. L. (2018). Interior structures and tidal heating in the TRAPPIST-1 planets. A&A, 613:A37.

Batalha, N., Domagal-Goldman, S. D., Ramirez, R., and Kasting, J. F. (2015). Testing the early Mars H2–CO2 greenhouse hypothesis with a 1-D photochemical model. *Icarus*, 258:337–349.

Batalha, N. E., Lewis, N. K., Line, M. R., Valenti, J., and Stevenson, K. (2018). Strategies for Constraining the Atmospheres of Temperate Terrestrial Planets with JWST. ApJ, 856:L34.

Batalha, N. E., Mandell, A., Pontoppidan, K., Stevenson, K. B., Lewis, N. K., Kalirai, J., Earl, N., Greene, T., Albert, L., and Nielsen, L. D. (2017). PandExo: A Community Tool for Transiting Exoplanet Science with JWST & HST. *Publications of the Astronomical Society of the Pacific*, 129(6):064501.

Baum, B. A., Yang, P., Heymsfield, A. J., Platnick, S., King, M. D., Hu, Y.-X., and Bedka, S. T. (2005). Bulk Scattering Properties for the Remote Sensing of Ice Clouds. Part II: Narrowband Models. *Journal of Applied Meteorology*, 44:1896–1911.

Bean, J. L., Abbot, D. S., and Kempton, E. M.-R. (2017). A statistical comparative planetology approach to the hunt for habitable exoplanets and life beyond the solar system. ApJ, 841(2):L24.

Belviso, S., Nguyen, B. C., and Allard, P. (1986). Estimate of carbonyl sulfide (OCS) volcanic source strength deduced from OCS/CO2 ratios in volcanic gases. Geophys. Res. Lett., 13:133–136.

Benz, W., Ehrenreich, D., and Isaak, K. (2018). CHEOPS: CHaracterizing ExOPlanets Satellite. In Deeg, H. J. and Belmonte, J. A., editors, *Handbook of Exoplanets*, pages 1257–1281. Springer, Cham, Switzerland.

Berta-Thompson, Z. K., Irwin, J., Charbonneau, D., Newton, E. R., Dittmann, J. A., Astudillo-Defru, N., Bonfils, X., Gillon, M., Jehin, E., Stark, A. A., Stalder, B., Bouchy, F., Delfosse, X., Forveille, T., Lovis, C., Mayor, M., Neves, V., Pepe, F., Santos, N. C., Udry, S., and Wünsche, A. (2015). A rocky planet transiting a nearby low-mass star. *Nature*, 527(7577):204–207.

Bétrémieux, Y. and Kaltenegger, L. (2013). Transmission Spectrum of Earth as a Transiting Exoplanet from the Ultraviolet to the Near-infrared. ApJ, 772:L31.

Bétrémieux, Y. and Kaltenegger, L. (2014). Impact of Atmospheric Refraction: How Deeply can We Probe Exo-Earth's Atmospheres during Primary Eclipse Observations? ApJ, 791:7.

Bezard, B., Baluteau, J. P., Marten, A., and Coron, N. (1987). The ^{12}C/ ^{13}C and ^{16}O/ ^{18}O ratios in the atmosphere of Venus from high-resolution 10-μm spectroscopy. Icarus, 72:623–634.

Billmers, R. I. and Smith, A. L. (1991). Ultraviolet-visible absorption spectra of equilibrium sulfur vapor: Molar absorptivity spectra of s3 and s4. *The Journal of Physical Chemistry*, 95(11):4242–4245.

Bin, J., Tian, F., and Liu, L. (2018). New inner boundaries of the habitable zones around M dwarfs. *Earth and Planetary Science Letters*, 492:121–129.

Blackadar, A. K. (1962). The vertical distribution of wind and turbulent exchange in a neutral atmosphere. *J. Geophys. Res.*, 67(8):3095–3102.

Bogumil, K., Orphal, J., Homann, T., Voigt, S., Spietz, P., Fleischmann, O., Vogel, A., Hartmann, M., Kromminga, H., Bovensmann, H., et al. (2003). Measurements of molecular absorption spectra with the sciamachy pre-flight model: instrument characterization and reference data for atmospheric remote-sensing in the 230–2380 nm region. *Journal of Photochemistry and Photobiology A: Chemistry*, 157(2-3):167–184.

Bolmont, E., Selsis, F., Owen, J. E., Ribas, I., Raymond, S. N., Leconte, J., and Gillon, M. (2017). Water loss from terrestrial planets orbiting ultracool dwarfs: implications for the planets of TRAPPIST-1. MNRAS, 464:3728–3741.

Borucki, W. J. (2016). KEPLERMission: development and overview. *Reports on Progress in Physics*, 79(3):036901.

Borysow, A. (2002). Collision-induced absorption coefficients of H_2 pairs at temperatures from 60 K to 1000 K. A&A, 390:779–782.

Bourrier, V., Ehrenreich, D., Wheatley, P. J., Bolmont, E., Gillon, M., de Wit, J., Burgasser, A. J., Jehin, E., Queloz, D., and Triaud, A. H. M. J. (2017). Reconnaissance of the TRAPPIST-1 exoplanet system in the Lyman-α line. A&A, 599:L3.

Boutle, I. A., Mayne, N. J., Drummond, B., Manners, J., Goyal, J., Hugo Lambert, F., Acreman, D. M., and Earnshaw, P. D. (2017). Exploring the climate of Proxima B with the Met Office Unified Model. A&A, 601:A120.

Brasseur, G. P. and Solomon, S. (2006). *Aeronomy of the middle atmosphere: chemistry and physics of the stratosphere and mesosphere*, volume 32. Springer Science & Business Media.

Brion, C., Dyck, M., and Cooper, G. (2005). Absolute photoabsorption cross-sections (oscillator strengths) for valence and inner shell excitations in hydrogen chloride, hydrogen bromide and hydrogen iodide. *Journal of electron spectroscopy and related phenomena*, 144:127–130.

Broeg, C., Fortier, A., Ehrenreich, D., Alibert, Y., Baumjohann, W., Benz, W., Deleuil, M., Gillon, M., Ivanov, A., Liseau, R., Meyer, M., Oloffson, G., Pagano, I., Piotto, G., Pollacco, D., Queloz, D., Ragazzoni, R., Renotte, E., Steller, M., and Thomas, N. (2013). CHEOPS: A transit photometry mission for ESA's small mission programme. In *European Physical Journal Web of Conferences*, volume 47 of *European Physical Journal Web of Conferences*, page 03005.

Brugger, B., Mousis, O., Deleuil, M., and Lunine, J. I. (2016). Possible Internal Structures and Compositions of Proxima Centauri b. ApJ, 831(2):L16.

Bryson III, C., Cazcarra, V., and Levenson, L. (1974). Condensation coefficient measurements of H_2O, N_2O, and CO_2. *Journal of Vacuum Science Technology*, 11(1):411.

Buccino, A. P., Lemarchand, G. A., and Mauas, P. J. D. (2007). UV habitable zones around M stars. Icarus, 192(2):582–587.

Bullock, M. A. and Grinspoon, D. H. (2001). The Recent Evolution of Climate on Venus. *Icarus*, 150(1):19–37.

Bullock, M. A. and Grinspoon, D. H. (2013). The atmosphere and climate of venus. In Mackwell, S. J., Simon-Miller, A. A., Harder, J. W., and Bullock, M. A., editors, *Comparative Climatology of Terrestrial Planets*, pages 19–54. University of Arizona Press, Tucson.

Burkholder, J., Sander, S., Abbatt, J., Barker, J., Huie, R., Kolb, C., Kurylo, M., Orkin, V., Wilmouth, D., and Wine, P. (2015). Chemical kinetics and photochemical data for use in atmospheric studies–evaluation number 18. *Nasa panel for data evaluation technical report*.

Burkholder, J. B., Talukdar, R. K., Ravishankara, A. R., and Solomon, S. (1993). Temperature dependence of the HNO¡SUB¿3¡/SUB¿ UV absorption cross sections. *Journal of Geophysical Research*, 98:22,937–22,948.

Burton, M. R., Oppenheimer, C., Horrocks, L. A., and Francis, P. W. (2000). Remote sensing of CO_2 and H_2O emission rates from Masaya volcano, Nicaragua. *Geology*, 28:915.

Canuto, V. M., Cheng, Y., Howard, A. M., and Esau, I. N. (2008). Stably Stratified Flows: A Model with No Ri(cr)*. *Journal of Atmospheric Sciences*, 65:2437.

Carissimo, B. C., Oort, A. H., and Vonder Haar, T. H. (1985). Estimating the Meridional Energy Transports in the Atmosphere and Ocean. *Journal of Physical Oceanography*, 15(1):82–91.

Carn, S. A., Fioletov, V. E., McLinden, C. A., Li, C., and Krotkov, N. A. (2017). A decade of global volcanic SO_2 emissions measured from space. *Nature Scientific*, 7:44095.

Catling, D. C. and Kasting, J. F. (2017). *Atmospheric Evolution on Inhabited and Lifeless Worlds*. Cambridge University Press.

Catling, D. C., Krissansen-Totton, J., Kiang, N. Y., Crisp, D., Robinson, T. D., DasSarma, S., Rushby, A. J., Del Genio, A., Bains, W., and Domagal-Goldman, S. (2018). Exoplanet Biosignatures: A Framework for Their Assessment. *Astrobiology*, 18:709–738.

Charbonneau, D., Brown, T. M., Burrows, A., and Laughlin, G. (2007). When Extrasolar Planets Transit Their Parent Stars. In Reipurth, B., Jewitt, D., and Keil, K., editors, *Protostars and Planets V*, page 701.

Charbonneau, D., Brown, T. M., Noyes, R. W., and Gilliland, R. L. (2002). Detection of an Extrasolar Planet Atmosphere. ApJ, 568(1):377–384.

Charnay, B., Meadows, V., and Leconte, J. (2015). 3D Modeling of GJ1214b's Atmosphere: Vertical Mixing Driven by an Anti-Hadley Circulation. ApJ, 813(1):15.

Chassefière, E. (1996). Hydrodynamic Escape of Oxygen from Primitive Atmospheres: Applications to the Cases of Venus and Mars. Icarus, 124:537–552.

Chassefière, E., Wieler, R., Marty, B., and Leblanc, F. (2012). The evolution of Venus: Present state of knowledge and future exploration. *Planetary and Space Science*, 63:15–23.

Chen, H., Wolf, E. T., Kopparapu, R., Domagal-Goldman, S., and Horton, D. E. (2018). Biosignature Anisotropy Modeled on Temperate Tidally Locked M-dwarf Planets. *The Astrophysical Journal*, 868(1):L6.

Chen, H., Wolf, E. T., Zhan, Z., and Horton, D. E. (2019). Habitability and Spectroscopic Observability of Warm M-dwarf Exoplanets Evaluated with a 3D Chemistry-Climate Model. ApJ, 886(1):16.

Cheng, B.-M., Chung, C.-Y., Bahou, M., Lee, Y.-P., and Lee, L. (2002). Quantitative spectral analysis of hcl and dcl in 120–220 nm: Effects of singlet–triplet mixing. J. Chem. Phys., 117(9):4293–4298.

Chyba, C. F. (1990). Impact delivery and erosion of planetary oceans in the early inner solar system. *Nature*, 343(6254):129.

Clark, R. N., Swayze, G. A., Wise, R., Livo, K. E., Hoefen, T., Kokaly, R. F., and Sutley, S. J. (2007). USGS digital spectral library splib06a. *US Geological Survey, Digital Data Series*, 231.

Clough, S. A., Kneizys, F. X., and Davies, R. W. (1989). Line shape and the water vapor continuum. *Atmospheric Research*, 23(3):229–241.

Clough, S. A., Shephard, M. W., Mlawer, E. J., Delamere, J. S., Iacono, M. J., Cady-Pereira, K., Boukabara, S., and Brown, P. D. (2005). Atmospheric radiative transfer modeling: a summary of the AER codes. J. Quant. Spec. Radiat. Transf., 91(2):233–244.

Coleman, G. A. L., Nelson, R. P., Paardekooper, S. J., Dreizler, S., Giesers, B., and Anglada-Escudé, G. (2017). Exploring plausible formation scenarios for the planet candidate orbiting Proxima Centauri. MNRAS, 467:996–1007.

Collinson, G. A., Frahm, R. A., Glocer, A., Coates, A. J., Grebowsky, J. M., Barabash, S., Domagal-Goldman, S. D., Fedorov, A., Futaana, Y., Gilbert, L. K., Khazanov, G., Nordheim, T. A., Mitchell, D., Moore, T. E., Peterson, W. K., Winningham, J. D., and Zhang, T. L. (2016). The electric wind of Venus: A global and persistent "polar wind"-like ambipolar electric field sufficient for the direct escape of heavy ionospheric ions. Geophys. Res. Lett., 43:5926–5934.

Cooper, G., Anderson, J. E., and Brion, C. E. (1996). Absolute photoabsorption and photoionization of formaldehyde in the VUV and soft X-ray regions (3 200 eV). *Chemical Physics*, 209:61–77.

Coplen, T. (1995). Reporting of stable carbon, hydrogen, and oxygen isotopic abundances. *Reference and intercomparison materials for stable isotopes of light elements*, 825:31–34.

Cowan, N. B., Greene, T., Angerhausen, D., Batalha, N. E., Clampin, M., Colón, K., Crossfield, I. J. M., Fortney, J. J., Gaudi, B. S., Harrington, J., Iro, N., Lillie, C. F., Linsky, J. L., Lopez-Morales, M., Mandell, A. M., and Stevenson, K. B. (2015). Characterizing Transiting Planet Atmospheres through 2025. PASP, 127:311.

Crisp, D. (1986). Radiative forcing of the Venus mesosphere. *Icarus*, 514(67):484–514.

Crisp, D. (1997). Absorption of sunlight by water vapor in cloudy conditions: A partial explanation for the cloud absorption anomaly. Geophys. Res. Lett., 24:571–574.

Crisp, D. and Titov, D. (1997). The thermal balance of the venus atmosphere. *Venus II*, pages 353–384.

Cronin, T. W. (2014). On the choice of average solar zenith angle. *Journal of the Atmospheric Sciences*, 71(8):2994–3003.

Cullum, J., Stevens, D., and Joshi, M. (2014). The Importance of Planetary Rotation Period for Ocean Heat Transport. *Astrobiology*, 14(8):645–650.

Davenport, A. G., Grimmond, C. S. B., Oke, T. R., and Wieringa, J. (2000). Estimating the roughness of cities and sheltered country. In *Proceedings 12th Conference on Applied Climatology, Asheville, NC, American Meteorological Society, Boston*, pages 96–99.

Davies, K. J. (1995). Oxidative stress: the paradox of aerobic life. In *Biochemical Society Symposia*, volume 61, pages 1–31. Portland Press Limited.

De Bergh, C., Bezard, B., Owen, T., Crisp, D., Maillard, J.-P., and Lutz, B. L. (1991). Deuterium on venus: observations from earth. *Science*, 251(4993):547–549.

de Wit, J., Wakeford, H. R., Gillon, M., Lewis, N. K., Valenti, J. A., Demory, B.-O., Burgasser, A. J., Burdanov, A., Delrez, L., Jehin, E., Lederer, S. M., Queloz, D., Triaud, A. H. M. J., and Van Grootel, V. (2016). A combined transmission spectrum of the Earth-sized exoplanets TRAPPIST-1 b and c. *Nature*, 537(7618):69–72.

de Wit, J., Wakeford, H. R., Lewis, N. K., Delrez, L., Gillon, M., Selsis, F., Leconte, J., Demory, B.-O., Bolmont, E., Bourrier, V., Burgasser, A. J., Grimm, S., Jehin, E., Lederer, S. M., Owen, J. E., Stamenković, V., and Triaud, A. H. M. J. (2018). Atmospheric reconnaissance of the habitable-zone Earth-sized planets orbiting TRAPPIST-1. *Nature Astronomy*, 2:214–219.

Deardorff, J. W. (1967). Empirical dependence of the eddy coefficient for heat upon stability above the lowest 50 m. *Journal of Applied Meteorology*, 6(4):631–643.

Deitrick, R., Barnes, R., Bitz, C., Fleming, D., Charnay, B., Meadows, V., Wilhelm, C., Armstrong, J., and Quinn, T. R. (2018). Exo-Milankovitch Cycles. II. Climates of G-dwarf Planets in Dynamically Hot Systems. AJ, 155(6):266.

Del Genio, A. D., Way, M. J., Amundsen, D. S., Aleinov, I., Kelley, M., Kiang, N. Y., and Clune, T. L. (2019). Habitable Climate Scenarios for Proxima Centauri b with a Dynamic Ocean. *Astrobiology*, 19(1):99–125.

Delrez, L., Gillon, M., Queloz, D., Demory, B.-O., Almleaky, Y., de Wit, J., Jehin, E., Triaud, A. H. M. J., Barkaoui, K., Burdanov, A., Burgasser, A. J., Ducrot, E., McCormac, J., Murray, C., Silva Fernandes, C., Sohy, S., Thompson, S. J., Van Grootel, V., Alonso, R., Benkhaldoun, Z., and Rebolo, R. (2018). SPECULOOS: a network of robotic telescopes to hunt for terrestrial planets around the nearest ultracool dwarfs. In *Ground-based and Airborne Telescopes VII*, volume 10700 of *Society of Photo-Optical Instrumentation Engineers (SPIE) Conference Series*, page 107001I.

Delrez, L., Gillon, M., Triaud, A. H. M. J., Demory, B.-O., de Wit, J., Ingalls, J. G., Agol, E., Bolmont, E., Burdanov, A., Burgasser, A. J., Carey, S. J., Jehin, E., Leconte, J., Lederer, S., Queloz, D., Selsis, F., and Van Grootel, V. (2018). Early 2017 observations of TRAPPIST-1 with *Spitzer*. MNRAS, 24(January):1–24.

Demory, B.-O., Gillon, M., de Wit, J., Madhusudhan, N., Bolmont, E., Heng, K., Kataria, T., Lewis, N., Hu, R., Krick, J., Stamenković, V., Benneke, B., Kane, S., and Queloz, D. (2016). A map of the large day-night temperature gradient of a super-Earth exoplanet. *Nature*, 532(7598):207–209.

Des Marais, D. J., Harwit, M. O., Jucks, K. W., Kasting, J. F., Lin, D. N. C., Lunine, J. I., Schneider, J., Seager, S., Traub, W. a., and Woolf, N. J. (2002). Remote sensing of planetary properties and biosignatures on extrasolar terrestrial planets. *Astrobiology*, 2(2):153–181.

Ding, F. and Wordsworth, R. D. (2019). A New Line-by-line General Circulation Model for Sim-

ulations of Diverse Planetary Atmospheres: Initial Validation and Application to the Exoplanet GJ 1132b. ApJ, 878(2):117.

Dittmann, J. A., Irwin, J. M., Charbonneau, D., Bonfils, X., Astudillo-Defru, N., Haywood, R. D., Berta-Thompson, Z. K., Newton, E. R., Rodriguez, J. E., Winters, J. G., et al. (2017). A temperate rocky super-earth transiting a nearby cool star. *Nature*, 544(7650):333–336.

Dole, S. H. (1964). *Habitable planets for man*.

Donahue, T. M., Hoffman, J. H., Hodges, R. R., and Watson, A. J. (1982). Venus Was Wet: A Measurement of the Ratio of Deuterium to Hydrogen. *Science*, 216:630–633.

Donahue, T. M. and Pollack, J. B. (1983). *Origin and evolution of the atmosphere of Venus*, pages 1003–1036. University of Arizona Press.

Dong, C., Jin, M., Lingam, M., Airapetian, V. S., Ma, Y., and van der Holst, B. (2018). Atmospheric escape from the TRAPPIST-1 planets and implications for habitability. *Proceedings of the National Academy of Science*, 115(2):260–265.

Dong, C., Lingam, M., Ma, Y., and Cohen, O. (2017). Is Proxima Centauri b Habitable? A Study of Atmospheric Loss. ApJ, 837:L26.

Dorn, C., Mosegaard, K., Grimm, S. L., and Alibert, Y. (2018). Interior Characterization in Multiplanetary Systems: TRAPPIST-1. ApJ, 865(1):20.

Dressing, C. D. and Charbonneau, D. (2015). The Occurrence of Potentially Habitable Planets Orbiting M Dwarfs Estimated from the Full Kepler Dataset and an Empirical Measurement of the Detection Sensitivity. ApJ, 807:45.

Dressing, C. D., Spiegel, D. S., Scharf, C. A., Menou, K., and Raymond, S. N. (2010). Habitable Climates: The Influence of Eccentricity. ApJ, 721(2):1295–1307.

Dunkerton, T. (1978). On the Mean Meridional Mass Motions of the Stratosphere and Mesosphere. *Journal of Atmospheric Sciences*, 35(12):2325–2333.

Egan, H., Jarvinen, R., and Brain, D. (2019). Stellar influence on heavy ion escape from unmagnetized exoplanets. MNRAS, 486(1):1283–1291.

Ehrenreich, D., Vidal-Madjar, A., Widemann, T., Gronoff, G., Tanga, P., Barthélemy, M., Lilensten, J., Lecavelier Des Etangs, A., and Arnold, L. (2012). Transmission spectrum of Venus as a transiting exoplanet. A&A, 537:L2.

Eiler, J. M. (2007). "clumped-isotope" geochemistry—the study of naturally-occurring, multiply-substituted isotopologues. *Earth and Planetary Science Letters*, 262(3-4):309–327.

Ellingson, R. G. and Fouquart, Y. (1991). The intercomparison of radiation codes in climate models: An overview. *Journal of Geophysical Research: Atmospheres*, 96(D5):8925–8927.

Emanuel, K. A. (1991). A Scheme for Representing Cumulus Convection in Large-Scale Models. *Journal of Atmospheric Sciences*, 48(21):2313–2329.

Encrenaz, T., DeWitt, C., Richter, M., Greathouse, T., Fouchet, T., Montmessin, F., Lefèvre, F., Bézard, B., Atreya, S., Aoki, S., et al. (2018). New measurements of d/h on mars using exes aboard sofia. *Å*, 612:A112.

Fauchez, T. J., Turbet, M., Villanueva, G. L., Wolf, E. T., Arney, G., Kopparapu, R. K., Lincowski, A., Mandell, A., de Wit, J., Pidhorodetska, D., Domagal-Goldman, S. D., and Stevenson, K. B. (2019). Impact of Clouds and Hazes on the Simulated JWST Transmission Spectra of Habitable Zone Planets in the TRAPPIST-1 System. ApJ, 887(2):194.

Fauchez, T. J., Turbet, M., Wolf, E. T., Boutle, I., Way, M. J., Del Genio, A. D., Mayne, N. J., Tsigaridis, K., Kopparapu, R. K., Yang, J., Forget, F., Mandell, A., and Domagal Goldman, S. D. (2020). Trappist-1 habitable atmosphere intercomparison (thai): motivations and protocol version 1.0. *Geoscientific Model Development*, 13(2):707–716.

Feng, R., Cooper, G., and Brion, C. E. (1999). Absolute oscillator strengths for hydrogen sulphide:. I. Photoabsorption in the valence-shell and the S 2p and 2s inner-shell regions (4-260 eV). *Chemical Physics*, 244:127–142.

Fleming, E. L., Jackman, C. H., Stolarski, R. S., and Considine, D. B. (1999). Simulation of stratospheric tracers using an improved empirically based two-dimensional model transport formulation. J. Geophys. Res., 104(D19):23911–23934.

Foley, B. J. and Smye, A. J. (2018). Carbon Cycling and Habitability of Earth-Sized Stagnant Lid Planets. *Astrobiology*, 18(7):873–896.

Forget, F. and Pierrehumbert, R. T. (1997). Warming early Mars with carbon dioxide clouds that scatter infrared radiation. *Science*, 278(5341):1273–1276.

Forget, F., Wordsworth, R., Millour, E., Madeleine, J. B., Kerber, L., Leconte, J., Marcq, E., and Haberle, R. M. (2013). 3D modelling of the early martian climate under a denser CO 2 atmosphere: Temperatures and CO 2 ice clouds. *Icarus*, 222(1):81–99.

France, K., Froning, C. S., Linsky, J. L., Roberge, A., Stocke, J. T., Tian, F., Bushinsky, R., Désert, J.-M., Mauas, P., Vieytes, M., and Walkowicz, L. M. (2013). the Ultraviolet Radiation Environment Around M Dwarf Exoplanet Host Stars. ApJ, 763(2):149.

Fujii, Y., Angerhausen, D., Deitrick, R., Domagal-Goldman, S., Grenfell, J. L., Hori, Y., Kane, S. R., Pallé, E., Rauer, H., Siegler, N., Stapelfeldt, K., and Stevenson, K. B. (2018). Exoplanet Biosignatures: Observational Prospects. *Astrobiology*, 18:739–778.

Fulton, B. J., Petigura, E. A., Howard, A. W., Isaacson, H., Marcy, G. W., Cargile, P. A., Hebb, L., Weiss, L. M., Johnson, J. A., Morton, T. D., Sinukoff, E., Crossfield, I. J. M., and Hirsch, L. A. (2017). The California-Kepler Survey. III. A Gap in the Radius Distribution of Small Planets. AJ, 154:109.

Gaia Collaboration, Brown, A. G. A., Vallenari, A., Prusti, T., de Bruijne, J. H. J., Babusiaux, C., Bailer-Jones, C. A. L., Biermann, M., Evans, D. W., Eyer, L., Jansen, F., Jordi, C., Klioner, S. A., Lammers, U., Lindegren, L., Luri, X., Mignard, F., Panem, C., Pourbaix, D., Randich, S., Sartoretti, P., Siddiqui, H. I., Soubiran, C., van Leeuwen, F., Walton, N. A., Arenou, F., Bastian, U., Cropper, M., Drimmel, R., Katz, D., Lattanzi, M. G., Bakker, J., Cacciari, C., Castañeda, J.,

Chaoul, L., Cheek, N., De Angeli, F., Fabricius, C., Guerra, R., Holl, B., Masana, E., Messineo, R., Mowlavi, N., Nienartowicz, K., Panuzzo, P., Portell, J., Riello, M., Seabroke, G. M., Tanga, P., Thévenin, F., Gracia-Abril, G., Comoretto, G., Garcia-Reinaldos, M., Teyssier, D., Altmann, M., Andrae, R., Audard, M., Bellas-Velidis, I., Benson, K., Berthier, J., Blomme, R., Burgess, P., Busso, G., Carry, B., Cellino, A., Clementini, G., Clotet, M., Creevey, O., Davidson, M., De Ridder, J., Delchambre, L., Dell'Oro, A., Ducourant, C., Fernández-Hernández, J., Fouesneau, M., Frémat, Y., Galluccio, L., García-Torres, M., González-Núñez, J., González-Vidal, J. J., Gosset, E., Guy, L. P., Halbwachs, J. L., Hambly, N. C., Harrison, D. L., Hernández, J., Hestroffer, D., Hodgkin, S. T., Hutton, A., Jasniewicz, G., Jean-Antoine-Piccolo, A., Jordan, S., Korn, A. J., Krone-Martins, A., Lanzafame, A. C., Lebzelter, T., Löffler, W., Manteiga, M., Marrese, P. M., Martín-Fleitas, J. M., Moitinho, A., Mora, A., Muinonen, K., Osinde, J., Pancino, E., Pauwels, T., Petit, J. M., Recio-Blanco, A., Richards, P. J., Rimoldini, L., Robin, A. C., Sarro, L. M., Siopis, C., Smith, M., Sozzetti, A., Süveges, M., Torra, J., van Reeven, W., Abbas, U., Abreu Aramburu, A., Accart, S., Aerts, C., Altavilla, G., Álvarez, M. A., Alvarez, R., Alves, J., Anderson, R. I., Andrei, A. H., Anglada Varela, E., Antiche, E., Antoja, T., Arcay, B., Astraatmadja, T. L., Bach, N., Baker, S. G., Balaguer-Núñez, L., Balm, P., Barache, C., Barata, C., Barbato, D., Barblan, F., Barklem, P. S., Barrado, D., Barros, M., Barstow, M. A., Bartholomé Muñoz, S., Bassilana, J. L., Becciani, U., Bellazzini, M., Berihuete, A., Bertone, S., Bianchi, L., Bienaymé, O., Blanco-Cuaresma, S., Boch, T., Boeche, C., Bombrun, A., Borrachero, R., Bossini, D., Bouquillon, S., Bourda, G., Bragaglia, A., Bramante, L., Breddels, M. A., Bressan, A., Brouillet, N., Brüsemeister, T., Brugaletta, E., Bucciarelli, B., Burlacu, A., Busonero, D., Butkevich, A. G., Buzzi, R., Caffau, E., Cancelliere, R., Cannizzaro, G., Cantat-Gaudin, T., Carballo, R., Carlucci, T., Carrasco, J. M., Casamiquela, L., Castellani, M., Castro-Ginard, A., Charlot, P., Chemin, L., Chiavassa, A., Cocozza, G., Costigan, G., Cowell, S., Crifo, F., Crosta, M., Crowley, C., Cuypers, J., Dafonte, C., Damerdji, Y., Dapergolas, A., David, P., David, M., de Laverny, P., De Luise, F., De March, R., de Martino, D., de Souza, R., de Torres, A., Debosscher, J., del Pozo, E., Delbo, M., Delgado, A., Delgado, H. E., Di Matteo, P., Diakite, S., Diener, C., Distefano, E., Dolding, C., Drazinos, P., Durán, J., Edvardsson, B., Enke, H., Eriksson,

K., Esquej, P., Eynard Bontemps, G., Fabre, C., Fabrizio, M., Faigler, S., Falcão, A. J., Farràs Casas, M., Federici, L., Fedorets, G., Fernique, P., Figueras, F., Filippi, F., Findeisen, K., Fonti, A., Fraile, E., Fraser, M., Frézouls, B., Gai, M., Galleti, S., Garabato, D., García-Sedano, F., Garofalo, A., Garralda, N., Gavel, A., Gavras, P., Gerssen, J., Geyer, R., Giacobbe, P., Gilmore, G., Girona, S., Giuffrida, G., Glass, F., Gomes, M., Granvik, M., Gueguen, A., Guerrier, A., Guiraud, J., Gutiérrez-Sánchez, R., Haigron, R., Hatzidimitriou, D., Hauser, M., Haywood, M., Heiter, U., Helmi, A., Heu, J., Hilger, T., Hobbs, D., Hofmann, W., Holland, G., Huckle, H. E., Hypki, A., Icardi, V., Janßen, K., Jevardat de Fombelle, G., Jonker, P. G., Juhász, Á. L., Julbe, F., Karampelas, A., Kewley, A., Klar, J., Kochoska, A., Kohley, R., Kolenberg, K., Kontizas, M., Kontizas, E., Koposov, S. E., Kordopatis, G., Kostrzewa-Rutkowska, Z., Koubsky, P., Lambert, S., Lanza, A. F., Lasne, Y., Lavigne, J. B., Le Fustec, Y., Le Poncin-Lafitte, C., Lebreton, Y., Leccia, S., Leclerc, N., Lecoeur-Taibi, I., Lenhardt, H., Leroux, F., Liao, S., Licata, E., Lindstrøm, H. E. P., Lister, T. A., Livanou, E., Lobel, A., López, M., Managau, S., Mann, R. G., Mantelet, G., Marchal, O., Marchant, J. M., Marconi, M., Marinoni, S., Marschalkó, G., Marshall, D. J., Martino, M., Marton, G., Mary, N., Massari, D., Matijevič, G., Mazeh, T., McMillan, P. J., Messina, S., Michalik, D., Millar, N. R., Molina, D., Molinaro, R., Molnár, L., Montegriffo, P., Mor, R., Morbidelli, R., Morel, T., Morris, D., Mulone, A. F., Muraveva, T., Musella, I., Nelemans, G., Nicastro, L., Noval, L., O'Mullane, W., Ordénovic, C., Ordóñez-Blanco, D., Osborne, P., Pagani, C., Pagano, I., Pailler, F., Palacin, H., Palaversa, L., Panahi, A., Pawlak, M., Piersimoni, A. M., Pineau, F. X., Plachy, E., Plum, G., Poggio, E., Poujoulet, E., Prša, A., Pulone, L., Racero, E., Ragaini, S., Rambaux, N., Ramos-Lerate, M., Regibo, S., Reylé, C., Riclet, F., Ripepi, V., Riva, A., Rivard, A., Rixon, G., Roegiers, T., Roelens, M., Romero-Gómez, M., Rowell, N., Royer, F., Ruiz-Dern, L., Sadowski, G., Sagristà Sellés, T., Sahlmann, J., Salgado, J., Salguero, E., Sanna, N., Santana-Ros, T., Sarasso, M., Savietto, H., Schultheis, M., Sciacca, E., Segol, M., Segovia, J. C., Ségransan, D., Shih, I. C., Siltala, L., Silva, A. F., Smart, R. L., Smith, K. W., Solano, E., Solitro, F., Sordo, R., Soria Nieto, S., Souchay, J., Spagna, A., Spoto, F., Stampa, U., Steele, I. A., Steidelmüller, H., Stephenson, C. A., Stoev, H., Suess, F. F., Surdej, J., Szabados, L., Szegedi-Elek, E., Tapiador, D., Taris, F., Tauran, G., Taylor, M. B., Teixeira,

R., Terrett, D., Teyssand ier, P., Thuillot, W., Titarenko, A., Torra Clotet, F., Turon, C., Ulla, A., Utrilla, E., Uzzi, S., Vaillant, M., Valentini, G., Valette, V., van Elteren, A., Van Hemelryck, E., van Leeuwen, M., Vaschetto, M., Vecchiato, A., Veljanoski, J., Viala, Y., Vicente, D., Vogt, S., von Essen, C., Voss, H., Votruba, V., Voutsinas, S., Walmsley, G., Weiler, M., Wertz, O., Wevers, T., Wyrzykowski, Ł., Yoldas, A., Žerjal, M., Ziaeepour, H., Zorec, J., Zschocke, S., Zucker, S., Zurbach, C., and Zwitter, T. (2018). Gaia Data Release 2. Summary of the contents and survey properties. A&A, 616:A1.

Gaia Collaboration, Prusti, T., de Bruijne, J. H. J., Brown, A. G. A., Vallenari, A., Babusiaux, C., Bailer-Jones, C. A. L., Bastian, U., Biermann, M., Evans, D. W., Eyer, L., Jansen, F., Jordi, C., Klioner, S. A., Lammers, U., Lindegren, L., Luri, X., Mignard, F., Milligan, D. J., Panem, C., Poinsignon, V., Pourbaix, D., Randich, S., Sarri, G., Sartoretti, P., Siddiqui, H. I., Soubiran, C., Valette, V., van Leeuwen, F., Walton, N. A., Aerts, C., Arenou, F., Cropper, M., Drimmel, R., Høg, E., Katz, D., Lattanzi, M. G., O'Mullane, W., Grebel, E. K., Holland, A. D., Huc, C., Passot, X., Bramante, L., Cacciari, C., Castañeda, J., Chaoul, L., Cheek, N., De Angeli, F., Fabricius, C., Guerra, R., Hernández, J., Jean-Antoine-Piccolo, A., Masana, E., Messineo, R., Mowlavi, N., Nienartowicz, K., Ordóñez-Blanco, D., Panuzzo, P., Portell, J., Richards, P. J., Riello, M., Seabroke, G. M., Tanga, P., Thévenin, F., Torra, J., Els, S. G., Gracia-Abril, G., Comoretto, G., Garcia-Reinaldos, M., Lock, T., Mercier, E., Altmann, M., Andrae, R., Astraatmadja, T. L., Bellas-Velidis, I., Benson, K., Berthier, J., Blomme, R., Busso, G., Carry, B., Cellino, A., Clementini, G., Cowell, S., Creevey, O., Cuypers, J., Davidson, M., De Ridder, J., de Torres, A., Delchambre, L., Dell'Oro, A., Ducourant, C., Frémat, Y., García-Torres, M., Gosset, E., Halbwachs, J. L., Hambly, N. C., Harrison, D. L., Hauser, M., Hestroffer, D., Hodgkin, S. T., Huckle, H. E., Hutton, A., Jasniewicz, G., Jordan, S., Kontizas, M., Korn, A. J., Lanzafame, A. C., Manteiga, M., Moitinho, A., Muinonen, K., Osinde, J., Pancino, E., Pauwels, T., Petit, J. M., Recio-Blanco, A., Robin, A. C., Sarro, L. M., Siopis, C., Smith, M., Smith, K. W., Sozzetti, A., Thuillot, W., van Reeven, W., Viala, Y., Abbas, U., Abreu Aramburu, A., Accart, S., Aguado, J. J., Allan, P. M., Allasia, W., Altavilla, G., Álvarez, M. A., Alves, J., Anderson,

R. I., Andrei, A. H., Anglada Varela, E., Antiche, E., Antoja, T., Antón, S., Arcay, B., Atzei, A., Ayache, L., Bach, N., Baker, S. G., Balaguer-Núñez, L., Barache, C., Barata, C., Barbier, A., Barblan, F., Baroni, M., Barrado y Navascués, D., Barros, M., Barstow, M. A., Becciani, U., Bellazzini, M., Bellei, G., Bello García, A., Belokurov, V., Bendjoya, P., Berihuete, A., Bianchi, L., Bienaymé, O., Billebaud, F., Blagorodnova, N., Blanco-Cuaresma, S., Boch, T., Bombrun, A., Borrachero, R., Bouquillon, S., Bourda, G., Bouy, H., Bragaglia, A., Breddels, M. A., Brouillet, N., Brüsemeister, T., Bucciarelli, B., Budnik, F., Burgess, P., Burgon, R., Burlacu, A., Busonero, D., Buzzi, R., Caffau, E., Cambras, J., Campbell, H., Cancelliere, R., Cantat-Gaudin, T., Carlucci, T., Carrasco, J. M., Castellani, M., Charlot, P., Charnas, J., Charvet, P., Chassat, F., Chiavassa, A., Clotet, M., Cocozza, G., Collins, R. S., Collins, P., Costigan, G., Crifo, F., Cross, N. J. G., Crosta, M., Crowley, C., Dafonte, C., Damerdji, Y., Dapergolas, A., David, P., David, M., De Cat, P., de Felice, F., de Laverny, P., De Luise, F., De March, R., de Martino, D., de Souza, R., Debosscher, J., del Pozo, E., Delbo, M., Delgado, A., Delgado, H. E., di Marco, F., Di Matteo, P., Diakite, S., Distefano, E., Dolding, C., Dos Anjos, S., Drazinos, P., Durán, J., Dzigan, Y., Ecale, E., Edvardsson, B., Enke, H., Erdmann, M., Escolar, D., Espina, M., Evans, N. W., Eynard Bontemps, G., Fabre, C., Fabrizio, M., Faigler, S., Falcão, A. J., Farràs Casas, M., Faye, F., Federici, L., Fedorets, G., Fernández-Hernández, J., Fernique, P., Fienga, A., Figueras, F., Filippi, F., Findeisen, K., Fonti, A., Fouesneau, M., Fraile, E., Fraser, M., Fuchs, J., Furnell, R., Gai, M., Galleti, S., Galluccio, L., Garabato, D., García-Sedano, F., Garé, P., Garofalo, A., Garralda, N., Gavras, P., Gerssen, J., Geyer, R., Gilmore, G., Girona, S., Giuffrida, G., Gomes, M., González-Marcos, A., González-Núñez, J., González-Vidal, J. J., Granvik, M., Guerrier, A., Guillout, P., Guiraud, J., Gúrpide, A., Gutiérrez-Sánchez, R., Guy, L. P., Haigron, R., Hatzidimitriou, D., Haywood, M., Heiter, U., Helmi, A., Hobbs, D., Hofmann, W., Holl, B., Holland , G., Hunt, J. A. S., Hypki, A., Icardi, V., Irwin, M., Jevardat de Fombelle, G., Jofré, P., Jonker, P. G., Jorissen, A., Julbe, F., Karampelas, A., Kochoska, A., Kohley, R., Kolenberg, K., Kontizas, E., Koposov, S. E., Kordopatis, G., Koubsky, P., Kowalczyk, A., Krone-Martins, A., Kudryashova, M., Kull, I., Bachchan, R. K., Lacoste-Seris, F., Lanza, A. F., Lavigne, J. B., Le Poncin-Lafitte, C., Lebreton, Y., Lebzelter, T., Leccia, S., Leclerc, N., Lecoeur-Taibi, I., Lemaitre, V., Lenhardt,

H., Leroux, F., Liao, S., Licata, E., Lindstrøm, H. E. P., Lister, T. A., Livanou, E., Lobel, A., Löffler, W., López, M., Lopez-Lozano, A., Lorenz, D., Loureiro, T., MacDonald, I., Magalhães Fernandes, T., Managau, S., Mann, R. G., Mantelet, G., Marchal, O., Marchant, J. M., Marconi, M., Marie, J., Marinoni, S., Marrese, P. M., Marschalkó, G., Marshall, D. J., Martín-Fleitas, J. M., Martino, M., Mary, N., Matijevič, G., Mazeh, T., McMillan, P. J., Messina, S., Mestre, A., Michalik, D., Millar, N. R., Miranda, B. M. H., Molina, D., Molinaro, R., Molinaro, M., Molnár, L., Moniez, M., Montegriffo, P., Monteiro, D., Mor, R., Mora, A., Morbidelli, R., Morel, T., Morgenthaler, S., Morley, T., Morris, D., Mulone, A. F., Muraveva, T., Musella, I., Narbonne, J., Nelemans, G., Nicastro, L., Noval, L., Ordénovic, C., Ordieres-Meré, J., Osborne, P., Pagani, C., Pagano, I., Pailler, F., Palacin, H., Palaversa, L., Parsons, P., Paulsen, T., Pecoraro, M., Pedrosa, R., Pentikäinen, H., Pereira, J., Pichon, B., Piersimoni, A. M., Pineau, F. X., Plachy, E., Plum, G., Poujoulet, E., Prša, A., Pulone, L., Ragaini, S., Rago, S., Rambaux, N., Ramos-Lerate, M., Ranalli, P., Rauw, G., Read, A., Regibo, S., Renk, F., Reylé, C., Ribeiro, R. A., Rimoldini, L., Ripepi, V., Riva, A., Rixon, G., Roelens, M., Romero-Gómez, M., Rowell, N., Royer, F., Rudolph, A., Ruiz-Dern, L., Sadowski, G., Sagristà Sellés, T., Sahlmann, J., Salgado, J., Salguero, E., Sarasso, M., Savietto, H., Schnorhk, A., Schultheis, M., Sciacca, E., Segol, M., Segovia, J. C., Segransan, D., Serpell, E., Shih, I. C., Smareglia, R., Smart, R. L., Smith, C., Solano, E., Solitro, F., Sordo, R., Soria Nieto, S., Souchay, J., Spagna, A., Spoto, F., Stampa, U., Steele, I. A., Steidelmüller, H., Stephenson, C. A., Stoev, H., Suess, F. F., Süveges, M., Surdej, J., Szabados, L., Szegedi-Elek, E., Tapiador, D., Taris, F., Tauran, G., Taylor, M. B., Teixeira, R., Terrett, D., Tingley, B., Trager, S. C., Turon, C., Ulla, A., Utrilla, E., Valentini, G., van Elteren, A., Van Hemelryck, E., van Leeuwen, M., Varadi, M., Vecchiato, A., Veljanoski, J., Via, T., Vicente, D., Vogt, S., Voss, H., Votruba, V., Voutsinas, S., Walmsley, G., Weiler, M., Weingrill, K., Werner, D., Wevers, T., Whitehead, G., Wyrzykowski, Ł., Yoldas, A., Žerjal, M., Zucker, S., Zurbach, C., Zwitter, T., Alecu, A., Allen, M., Allende Prieto, C., Amorim, A., Anglada-Escudé, G., Arsenijevic, V., Azaz, S., Balm, P., Beck, M., Bernstein, H. H., Bigot, L., Bijaoui, A., Blasco, C., Bonfigli, M., Bono, G., Boudreault, S., Bressan, A., Brown, S., Brunet, P. M., Bunclark, P., Buonanno, R., Butkevich, A. G., Carret, C., Carrion, C., Chemin,

L., Chéreau, F., Corcione, L., Darmigny, E., de Boer, K. S., de Teodoro, P., de Zeeuw, P. T., Delle Luche, C., Domingues, C. D., Dubath, P., Fodor, F., Frézouls, B., Fries, A., Fustes, D., Fyfe, D., Gallardo, E., Gallegos, J., Gardiol, D., Gebran, M., Gomboc, A., Gómez, A., Grux, E., Gueguen, A., Heyrovsky, A., Hoar, J., Iannicola, G., Isasi Parache, Y., Janotto, A. M., Joliet, E., Jonckheere, A., Keil, R., Kim, D. W., Klagyivik, P., Klar, J., Knude, J., Kochukhov, O., Kolka, I., Kos, J., Kutka, A., Lainey, V., LeBouquin, D., Liu, C., Loreggia, D., Makarov, V. V., Marseille, M. G., Martayan, C., Martinez-Rubi, O., Massart, B., Meynadier, F., Mignot, S., Munari, U., Nguyen, A. T., Nordlander, T., Ocvirk, P., O'Flaherty, K. S., Olias Sanz, A., Ortiz, P., Osorio, J., Oszkiewicz, D., Ouzounis, A., Palmer, M., Park, P., Pasquato, E., Peltzer, C., Peralta, J., Péturaud, F., Pieniluoma, T., Pigozzi, E., Poels, J., Prat, G., Prod'homme, T., Raison, F., Rebordao, J. M., Risquez, D., Rocca-Volmerange, B., Rosen, S., Ruiz-Fuertes, M. I., Russo, F., Sembay, S., Serraller Vizcaino, I., Short, A., Siebert, A., Silva, H., Sinachopoulos, D., Slezak, E., Soffel, M., Sosnowska, D., Straižys, V., ter Linden, M., Terrell, D., Theil, S., Tiede, C., Troisi, L., Tsalmantza, P., Tur, D., Vaccari, M., Vachier, F., Valles, P., Van Hamme, W., Veltz, L., Virtanen, J., Wallut, J. M., Wichmann, R., Wilkinson, M. I., Ziaeepour, H., and Zschocke, S. (2016). The Gaia mission. A&A, 595:A1.

Gaidos, E. and Mann, A. W. (2012). Objects in kepler's mirror may be larger than they appear: Bias and selection effects in transiting planet surveys. *The Astrophysical Journal*, 762(1):41.

Gao, P., Hu, R., Robinson, T. D., Li, C., and Yung, Y. L. (2015). STABILITY OF CO_2 ATMOSPHERES ON DESICCATED M DWARF EXOPLANETS. ApJ, 806(2):249.

Gao, P., Zhang, X., Crisp, D., Bardeen, C. G., and Yung, Y. L. (2014). Bimodal distribution of sulfuric acid aerosols in the upper haze of Venus. Icarus, 231:83–98.

Garcia-Sage, K., Glocer, A., Drake, J. J., Gronoff, G., and Cohen, O. (2017). On the Magnetic Protection of the Atmosphere of Proxima Centauri b. ApJ, 844:L13.

Gaudi, B. S., Seager, S., Mennesson, B., Kiessling, A., Warfield, K., Kuan, G., Cahoy, K., Clarke,

J. T., Domagal-Goldman, S., and Feinberg, L. (2018). The Habitable Exoplanet Observatory (HabEx) Mission Concept Study Interim Report. *arXiv e-prints*, page arXiv:1809.09674.

Giauque, W. F. and Egan, C. J. (1937). Carbon Dioxide. The Heat Capacity and Vapor Pressure of the Solid. The Heat of Sublimation. Thermodynamic and Spectroscopic Values of the Entropy. J. Chem. Phys., 5(1):45–54.

Gille, J. C., Lyjak, L. V., and Smith, A. K. (1987). The Global Residual Mean Circulation in the Middle Atmosphere for the Northern Winter Period. *Journal of Atmospheric Sciences*, 44(10):1437–1454.

Gillmann, C., Chassefière, E., and Lognonné, P. (2009). A consistent picture of early hydrodynamic escape of venus atmosphere explaining present ne and ar isotopic ratios and low oxygen atmospheric content. *Earth and Planetary Science Letters*, 286(3-4):503–513.

Gillon, M., Jehin, E., Fumel, A., Magain, P., and Queloz, D. (2013). TRAPPIST-UCDTS: A prototype search for habitable planets transiting ultra-cool stars. In *European Physical Journal Web of Conferences*, volume 47, page 03001.

Gillon, M., Jehin, E., Lederer, S. M., Delrez, L., de Wit, J., Burdanov, A., Van Grootel, V., Burgasser, A. J., Triaud, A. H. M. J., Opitom, C., Demory, B.-O., Sahu, D. K., Bardalez Gagliuffi, D., Magain, P., and Queloz, D. (2016). Temperate Earth-sized planets transiting a nearby ultra-cool dwarf star. *Nature*, 533(7602):221–224.

Gillon, M., Jehin, E., Magain, P., Chantry, V., Hutsemékers, D., Manfroid, J., Queloz, D., and Udry, S. (2011). TRAPPIST: a robotic telescope dedicated to the study of planetary systems. In *European Physical Journal Web of Conferences*, volume 11 of *European Physical Journal Web of Conferences*, page 06002.

Gillon, M., Triaud, A. H. M. J., Demory, B.-O., Jehin, E., Agol, E., Deck, K. M., Lederer, S. M., de Wit, J., Burdanov, A., Ingalls, J. G., Bolmont, E., Leconte, J., Raymond, S. N., Selsis, F.,

Turbet, M., Barkaoui, K., Burgasser, A., Burleigh, M. R., Carey, S. J., Chaushev, A., Copperwheat, C. M., Delrez, L., Fernandes, C. S., Holdsworth, D. L., Kotze, E. J., Van Grootel, V., Almleaky, Y., Benkhaldoun, Z., Magain, P., and Queloz, D. (2017). Seven temperate terrestrial planets around the nearby ultracool dwarf star TRAPPIST-1. *Nature*, 542(7642):456–460.

Glein, C. R., Desch, S. J., and Shock, E. L. (2009). The absence of endogenic methane on Titan and its implications for the origin of atmospheric nitrogen. Icarus, 204(2):637–644.

Godolt, M., Grenfell, J. L., Kitzmann, D., Kunze, M., Langematz, U., Patzer, A. B. C., Rauer, H., and Stracke, B. (2016). Assessing the habitability of planets with Earth-like atmospheres with 1D and 3D climate modeling. A&A, 592:A36.

Goldblatt, C. (2016). Tutorial models of the climate and habitability of Proxima Centauri b: a thin atmosphere is sufficient to distribute heat given low stellar flux. *ArXiv e-prints*.

Goldblatt, C., Robinson, T. D., Zahnle, K. J., and Crisp, D. (2013). Low simulated radiation limit for runaway greenhouse climates. *Nature Geoscience*, 6(8):661–667.

Gordon, I. E., Rothman, L. S., Hill, C., Kochanov, R. V., Tan, Y., Bernath, P. F., Birk, M., Boudon, V., Campargue, A., Chance, K. V., Drouin, B. J., Flaud, J. M., Gamache, R. R., Hodges, J. T., Jacquemart, D., Perevalov, V. I., Perrin, A., Shine, K. P., Smith, M. A. H., Tennyson, J., Toon, G. C., Tran, H., Tyuterev, V. G., Barbe, A., Császár, A. G., Devi, V. M., Furtenbacher, T., Harrison, J. J., Hartmann, J. M., Jolly, A., Johnson, T. J., Karman, T., Kleiner, I., Kyuberis, A. A., Loos, J., Lyulin, O. M., Massie, S. T., Mikhailenko, S. N., Moazzen-Ahmadi, N., Müller, H. S. P., Naumenko, O. V., Nikitin, A. V., Polyansky, O. L., Rey, M., Rotger, M., Sharpe, S. W., Sung, K., Starikova, E., Tashkun, S. A., Auwera, J. V., Wagner, G., Wilzewski, J., Wcisło, P., Yu, S., and Zak, E. J. (2017). The HITRAN2016 molecular spectroscopic database. *Journal of Quantitative Spectroscopy and Radiative Transfer*, 203:3–69.

Greenblatt, G. D., Orlando, J. J., Burkholder, J. B., and Ravishankara, A. R. (1990). Absorption measurements of oxygen between 330 and 1140 nm. J. Geophys. Res., 95:18577–18582.

Greene, T. P., Line, M. R., Montero, C., Fortney, J. J., Lustig-Yaeger, J., and Luther, K. (2016). Characterizing transiting exoplanet atmospheres with JWST. ApJ, 817(1):17.

Grenfell, J. L., Gebauer, S., V. Paris, P., Godolt, M., and Rauer, H. (2014). Sensitivity of biosignatures on Earth-like planets orbiting in the habitable zone of cool M-dwarf Stars to varying stellar UV radiation and surface biomass emissions. Planet. Space Sci., 98:66–76.

Grenfell, J. L., Stracke, B., von Paris, P., Patzer, B., Titz, R., Segura, A., and Rauer, H. (2007). The response of atmospheric chemistry on earthlike planets around F, G and K Stars to small variations in orbital distance. Planet. Space Sci., 55:661–671.

Grimm, S. L., Demory, B.-O., Gillon, M., Dorn, C., Agol, E., Burdanov, A., Delrez, L., Sestovic, M., Triaud, A. H. M. J., Turbet, M., Bolmont, É., Caldas, A., Wit, J. d., Jehin, E., Leconte, J., Raymond, S. N., Grootel, V. V., Burgasser, A. J., Carey, S., Fabrycky, D., Heng, K., Hernandez, D. M., Ingalls, J. G., Lederer, S., Selsis, F., and Queloz, D. (2018). The nature of the TRAPPIST-1 exoplanets. A&A, 613:A68.

Grinspoon, D. H. (1993). Implications of the high D/H ratio for the sources of water in Venus' atmosphere. Nature, 363:428–431.

Gruszka, M. and Borysow, A. (1997). Roto-Translational Collision-Induced Absorption of CO $_2$for the Atmosphere of Venus at Frequencies from 0 to 250 cm $^{-1}$, at Temperatures from 200 to 800 K. Icarus, 129:172–177.

Guillot, T., Burrows, A., Hubbard, W. B., Lunine, J. I., and Saumon, D. (1996). Giant Planets at Small Orbital Distances. ApJ, 459:L35.

Guzmán-Marmolejo, A., Segura, A., and Escobar-Briones, E. (2013). Abiotic Production of Methane in Terrestrial Planets full access. *Astrobiology*, 13:550–559.

Haberle, R. M., McKay, C. P., Tyler, D., and Reynolds, R. T. (1996). Can Synchronously Rotating Planets Support An Atmosphere? In Doyle, L. R., editor, *Circumstellar Habitable Zones*, page 29.

Hagemann, R., Nief, G., and Roth, E. (1970). Absolute isotopic scale for deuterium analysis of natural waters. absolute d/h ratio for smow. *Tellus*, 22(6):712–715.

Hale, G. M. and Querry, M. R. (1973). Optical constants of water in the 200-nm to 200-micrometer wavelength region. Appl. Opt., 12:555.

Halevy, I., Pierrehumbert, R. T., and Schrag, D. P. (2009). Radiative transfer in CO_2-rich paleoatmospheres. *Journal of Geophysical Research (Atmospheres)*, 114(D18):D18112.

Hamano, K., Abe, Y., and Genda, H. (2013). Emergence of two types of terrestrial planet on solidification of magma ocean. Nature, 497:607–610.

Haqq-Misra, J., Kopparapu, R. K., Batalha, N. E., Harman, C. E., and Kasting, J. F. (2016). Limit Cycles Can Reduce the Width of the Habitable Zone. ApJ, 827:120.

Haqq-Misra, J., Wolf, E. T., Joshi, M., Zhang, X., and Kopparapu, R. K. (2018). Demarcating Circulation Regimes of Synchronously Rotating Terrestrial Planets within the Habitable Zone. ApJ, 852(2):67.

Hartle, R. E. and Taylor, H. A. (1983). Identification of deuterium ions in the ionosphere of Venus. Geophys. Res. Lett., 10:965–968.

Hartmann, J. M., Boulet, C., and Toon, G. C. (2017). Collision-induced absorption by N_2 near 2.16 μm: Calculations, model, and consequences for atmospheric remote sensing. *Journal of Geophysical Research (Atmospheres)*, 122(4):2419–2428.

Hashimoto, G. L., Abe, Y., and Sasaki, S. (1997). Co2 amount on venus constrained by a criterion of topographic-greenhouse instability. *Geophysical research letters*, 24(3):289–292.

Hastenrath, S. (1980). Heat Budget of Tropical Ocean and Atmosphere. *Journal of Physical Oceanography*, 10(2):159–170.

Hauglustaine, D. A., Granier, C., Brasseur, G. P., and MéGie, G. (1994). The importance of atmospheric chemistry in the calculation of radiative forcing on the climate system. J. Geophys. Res., 99(D1):1173–1186.

He, C., Hörst, S. M., Lewis, N. K., Yu, X., Moses, J. I., Kempton, E. M. R., McGuiggan, P., Morley, C. V., Valenti, J. A., and Vuitton, V. (2018). Laboratory Simulations of Haze Formation in the Atmospheres of Super-Earths and Mini-Neptunes: Particle Color and Size Distribution. ApJ, 856(1):L3.

Henry, T. J., Jao, W.-C., Subasavage, J. P., Beaulieu, T. D., Ianna, P. A., Costa, E., and Méndez, R. A. (2006). The Solar Neighborhood. XVII. Parallax Results from the CTIOPI 0.9 m Program: 20 New Members of the RECONS 10 Parsec Sample. AJ, 132:2360–2371.

Hermans, C., Vandaele, A. C., Carleer, M., Fally, S., Colin, R., Jenouvrier, A., Coquart, B., and Mérienne, M.-F. (1999). Absorption cross-sections of atmospheric constituents: No 2, o 2, and h 2 o. *Environmental Science and Pollution Research*, 6(3):151–158.

Hinson, D. P. and Wilson, R. J. (2004). Temperature inversions, thermal tides, and water ice clouds in the Martian tropics. *Journal of Geophysical Research (Planets)*, 109:E01002.

Hintze, P. E., Kjaergaard, H. G., Vaida, V., and Burkholder, J. B. (2003). Vibrational and Electronic Spectroscopy of Sulfuric Acid Vapor. *Journal of Physical Chemistry A*, 107:1112–1118.

Hirono, M. and Nakazawa, T. (1982). The shape of spectral lines with combined impact and statistical broadenings. *Journal of the Physical Society of Japan*, 51:265–268.

Hodges, R. (1969). Eddy diffusion coefficients due to instabilities in internal gravity waves. *Journal of Geophysical Research*, 74(16):4087–4090.

Hoffman, J. H., Hodges, R. R., Donahue, T. M., and McElroy, M. M. (1980). Composition of the Venus lower atmosphere from the Pioneer Venus mass spectrometer. *Journal of Geophysical Research*, 85:7882–7890.

Hogan, R. J. and Hirahara, S. (2015). *Effect of solar zenith angle specification on mean shortwave fluxes and stratospheric temperatures*. European Centre for Medium-Range Weather Forecasts. Technical Memorandum No. 758.

Holtslag, A. A. M. and Moeng, C.-H. (1991). Eddy Diffusivity and Countergradient Transport in the Convective Atmospheric Boundary Layer. *Journal of Atmospheric Sciences*, 48(14):1690–1700.

Hoyle, F. (1955). *Frontiers of astronomy.*

Hu, L., Yvon-Lewis, S. A., Liu, Y., Salisbury, J. E., and O'Hern, J. E. (2010). Coastal emissions of methyl bromide and methyl chloride along the eastern Gulf of Mexico and the east coast of the United States. *Global Biogeochemical Cycles*, 24(1):GB1007.

Hu, R., Cahoy, K., and Zuber, M. T. (2012). Condensation Above the North and South Poles As Revealed By Radio Occultation, Climate Sounder, and Laser Ranging Observations. J. Geophys. Res., 117:1–21.

Hu, R. and Seager, S. (2014). Photochemistry in Terrestrial Exoplanet Atmospheres. III. Photochemistry and Thermochemistry in Thick Atmospheres on Super Earths and Mini Neptunes. ApJ, 784:63.

Hu, Y. and Yang, J. (2014). Role of ocean heat transport in climates of tidally locked exoplanets around M dwarf stars. *Proc. Natl. Acad. Sci. U. S. A.*, 111(2):629–34.

Huang, S.-S. (1959). Occurrence of Life in the Universe. *American Scientist*, 47(3):397–402.

Huang, S.-S. (1960). Life Outside the Solar System. *Scientific American*, 202(4):55–63.

Huang, X., Schwenke, D. W., Freedman, R. S., and Lee, T. J. (2017). Ames-2016 line lists for 13 isotopologues of CO_2: Updates, consistency, and remaining issues. *Journal of Quantitative Spectroscopy and Radiative Transfer*, 203:224–241.

Hubinger, S. and Nee, J. (1994). Photoabsorpton spectrum for oclo between 125 and 470 nm. *Chemical physics*, 181(1-2):247–257.

Hunt, B. G. (1982). The impact of large variations of the earth's obliquity on the climate. *Journal of the Meteorological Society of Japan. Ser. II*, 60(1):309–318.

Hunten, D. M. (1975). Estimates of stratospheric pollution by an analytic model. *Proceedings of the National Academy of Science*, 72:4711–4715.

Hunten, D. M. (1982). Thermal and nonthermal escape mechanisms for terrestrial bodies. *Planetary and Space Science*, 30(8):773–783.

Hunten, D. M., Pepin, R. O., and Walker, J. C. G. (1987). Mass fractionation in hydrodynamic escape. Icarus, 69:532–549.

Ignatiev, N. i., Moroz, V. i., Zasova, L. V., and Khatuntsev, I. v. (1999). Water vapour in the middle atmosphere of Venus:. An improved treatment of the Venera 15 ir spectra. *Planetary and Space Science*, 47:1061–1075.

Iida, Y., Carnovale, F., Daviel, S., and Brion, C. E. (1986). Absolute oscillator strengths for photoabsorption and the molecular and dissociative photoionization of nitric oxide. *Chemical Physics*, 105:211–225.

Ingersoll, A. P. (1969). The Runaway Greenhouse: A History of Water on Venus. *Journal of Atmospheric Sciences*, 26(6):1191–1198.

Isson, T. T. and Planavsky, N. J. (2018). Reverse weathering as a long-term stabilizer of marine pH and planetary climate. Nature, 560(7719):471–475.

Iwagami, N., Hashimoto, G. L., Ohtsuki, S., Takagi, S., and Robert, S. (2015). Ground-based IR observation of oxygen isotope ratios in Venus's atmosphere. *Planetary and Space Science*, 113:292–297.

Izakov, M. N. (2001). Turbulence and anomalous heat fluxes in the atmospheres of Mars and Venus. Planet. Space Sci., 49:47–58.

Jacobson, M. Z., Turco, R. P., Jensen, E. J., and Toon, O. B. (1994). Modeling coagulation among particles of different composition and size. *Atmospheric Environment*, 28(7):1327–1338.

Jarraud, M. (2008). Guide to meteorological instruments and methods of observation (wmo-no. 8). *World Meteorological Organisation: Geneva, Switzerland*.

Johnston, H. S., Serang, O., and Podolske, J. (1979). Instantaneous global nitrous oxide photochemical rates. J. Geophys. Res., 84:5077–5082.

Jones, T. D. and Lewis, J. S. (1987). Estimated impact shock production of N $_2$ and organic compounds on early Titan. Icarus, 72(2):381–393.

Joshi, M. (2003). Climate Model Studies of Synchronously Rotating Planets. *Astrobiology*, 3(2):415–427.

Joshi, M. M., Haberle, R. M., and Reynolds, R. T. (1997). Simulations of the Atmospheres of Synchronously Rotating Terrestrial Planets Orbiting M Dwarfs: Conditions for Atmospheric Collapse and the Implications for Habitability. *Icarus*, 129:450–465.

Jura, M. (2004). An Observational Signature of Evolved Oceans on Extrasolar Terrestrial Planets. ApJ, 605(1):L65–L68.

Kadoya, S. and Tajika, E. (2014). Conditions for Oceans on Earth-like Planets Orbiting within the Habitable Zone: Importance of Volcanic CO_2 Degassing. ApJ, 790(2):107.

Kane, S. R., Kopparapu, R. K., and Domagal-Goldman, S. D. (2014). ON THE FREQUENCY OF POTENTIAL VENUS ANALOGS FROM *KEPLER* DATA. ApJ, 794(1):L5.

Kang, W. (2019). Wetter Stratospheres on High-obliquity Planets. ApJ, 877(1):L6.

Karman, T., Gordon, I. E., van der Avoird, A., Baranov, Y. I., Boulet, C., Drouin, B. J., Groenenboom, G. C., Gustafsson, M., Hartmann, J.-M., Kurucz, R. L., Rothman, L. S., Sun, K., Sung, K., Thalman, R., Tran, H., Wishnow, E. H., Wordsworth, R., Vigasin, A. A., Volkamer, R., and van der Zande, W. J. (2019). Update of the HITRAN collision-induced absorption section. Icarus, 328:160–175.

Karman, T., Koenis, M. A. J., Banerjee, A., Parker, D. H., Gordon, I. E., van der Avoird, A., van der Zande, W. J., and Groenenboom, G. C. (2018). O_2-O_2 and O_2-N_2 collision-induced absorption mechanisms unravelled. *Nature Chemistry*, 10(5):549–554.

Kaspi, Y. and Showman, A. P. (2015). Atmospheric Dynamics of Terrestrial Exoplanets over a Wide Range of Orbital and Atmospheric Parameters. ApJ, 804(1):60.

Kasting, J. F. (1988). Runaway and moist greenhouse atmospheres and the evolution of Earth and Venus. *Icarus*, 74(3):472–494.

Kasting, J. F. (1995). On ¡SUB¿2¡/SUB¿ concentrations in dense primitive atmospheres: commentary. *Planetary and Space Science*, 43:11–13.

Kasting, J. F., Liu, S. C., and Donahue, T. M. (1979). Oxygen levels in the prebiological atmosphere. J. Geophys. Res., 84:3097–3107.

Kasting, J. F. and Pollack, J. B. (1983). Loss of water from Venus. I. Hydrodynamic escape of hydrogen. Icarus, 53:479–508.

Kasting, J. F., Pollack, J. B., and Ackerman, T. P. (1984). Response of Earth's atmosphere to increases in solar flux and implications for loss of water from Venus. *Icarus*, 57(3):335–355.

Kasting, J. F., Whitmire, D. P., and Reynolds, R. T. (1993). Habitable Zones around Main Sequence Stars. *Icarus*, 101(1):108–128.

Keller-Rudek, H., Moortgat, G. K., Sander, R., and Sörensen, R. (2013). The mpi-mainz uv/vis

spectral atlas of gaseous molecules of atmospheric interest. *Earth System Science Data*, 5(2):365.

Kerzhanovich, V. V. and Marov, M. I. (1983). *The atmospheric dynamics of Venus according to Doppler measurements by the Venera entry probes*, pages 766–778.

Khodachenko, M. L., Ribas, I., Lammer, H., Grießmeier, J.-M., Leitner, M., Selsis, F., Eiroa, C., Hanslmeier, A., Biernat, H. K., Farrugia, C. J., and Rucker, H. O. (2007). Coronal Mass Ejection (CME) Activity of Low Mass M Stars as An Important Factor for The Habitability of Terrestrial Exoplanets. I. CME Impact on Expected Magnetospheres of Earth-Like Exoplanets in Close-In Habitable Zones. *Astrobiology*, 7:167–184.

Kilic, C., Raible, C. C., and Stocker, T. F. (2017). Multiple Climate States of Habitable Exoplanets: The Role of Obliquity and Irradiance. ApJ, 844(2):147.

Kitzmann, D. (2016). Revisiting the scattering greenhouse effect of CO2 ice clouds. ApJ, 817(2):L18.

Kitzmann, D. (2017). Clouds in the atmospheres of extrasolar planets. V. The impact of CO_2 ice clouds on the outer boundary of the habitable zone. A&A, 600:A111.

Kitzmann, D., Patzer, A. B. C., and Rauer, H. (2013). Clouds in the atmospheres of extrasolar planets. IV. On the scattering greenhouse effect of CO_2 ice particles: Numerical radiative transfer studies. A&A, 557:A6.

Kitzmann, D., Patzer, A. B. C., von Paris, P., Godolt, M., Stracke, B., Gebauer, S., Grenfell, J. L., and Rauer, H. (2010). Clouds in the atmospheres of extrasolar planets. I. Climatic effects of multi-layered clouds for Earth-like planets and implications for habitable zones. A&A, 511:A66.

Knutson, H. A., Charbonneau, D., Allen, L. E., Burrows, A., and Megeath, S. T. (2008). The 3.6-8.0 μm Broadband Emission Spectrum of HD 209458b: Evidence for an Atmospheric Temperature Inversion. ApJ, 673(1):526–531.

Knutson, H. A., Charbonneau, D., Cowan, N. B., Fortney, J. J., Showman, A. P., Agol, E., Henry, G. W., Everett, M. E., and Allen, L. E. (2009). Multiwavelength Constraints on the Day-Night Circulation Patterns of HD 189733b. ApJ, 690(1):822–836.

Koll, D. D. B. and Abbot, D. S. (2016). Temperature Structure and Atmospheric Circulation of Dry Tidally Locked Rocky Exoplanets. ApJ, 825(2):99.

Komacek, T. D. and Abbot, D. S. (2019). The Atmospheric Circulation and Climate of Terrestrial Planets Orbiting Sun-like and M Dwarf Stars over a Broad Range of Planetary Parameters. ApJ, 871(2):245.

Komacek, T. D., Fauchez, T. J., Wolf, E. T., and Abbot, D. S. (2020). Clouds will Likely Prevent the Detection of Water Vapor in JWST Transmission Spectra of Terrestrial Exoplanets. ApJ, 888(2):L20.

Kondo, J., Kanechika, O., and Yasuda, N. (1978). Heat and Momentum Transfers under Strong Stability in the Atmospheric Surface Layer. *Journal of Atmospheric Sciences*, 35:1012–1021.

Kopparapu, R. K., Kasting, J. F., and Zahnle, K. J. (2011). A photochemical model for the carbon-rich planet wasp-12b. *The Astrophysical Journal*, 745(1):77.

Kopparapu, R. K., Ramirez, R., Kasting, J. F., Eymet, V., Robinson, T. D., Mahadevan, S., Terrien, R. C., Domagal-Goldman, S., Meadows, V., and Deshpande, R. (2013). Habitable Zones Around Main-Sequence Stars: New Estimates. ApJ, 765(1993):16.

Kopparapu, R. K., Ramirez, R. M., SchottelKotte, J., Kasting, J. F., Domagal-Goldman, S., and Eymet, V. (2014). Habitable Zones around Main-sequence Stars: Dependence on Planetary Mass. ApJ, 787:L29.

Kopparapu, R. k., Wolf, E. T., Arney, G., Batalha, N. E., Haqq-Misra, J., Grimm, S. L., and Heng, K. (2017). Habitable Moist Atmospheres on Terrestrial Planets near the Inner Edge of the Habitable Zone around M Dwarfs. ApJ, 845(1):5.

Kopparapu, R. K., Wolf, E. T., Haqq-Misra, J., Yang, J., Kasting, J. F., Meadows, V., Terrien, R., and Mahadevan, S. (2016). the Inner Edge of the Habitable Zone for Synchronously Rotating Planets Around Low-Mass Stars Using General Circulation Models. ApJ, 819(1):84.

Kral, Q., Wyatt, M. C., Triaud, A. H. M. J., Marino, S., Thébault, P., and Shorttle, O. (2018). Cometary impactors on the TRAPPIST-1 planets can destroy all planetary atmospheres and rebuild secondary atmospheres on planets f, g, and h. MNRAS, 479:2649–2672.

Krasnopolsky, V. A. (2012). A photochemical model for the Venus atmosphere at 47-112 km. Icarus, 218:230–246.

Krasnopolsky, V. A. (2013). S_3 and S_4 abundances and improved chemical kinetic model for the lower atmosphere of Venus. Icarus, 225:570–580.

Krasnopolsky, V. A. (2015). Vertical profiles of H_2O, H_2SO_4, and sulfuric acid concentration at 45-75 km on Venus. Icarus, 252:327–333.

Krasnopolsky, V. A. and Parshev, V. A. (1983). *Photochemistry of the Venus atmosphere*, pages 461–458.

Kreidberg, L., Bean, J. L., Désert, J.-M., Benneke, B., Deming, D., Stevenson, K. B., Seager, S., Berta-Thompson, Z., Seifahrt, A., and Homeier, D. (2014). Clouds in the atmosphere of the super-Earth exoplanet GJ1214b. Nature, 505:69–72.

Kreidberg, L., Koll, D. D. B., Morley, C., Hu, R., Schaefer, L., Deming, D., Stevenson, K. B., Dittmann, J., Vanderburg, A., Berardo, D., Guo, X., Stassun, K., Crossfield, I., Charbonneau, D., Latham, D. W., Loeb, A., Ricker, G., Seager, S., and Vand erspek, R. (2019). Absence of a thick atmosphere on the terrestrial exoplanet LHS 3844b. Nature, 573(7772):87–90.

Krissansen-Totton, J., Bergsman, D. S., and Catling, D. C. (2016). On Detecting Biospheres from Chemical Thermodynamic Disequilibrium in Planetary Atmospheres. *Astrobiology*, 16:39–67.

Krissansen-Totton, J., Garland, R., Irwin, P., and Catling, D. C. (2018). Detectability of Biosignatures in Anoxic Atmospheres with the James Webb Space Telescope: A TRAPPIST-1e Case Study. AJ, 156(3):114.

Kruse, E., Agol, E., Luger, R., and Foreman-Mackey, D. (2019). Detection of Hundreds of New Planet Candidates and Eclipsing Binaries in K2 Campaigns 0-8. ApJS, 244(1):11.

Kulikov, Y. N., Lammer, H., Lichtenegger, H. I. M., Terada, N., Ribas, I., Kolb, C., Langmayr, D., Lundin, R., Guinan, E. F., Barabash, S., and Biernat, H. K. (2006). Atmospheric and water loss from early Venus. *Planetary and Space Science*, 54:1425–1444.

Kumar, S. and Taylor, H. A. (1985). Deuterium on Venus: Model comparisons with pioneer Venus observations of the predawn bulge ionosphere. Icarus, 62(3):494–504.

Lafferty, W. J., Solodov, A. M., Weber, A., Olson, W. B., and Hartmann, J.-M. (1996). Infrared collision-induced absorption by n 2 near 4.3 μm for atmospheric applications: Measurements and empirical modeling. *Applied optics*, 35(30):5911–5917.

Lammer, H., Kislyakova, K. G., Odert, P., Leitzinger, M., Schwarz, R., Pilat-Lohinger, E., Kulikov, Y. N., Khodachenko, M. L., Güdel, M., and Hanslmeier, A. (2011). Pathways to Earth-Like Atmospheres. Extreme Ultraviolet (EUV)-Powered Escape of Hydrogen-Rich Protoatmospheres. *Origins of Life and Evolution of the Biosphere*, 41:503–522.

Lammer, H., Lichtenegger, H. I. M., Kulikov, Y. N., Grießmeier, J.-M., Terada, N., Erkaev, N. V., Biernat, H. K., Khodachenko, M. L., Ribas, I., Penz, T., and Selsis, F. (2007). Coronal Mass Ejection (CME) Activity of Low Mass M Stars as An Important Factor for The Habitability of Terrestrial Exoplanets. II. CME- Induced Ion Pick Up of Earth-like Exoplanets in Close-In Habitable Zones. *Astrobiology*, 7:185–207.

Lammer, H., Zerkle, A. L., Gebauer, S., Tosi, N., Noack, L., Scherf, M., Pilat-Lohinger, E., Güdel, M., Grenfell, J. L., Godolt, M., and Nikolaou, A. (2018). Origin and evolution of the atmospheres of early Venus, Earth and Mars. *Astronomy and Astrophysics Review*, 26:2.

Lana, A., Bell, T. G., Simó, R., Vallina, S. M., Ballabrera-Poy, J., Kettle, A. J., Dachs, J., Bopp, L., Saltzman, E. S., Stefels, J., Johnson, J. E., and Liss, P. S. (2011). An updated climatology of surface dimethlysulfide concentrations and emission fluxes in the global ocean. *Global Biogeochemical Cycles*, 25(1):GB1004.

Lane, J. R. and Kjaergaard, H. G. (2008). Calculated electronic transitions in sulfuric acid and implications for its photodissociation in the atmosphere. *The Journal of Physical Chemistry A*, 112(22):4958–4964.

Leconte, J., Forget, F., Charnay, B., Wordsworth, R., Selsis, F., Millour, E., and Spiga, A. (2013). 3D climate modeling of close-in land planets: Circulation patterns, climate moist bistability, and habitability. A&A, 554:A69.

Leconte, J., Wu, H., Menou, K., and Murray, N. (2015). Asynchronous rotation of earth-mass planets in the habitable zone of lower-mass stars. *Science*, 347(6222):632–635.

Lee, A. Y. T., Yung, Y. L., Cheng, B.-M., Bahou, M., Chung, C.-Y., and Lee, Y.-P. (2001). Enhancement of Deuterated Ethane on Jupiter. ApJ, 551:L93–L96.

Lee, Y. J., Sagawa, H., Haus, R., Stefani, S., Imamura, T., Titov, D. V., and Piccioni, G. (2016). Sensitivity of net thermal flux to the abundance of trace gases in the lower atmosphere of venus. *Journal of Geophysical Research: Planets*, 121(9):1737–1752.

Lenardic, A., Crowley, J. W., Jellinek, A. M., and Weller, M. (2016). The Solar System of Forking Paths: Bifurcations in Planetary Evolution and the Search for Life-Bearing Planets in Our Galaxy. *Astrobiology*, 16(7):551–559.

Lewis, B. R. and Carver, J. H. (1983). Temperature dependence of the carbon dioxide photoabsorption cross section between 1200 and 1970 A. J. Quant. Spec. Radiat. Transf., 30:297–309.

Lewis, N. T., Lambert, F. H., Boutle, I. A., Mayne, N. J., Manners, J., and Acreman, D. M. (2018). The Influence of a Substellar Continent on the Climate of a Tidally Locked Exoplanet. ApJ, 854(2):171.

Li, J. (2017). Comments on "On the Choice of Average Solar Zenith Angle". *Journal of Atmospheric Sciences*, 74:1669–1676.

Liang, M.-C., Blake, G. A., Lewis, B. R., and Yung, Y. L. (2007). Oxygen isotopic composition of carbon dioxide in the middle atmosphere. *Proceedings of the National Academy of Science*, 104:21–25.

Lichtenegger, H. I. M., Kislyakova, K. G., Odert, P., Erkaev, N. V., Lammer, H., Gröller, H., Johnstone, C. P., Elkins-Tanton, L., Tu, L., Güdel, M., and Holmström, M. (2016). Solar XUV and ENA-driven water loss from early Venus' steam atmosphere. *Journal of Geophysical Research (Space Physics)*, 121:4718–4732.

Liebert, J. and Gizis, J. E. (2006). RI Photometry of 2MASS-selected Late M and L Dwarfs. PASP, 118:659–670.

Limão-Vieira, P., Ferreira da Silva, F., Almeida, D., Hoshino, M., Tanaka, H., Mogi, D., Tanioka, T., Mason, N., Hoffmann, S., Hubin-Franskin, M.-J., et al. (2015). Electronic excitation of carbonyl sulphide (cos) by high-resolution vacuum ultraviolet photoabsorption and electron-impact spectroscopy in the energy region from 4 to 11 ev. *The Journal of Chemical Physics*, 142(6):064303.

Lincowski, A. P., Lustig-Yaeger, J., and Meadows, V. S. (2019). Observing Isotopologue Bands in Terrestrial Exoplanet Atmospheres with the James Webb Space Telescope: Implications for Identifying Past Atmospheric and Ocean Loss. AJ, 158(1):26.

Lincowski, A. P., Meadows, V. S., Crisp, D., Robinson, T. D., Luger, R., Lustig-Yaeger, J., and Arney, G. N. (2018). Evolved Climates and Observational Discriminants for the TRAPPIST-1 Planetary System. ApJ, 867:76.

Lindzen, R. and Forbes, J. (1983). Turbulence originating from convectively stable internal waves. *Journal of Geophysical Research: Oceans*, 88(C11):6549–6553.

Line, M. R., Wolf, A. S., Zhang, X., Knutson, H., Kammer, J. A., Ellison, E., Deroo, P., Crisp, D., and Yung, Y. L. (2013). A Systematic Retrieval Analysis of Secondary Eclipse Spectra. I. A Comparison of Atmospheric Retrieval Techniques. ApJ, 775:137.

Linsenmeier, M., Pascale, S., and Lucarini, V. (2015). Climate of Earth-like planets with high obliquity and eccentric orbits: Implications for habitability conditions. Planet. Space Sci., 105:43–59.

Linsky, J. L., Draine, B. T., Moos, H. W., Jenkins, E. B., Wood, B. E., Oliveira, C., Blair, W. P., Friedman, S. D., Gry, C., Knauth, D., Kruk, J. W., Lacour, S., Lehner, N., Redfield, S., Shull, J. M., Sonneborn, G., and Williger, G. M. (2006). What Is the Total Deuterium Abundance in the Local Galactic Disk? ApJ, 647:1106–1124.

López-Morales, M., Ben-Ami, S., Gonzalez-Abad, G., García-Mejía, J., Dietrich, J., and Szentgyorgyi, A. (2019). Optimizing Ground-based Observations of O_2 in Earth Analogs. AJ, 158(1):24.

Lovis, C., Snellen, I., Mouillet, D., Pepe, F., Wildi, F., Astudillo-Defru, N., Beuzit, J.-L., Bonfils, X., Cheetham, A., Conod, U., Delfosse, X., Ehrenreich, D., Figueira, P., Forveille, T., Martins, J. H. C., Quanz, S. P., Santos, N. C., Schmid, H.-M., Ségransan, D., and Udry, S. (2017). Atmospheric characterization of Proxima b by coupling the SPHERE high-contrast imager to the ESPRESSO spectrograph. A&A, 599:A16.

Lu, H.-C., Chen, H.-K., Chen, H.-F., Cheng, B.-M., and Ogilvie, J. (2010). Absorption cross section of molecular oxygen in the transition e 3σu-v= 0–x 3σg-v= 0 at 38 k. *Astronomy & Astrophysics*, 520:A19.

Luger, R. and Barnes, R. (2015). Extreme Water Loss and Abiotic O2 Buildup on Planets. *Astrobiology*, 15(2):119–143.

Luger, R., Barnes, R., Lopez, E., Fortney, J. J., Jackson, B., and Meadows, V. (2015). Habitable Evaporated Cores: Transforming Mini-Neptunes into Super-Earths in the Habitable Zones of M Dwarfs. *Astrobiology*, 15(1):57.

Luger, R., Lustig-Yaeger, J., and Agol, E. (2017a). Planet-Planet Occultations in TRAPPIST-1 and Other Exoplanet Systems. ApJ, 851(2):94.

Luger, R., Lustig-Yaeger, J., Fleming, D. P., Tilley, M. A., Agol, E., Meadows, V. S., Deitrick, R., and Barnes, R. (2017b). The Pale Green Dot: A Method to Characterize Proxima Centauri b Using Exo-Aurorae. ApJ, 837:63.

Luger, R., Sestovic, M., Kruse, E., Grimm, S. L., Demory, B.-O., Agol, E., Bolmont, E., Fabrycky, D., Fernandes, C. S., Van Grootel, V., Burgasser, A., Gillon, M., Ingalls, J. G., Jehin, E., Raymond, S. N., Selsis, F., Triaud, A. H. M. J., Barclay, T., Barentsen, G., Howell, S. B., Delrez, L., de Wit, J., Foreman-Mackey, D., Holdsworth, D. L., Leconte, J., Lederer, S., Turbet, M., Almleaky, Y., Benkhaldoun, Z., Magain, P., Morris, B. M., Heng, K., and Queloz, D. (2017c). A seven-planet resonant chain in TRAPPIST-1. *Nature Astronomy*, 1:0129.

Lustig-Yaeger, J., Meadows, V. S., and Lincowski, A. P. (2019a). The Detectability and Characterization of the TRAPPIST-1 Exoplanet Atmospheres with JWST. AJ, 158(1):27.

Lustig-Yaeger, J., Meadows, V. S., and Lincowski, A. P. (2019b). A Mirage of the Cosmic Shoreline: Venus-like Clouds as a Statistical False Positive for Exoplanet Atmospheric Erosion. ApJ, 887(1):L11.

Lustig-Yaeger, J., Meadows, V. S., Tovar Mendoza, G., Schwieterman, E. W., Fujii, Y., Luger, R., and Robinson, T. D. (2018). Detecting Ocean Glint on Exoplanets Using Multiphase Mapping. AJ, 156(6):301.

Luther, F. M., Ellingson, R. G., Fouquart, Y., Fels, S., Scott, N. A., and Wiscombe, W. J. (1988). Intercomparison of radiation codes in climate models (icrccm): longwave clear-sky results—a workshop summary. *Bulletin of the American Meteorological Society*, 69(1):40–48.

Manabe, S. and Strickler, R. F. (1964). Thermal Equilibrium of the Atmosphere with a Convective Adjustment. *J. Atmos. Sci.*, 21(4):361–385.

Manabe, S. and Wetherald, R. T. (1967). Thermal Equilibrium of the Atmosphere with a Given Distribution of Relative Humidity. *J. Atmos. Sci.*, 24(3):241–259.

Manatt, S. L. and Lane, A. L. (1993). A compilation of the absorption cross-sections of SO_2 from 106 to 403 nm. J. Quant. Spec. Radiat. Transf., 50:267–276.

Mandt, K. E., Mousis, O., Lunine, J., and Gautier, D. (2014). Protosolar Ammonia as the Unique Source of Titan's nitrogen. ApJ, 788(2):L24.

Marley, M. S. and McKay, C. P. (1999). Thermal Structure of Uranus' Atmosphere. Icarus, 138(2):268–286.

Massie, S. T. and Hunten, D. M. (1981). Stratospheric eddy diffusion coefficients from tracer data. J. Geophys. Res., 86:9859–9868.

Maté, B., Lugez, C., Fraser, G. T., and Lafferty, W. J. (1999). Absolute intensities for the o2 1.27 μm continuum absorption. *Journal of Geophysical Research: Atmospheres*, 104(D23):30585–30590.

Matsui, H., Iwagami, N., Hosouchi, M., Ohtsuki, S., and Hashimoto, G. L. (2012). Latitudinal distribution of HDO abundance above Venus' clouds by ground- based 2.3 μm spectroscopy. Icarus, 217:610–614.

Matsumi, Y., Comes, F. J., Hancock, G., Hofzumahaus, A., Hynes, A. J., Kawasaki, M., and Ravishankara, A. R. (2002). Quantum yields for production of $O(^1D)$ in the ultraviolet photolysis of ozone: Recommendation based on evaluation of laboratory data. *Journal of Geophysical Research (Atmospheres)*, 107:4024.

Mayor, M., Pepe, F., Queloz, D., Bouchy, F., Rupprecht, G., Lo Curto, G., Avila, G., Benz, W., Bertaux, J.-L., Bonfils, X., Dall, T., Dekker, H., Delabre, B., Eckert, W., Fleury, M., Gilliotte, A., Gojak, D., Guzman, J. C., Kohler, D., Lizon, J.-L., Longinotti, A., Lovis, C., Megevand, D., Pasquini, L., Reyes, J., Sivan, J.-P., Sosnowska, D., Soto, R., Udry, S., van Kesteren, A.,

Weber, L., and Weilenmann, U. (2003). Setting New Standards with HARPS. *The Messenger*, 114:20–24.

McElroy, M. B., Prather, M. J., and Rodriguez, J. M. (1982). Escape of Hydrogen from Venus. *Science*, 215(4540):1614–1615.

McKay, C. P., Scattergood, T. W., Pollack, J. B., Borucki, W. J., and van Ghyseghem, H. T. (1988). High-temperature shock formation of N_2 and organics on primordial Titan. Nature, 332(6164):520–522.

Meadows, V. S. (2017). Reflections on O_2 as a Biosignature in Exoplanetary Atmospheres. *Astrobiology*, 17:1022–1052.

Meadows, V. S., Arney, G. N., Schwieterman, E. W., Lustig-Yaeger, J., Lincowski, A. P., Robinson, T., Domagal-Goldman, S. D., Deitrick, R., Barnes, R. K., Fleming, D. P., Luger, R., Driscoll, P. E., Quinn, T. R., and Crisp, D. (2018). The Habitability of Proxima Centauri b: Environmental States and Observational Discriminants. *Astrobiology*, 18(2):133–189.

Meadows, V. S. and Barnes, R. K. (2018). Factors affecting exoplanet habitability. In Deeg, H. J. and Belmonte, J. A., editors, *Handbook of Exoplanets*. Springer Science & Business Media.

Meadows, V. S. and Crisp, D. (1996). Ground-based near-infrared observations of the Venus nightside: The thermal structure and water abundance near the surface. J. Geophys. Res., 101:4595–4622.

Meadows, V. S., Lincowski, A. P., and Lustig-Yaeger, J. (2020). The Feasibility of Detecting Biosignatures in the TRAPPIST-1 Planetary System with JWST.

Meadows, V. S., Reinhard, C. T., Arney, G. N., Parenteau, M. N., Schwieterman, E. W., Domagal-Goldman, S. D., Lincowski, A. P., Stapelfeldt, K. R., Rauer, H., DasSarma, S., Hegde, S., Narita, N., Deitrick, R., Lustig-Yaeger, J., Lyons, T. W., Siegler, N., and Grenfell, J. L. (2018). Exoplanet Biosignatures: Understanding Oxygen as a Biosignature in the Context of Its Environment. *Astrobiology*, 18:630–662.

Meija, J., Coplen, T. B., Berglund, M., Brand, W. A., De Bièvre, P., Gröning, M., Holden, N. E., Irrgeher, J., Loss, R. D., Walczyk, T., et al. (2016). Isotopic compositions of the elements 2013 (iupac technical report). *Pure and Applied Chemistry*, 88(3):293–306.

Mellor, G. L. and Yamada, T. (1974). A Hierarchy of Turbulence Closure Models for Planetary Boundary Layers. *J. Atmos. Sci.*, 31(7):1791–1806.

Mellor, G. L. and Yamada, T. (1982). Development of a Turbulence Closure Model for Geophysical Fluid Problems (Paper 2R0808). *Reviews of Geophysics and Space Physics*, 20:851.

Ment, K., Dittmann, J. A., Astudillo-Defru, N., Charbonneau, D., Irwin, J., Bonfils, X., Murgas, F., Almenara, J.-M., Forveille, T., Agol, E., Ballard, S., Berta-Thompson, Z. K., Bouchy, F., Cloutier, R., Delfosse, X., Doyon, R., Dressing, C. D., Esquerdo, G. A., Haywood, R. D., Kipping, D. M., Latham, D. W., Lovis, C., Newton, E. R., Pepe, F., Rodriguez, J. E., Santos, N. C., Tan, T.-G., Udry, S., Winters, J. G., and Wünsche, A. (2019). A Second Terrestrial Planet Orbiting the Nearby M Dwarf LHS 1140. AJ, 157:32.

Merlis, T. M. and Schneider, T. (2010). Atmospheric dynamics of Earth-like tidally locked aquaplanets. *Journal of Advances in Modeling Earth Systems*, 2:13.

Milankovitch, M. K. (1941). Kanon der erdbestrahlung und seine anwendung auf das eiszeitenproblem. *Royal Serbian Academy Special Publication*, 133:1–633.

Miller-Ricci, E., Seager, S., and Sasselov, D. (2009). THE ATMOSPHERIC SIGNATURES OF SUPER-EARTHS: HOW TO DISTINGUISH BETWEEN HYDROGEN-RICH AND HYDROGEN-POOR ATMOSPHERES. *The Astrophysical Journal*, 690(2):1056–1067.

Mills, M. J., Toon, O. B., Vaida, V., Hintze, P. E., Kjaergaard, H. G., Schofield, D. P., and Robinson, T. W. (2005). Photolysis of sulfuric acid vapor by visible light as a source of the polar stratospheric CN layer. *Journal of Geophysical Research (Atmospheres)*, 110:D08201.

Mischna, M., Kasting, J. F., Pavlov, A., and Freedman, R. (2000). Influence of Carbon Dioxide Clouds on Early Martian Climate. *Icarus*, 145(2):546–554.

Misra, A., Meadows, V., and Crisp, D. (2014). the Effects of Refraction on Transit Transmission Spectroscopy: Application To Earth-Like Exoplanets. ApJ, 792(1):61.

Molina, L. T., Lamb, J. J., and Molina, M. J. (1981). Temperature dependent UV absorption cross sections for carbonyl sulfide. Geophys. Res. Lett., 8:1008–1011.

Mollière, P. and Snellen, I. A. G. (2019). Detecting isotopologues in exoplanet atmospheres using ground-based high-dispersion spectroscopy. A&A, 622:A139.

Montmessin, F., Gondet, B., Bibring, J.-P., Langevin, Y., Drossart, P., Forget, F., and Fouchet, T. (2007). Hyperspectral imaging of convective CO 2 ice clouds in the equatorial mesosphere of Mars. *J. Geophys. Res.*, 112(E11):E11S90.

Moore, J. F. (1972). *Infrared absorption of carbon dioxide at high densities with application to the atmosphere of Venus.* PhD thesis, Columbia Univ.

Moran, S. E., Hörst, S. M., Batalha, N. E., Lewis, N. K., and Wakeford, H. R. (2018). Limits on Clouds and Hazes for the TRAPPIST-1 Planets. AJ, 156(6):252.

Morley, C. V., Kreidberg, L., Rustamkulov, Z., Robinson, T., and Fortney, J. J. (2017). Observing the Atmospheres of Known Temperate Earth-sized Planets with JWST. ApJ, 850(2):121.

Morris, B. M., Agol, E., Hebb, L., and Hawley, S. L. (2018). Robust Transiting Exoplanet Radii in the Presence of Starspots from Ingress and Egress Durations. AJ, 156(3):91.

Mota, R., Parafita, R., Giuliani, A., Hubin-Franskin, M.-J., Lourenço, J. M. C., Garcia, G., Hoffmann, S. V., Mason, N. J., Ribeiro, P. A., Raposo, M., and Limão-Vieira, P. (2005). Water VUV electronic state spectroscopy by synchrotron radiation. *Chemical Physics Letters*, 416:152–159.

Nilsson, J. and Emanuel, K. A. (1999). Equilibrium atmospheres of a two-column radiative-convective model. *Quarterly Journal of the Royal Meteorological Society*, 125(558):2239–2264.

Nishida, S., Taketani, F., Takahashi, K., and Matsumi, Y. (2004). Quantum yield for o (1d) production from ozone photolysis in the wavelength range of 193- 225 nm. *The Journal of Physical Chemistry A*, 108(14):2710–2714.

Noack, L., Rivoldini, A., and Van Hoolst, T. (2017). Volcanism and outgassing of stagnant-lid planets: Implications for the habitable zone. *Physics of the Earth and Planetary Interiors*, 269:40–57.

Nowajewski, P., Rojas, M., Rojo, P., and Kimeswenger, S. (2018). Atmospheric dynamics and habitability range in Earth-like aquaplanets obliquity simulations. Icarus, 305:84–90.

Nutzman, P. and Charbonneau, D. (2008). Design Considerations for a Ground-Based Transit Search for Habitable Planets Orbiting M Dwarfs. PASP, 120:317.

Osborne, B. A., Marston, G., Kaminski, L., Jones, N., Gingell, J., Mason, N., Walker, I. C., Delwiche, J., and Hubin-Franskin, M.-J. (2000). Vacuum ultraviolet spectrum of dinitrogen pentoxide. *Journal of Quantitative Spectroscopy and Radiative Transfer*, 64(1):67–74.

Owen, T., Maillard, J. P., de Bergh, C., and Lutz, B. L. (1988). Deuterium on Mars: The Abundance of HDO and the Value of D/H. *Science*, 240:1767–1770.

Pallé, E., Zapatero Osorio, M. R., and García Muñoz, A. (2011). Characterizing the Atmospheres of Transiting Rocky Planets Around Late-type Dwarfs. ApJ, 728(1):19.

Palmer, K. F. and Williams, D. (1975). Optical constants of sulfuric acid - Application to the clouds of Venus. Appl. Opt., 14:208–219.

Patra, P. K. and Lal, S. (1997). Variability of eddy diffusivity in the stratosphere deduced from vertical distributions of N_2O and CFC-12. 59.

Pavlov, A. A., Brown, L. L., and Kasting, J. F. (2001). UV shielding of NH_3 and O_2 by organic hazes in the Archean atmosphere. *Journal of Geophysical Research: Planets*, 106(E10):23267–23287.

Peacock, S., Barman, T., Shkolnik, E. L., Hauschildt, P. H., and Baron, E. (2019). Predicting the Extreme Ultraviolet Radiation Environment of Exoplanets around Low-mass Stars: The TRAPPIST-1 System. ApJ, 871(2):235.

Perrin, M. Y. and Hartmann, J. M. (1989). Temperature-dependent measurements and modeling of absorption by CO_2-N_2 mixtures in the far line-wings of the 4.3 μm CO_2 band. J. Quant. Spec. Radiat. Transf., 42:311–317.

Pidhorodetska, D., Fauchez, T., Villanueva, G., and Domagal-Goldman, S. (2020). Detectability of Molecular Signatures on TRAPPIST-1e through Transmission Spectroscopy Simulated for Future Space-Based Observatories. *arXiv e-prints*, page arXiv:2001.01338.

Pierrehumbert, R. and Gaidos, E. (2011). Hydrogen greenhouse planets beyond the habitable zone. *The Astrophysical Journal Letters*, 734(1):L13.

Pierrehumbert, R. T. (1995). Thermostats, Radiator Fins, and the Local Runaway Greenhouse. *Journal of Atmospheric Sciences*, 52(10):1784–1806.

Pierrehumbert, R. T. (2011). A Palette of Climates for Gliese 581g. ApJ, 726(1):L8.

Pierrehumbert, R. T. (2011). *Principles of Planetary Climate*. Cambridge University Press.

Pierrehumbert, R. T. and Erlick, C. (1998). On the scattering greenhouse effect of CO_2 ice clouds. *J. Atmospheric Sci.*, pages 1897–1903.

Pollack, J. B., Dalton, J. B., Grinspoon, D., Wattson, R. B., Freedman, R., Crisp, D., Allen, D. A., Bezard, B., DeBergh, C., Giver, L. P., Ma, Q., and Tipping, R. (1993). Near-Infrared Light from Venus' Nightside: A Spectroscopic Analysis. Icarus, 103:1–42.

Pollack, J. B., Toon, O. B., and Boese, R. (1980). Greenhouse models of Venus' high surface temperature, as constrained by Pioneer Venus measurements. J. Geophys. Res., 85:8223–8231.

Press, W. H. (1996). Numerical recipes in fortran. Technical report.

Priestley, C. H. B. (1959). Turbulent transfer in the lower atmosphere.

Programme, W. C. and Luther, F. (1984). *The intercomparison of radiation codes in climate models (ICRCCM): longwave clear-sky calculations*.

Quanz, S. P., Crossfield, I., Meyer, M. R., Schmalzl, E., and Held, J. (2015). Direct detection of exoplanets in the 3–10 μm range with e-elt/metis. *International Journal of Astrobiology*, 14(02):279–289.

Quarles, B., Quintana, E. V., Lopez, E., Schlieder, J. E., and Barclay, T. (2017). Plausible Compositions of the Seven TRAPPIST-1 Planets Using Long-term Dynamical Simulations. ApJ, 842:L5.

Quirrenbach, A., Amado, P. J., Ribas, I., Reiners, A., Caballero, J. A., Seifert, W., Aceituno, J., Azzaro, M., Baroch, D., Barrado, D., and et al. (2018). CARMENES: high-resolution spectra and precise radial velocities in the red and infrared. In *Ground-based and Airborne Instrumentation for Astronomy VII*, volume 10702 of *Society of Photo-Optical Instrumentation Engineers (SPIE) Conference Series*, page 107020W.

Rackham, B. V., Apai, D., and Giampapa, M. S. (2018). The Transit Light Source Effect: False Spectral Features and Incorrect Densities for M-dwarf Transiting Planets. ApJ, 853(2):122.

Rackham, B. V., Apai, D., and Giampapa, M. S. (2019). The Transit Light Source Effect. II. The Impact of Stellar Heterogeneity on Transmission Spectra of Planets Orbiting Broadly Sun-like Stars. AJ, 157(3):96.

Rajpurohit, A. S., Reylé, C., Allard, F., Homeier, D., Schultheis, M., Bessell, M. S., and Robin, A. C. (2013). The effective temperature scale of M dwarfs. A&A, 556:A15.

Ramanathan, V. and Coakley, J. A., J. (1978). Climate Modeling Through Radiative-Convective Models (Paper 8R0533). *Reviews of Geophysics and Space Physics*, 16:465.

Ramirez, R. M. and Kaltenegger, L. (2017). A volcanic hydrogen habitable zone. *The Astrophysical Journal Letters*, 837(1):L4.

Ramirez, R. M. and Kaltenegger, L. (2018). A Methane Extension to the Classical Habitable Zone. ApJ, 858(2):72.

Ranjan, S., Wordsworth, R., and Sasselov, D. D. (2017). The Surface UV Environment on Planets Orbiting M Dwarfs: Implications for Prebiotic Chemistry and the Need for Experimental Follow-up. ApJ, 843(2):110.

Rauer, H., Catala, C., Aerts, C., Appourchaux, T., Benz, W., Brandeker, A., Christensen-Dalsgaard, J., Deleuil, M., Gizon, L., Goupil, M. J., Güdel, M., Janot-Pacheco, E., Mas-Hesse, M., Pagano, I., Piotto, G., Pollacco, D., Santos, Ċ., Smith, A., Suárez, J. C., Szabó, R., Udry, S., Adibekyan, V., Alibert, Y., Almenara, J. M., Amaro-Seoane, P., Eiff, M. A.-v., Asplund, M., Antonello, E., Barnes, S., Baudin, F., Belkacem, K., Bergemann, M., Bihain, G., Birch, A. C., Bonfils, X., Boisse, I., Bonomo, A. S., Borsa, F., Brand ão, I. M., Brocato, E., Brun, S., Burleigh, M., Burston, R., Cabrera, J., Cassisi, S., Chaplin, W., Charpinet, S., Chiappini, C., Church, R. P., Csizmadia, S., Cunha, M., Damasso, M., Davies, M. B., Deeg, H. J., Díaz, R. F., Dreizler, S., Dreyer, C., Eggenberger, P., Ehrenreich, D., Eigmüller, P., Erikson, A., Farmer, R., Feltzing, S., de Oliveira Fialho, F., Figueira, P., Forveille, T., Fridlund, M., García, R. A., Giommi, P., Giuffrida, G., Godolt, M., Gomes da Silva, J., Granzer, T., Grenfell, J. L., Grotsch-Noels, A., Günther, E., Haswell, C. A., Hatzes, A. P., Hébrard, G., Hekker, S., Helled, R., Heng, K., Jenkins, J. M., Johansen, A., Khodachenko, M. L., Kislyakova, K. G., Kley, W., Kolb, U., Krivova, N., Kupka, F., Lammer, H., Lanza, A. F., Lebreton, Y., Magrin, D., Marcos-Arenal, P., Marrese, P. M., Marques, J. P., Martins, J., Mathis, S., Mathur, S., Messina, S., Miglio, A., Montalban, J., Montalto, M., Monteiro, M. J. P. F. G., Moradi, H., Moravveji, E., Mordasini, C., Morel, T., Mortier, A., Nascimbeni, V., Nelson, R. P., Nielsen, M. B., Noack, L., Norton, A. J., Ofir, A., Oshagh, M., Ouazzani, R. M., Pápics, P., Parro, V. C., Petit, P., Plez, B., Poretti, E., Quirrenbach, A., Ragazzoni, R., Raimondo, G., Rainer, M., Reese, D. R., Redmer, R., Reffert, S., Rojas-Ayala, B., Roxburgh, I. W., Salmon, S., Santerne, A., Schneider, J., Schou, J., Schuh,

S., Schunker, H., Silva-Valio, A., Silvotti, R., Skillen, I., Snellen, I., Sohl, F., Sousa, S. G., Sozzetti, A., Stello, D., Strassmeier, K. G., Švanda, M., Szabó, G. M., Tkachenko, A., Valencia, D., Van Grootel, V., Vauclair, S. D., Ventura, P., Wagner, F. W., Walton, N. A., Weingrill, J., Werner, S. C., Wheatley, P. J., and Zwintz, K. (2014). The PLATO 2.0 mission. *Experimental Astronomy*, 38(1-2):249–330.

Rayleigh, L. (1896). Theoretical considerations respecting the separation of gases by diffusion and similar processes. *The London, Edinburgh, and Dublin Philosophical Magazine and Journal of Science*, 42(259):493–498.

Raymond, D. J. and Zeng, X. (2000). Instability and large-scale circulations in a two-column model of the tropical troposphere. *Quarterly Journal of the Royal Meteorological Society*, 126(570):3117–3135.

Raymond, D. J. and Zeng, X. (2005). Modelling tropical atmospheric convection in the context of the weak temperature gradient approximation. *Quarterly Journal of the Royal Meteorological Society*, 131(608):1301–1320.

Ribas, I., Bolmont, E., Selsis, F., Reiners, A., Leconte, J., Raymond, S. N., Engle, S. G., Guinan, E. F., Morin, J., Turbet, M., Forget, F., and Anglada-Escudé, G. (2016). The habitability of Proxima Centauri b. I. Irradiation, rotation and volatile inventory from formation to the present. A&A, 596:A111.

Ricker, G. R., Winn, J. N., Vanderspek, R., Latham, D. W., Bakos, G. Á., Bean, J. L., Berta-Thompson, Z. K., Brown, T. M., Buchhave, L., Butler, N. R., Butler, R. P., Chaplin, W. J., Charbonneau, D., Christensen-Dalsgaard, J., Clampin, M., Deming, D., Doty, J., De Lee, N., Dressing, C., Dunham, E. W., Endl, M., Fressin, F., Ge, J., Henning, T., Holman, M. J., Howard, A. W., Ida, S., Jenkins, J. M., Jernigan, G., Johnson, J. A., Kaltenegger, L., Kawai, N., Kjeldsen, H., Laughlin, G., Levine, A. M., Lin, D., Lissauer, J. J., MacQueen, P., Marcy, G., McCullough, P. R., Morton, T. D., Narita, N., Paegert, M., Palle, E., Pepe, F., Pepper, J., Quirrenbach, A., Rinehart, S. A., Sasselov, D., Sato, B., Seager, S., Sozzetti, A., Stassun, K. G., Sullivan, P.,

Szentgyorgyi, A., Torres, G., Udry, S., and Villasenor, J. (2015). Transiting Exoplanet Survey Satellite (TESS). *Journal of Astronomical Telescopes, Instruments, and Systems*, 1:014003.

Roberge, A. and Moustakas, L. A. (2018). The large ultraviolet/optical/infrared surveyor. *Nature Astronomy*, 2(8):605–607.

Robinson, T. D. (2017). A Theory of Exoplanet Transits with Light Scattering. ApJ, 836(2):236.

Robinson, T. D. and Crisp, D. (2018). Linearized Flux Evolution (LiFE): A technique for rapidly adapting fluxes from full-physics radiative transfer models. *Journal of Quantitative Spectroscopy and Radiative Transfer*, 211:78–95.

Robinson, T. D., Meadows, V. S., and Crisp, D. (2010). Detecting Oceans on Extrasolar Planets Using the Glint Effect. ApJ, 721(1):L67–L71.

Robinson, T. D., Meadows, V. S., Crisp, D., Deming, D., Hearn, M. F. A., Charbonneau, D., Livengood, T. A., Seager, S., Barry, R. K., Hearty, T., Hewagama, T., Lisse, C. M., Mcfadden, L. A., and Wellnitz, D. D. (2011). Earth as an Extrasolar Planet : Earth Model Validation Using EPOXI Earth Observations. *Astrobiology*, 11(5):393–408.

Rodler, F. and López-Morales, M. (2014). Feasibility Studies for the Detection of O¡SUB¿2¡/SUB¿ in an Earth-like Exoplanet. ApJ, 781:54.

Rogers, L. A. (2015). MOST 1.6 EARTH-RADIUS PLANETS ARE NOT ROCKY. *The Astrophysical Journal*, 801(1):41.

Rogers, R. and Yau, M. (1989). A short course in cloud physics, int. ser. *Nat. Philos*, 113:290.

Rothman, L. S., Gordon, I. E., Babikov, Y., Barbe, A., Chris Benner, D., Bernath, P. F., Birk, M., Bizzocchi, L., Boudon, V., Brown, L. R., Campargue, A., Chance, K., Cohen, E. A., Coudert, L. H., Devi, V. M., Drouin, B. J., Fayt, A., Flaud, J.-M., Gamache, R. R., Harrison, J. J., Hartmann, J.-M., Hill, C., Hodges, J. T., Jacquemart, D., Jolly, A., Lamouroux, J., Le Roy, R. J., Li, G., Long, D. A., Lyulin, O. M., Mackie, C. J., Massie, S. T., Mikhailenko, S., Müller,

H. S. P., Naumenko, O. V., Nikitin, A. V., Orphal, J., Perevalov, V., Perrin, A., Polovtseva, E. R., Richard, C., Smith, M. A. H., Starikova, E., Sung, K., Tashkun, S., Tennyson, J., Toon, G. C., Tyuterev, V. G., and Wagner, G. (2013). The HITRAN2012 molecular spectroscopic database. J. Quant. Spec. Radiat. Transf., 130:4–50.

Rothman, L. S., Gordon, I. E., Barber, R. J., Dothe, H., Gamache, R. R., Goldman, A., Perevalov, V. I., Tashkun, S. A., and Tennyson, J. (2010). HITEMP, the high-temperature molecular spectroscopic database. J. Quant. Spec. Radiat. Transf., 111:2139–2150.

Rugheimer, S., Kaltenegger, L., Segura, A., Linsky, J., and Mohanty, S. (2015). Effect of Uv Radiation on the Spectral Fingerprints of Earth-Like Planets Orbiting M Stars. ApJ, 809(1):57.

Sander, S., Friedl, R., Barker, J., Golden, D., Kurylo, M., Wine, P., Abbatt, J., Burkholder, J., Kolb, C., Moortgat, G., et al. (2011). Chemical kinetics and photochemical data for use in atmospheric studies, nasa/jpl data evaluation, jpl publication 06-2 evaluation no. 17, nasa, pasadena, ca, june 1, 2011.

Santee, M. and Crisp, D. (1993). Thermal structure and dust loading of the Martian atmosphere during late southern summer: Mariner 9 revisited. J. Geophys. Res., 98(E2):3261–3279.

Savijarvi, H. (1999). A model study of the atmospheric boundary layer in the mars pathfinder lander conditions. *Quarterly Journal of the Royal Meteorological Society*, 125(554):483–493.

Savijärvi, H. I. (1988). Global Energy and Moisture Budgets from Rawinsonde Data. *Monthly Weather Review*, 116(2):417.

Schaefer, L. and Fegley, B. (2009). Chemistry of Silicate Atmospheres of Evaporating Super-Earths. ApJ, 703(2):L113–L117.

Schaefer, L., Wordsworth, R. D., Berta-Thompson, Z., and Sasselov, D. (2016). Predictions of the Atmospheric Composition of GJ 1132b. ApJ, 829:63.

Scheucher, M., Grenfell, J. L., Wunderlich, F., Godolt, M., Schreier, F., and Rauer, H. (2018). New Insights into Cosmic-Ray-induced Biosignature Chemistry in Earth-like Atmospheres. ApJ, 863(1):6.

Schneider, A. C. and Shkolnik, E. L. (2018). HAZMAT. III. The UV Evolution of Mid- to Late-M Stars with GALEX. AJ, 155:122.

Schürgers, M. and Welge, K. H. (1968). Absorptionskoeffizient von H_2O_2 und N_2H_4 zwischen 1200 und 2000 *Å*. *Zeitschrift Naturforschung Teil A*, 23:1508–1510.

Schwieterman, E. W., Kiang, N. Y., Parenteau, M. N., Harman, C. E., DasSarma, S., Fisher, T. M., Arney, G. N., Hartnett, H. E., Reinhard, C. T., and Olson, S. L. (2018). Exoplanet Biosignatures: A Review of Remotely Detectable Signs of Life. *Astrobiology*, 18(6):663–708.

Schwieterman, E. W., Meadows, V. S., Domagal-Goldman, S. D., Deming, D., Arney, G. N., Luger, R., Harman, C. E., Misra, A., and Barnes, R. (2016). Identifying Planetary Biosignature Impostors: Spectral Features of CO and O_4 Resulting from Abiotic O_2/O_3 Production. ApJ, 819:L13.

Schwieterman, E. W., Robinson, T. D., Meadows, V. S., Misra, A., and Domagal-Goldman, S. (2015). Detecting and Constraining N_2 Abundances in Planetary Atmospheres Using Collisional Pairs. ApJ, 810:57.

Seager, S., Deming, D., and Valenti, J. (2009). Transiting exoplanets with jwst. In *Astrophysics in the Next Decade*, pages 123–145. Springer.

Segura, A., Kasting, J. F., Meadows, V., Cohen, M., Scalo, J., Crisp, D., Butler, R. A. H., and Tinetti, G. (2005). Biosignatures from Earth-Like Planets Around M Dwarfs. *Astrobiology*, 5:706–725.

Segura, A., Krelove, K., Kasting, J. F., Sommerlatt, D., Meadows, V., Crisp, D., Cohen, M., and Mlawer, E. (2003). Ozone concentrations and ultraviolet fluxes on Earth-like planets around other stars. *Astrobiology*, 3(4):689–708.

Segura, a., Meadows, V. S., Kasting, J. F., Crisp, D., and Cohen, M. (2007). Abiotic formation of O_2 and O_3 in high-CO_2 terrestrial atmospheres. *Astronomy and Astrophysics*, 472(2):665–679.

Segura, A., Walkowicz, L. M., Meadows, V., Kasting, J., and Hawley, S. (2010). The Effect of a Strong Stellar Flare on the Atmospheric Chemistry of an Earth-like Planet Orbiting an M Dwarf. *Astrobiology*, 10:751–771.

Sehmel, G. A. (1980). Particle and gas dry deposition: A review. *Atmospheric Environment*, 14(9):983–1011.

Seiff, A., Schofield, J. T., Kliore, A. J., Taylor, F. W., Limaye, S. S., Revercomb, H. E., Sromovsky, L. A., Kerzhanovich, V. V., Moroz, V. I., and Marov, M. Y. (1985). Models of the structure of the atmosphere of Venus from the surface to 100 kilometers altitude. *Advances in Space Research*, 5(11):3–58.

Seinfeld, J. and Pandis, S. (2006). Atmospheric chemistry and physics.

Selsis, F., Despois, D., and Parisot, J.-P. (2002). Signature of life on exoplanets: Can darwin produce false positive detections? A&A, 388(3):985–1003.

Selsis, F., Wordsworth, R. D., and Forget, F. (2011). Thermal phase curves of nontransiting terrestrial exoplanets. I. Characterizing atmospheres. A&A, 532:A1.

Serdyuchenko, A., Gorshelev, V., Weber, M., and Burrow, J. P. (2011). New broadband high-resolution ozone absorption cross-sections. *Spectroscopy Europe*, 23(6):14.

Shaheen, R., Janssen, C., and Röckmann, T. (2007). Investigations of the photochemical isotope equilibrium between O¡sub¿2¡/sub¿, CO¡sub¿2¡/sub¿ and O¡sub¿3¡/sub¿. *Atmospheric Chemistry and Physics*, 7(2):509.

Sharp, Z. (2017). Principles of stable isotope geochemistry.

Shemansky, D. E. (1972). CO2 Extinction Coefficient 1700–3000 . *J. Chem. Phys.*, 56(4):1582.

Shields, A. L., Ballard, S., and Johnson, J. A. (2016). The habitability of planets orbiting M-dwarf stars. Phys. Rep., 663:1.

Shields, A. L., Meadows, V. S., Bitz, C. M., Pierrehumbert, R. T., Joshi, M. M., and Robinson, T. D. (2013). The effect of host star spectral energy distribution and ice-albedo feedback on the climate of extrasolar planets. *Astrobiology*, 13(8):715–739.

Shine, K. (1989). Sources and sinks of zonal momentum in the middle atmosphere diagnosed using the diabatic circulation. *Quarterly Journal of the Royal Meteorological Society*, 115(486):265–292.

Shvartzvald, Y., Yee, J. C., Calchi Novati, S., Gould, A., Lee, C.-U., Beichman, C., Bryden, G., Carey, S., Gaudi, B. S., Henderson, C. B., Zhu, W., Spitzer team, Albrow, M. D., Cha, S.-M., Chung, S.-J., Han, C., Hwang, K.-H., Jung, Y. K., Kim, D.-J., Kim, H.-W., Kim, S.-L., Lee, Y., Park, B.-G., Pogge, R. W., Ryu, Y.-H., Shin, I.-G., and KMTNet group (2017). An Earth-mass Planet in a 1 au Orbit around an Ultracool Dwarf. ApJ, 840:L3.

Simon, F., Schneider, W., Moortgat, G., and Burrows, J. (1990). A study of the clo absorption cross-section between 240 and 310 nm and the kinetics of the self-reaction at 300 k. *Journal of Photochemistry and Photobiology A: Chemistry*, 55(1):1–23.

Simoncini, E., Virgo, N., and Kleidon, A. (2013). Quantifying drivers of chemical disequilibrium: theory and application to methane in the earth's atmosphere. *Earth System Dynamics*, 4(2):317–331.

Sing, D. K., Pont, F., Aigrain, S., Charbonneau, D., Désert, J. M., Gibson, N., Gilliland, R., Hayek, W., Henry, G., and Knutson, H. (2011). Hubble Space Telescope transmission spectroscopy of the exoplanet HD 189733b: high-altitude atmospheric haze in the optical and near-ultraviolet with STIS. MNRAS, 416(2):1443–1455.

Snellen, I. (2014). High-dispersion spectroscopy of extrasolar planets: from CO in hot Jupiters

to O2 in exo-Earths. *Philos. Trans. R. Soc. A Math. Phys. Eng. Sci.*, 372(2014):20130075–20130075.

Snellen, I., de Kok, R., Birkby, J. L., Brandl, B., Brogi, M., Keller, C., Kenworthy, M., Schwarz, H., and Stuik, R. (2015). Combining high-dispersion spectroscopy with high contrast imaging: Probing rocky planets around our nearest neighbors. A&A, 576:A59.

Snellen, I. A. G., de Kok, R. J., le Poole, R., Brogi, M., and Birkby, J. (2013). Finding Extraterrestrial Life Using Ground-based High-dispersion Spectroscopy. ApJ, 764(2):182.

Solomon, S. C. and Head, J. W. (1991). Fundamental Issues in the Geology and Geophysics of Venus. *Science*, 252:252–260.

Spiering, F. R., Kiseleva, M. B., Filippov, N. N., van Kesteren, L., and van der Zand e, W. J. (2011). Collision-induced absorption in the O2 B-band region near 670 nm. *Physical Chemistry Chemical Physics (Incorporating Faraday Transactions)*, 13(20):9616.

Spiering, F. R. and van der Zande, W. J. (2012). Collision induced absorption in the $a^1\Delta$(v = 2) $\leftarrow\!\!-$ $X^3\Sigma_g^-$(v = 0) band of molecular oxygen. *Physical Chemistry Chemical Physics (Incorporating Faraday Transactions)*, 14(28):9923.

Stamnes, K., Tsay, S. C., Wiscombe, W., and Jayaweerz, K. (1988). Numerically stable algorithm for discrete-ordinate-method radiative transfer in multiple scattering and emitting layered media. Appl. Opt., 42(15):2502–2509.

Stamnes, K., Tsay, S. C., Wiscombe, W., and Laszlo, I. (2000). DISORT, a general-purpose Fortran program for discrete-ordinate-method radiative transfer in scattering and emitting layered media: documentation of methodology. `ftp://climate.gsfc.nasa.gov/pub/wiscombe/MultipleScatt/`.

Stephenson, R. and Malanowski, S. (1987). Handbook of the thermodynamics of organic compounds. *ISBN*, 978(94):010.

Stull, D. R. (1947). Vapor pressure of pure substances. organic and inorganic compounds. *Industrial & Engineering Chemistry*, 39(4):517–540.

Suto, M. and Lee, L. C. (1984). Photoabsorption and photodissociation of HONO¡SUB¿2¡/SUB¿ in the 105-220 nm region. J. Chem. Phys., 81:1294–1297.

Tajika, E. (2003). Faint young Sun and the carbon cycle: implication for the Proterozoic global glaciations. *Earth and Planetary Science Letters*, 214(3-4):443–453.

Tarter, J. C., Backus, P. R., Mancinelli, R. L., Aurnou, J. M., Backman, D. E., Basri, G. S., Boss, A. P., Clarke, A., Deming, D., Doyle, L. R., Feigelson, E. D., Freund, F., Grinspoon, D. H., Haberle, R. M., Hauck, II, S. A., Heath, M. J., Henry, T. J., Hollingsworth, J. L., Joshi, M. M., Kilston, S., Liu, M. C., Meikle, E., Reid, I. N., Rothschild, L. J., Scalo, J., Segura, A., Tang, C. M., Tiedje, J. M., Turnbull, M. C., Walkowicz, L. M., Weber, A. L., and Young, R. E. (2007). A Reappraisal of The Habitability of Planets around M Dwarf Stars. *Astrobiology*, 7:30–65.

Thalman, R. and Volkamer, R. (2013). Temperature dependent absorption cross-sections of O_2-O_2 collision pairs between 340 and 630 nm and at atmospherically relevant pressure. *Physical Chemistry Chemical Physics (Incorporating Faraday Transactions)*, 15(37):15371.

Tian, F. (2015). History of water loss and atmospheric O_2 buildup on rocky exoplanets near M dwarfs. *Earth and Planetary Science Letters*, 432:126–132.

Tilley, M. A., Segura, A., Meadows, V., Hawley, S., and Davenport, J. (2019). Modeling Repeated M Dwarf Flaring at an Earth-like Planet in the Habitable Zone: Atmospheric Effects for an Unmagnetized Planet. *Astrobiology*, 19(1):64–86.

Tinetti, G., Meadows, V. S., Crisp, D., Fong, W., Velusamy, T., and Snively, H. (2005). Disk-averaged synthetic spectra of Mars. *Astrobiology*, 5(4):461–82.

Tinetti, G., Vidal-Madjar, A., Liang, M.-C., Beaulieu, J.-P., Yung, Y., Carey, S., Barber, R. J., Tennyson, J., Ribas, I., and Allard, N. (2007). Water vapour in the atmosphere of a transiting extrasolar planet. Nature, 448(7150):169–171.

Toon, O. B., McKay, C. P., Ackerman, T. P., and Santhanam, K. (1989). Rapid calculation of radiative heating rates and photodissociation rates in inhomogeneous multiple scattering atmospheres. J. Geophys. Res., 94:16287–16301.

Toon, O. B., Turco, R. P., Westphal, D., Malone, R., and Liu, M. S. (1988). A multidimensional model for aerosols - Description of computational analogs. *Journal of Atmospheric Sciences*, 45:2123–2143.

Tran, H., Boulet, C., and Hartmann, J. M. (2006). Line mixing and collision-induced absorption by oxygen in the A band: Laboratory measurements, model, and tools for atmospheric spectra computations. *Journal of Geophysical Research (Atmospheres)*, 111(D15):D15210.

Trenberth, K. E. and Caron, J. M. (2001). Estimates of Meridional Atmosphere and Ocean Heat Transports. *Journal of Climate*, 14(16):3433–3443.

Trenberth, K. E., Fasullo, J. T., and Kiehl, J. (2009). Earth's Global Energy Budget. *Bulletin of the American Meteorological Society*, 90(3):311.

Turbet, M., Bolmont, E., Leconte, J., Forget, F., Selsis, F., Tobie, G., Caldas, A., Naar, J., and Gillon, M. (2018). Modeling climate diversity, tidal dynamics and the fate of volatiles on TRAPPIST-1 planets. A&A, 612:A86.

Turbet, M., Leconte, J., Selsis, F., Bolmont, E., Forget, F., Ribas, I., Raymond, S. N., and Anglada-Escudé, G. (2016). The habitability of Proxima Centauri b. II. Possible climates and observability. A&A, 596:A112.

Turco, R. P., Hamill, P., Toon, O. B., Whitten, R. C., and Kiang, C. S. (1979). A One-Dimensional Model Describing Aerosol Formation and Evolution in the Stratosphere: I. Physical Processes and Mathematical Analogs. *Journal of Atmospheric Sciences*, 36(4):699–717.

Twicken, J. D., Jenkins, J. M., Seader, S. E., Tenenbaum, P., Smith, J. C., Brownston, L. S., Burke, C. J., Catanzarite, J. H., Clarke, B. D., Cote, M. T., Girouard, F. R., Klaus, T. C., Li, J.,

McCauliff, S. D., Morris, R. L., Wohler, B., Campbell, J. R., Kamal Uddin, A., Zamudio, K. A., Sabale, A., Bryson, S. T., Caldwell, D. A., Christiansen, J. L., Coughlin, J. L., Haas, M. R., Henze, C. E., Sand erfer, D. T., and Thompson, S. E. (2016). Detection of Potential Transit Signals in 17 Quarters of Kepler Data: Results of the Final Kepler Mission Transiting Planet Search (DR25). AJ, 152(6):158.

Unterborn, C. T., Desch, S. J., Hinkel, N. R., and Lorenzo, A. (2018a). Inward migration of the TRAPPIST-1 planets as inferred from their water- rich compositions. *Nature Astronomy*, 2:297–302.

Unterborn, C. T., Hinkel, N. R., and Desch, S. J. (2018b). Updated Compositional Models of the TRAPPIST-1 Planets. *Research Notes of the American Astronomical Society*, 2(3):116.

Uthman, A., Demlein, P., Allston, T., Withiam, M., McClements, M., and Takacs, G. (1978). Photoabsorption spectra of gaseous methyl bromide, ethylene dibromide, nitrosyl bromide, thionyl chloride, and sulfuryl chloride. *The Journal of Physical Chemistry*, 82(20):2252–2257.

Van Grootel, V., Fernandes, C. S., Gillon, M., Jehin, E., Manfroid, J., Scuflaire, R., Burgasser, A. J., Barkaoui, K., Benkhaldoun, Z., and Burdanov, A. (2018). Stellar Parameters for Trappist-1. ApJ, 853(1):30.

Vandaele, A. C., Hermans, C., Simon, P. C., Carleer, M., Colin, R., Fally, S., Mérienne, M. F., Jenouvrier, A., and Coquart, B. (1998). Measurements of the NO_2 absorption cross-section from 42,000 cm^{-1} to 10,000 cm^{-1} (238-1000 nm) at 220 K and 294 K. J. Quant. Spec. Radiat. Transf., 59:171–184.

Vidal-Madjar, A., Désert, J. M., Lecavelier des Etangs, A., Hébrard, G., Ballester, G. E., Ehrenreich, D., Ferlet, R., McConnell, J. C., Mayor, M., and Parkinson, C. D. (2004). Detection of Oxygen and Carbon in the Hydrodynamically Escaping Atmosphere of the Extrasolar Planet HD 209458b. ApJ, 604(1):L69–L72.

Villanueva, G. L., Mumma, M. J., Novak, R. E., Käufl, H. U., Hartogh, P., Encrenaz, T., Tokunaga, A., Khayat, A., and Smith, M. D. (2015). Strong water isotopic anomalies in the martian atmosphere: Probing current and ancient reservoirs. *Science*, 348:218–221.

Wagner, W., Saul, A., and Pruss, A. (1994). International Equations for the Pressure Along the Melting and Along the Sublimation Curve of Ordinary Water Substance. *Journal of Physical and Chemical Reference Data*, 23:515–527.

Wakeford, H. R., Lewis, N. K., Fowler, J., Bruno, G., Wilson, T. J., Moran, S. E., Valenti, J., Batalha, N. E., Filippazzo, J., Bourrier, V., Hörst, S. M., Lederer, S. M., and de Wit, J. (2019). Disentangling the Planet from the Star in Late-Type M Dwarfs: A Case Study of TRAPPIST-1g. AJ, 157(1):11.

Walker, J. C., Hays, P., and Kasting, J. F. (1981). A negative feedback mechanism for the long-term stabilization of earth's surface temperature. *Journal of Geophysical Research: Oceans*, 86(C10):9776–9782.

Walker, S. I., Bains, W., Cronin, L., DasSarma, S., Danielache, S., Domagal- Goldman, S., Kacar, B., Kiang, N. Y., Lenardic, A., Reinhard, C. T., Moore, W., Schwieterman, E. W., Shkolnik, E. L., and Smith, H. B. (2018). Exoplanet Biosignatures: Future Directions. *Astrobiology*, 18:779–824.

Wang, Y., Liu, Y., Tian, F., Yang, J., Ding, F., Zhou, L., and Hu, Y. (2016). Effects of Obliquity on the Habitability of Exoplanets around M Dwarfs. ApJ, 823(1):L20.

Way, M. J., Aleinov, I., Amundsen, D. S., Chand ler, M. A., Clune, T. L., Del Genio, A. D., Fujii, Y., Kelley, M., Kiang, N. Y., Sohl, L., and Tsigaridis, K. (2017). Resolving Orbital and Climate Keys of Earth and Extraterrestrial Environments with Dynamics (ROCKE-3D) 1.0: A General Circulation Model for Simulating the Climates of Rocky Planets. *The Astrophysical Journal Supplement Series*, 231(1):12.

Way, M. J., Del Genio, A. D., Aleinov, I., Clune, T. L., Kelley, M., and Kiang, N. Y. (2018). Climates of warm earth-like planets. i. 3d model simulations. *The Astrophysical Journal Supplement Series*, 239(2):24.

Weiss, L. M. and Marcy, G. W. (2014). The Mass-Radius Relation for 65 Exoplanets Smaller than 4 Earth Radii. ApJ, 783(1):L6.

Williams, D. M. and Gaidos, E. (2008). Detecting the glint of starlight on the oceans of distant planets. Icarus, 195(2):927–937.

Williams, D. M. and Pollard, D. (2002). Earth-like worlds on eccentric orbits: excursions beyond the habitable zone. *International Journal of Astrobiology*, 1:61–69.

Williams, D. M. and Pollard, D. (2003). Extraordinary climates of Earth-like planets: three-dimensional climate simulations at extreme obliquity. *International Journal of Astrobiology*, 2(1):1–19.

Williams, S. N., Schaeffer, S. J., Calvache, M. L., and Lopez, D. (1992). Global carbon dioxide emission to the atmosphere by volcanoes. Geochim. Cosmochim. Acta, 56:1765–1770.

Winn, J. N. (2010). Exoplanet Transits and Occultations. In Seager, S., editor, *Exoplanets*, pages 55–77. University of Arizona Press, Tucson.

Wofsy, S. C., McConnell, J. C., and McElroy, M. B. (1972). Atmospheric CH_4, CO, and CO_2. J. Geophys. Res., 77:4477.

Wolf, E. T. (2017). Assessing the Habitability of the TRAPPIST-1 System Using a 3D Climate Model. ApJ, 839(1):L1.

Wolf, E. T. (2018). Erratum: "Assessing the Habitability of the TRAPPIST-1 System Using a 3D Climate Model" (2017, ApJL, 839, L1). ApJ, 855(1):L14.

Wolf, E. T., Kopparapu, R. K., and Haqq-Misra, J. (2019). Simulated Phase-dependent Spectra of Terrestrial Aquaplanets in M Dwarf Systems. ApJ, 877(1):35.

Wolf, E. T. and Toon, O. B. (2013). Hospitable Archean Climates Simulated by a General Circulation Model. *Astrobiology*, 13(7):656–673.

Woo, R. and Ishimaru, A. (1981). Eddy diffusion coefficient for the atmosphere of Venus from radio scintillation measurements. Nature, 289:383.

Wordsworth, R. (2015). Atmospheric Heat Redistribution and Collapse on Tidally Locked Rocky Planets. ApJ, 806(2):180.

Wordsworth, R., Forget, F., and Eymet, V. (2010). Infrared collision-induced and far-line absorption in dense CO $_2$ atmospheres. Icarus, 210:992–997.

Wordsworth, R., Forget, F., Millour, E., Head, J., Madeleine, J.-B., and Charnay, B. (2013). Global modelling of the early martian climate under a denser CO2 atmosphere: Water cycle and ice evolution. *Icarus*, 222(1):1–19.

Wordsworth, R., Kalugina, Y., Lokshtanov, S., Vigasin, A., Ehlmann, B., Head, J., Sanders, C., and Wang, H. (2017). Transient reducing greenhouse warming on early Mars. Geophys. Res. Lett., 44:665–671.

Wordsworth, R. and Pierrehumbert, R. (2014). ABIOTIC OXYGEN-DOMINATED ATMOSPHERES ON TERRESTRIAL HABITABLE ZONE PLANETS. *Astrophys. J.*, 785(2):L20.

Wordsworth, R. D. (2016). The Climate of Early Mars. *Annual Review of Earth and Planetary Sciences*, 44:381–408.

Wordsworth, R. D., Forget, F., Selsis, F., Millour, E., Charnay, B., and Madeleine, J.-B. (2011). Gliese 581d is the First Discovered Terrestrial-mass Exoplanet in the Habitable Zone. ApJ, 733(2):L48.

Wordsworth, R. D., Schaefer, L. K., and Fischer, R. A. (2018). Redox Evolution via Gravitational Differentiation on Low-mass Planets: Implications for Abiotic Oxygen, Water Loss, and Habitability. AJ, 155(195).

Wu, C. Y. R. and Chen, F. Z. (1998). Temperature-dependent photoabsorption cross sections of H_2S in the 1600-2600 Å region. J. Quant. Spec. Radiat. Transf., 60:17–23.

Wunderlich, F., Godolt, M., Grenfell, J. L., Städt, S., Smith, A. M. S., Gebauer, S., Schreier, F., Hedelt, P., and Rauer, H. (2019). Detectability of atmospheric features of Earth-like planets in the habitable zone around M dwarfs. A&A, 624:A49.

Wunsch, C. (2005). The Total Meridional Heat Flux and Its Oceanic and Atmospheric Partition. *Journal of Climate*, 18(21):4374–4380.

Yang, J. and Abbot, D. S. (2014). a Low-Order Model of Water Vapor, Clouds, and Thermal Emission for Tidally Locked Terrestrial Planets. ApJ, 784(2):155.

Yang, J., Abbot, D. S., Koll, D. D. B., Hu, Y., and Showman, A. P. (2019a). Ocean Dynamics and the Inner Edge of the Habitable Zone for Tidally Locked Terrestrial Planets. ApJ, 871(1):29.

Yang, J., Boué, G., Fabrycky, D. C., and Abbot, D. S. (2014). Strong Dependence of the Inner Edge of the Habitable Zone on Planetary Rotation Rate. ApJ, 787:L2.

Yang, J., Cowan, N. B., and Abbot, D. S. (2013). Stabilizing Cloud Feedback Dramatically Expands the Habitable Zone of Tidally Locked Planets. ApJ, 771(2):L45.

Yang, J., Ji, W., and Zeng, Y. (2019b). Transition from eyeball to snowball driven by sea-ice drift on tidally locked terrestrial planets. *Nature Astronomy*, page 447.

Yang, J., Leconte, J., Wolf, E. T., Goldblatt, C., Feldl, N., Merlis, T., Wang, Y., Koll, D. D. B., Ding, F., and Forget, F. (2016). Differences in Water Vapor Radiative Transfer among 1D Models Can Significantly Affect the Inner Edge of the Habitable Zone. ApJ, 826(2):222.

Yang, J., Leconte, J., Wolf, E. T., Merlis, T., Koll, D. D. B., Forget, F., and Abbot, D. S. (2019c). Simulations of Water Vapor and Clouds on Rapidly Rotating and Tidally Locked Planets: A 3D Model Intercomparison. ApJ, 875(1):46.

Yates, J. S., Palmer, P. I., Manners, J., Boutle, I., Kohary, K., Mayne, N., and Abraham, L. (2020). Ozone chemistry on tidally locked M dwarf planets. MNRAS, 492(2):1691–1705.

Yoshino, K., Cheung, A. S.-C., Esmond, J. R., Parkinson, W. H., and Freeman, D. E. (1988). Improved absorption cross-sections of oxygen in the wavelength region 205-240 nm of the Herzberg continuum. Planet. Space Sci., 36:1469–1475.

Yoshino, K., Esmond, J. R., Cheung, A. S.-C., Freeman, D. E., and Parkinson, W. H. (1992). High resolution absorption cross sections in the transmission window region of the Schumann-Runge bands and Herzberg continuum of O2. Planet. Space Sci., 40:185–192.

Yung, Y. L., Allen, M., and Pinto, J. P. (1984). Photochemistry of the atmosphere of Titan - Comparison between model and observations. *Astrophys. J. Suppl. Ser.*, 55(1981):465.

Zahnle, K., Claire, M., and Catling, D. (2006). The loss of mass-independent fractionation in sulfur due to a Palaeoproterozoic collapse of atmospheric methane. *Geobiology*, 4(4):271–283.

Zechmeister, M., Dreizler, S., Ribas, I., Reiners, A., Caballero, J. A., Bauer, F. F., Béjar, V. J. S., González-Cuesta, L., Herrero, E., Lalitha, S., López-González, M. J., Luque, R., Morales, J. C., Pallé, E., Rodríguez, E., Rodríguez López, C., Tal-Or, L., Anglada-Escudé, G., Quirrenbach, A., Amado, P. J., Abril, M., Aceituno, F. J., Aceituno, J., Alonso-Floriano, F. J., Ammler-von Eiff, M., Antona Jiménez, R., Anwand-Heerwart, H., Arroyo-Torres, B., Azzaro, M., Baroch, D., Barrado, D., Becerril, S., Benítez, D., Berdiñas, Z. M., Bergond, G., Bluhm, P., Brinkmöller, M., del Burgo, C., Calvo Ortega, R., Cano, J., Cardona Guillén, C., Carro, J., Cárdenas Vázquez, M. C., Casal, E., Casasayas-Barris, N., Casanova, V., Chaturvedi, P., Cifuentes, C., Claret, A., Colomé, J., Cortés-Contreras, M., Czesla, S., Díez-Alonso, E., Dorda, R., Fernández, M., Fernández-Martín, A., Fuhrmeister, B., Fukui, A., Galadí-Enríquez, D., Gallardo Cava, I., Garcia de la Fuente, J., Garcia-Piquer, A., García Vargas, M. L., Gesa, L., Góngora Rueda, J., González-Álvarez, E., González Hernández, J. I., González-Peinado, R., Grözinger, U., Guàrdia, J., Guijarro, A., de Guindos, E., Hatzes, A. P., Hauschildt, P. H., Hedrosa, R. P., Helmling, J., Henning, T., Hermelo, I., Hernández Arabi, R., Hernández Castaño, L., Hernández Otero, F., Hintz, D.,

Huke, P., Huber, A., Jeffers, S. V., Johnson, E. N., de Juan, E., Kaminski, A., Kemmer, J., Kim, M., Klahr, H., Klein, R., Klüter, J., Klutsch, A., Kossakowski, D., Kürster, M., Labarga, F., Lafarga, M., Llamas, M., Lampón, M., Lara, L. M., Launhardt, R., Lázaro, F. J., Lodieu, N., López del Fresno, M., López-Puertas, M., López Salas, J. F., López-Santiago, J., Magán Madinabeitia, H., Mall, U., Mancini, L., Mand el, H., Marfil, E., Marín Molina, J. A., Maroto Fernández, D., Martín, E. L., Martín-Fernández, P., Martín-Ruiz, S., Marvin, C. J., Mirabet, E., Montañés-Rodríguez, P., Montes, D., Moreno-Raya, M. E., Nagel, E., Naranjo, V., Narita, N., Nortmann, L., Nowak, G., Ofir, A., Oshagh, M., Panduro, J., Parviainen, H., Pascual, J., Passegger, V. M., Pavlov, A., Pedraz, S., Pérez-Calpena, A., Pérez Medialdea, D., Perger, M., Perryman, M. A. C., Rabaza, O., Ramón Ballesta, A., Rebolo, R., Redondo, P., Reffert, S., Reinhardt, S., Rhode, P., Rix, H. W., Rodler, F., Rodríguez Trinidad, A., Rosich, A., Sadegi, S., Sánchez-Blanco, E., Sánchez Carrasco, M. A., Sánchez-López, A., Sanz-Forcada, J., Sarkis, P., Sarmiento, L. F., Schäfer, S., Schmitt, J. H. M. M., Schöfer, P., Schweitzer, A., Seifert, W., Shulyak, D., Solano, E., Sota, A., Stahl, O., Stock, S., Strachan, J. B. P., Stuber, T., Stürmer, J., Suárez, J. C., Tabernero, H. M., Tala Pinto, M., Trifonov, T., Veredas, G., Vico Linares, J. I., Vilardell, F., Wagner, K., Wolthoff, V., Xu, W., Yan, F., and Zapatero Osorio, M. R. (2019). The CARMENES search for exoplanets around M dwarfs. Two temperate Earth-mass planet candidates around Teegarden's Star. A&A, 627:A49.

Zelikoff, M., Watanabe, K., and Inn, E. C. Y. (1953). Absorption Coefficients of Gases in the Vacuum Ultraviolet. Part II. Nitrous Oxide. J. Chem. Phys., 21:1643–1647.

Zhang, G. J. and McFarlane, N. A. (1995). Sensitivity of climate simulations to the parameterization of cumulus convection in the canadian climate centre general circulation model. *Atmosphere-ocean*, 33(3):407–446.

Zhang, X., Chang, M., Mills, F. P., Belyaev, D. A., and Yung, Y. L. (2012). Sulfur chemistry in the middle atmosphere of Venus. *Icarus*, 217(2):714–739.

Zhou, B., Sun, S., Yao, K., and Zhu, K. (2018). Reexamining the Gradient and Countergradi-

ent Representation of the Local and Nonlocal Heat Fluxes in the Convective Boundary Layer. *Journal of Atmospheric Sciences*, 75(7):2317–2336.

Appendix A

VITA

VITA

Andrew P. Lincowski

EDUCATION

University of Washington

Ph.D., Astronomy & Astrobiology *2020*

Dissertation advisor: Professor Victoria S. Meadows

University of Washington

M.Sc., Astronomy *2017*

University of Arizona

B.Sc., Physics & Astronomy, *magna cum laude*, with Honors (Astronomy) *2015*

Thesis advisors: Dr. Aki Roberge (NASA/GSFC) and Professor Philip A. Pinto

University of Arizona

B.S.B.A., Accounting, *magna cum laude* *2006*

FELLOWSHIPS & SCHOLARSHIPS

NASA Earth & Space Sciences Fellowship, 2017–2020

John Mather Nobel Scholar, 2014

Angelos C. Langadas Scholarship, 2014

William F. Lucas Scholarship, 2014

Glenn C. Purviance Scholarship, 2014

Galileo Circle Scholar, 2013 & 2014

PUBLICATIONS

1. Fauchez, T. J., Turbet, M., Villanueva, G. L., Wolf, E. T., Arney, G., Kopparapu, R. K., **Lincowski, Andrew**, Mandell, A., de Wit, J., Pidhorodetska, D., Domagal-Goldman, S. D., and Stevenson, K. B. (2019). Impact of Clouds and Hazes on the Simulated JWST Transmission Spectra of Habitable Zone Planets in the TRAPPIST-1 System. ApJ, 887(2):194
2. Lustig-Yaeger, J., Meadows, V. S., and **Lincowski, Andrew P.** (2019b). A Mirage of the Cosmic Shoreline: Venus-like Clouds as a Statistical False Positive for Exoplanet Atmospheric Erosion. ApJ, 887(1):L11
3. Lustig-Yaeger, J., Meadows, V. S., and **Lincowski, Andrew P.** (2019a). The Detectability and Characterization of the TRAPPIST-1 Exoplanet Atmospheres with JWST. AJ, 158(1):27
4. **Lincowski, Andrew P.**, Lustig-Yaeger, J., and Meadows, V. S. (2019). Observing Isotopologue Bands in Terrestrial Exoplanet Atmospheres with the James Webb Space Telescope: Implications for Identifying Past Atmospheric and Ocean Loss. AJ, 158(1):26
5. **Lincowski, Andrew P.**, Meadows, V. S., Crisp, D., Robinson, T. D., Luger, R., Lustig-Yaeger, J., and Arney, G. N. (2018b). Evolved Climates and Observational Discriminants for the TRAPPIST-1 Planetary System. ApJ, 867:76
6. Meadows, V. S., Reinhard, C. T., Arney, G. N., Parenteau, M. N., Schwieterman, E. W., Domagal-Goldman, S. D., **Lincowski, Andrew P.**, Stapelfeldt, K. R., Rauer, H., DasSarma, S., Hegde, S., Narita, N., Deitrick, R., Lustig-Yaeger, J., Lyons, T. W., Siegler, N., and Grenfell, J. L. (2018b). Exoplanet Biosignatures: Understanding Oxygen as a Biosignature in the Context of Its Environment. *Astrobiology*, 18:630–662
7. Meadows, V. S., Arney, G. N., Schwieterman, E. W., Lustig-Yaeger, J., **Lincowski, Andrew P.**, Robinson, T., Domagal-Goldman, S. D., Deitrick, R., Barnes, R. K., Fleming, D. P., Luger, R., Driscoll, P. E., Quinn, T. R., and Crisp, D. (2018a). The Habitability of Proxima Centauri b: Environmental States and Observational Discriminants. *Astrobiology*, 18:133–189
8. Roberge, A., Rizzo, M. J., **Lincowski, Andrew P.**, Arney, G. N., Stark, C. C., Robinson, T. D., Snyder, G. F., Pueyo, L., Zimmerman, N. T., Jansen, T., Nesvold, E. R., Meadows, V. S., and

Turnbull, M. C. (2017). Finding the Needles in the Haystacks: High-fidelity Models of the Modern and Archean Solar System for Simulating Exoplanet Observations. *Publications of the Astronomical Society of the Pacific*, 129:124401

9. **Lincowski, A. P.**, Halfen, D. T., and Ziurys, L. M. (2016). Millimeter/Submillimeter Spectroscopy of TiO ($X^3\Delta_r$): The Rare Titanium Isotopologues. ApJ, 833:9

10. Stark, C. C., Kuchner, M. J., and **Lincowski, Andrew** (2015). The Pseudo-Zodi Problem for Edge-On Planetary Systems. ApJ, 801:128

PRESS

Study brings new climate models of small star TRAPPIST 1's seven intriguing worlds. Peter Kelley, UW News, Nov 20 2018; `https://www.washington.edu/news/2018/11/20/study-brings-new-climate-models-of-small-star-trappist-1s-seven-intriguing-worlds/` (reported by over 70 other online news outlets)

First responders: Getting the bad guys and fighting fires ... as physicists. Alaina G. Levine, APS News, May 2015; `https://www.aps.org/publications/apsnews/201505/profiles.cfm`

Using the Force: UA Police Officer Completes NASA Project. Raymond Sanchez, UA News, Sept 26 2014;`https://uanews.arizona.edu/story/using-the-force-ua-police-officer-completes-nasa-project` (reported by other news outlets as e.g. "Guardian of the Galaxy? Cop's beat includes outer space"

CONFERENCE PROCEEDINGS (ORAL)

1. **Lincowski, A. P.**, Meadows, V. S., and Lustig-Yaeger, J. (2019). Constaining Past Ocean Loss From M Dwarf PLanets with Transit Transmission Spectroscopy. In *AbSciCon2019*

2. **Lincowski, Andrew**, Lustig-Yaeger, J., and Meadows, V. (2019). Probing Terrestrial Exoplanet Atmospheric Escape By Observing H_2O and CO_2 Isotopologue Bands with the *James Webb Space Telescope*. In *American Astronomical Society Meeting Abstracts #233*, volume 233 of *American Astronomical Society Meeting Abstracts*, page 226.05

3. **Lincowski, A. P.**, Meadows, V. S., Crisp, D., Robinson, T. D., Luger, R., and Lustig-Yaeger, J. (2018). Evolved Climates of the TRAPPIST-1 Planetary System. *LPI Contributions*, 2065:2024

4. **Lincowski, A. P.**, Meadows, V. S., Crisp, D., Robinson, T. D., Luger, R., and Arney, G. N. (2017c). Habitability Imposters: Extreme Terrestrial Climates in the Habitable Zone of M Dwarf Stars. In *Habitable Worlds 2017: A System Science Workshop*, volume 2042, page 4091

5. **Lincowski, A. P.**, Meadows, V. S., Crisp, D., Robinson, T. D., and Arney, G. N. (2017a). Climates of Venus-Like Exoplanets. In *Venus Modeling Workshop*, volume 2022, page 8037

6. **Lincowski, A. P.**, Meadows, V. S., Crisp, D., Robinson, T. D., and Arney, G. N. (2017b). Condensible Atmospheres of Terrestrial Planets. In *AbSciCon2017*

7. **Lincowski, Andrew**, Meadows, V., Robinson, T. D., and Crisp, D. (2016a). The Effect of Carbon Dioxide (CO $_2$) Ice Cloud Condensation on the Habitable Zone. In *AAS/Division for Planetary Sciences Meeting Abstracts #48*, AAS/Division for Planetary Sciences Meeting Abstracts, page 302.09

8. **Lincowski, Andrew**, Meadows, V., Robinson, T. D., and Crisp, D. (2016b). The Effect of Carbon Dioxide (CO $_2$) Ice Cloud Condensation on the Habitable Zone. In *The Astrophysics of Planetary Habitability*

9. **Lincowski, Andrew** (2014). Finding the Needle in the Haystack: A High-Fidelity Solar System Model. In *5th National Capital Area Disk Meeting*

CONFERENCE PROCEEDINGS (POSTER)

1. **Lincowski, Andrew P.**, Meadows, V. S., Crisp, D., Robinson, T. D., Luger, R., and Lustig-Yaeger (2018a). Evolved Climates and Observational Discriminants for the TRAPPIST-1 Planetary System. In *AGU Fall Meeting 2018*, pages P41E–3776

2. **Lincowski, Andrew**, Meadows, V., Robinson, T. D., and Crisp, D. (2016c). The Effect of Carbon Dioxide (CO_2) Ice Cloud Condensation on the Habitable Zone. In *Exoclimes 2016*

3. **Lincowski, Andrew**, Roberge, A., Stark, C. C., Wilkins, A. N., Nesvold, E., and Haystacks Team (2015). Finding the Needle in the Haystack: High-Fidelity Models of Planetary Systems for Simulating Exoplanet Observations. In *American Astronomical Society Meeting Abstracts #225*, volume 225 of *American Astronomical Society Meeting Abstracts*, page 258.16

TEACHING & SERVICE

Referee for the journal *Astronomy & Astrophysics*

Mentor for UW Undergraduate student Tom Hemphill (2019)

Co-mentor for undergraduate intern Leah Zuckerman (summer 2019)

Teaching Assistant, ASTROBIO115 "Astrobiology" (Winter 2019)

Pre-Major in Astronomy Program co-mentor for Min Young Kim (Fall 2007–Spring 2018)

Co-mentor for Northwest Indian College Undergraduate students Melvin "Sunny" Miles and Renae Stanley (Summer 2017)

Teaching Assistant, ASTR101 "Astronomy" (Spring 2016)

Teaching Assistant, ASTR150 "The Planets" (Fall 2015)

PUBLIC OUTREACH

Seattle Science Slam presentation at local pub, "Characterizing Terrestrial Planets in the TRAPPIST-1 System with the *James Webb Space Telescope*" (2018)

Mensa Pacific Northwest, "Near-Future Characterization of Potentially Habitable Exoplanets" (2018)

Mensa Pacific Northwest Science Interest Group, "Proxima Centauri b: A Pale Purple Dot Orbiting the Nearest Star" (2016)